

Bremsstrahlung radiation and fast electron transport in laser-plasma interactions



Chris D. Armstrong

Department of Physics

University of Strathclyde

A thesis submitted for the degree of

Doctor of Philosophy

2019

Copyright Declaration

This thesis is the result of the author's original research. It has been composed by the author and has not been previously submitted for examination which has led to the award of a degree.

The copyright of this thesis belongs to the author under the terms of the United Kingdom Copyright Acts as qualified by University of Strathclyde Regulation 3.50. Due acknowledgement must always be made of the use of any material contained in, or derived from, this thesis.

Signed: *C. Armstrong*

Date: 01/10/2019

Abstract

This thesis reports on experimental investigations using high-intensity ($> 10^{18}$ W/cm²) laser pulses to ionise and accelerate electrons from thick solid targets in order to generate a bright bremsstrahlung source. Throughout the work the focus has been, firstly, to better understand the process behind the generation of x-rays within solid target interactions and, secondly, to apply this understanding to radiography of industrial samples. Across three experimental investigations aspects of the x-ray source are addressed; in the first the spatial evolution of the x-ray source is investigated; in the second a mechanism to increase conversion from laser into electrons is considered; and in the third a simple method to increase the conversion from electrons to x-rays is explored.

As part of the research presented within this thesis, a novel diagnostic was developed to overcome limitations in current diagnostics that measure the spatial characteristics of the emitted x-ray source. This diagnostic was a curved foil, designed to ensure that over a large field of view the x-ray experienced a uniform transmission length – reducing the inherent uncertainty in knife edge techniques. The foil was calibrated to ensure accurate measurements at x-ray energies > 100 keV and applied throughout the research herein to characterise the emitted profile.

The first experimental chapter explores the spatial characteristics of the x-ray profile. Using the curved foil, a two source structure was measured consistently in solid target interactions that emerges due to the recirculation of electrons. A narrow central source, and a broad secondary source. By defocus-

ing the laser (and reducing the intensity on target) the x-ray flux produced by the small central source dominates over the secondary source and produces a sharper radiograph. The flux of this second source was investigated through an analytical model that treated the sheath as a threshold to drive recirculation of electrons through the target. This model found good agreement with the measured results, and can be applied to predict the optimum defocus for different target materials and thicknesses.

The second chapter utilises a capillary target to trap the laser light and increase the conversion into electrons, the initial concept was to invoke numerous low intensity interactions as the laser propagated through the capillary. This would, in theory, produce a high flux – low temperature electron population that in turn would produce a high flux of x-rays. However, it was found that the flux increased but the temperature remained similar to that of a solid target. PIC simulations demonstrate that the electrons experience a series of accelerations within the capillary, undergoing direct-laser-acceleration (DLA) as lateral fields emerge within the channel.

The final chapter outlines a simple targetry change to confine and enhance the x-ray emission from solid targets. By using a standing wire geometry, instead of a foil target, the electron expansion is confined to the lateral extent of the wire. The resultant field that emerges on the surface of the wire is greater in magnitude than that of a foil and develops sooner into the acceleration window recirculating more of the electrons within the target. This results in a significant, 50%, increase in total x-ray flux from the same laser conditions, and an increase in imaging quality of $\times 2.6$ due to the increase in flux and the confinement of the lateral x-ray source.

Acknowledgements

To paraphrase a very old friend, 'a thesis is never late, nor is it early, it arrives precisely when it means to'.

This thesis, and the years of work that it represents, was possible because of the support of friends, family, and colleagues alike. Firstly I have to thank my three supervisors; Ceri, David, and Paul. You encouraged me to pursue areas that interested me, allowed me to fail at "fixing everything", and challenged my research to be better at each turn. Ceri; you are an extraordinarily talented communicator, able to explain the work you do to other scientists and a general audience alike. I will be forever thankful that you pushed me to do my own outreach. David, you are a kid in a sweet shop when it comes to science, the endless enthusiasm and persistent passion to figure something out, or measure something new, is a refreshing change to my constant cynicism. Also to Paul, the final check, I agonised over any draft I sent your way knowing that I had missed something simple and that in the morning I would see a PDF full of yellow highlights. Your attention to detail and - if my inability to stop italicising units is anything to go by - endless patience were unbelievably helpful to me.

I am fortunate to have worked with fantastic people throughout my PhD. To the group here and in Strathclyde I am grateful for all of the support on experiments, the arguing and explanations of physics so that I could get my head round it. Special thanks to Ross and Robbie, both of whom allowed me to sleep on a sofa after one too many down the Todd and invited me to every

experiment that had even a whiff of x-rays on. To Dean for being exactly the friend I needed throughout this PhD and despite his best protests there is still a chance he is Tyler Durdean. To Graeme for never asking how the thesis was going. To ESG, I'm sorry I never learned how to use the WASP system but I am incredibly thankful for all the support throughout this work. DC, Mags, the Robs, the Chrises, Dan, James, and Yiftak I am 100% sure that this place would grind to a halt without your expertise.

Despite a valiant effort on my part I did actually maintain the "life" half of a work-life balance. Well, maybe, quarter? Anyway... Mum you taught me to reason, and Dad you taught me to argue. If you take those away from science what is really left? I don't know when I started wanting to be a scientist, but I do know that without you both I never would have made it to where I am today. To my brother and sister, you now legally have to refer to me as Dr Armstrong in all correspondence, and in exchange I promise that I will only become slightly more unbearable. To Darryl and Louise, CUGMA is now an officially published acronym and I am forever grateful to be part of it. To Dean and Will, I think I now have time for that coffee.

Finally, to Jen. I couldn't have done it without you, and I wouldn't have wanted to either. This thesis is dedicated to you.

Role of the Author

The analysis and the simulations presented in this thesis have been conducted solely by the author. Development of the model presented in Chapter 5 was aided by discussion with D. R. Rusby, and the contrast model in Chapter 7 was the result of a series of discussions with D. Neely. For more information regarding the role in each publication, please refer to the Publication List.

Penumbral Foil The author designed and developed a curved foil diagnostic to accurately measure the hard x-ray source profile emitted from laser-plasma interactions. The diagnostic played a crucial role in measurements throughout the thesis. It is designed to mitigate the issues that arise with using conventional x-ray measurement techniques at high energies. These issues and the design are discussed in Chapter 4.

Chapter 5 The author was the Deputy Target Area Operator (DTAO) for the experimental campaign, designed and operated the diagnostic on which the measurements were taken. The accompanying electron data was acquired via a Cherenkov Fibre Diagnostic designed and operated by H. Li. The Target Area Operator (TAO) for the experiment was G. G. Scott. The analysis and development of the model presented were completed by the author.

Chapter 6 The author was the TAO for the experimental campaign, operated the penumbral diagnostic for the spatial x-ray measurements. The spectral x-ray measurements were taken by D. R. Rusby and J. Wragg via two scintillator rails initially designed and calibrated by D. R. Rusby. The optical backscatter diagnostic was operated by J. Wragg. The analysis of the experimental results was completed by the author. The PIC simulations were conducted on the SCARF computing cluster by the author.

Chapter 7 Data was taken from the same experiment as Chapter 6, the author was additionally responsible for primary imaging diagnostics. The analysis of the experimental data and the supporting PIC and Monte Carlo modelling was conducted solely by the author. The analytical model presented was developed by the author.

Publication List

The author contributed significantly to the papers below, which report on results obtained in the context of this PhD project.

1. **Bremsstrahlung emission profile from intense laser-solid interactions as a function of laser focal spot size.**

C. D. Armstrong, C. M. Brenner, E. Zemaityte, G. G. Scott, D. R. Rusby, G. Liao, H. Liu, Y. Li, Z. Zhang, B. Zhu, P. Bradford, N. C. Woolsey, P. Oliveira, C. Spindloe, W. Wang, P. McKenna, and D. Neely. *Plasma Physics and Controlled Fusion*, **61** 034001, (2019).

The author was DTAO on the experimental campaign, designed and operated the primary x-ray diagnostics used in this paper. Characterisation of the source profile and modelling was conducted solely by the author. The experimental results are discussed in Chapter 4

2. **Bremsstrahlung emission from high power laser interactions with constrained targets for industrial radiography.**

C. D. Armstrong, C. M. Brenner, C. Jones, D. R. Rusby, Z. E. Davidson, Y. Zhang, J. Wragg, S. Richards, C. Spindloe, P. Oliveira, M. Notley, R. Clarke, S. R. Mirfayzi, S. Kar, Y. Li, T. Scott, P. McKenna, and D. Neely. *High Power Laser Science and Engineering*, **7**, (2019).

The author was TAO on the experimental campaign, designed and operated the spatial x-ray diagnostics used in this paper. All analysis and simulations were conducted by the author, the experimental results and discussion are in Chapter 6.

3. Laser-driven x-ray and neutron source development for industrial applications of plasma accelerators.

C. M. Brenner, S. R. Mirfayzi, D. R. Rusby, **C. Armstrong**, A. Alejo, L. A. Wilson, R. Clarke, H. Ahmed, N. M. H. Butler, D. Haddock, A. Higginson, A. McClymont, C. Murphy, M. Notley, P. Oliver, R. Allott, C. Hernandez-Gomez, S. Kar, P. McKenna, and D. Neely. *Plasma Physics and Controlled Fusion*, 58(1):014039, (2016).

The author characterised the x-ray radiography images and operated the primary imaging diagnostics during this campaign.

4. Novel scintillator-based x-ray spectrometer for use on high repetition laser plasma interaction experiments

D R Rusby, **C D Armstrong**, CM Brenner, RJ Clarke, P McKenna, and D Neely. *Review of Scientific Instruments*, 89(7):073502, (2018).

The author helped to design and operate the scintillators over several experimental campaigns. Analysis techniques and routines were developed from discussions between the author and D. R. Rusby.

5. Effect of Rear Surface Fields on Hot, Refluxing and Escaping Electron Populations via PIC Simulations.

D R Rusby, **C D Armstrong**, G G Scott, M King, P McKenna, and D Neely. *High Power Laser Science and Engineering*, 7, E45. (2019).

The author helped write the analysis technique with EPOCH in MATLAB that was used in this research. The author helped to develop the principle model for electron behaviour in the sheath field and ran several of the simulations.

The author played a supporting role in the research reported in the following publications. Many of these were conducted at the start of the PhD education in order for the author to gain insights in experimental methods and working with high power laser systems. This includes preparing and operating crucial diagnostics used on the experiments and in the publications; such as, large area x-ray detectors for imaging and spatial measurements of the x-ray source.

1. **Pulsed x-ray imaging of high-density objects using a ten picosecond high-intensity laser driver.**

D. R. Rusby, C. M. Brenner, **C. Armstrong**, L. A. Wilson, R. Clarke, A. Alejo, H. Ahmed, N. M. H. Butler, D. Haddock, A. Higginson, A. McClymont, S. R. Mirfayzi, C. Murphy, M. Notley, P. Oliver, R. Allott, C. Hernandez-Gomez, S. Kar, P. McKenna, D. Neely. SPIE Security + Defence, pages 99920E. International Society for Optics and Photonics, (2016).

2. **Evaluating laser-driven Bremsstrahlung radiation sources for imaging and analysis of nuclear waste packages.**

C. P. Jones, C. M. Brenner, C. A. Stitt, **C. Armstrong**, D. R. Rusby, S. R. Mirfayzi, L. A. Wilson, A. Alejo, H. Ahmed, R. Allott, N. M. Butler, R. J. Clarke, D. Haddock, C. Hernandez-Gomez, A. Higginson, C. Murphy, M. Notley, C. Paraskevoulakos, J. Jowsey, P. McKenna, D. Neely, S. Kar, and T. B. Scott. Journal of Hazardous Materials, 318:694-701, (2016).

3. **Near-100 MeV protons via a laser-driven transparency-enhanced hybrid acceleration scheme**

A Higginson, RJ Gray, M King, RJ Dance, SDR Williamson, NMH Butler, R Wilson, R Capdessus, **C Armstrong**, JS Green, SJ Hawkes, P Martin, WQ Wei, SR Mirfayzi, XH Yuan, S Kar, M Borghesi, RJ Clarke, D Neely, and P McKenna. Nature communications, 9(1):724, (2018).

4. **Ellipsoidal plasma mirror focusing of high power laser pulses to ultra-high intensities.**

R Wilson, M King, RJ Gray, DC Carroll, RJ Dance, **C Armstrong**, SJ Hawkes, RJ Clarke, DJ Robertson, D Neely, and P McKenna. *Physics of Plasmas*, 23(3):033106, (2016).

5. **EMP control and characterization on high-power laser systems.**

P Bradford, NC Woolsey, GG Scott, G Liao, H Liu, Y Zhang, B Zhu, **C Armstrong**, S Astbury, C Brenner, P Brummitt, F Consoli, I East, R Gray, D Haddock, P Huggard, PJR Jones, E Montgomery, I Musgrave, P Oliveira, DR Rusby, C Spindloe, B Summers, E Zemaityte, Z Zhang, Y Li, P McKenna, and D Neely. *High Power Laser Science and Engineering*, 6, (2018).

6. **Experimental demonstration of a compact epithermal neutron source based on a high power laser.**

SR Mirfayzi, A Alejo, H Ahmed, D Raspino, S Ansell, LA Wilson, **C Armstrong**, NMH Butler, RJ Clarke, A Higginson, J Kelleher, CD Murphy, M Notley, DR Rusby, E Schooneveld, M Borghesi, P McKenna, NJ Rhodes, D Neely, CM Brenner, S Kar. *Applied Physics Letters*, 111(4):044101, (2017).

7. **Cherenkov radiation-based optical fibre diagnostics of fast electrons generated in intense laser-plasma interactions**

H Liu, G-Q Liao, Y-H Zhang, B-J Zhu, Z Zhang, Y-T Li, GG Scott, D Rusby, **C Armstrong**, E Zemaityte, P Bradford, N Woolsey, P Huggard, P McKenna, and D Neely. *High Powered Laser Science and Engineering*, 2095-4719 (In Press), (2018).

8. **Development of focusing plasma mirrors for ultraintense laser-driven particle and radiation sources.**

R Wilson, M King, R J Gray, D C Carroll, R J Dance, N MH Butler, **C Armstrong**, S J Hawkes, R J Clarke, D J Robertson, C Bourgenot, D Neely, and P McKenna. *Quantum Beam Science*, 2(1):1, (2018).

9. **Enhanced laser-energy coupling to dense plasmas driven by recirculating electron currents.**

RJ Gray, R Wilson, M King, SDR Williamson, RJ Dance, **C Armstrong**, C Brabetz, F Wagner, B Zielbauer, V Bagnoud, D Neely, and P McKenna. *New Journal of Physics*, 20(3):033021. (2018).

Contents

Copyright Declaration	i
Abstract	ii
Acknowledgements	iv
Role of the Author	vi
Publication List	viii
Contents	xiii
List of Figures	xix
List of Tables	xl
1 Introduction	1
1.1 Historical context of the research	1
1.2 Applications of laser plasma interactions	4
1.2.1 Inertial Confinement Fusion	4
1.2.2 Laser Driven X-ray Radiography	6
1.2.3 Manufacture and inspection	7
1.3 Thesis Outline	9
2 Laser-Plasma Physics	11
2.1 Electromagnetic (EM) Fields	11
2.1.1 Maxwell’s Equations	12

2.1.2	Laser Parameters	13
2.2	Single particle motion	14
2.2.1	Quiver Velocity	14
2.2.2	Ponderomotive Force	17
2.3	Ionisation	18
2.3.1	Multi-photon ionisation (MPI)	18
2.3.2	Tunnelling Ionisation and Barrier Suppression Ionisation	19
2.3.3	Collisional Ionisation	20
2.3.4	Field Ionisation	21
2.4	Plasma	21
2.4.1	Plasma Parameters	22
2.4.1.1	Definitions	23
2.4.1.2	Debye Length	23
2.4.1.3	Wave Equation	24
2.4.2	Laser propagation in Plasma	25
2.4.2.1	Dispersion relation	25
2.4.2.2	Critical Density	26
2.4.2.3	Scale Length	26
2.4.2.4	Refractive Index	27
2.5	Absorption	29
2.5.1	Inverse Bremsstrahlung	29
2.5.2	Vacuum Heating	29
2.5.3	Resonance Absorption	30
2.5.4	$j \times B$ Heating	32
2.6	Electron Spectra	32
2.6.1	Distribution	33
2.6.2	Electron Temperature	34
2.7	Summary	36

3	Fast electron transport and radiation	37
3.1	Electron Transport	37
3.1.1	Return Current	38
3.1.2	Electron Divergence	39
3.1.3	Internal Field Growth	40
3.1.4	Sheath Development	43
3.1.5	Target Normal Sheath Acceleration	46
3.2	X-ray Generation	47
3.2.1	Bremsstrahlung	48
3.2.1.1	Line Emission	50
3.2.1.2	Emitted Spectra	52
3.3	K-alpha and bremsstrahlung emission	53
3.4	X-ray Attenuation	55
3.4.1	Detected X-ray Emission	58
3.5	Summary	62
4	Methodology	63
4.1	High intensity lasers	63
4.1.1	Amplified Spontaneous Emission	64
4.1.2	Plasma Mirrors	65
4.1.3	Laser Facilities	67
4.2	Detectors	68
4.2.1	Image Plate	69
4.2.1.1	IP Resolution	71
4.2.2	Scintillators	72
4.3	Measuring X-ray Source Size	73
4.3.1	Low energy (< 50 keV techniques)	74
4.3.2	High-energy, high resolution, approach	76
4.3.2.1	Penumbral Foil Characterisation	78

4.4	Characterising emitted x-ray spectra	81
4.5	Numerical Modelling	83
4.5.1	Monte Carlo Codes	84
4.5.2	PIC Codes	85
4.6	Summary	86
5	Investigation of recirculating electrons in solid targets as a function of laser intensity for x-ray generation	87
5.1	Introduction	88
5.1.1	X-ray production for recirculating electrons	89
5.2	Experimental Investigation	91
5.2.1	Layout	91
5.2.2	Focal Spot	92
5.2.3	Penumbral Measurements	94
5.2.3.1	Flux measurements	94
5.2.3.2	Spatial X-ray Measurements	98
5.2.4	Spatial Contrast Improvement	101
5.3	Analytical Modelling	103
5.4	PIC Simulations	109
5.4.1	Simulation Parameters	109
5.4.2	Sheath Field Strength	110
5.4.3	Divergence	112
5.5	Conclusion	115
6	Investigation into fast electron dynamics and laser propagation within laser-guiding capillary-targets	117
6.1	Complex Target Structure	118
6.2	Capillary target design	119
6.2.1	Experimental Investigation	121
6.2.2	Experimental Results	125

6.2.2.1	X-ray Measurements	125
6.2.2.2	Probing the laser-interaction	129
6.3	Discussion	130
6.3.1	Laser propagation model	131
6.3.2	Effect of laser divergence	135
6.3.3	Glancing Angle Considerations	136
6.4	Modelling	139
6.4.1	Effect of glancing angle interactions with the capillary walls	140
6.4.2	Effect of laser polarisation on spatial electron profile . .	143
6.4.3	Summary of simulations	145
6.5	Successive Acceleration	146
6.6	Conclusion	152
7	Optimising x-ray source characteristics for large scale radiography	153
7.1	X-ray Radiography with laser driven sources	154
7.2	Spatially Constrained Targets	155
7.2.1	Experimental Campaign	157
7.2.1.1	Spatial x-ray emission profile	160
7.2.1.2	Spectral x-ray characterisation	162
7.2.2	PIC Modelling	164
7.2.3	Monte-Carlo Modelling	169
7.2.4	Radiographs	173
7.3	Forming an image	174
7.3.1	Spectral optimisation for object and detector	177
7.3.2	Effect of atomic number	181
7.4	Conclusion	183
8	Conclusion	185

8.1	Investigation of recirculating electrons in solid targets as a function of laser intensity for x-ray generation	186
8.2	Investigation into electron dynamics with laser-guiding capillary-targets	187
8.3	Optimising x-ray source characteristics for large scale radiography	188
8.4	Future work	189
8.4.1	Tapered Capillary Targets	190
8.4.1.1	Phase Contrast Imaging	191
Appendix A		193
A.1	Considerations for the recirculation model in Chapter 5	193
A.1.1	X-ray radiography data	193
A.1.2	Escaping electron data	195
A.2	Considerations for the contrast model presented in Chapter 7 .	196
A.2.1	Demonstration of contrast	196
A.2.2	Image Plate	197
A.2.3	Scintillators	198
A.3	Kramer’s law for electron to x-ray energy	199
Appendix B		200
B.1	Comparison of laser-wakefield acceleration to “conventional” techniques	200
B.2	Derivation of the dispersion relation	201
B.3	Vulcan laser system	202
B.4	Numerical Modelling	204
Bibliography		206

List of Figures

1.1	Plot of achievable short pulse laser intensity since the invention of CPA, with notable laser facilities marked including three future facilities designed to reach higher intensities. Trend taken from [1], commissioning date and peak laser intensity collated from references [2–9].	2
1.2	Laser driven fusion as an energy source. (a) laser heats the outer shell of the fuel capsule, (b) core compresses and heats until (c) the core ignites and re-expands. In this schematic; 1. Cold uncompressed fuel, 2. Incident laser pulses, 3. Outer shell, 4. Ablated plasma, 5. Imploding core, 6. Hot spot ignition.	5
1.3	Schematic for x-ray radiography of a sample with internal structure. Laser accelerates electrons through a target, these electrons generate x-rays as they interact with the target. These x-rays illuminate the object, and as they are highly penetrative, variations in the density can be probed. Radiography from Brenner <i>et al.</i> [10].	6
2.1	The peak energy as a function of laser intensity for a single electron. E_{max} at 10^{19} and 10^{20} W/cm ² are shown in red and blue respectively [11].	16
2.2	Schematic of ionisation mechanisms. (a) multi-photon ionisation, (b) tunnelling ionisation, and (c) barrier suppression ionisation. Figure adapted from Reference [12].	20

2.3	Schematic of the four principle states of matter, each transition requires additional energy to break bonds between the molecules or, for plasma, free the electrons via ionisation. (a) Solid, (b) liquid, (c) gas, and (d) plasma. Grey circles represent neutral atoms, the red and blue circles in (d) represent electrons and ions respectively.	22
2.4	Schematic of a P-polarised laser pulse travelling through a pre-plasma with the scale length L_s . Red line indicates the path the laser takes, refracting away from the critical surface as the density increases. The dashed lines represent different densities within the pre-plasma; the turning point $n_c \cos^2(\theta_L)$ (Section 2.4.2.4), the critical density n_c , the relativistic critical density γn_c , and solid density n_c at the target surface [13].	31
2.5	Electron distributions of the form Eq. 2.46 - 2.47 and a Boltzmann distribution for a 1 MeV electron temperature. The inset shows the relationship between spectral peak and temperature for each distribution.	34
2.6	Electron temperature (in MeV) for different laser intensities as calculated by Beg (Eq. 2.48) and Wilks (Eq. 2.49) scaling laws.	36

3.1	Schematic of the mechanisms discussed in the following sections acting throughout a solid target. (a) Factors affecting the effective divergence of the electron beam. From left to right, ponderomotive ejection, hole-boring, collisional scattering, and field effects. (b) Electron current motion, depicting the major components of electron travel; hot, return, and recirculating/refluxing. (c) Field components inside the target and the sheath formation on the rear surface accelerating ions. During transport, magnetic field growth happens azimuthally to the beam resulting in hollowing (B_h) and pinching (B_p) magnetic fields.	39
3.2	Field lines of a charge in a travelling frame at ν , (a) Field lines at t_0 , (b) Field lines at t_1 after charge has accelerated to ν' , where $\nu' > \nu$. Radius of the inner circle is $r = ct$	48
3.3	Bremsstrahlung is generated as the electron decelerates in a field. The energy of this photon is dependent on the approach distance b and the energy of the incident particle.	50
3.4	Line emission is typically a by-product of collisional ionisation; as the lower electron is ionised through collisions and higher orbital electrons then decay to the lower levels emitting characteristic energies. The most common of these transitions is from the L (E_2) shell to the K (E_1) shell resulting in a K-alpha x-ray being emitted.	51
3.5	Total x-ray spectra from a 1 mm Ta thick target (black) 2.5 MeV temperature incident electron beam, modelled in GEANT4 assuming a single pass through the target. Single temperature fit is shown by a dashed white line. The shaded areas correspond to the two primary spectra regions, low energy (blue) dominated by target attenuation and the high energy (red) dominated by the Bremsstrahlung continuum.	52

3.6 Electron stopping power in copper. The solid line is the collective stopping, dashed is collisional, and dotted is radiative. K-alpha emission is caused by the first process and bremsstrahlung by the second. Cross-sections from the NIST ESTAR database [14]. 54

3.7 Cross-sections for the various processes occurring in x-ray attenuation for iron. Calculated from the NIST XCOM database [15] 58

3.8 (a) Schematic outlining the production of x-rays throughout a target, each slice of the target is denoted by x_n , which has thickness dl . (b) Peak detected x-ray energy as a function of effective x-ray temperature, the peak signal approaches 70 keV as the effective x-ray temperature is increased $> \text{MeV}$. There is an increase in expected energy on the rising edge for increased target thickness as self-attenuation hardens the emission of x-rays. . . 60

3.9 GEANT4 simulation results. (a) Number of detected x-rays as a function of their energy, an exponential fit of distribution is shown with an effective temperature of $\sim 37 \text{ keV}$. (b) The number of detected x-rays as a function of the incident electron energy. 61

3.10 Primary electron energy responsible for x-ray generation in Figure 3.8 as a function of temperature, determined from the graph shown in Figure3.9(b). Shaded region shows the area greater than 0.5 in Figure3.9(b) 61

4.1 Chirped pulse amplification. *From left to right*: initial short pulse, stretched pulse, amplified stretched pulse, re-compressed pulse. Damage threshold is indicated, compression only occurs under vacuum with minimal remaining optics in path. Schematics for each stage are shown above the pulse shape. 64

4.2	Laser temporal contrast. Contrast trace for Vulcan Petawatt, key features of the pulse are identified [16].	66
4.3	Plasma mirror operation, demonstrating the optical switching allowing transmission of the ASE and reflection of the main pulse. Image from Wilson [16]	67
4.4	Summary of detectors with respect to their x-ray energy sensitivity and resolution. The circles indicate categories of detector and their working ranges. ‘Passive’ detectors are primarily single shot, or require significant time between exposures. (γ , X) detectors are limited by the radioisotopes half-life (seconds-hours), and the spatial resolution comes from imaging the decay signal using a secondary detector. CCDs and scintillators can operate at many Hz repetition.	69
4.5	(a) raw image, (b) de-blurring function, (c) Gaussian-filtered image, (d) lineouts across each image at the transition from light to dark.	71
4.6	Inorganic scintillation schematic, the incident photon (1) excites the electron to the conduction band (2) with many times the binding energy, it collides with many other atoms in the crystal causing further excitation (3), these electrons eventually decay through the presence of activator crystals (4)	73
4.7	Bragg diffraction in crystals. Grey dots indicate the lattice structure of the crystal, and the red dashed line indicates the path of x-rays reflecting off the lattice structure.	75
4.8	Pinhole camera schematic, the hole - smaller than the source - projects an x-ray image onto the detector plane.	76

4.9	Schematic of issues with the standard penumbral technique at high energies. LHS shows increasing energy for a thin foil, RHS shows that increasing the foil thickness to offset the increased transmission introduces a different error.	77
4.10	Penumbral imaging x-ray measurement. The transition region between signal and dark is a projection of the source profile. . .	77
4.11	(a) Profile. (b) surface roughness, (c) is a convolution of the x-ray transmission and segment length through the determined radius of curvature to determine the depth at which 75% of the x-rays are attenuated.	78
4.12	PSF Simulation. (a) Schematic of GEANT4 simulation, red represents the x-rays emitted from a point source, (b) Histogram of x-rays recorded in the detector plane for 400 keV x-rays. (c) PSF as a function of x-ray energy for detector and just considering the foil (black).	80
4.13	Schematic outlining the expected response from a two source x-ray signal, red is the brighter central region surrounded by a larger substrate source (grey).	81
4.14	Isolating the central source from a full penumbral lineout. (a) Raw lineout (blue) with the gradient (orange) from the lineout, (b), highlighted gradients of the central (red) source and substrate (black) (c) isolated source profiles and flux contributions.	82
4.15	LYSO scintillator design. (a) Schematic of design, edited from Rusby <i>et al.</i> [17], (b) spectral response from fielded diagnostic, calculated using the NIST cross-section database [15]	82
4.16	Generalised process for PIC simulations, this cycle is completed numerous times for each population over the lifetime of the simulation.	85

- 5.1 Two source components for x-ray emission, (a) first pass of electrons through the target, (b) subsequent electron recirculation. The main channel of accelerated electrons (1) which travel through the target generating x-ray radiation (3). At the rear surface, electrons with energy lower than the potential are reflected, those with more energy can escape and cause the formation of the sheath field (2) through charge separation. Electrons can then recirculate the target due to this sheath field (4) and spread laterally through the target. These electrons can still have significant energies, \sim MeV, and thus still generate bremsstrahlung (5) as they continue to travel through the target. 90
- 5.2 (a) Top view of the experimental layout, showing the distances to the penumbral foil and detector stack, and the positioning of the Cherenkov diagnostic. θ is 15° , denoting the angle of the target from laser axis. Between the detector and the source is an 18 mm SiO₂ filter. (b) Absorption as a function of energy for the x-ray detector. Dashed line highlights peak response x-ray energy, \sim 50 keV. 92
- 5.3 Focal spot from the experimental campaign measured from images taken with the CW laser. (a) Width of the focal spot, ϕ_L , as a function of defocus, ΔZ , the dashed line is a fit with Eq. 5.2. (b-d) normalised images of the spot at $\Delta Z = -50, 0$, and $400 \mu\text{m}$, respectively. 93
- 5.4 X-ray and electron flux for varying focus position. (a) Total X-ray flux (black) and escaping electron (red) number per laser Joule, each are divided by the mean of the data to allow direct comparison. (b) X-ray flux at 50 keV contributed by each source, central (red) and substrate (blue) - origin of which is shown in Figure 5.1. Lines of best fit (dashed) are included as a visual aid. 95

5.5	Electron number $\sum f(E_h)$ (left axis) and total energy $\sum f(E_h) * E_h$ (right axis) as a function of intensity. Calculated using the Beg scaling law [18] and the absorption results by Davies [19] for a Maxwellian distribution of electrons.	96
5.6	Comparison between the x-ray flux in each region of the x-ray source for varying focus position. Ratio of the central source to the substrate source, more flux is contributed by the central source for increasing defocus. Inset shows the attenuation length, $\lambda_{Att.}$, normalised to the target thickness, d , for electrons with energy $E = k_B T_e$ in a copper target for Wilks (orange) and Beg (blue) scaling law as a function of defocus position.	98
5.7	Central and substrate x-ray source size as a function of defocus. (a) Central source size as measured (red), with the expected size from a simple geometric expansion for different electron divergences also shown (black dashed lines). (b) Source size for substrate x-ray source as a function of defocus position.	99
5.8	Electron divergence as a function of on target intensity, calculated from the central source measurements. Measurements from this experiment (red) extend the trend seen in numerous experiments collated by Green <i>et al.</i> (black), references of each in [20].	100
5.9	Brightness of the central and substrate sources as a function of defocus position showing an increase in central brightness as the laser is defocused.	102
5.10	Comparison of varying defocus in radiographs, (a) target at best focus, (b) target at -300 μm defocus. The significant image contrast improvement by reducing, or removing, the secondary source is clear.	102

- 5.11 Maxwellian distribution for electrons with temperature $k_B T_e$ at two different laser intensities, (a) High $I_L = 1 \times 10^{20}$ W/cm² and (b) Low $I_L = 4 \times 10^{18}$ W/cm², this correlates to the laser at best focus and 150 μ m defocus. The red dashed line indicates electron transmission through the target, black dashed line is the escape energy cut-off. The population of electrons between these two lines contributes to the substrate source (unshaded), the other two (red - collisional, grey - escaping) can only contribute to the central source. 105
- 5.12 Results from the analytical model. (a) Population of electrons that contribute only to the central source, Eq. 5.4 (black) as a function of defocus, the percentage of the electron spectra that are collisionally attenuated on the first pass (red), escape the target (blue), or recirculate the target (green). The relativistic correction from Maxwell-Juttner distribution is shown by the filled area for each population. (b) is the ratio of the central to the substrate source calculated as $\eta_R/2(1 - \eta_R)$, to account for the directionality of bremsstrahlung, for a Maxwell distribution (solid) and a Maxwell-Juttner distribution (dashed) with the experimental data in red, the model uses laser conditions from the experiment and Beg scaling to determine the electron spectra [18].107
- 5.13 Calculations using the analytical model. The central x-ray flux calculated for various targets: copper - solid, tantalum - dashed, and aluminium - dot-dash, the peak flux shown with a blue asterisk. 108

5.14	Sheath field from EPOCH simulations. (a) Peak field strength as a function of defocus, inset shows a figure of the sheath for the best focus simulation at 425 fs. (b) Sheath field potential as a function of mean electron temperature, in agreement with the model this potential scales linearly with electron temperature. The temperature was calculated at 425 fs.	111
5.15	Electron spectra from EPOCH simulations (a) best focus and (b) 150 μm defocus. The multiple temperature distribution are shown as independent fits with the corresponding temperature shown.	112
5.16	Electron density at best focus. (a) Electron density at 425 fs, front target surface is indicated by the dashed line at $X = 0 \mu\text{m}$. (b-c) Lineout of electron density at front (b) and rear (c) surface - averaged over the corresponding shaded region in (a). (d-f) is the same as (a-c) for the -75 μm defocus simulations.	113
5.17	X-ray emission area for central and substrate sources inferred by the hot electron divergence and the total stopping range for the accelerated electron population. Experimental and simulation results are normalised to best focus. a) central source, b) the substrate source.	114
5.18	The divergence of hot electrons as a function of time calculated from the electron momenta during the simulation.	115
6.1	Schematic showing laser interaction with a capillary target. (a) Demonstrates the single ray approximation that will be explored again in Section 6.3.1, (b) Demonstrates the various modes that will develop as the beam defocusses into the capillary.	120

6.2	Prototype capillary targets. (a) Schematic outlining the key target measurements; (b) image and measurements of one of the targets shot during the experimental campaign.	121
6.3	Schematic of the targets with key dimensions labelled. Solid wire targets (a) Vertical and (b) Horizontal orientation. (c) Capillary target. In each case the primary material is gold, capillary targets have a inner layer of glass.	122
6.4	Initial laser conditions with target geometry. (a) Schematic of the spot size due to glancing angle, (b) calculation of peak intensity as a function of angle (dashed line is 5° glancing angle).	122
6.5	Schematic of the primary imaging diagnostics. The set-up is the same as in Chapter 7. The main image shows the penumbral foils and X-ray spectrometers. The inset is an expansion of the penumbral foil set-up, with the grey cones representing the forward x-ray emission from the capillary walls. Magnets are required to remove the escaping electron population from the target. (All distances in mm measured from target position). . .	123
6.6	Detected x-rays in the experimental set-up. (a) Response curve for the image plate detectors through the chamber port, created from the NIST transmission tables [15]. (b) The peak x-ray energy as a function of x-ray temperature and attenuation length, at the low temperatures expected from the interaction with a capillary wall, the peak x-ray energy is at the K-edge of the barium in the image plate.	125
6.7	X-ray emission from each target measured by the gamma-spectrometers. (a) The effective X-ray temperature determined via the method outlined in Reference [21] and Chapter 4, (b) the first crystal flux converted into absorbed photons per mm.	126
6.8	Vertical and horizontal source size for each target configuration.	128

6.9	Penumbral profile from a capillary target from the (a) horizontal penumbral and (b) the vertical penumbral, demonstrating the source contribution from each wall is resolved in the horizontal axis. The walls measure as (31 ± 3) and (36 ± 3) μm FWHM - slightly larger than the actual profile of the walls as discussed in the text. In each graph, the signal across a transition is shown in blue, and the gradient in orange.	128
6.10	Data from the backscatter diagnostics. (a-b) Capillary and horizontal wire backscatter images; (c) backscattered spectrum for capillary (red) and horizontal wire (blue).	129
6.11	Schematic of collimated beam reflections through the capillary, the separation between the central axis of each interaction is shown.	131
6.12	Reflectivity of plasma mirror compiled from the results by Ziener <i>et al.</i> and Dromey <i>et al.</i> (black), with high intensity values by Streeter <i>et al.</i> (blue) [22–24]. The fit is a polynomial and was used to interpolate the reflectivity in the discussion.	133
6.13	Laser interactions with the capillary walls for 3 different angles (a,d) 15° , (b,e) 5° , (c,f) 2° . (a-c) show the path for a collimated laser, red is the centre axis and blue the edge of the beam. (d-f) show the number of injected electrons and the temperature from each interaction.	134
6.14	Number of electrons and average temperature accelerated at the capillary wall for varying incident angle. Capillary dimensions are fixed with a $20 \mu\text{m}$ aperture and 2 mm in length, each interaction is summed to determine the electrons injected.	135

6.15	Schematic of laser light focusing into a capillary for (a) $\theta_L < \theta_f$, (b) $\theta_L > \theta_f$. The maximum surface area that can be illuminated is determined by Eq. 6.4. In both panels the first interaction area is shown in red and the second in blue. The grey arrows in (a) indicate the angular range of laser that escapes from the capillary before interacting with the walls.	137
6.16	E_c as a function of channel length, l , taken from Figure 10 in Reference [25] at the point where N first drops to 1. Dashed line is a linear scaling of the form $E_c \propto l$	139
6.17	Electron spectra for each angle of incidence within the capillary. Spectrum was taken at the time step with the most accelerated electrons for each simulation.	141
6.18	Spectra of electrons in the wall (red dashed) and in the capillary (red solid) at separate times throughout the 5° simulation. Compared to a solid wire (black) under the same laser conditions, the capillary quickly exceeds the total number and temperature. The temperature of the electrons within the capillary and within the walls is $k_B T_h = (3.5 \pm 0.3)$ MeV, compared to the solid target of $k_B T_h = (0.9 \pm 0.1)$ MeV at $t = 500$ fs.	142
6.19	Hot electron density in 3D. (a) View from above demonstrating two lobes of electrons on either wall corresponding to the P-pol acceleration. (b) Side view of the target. (c) A cut through of the capillary showing the electron lobes emerging only in the horizontal axis for P-Pol and (d) the vertical axis of S-Pol. Each plot is taken at $t = 250$ fs.	144
6.20	Integrated electron density in the horizontal (blue) and vertical (orange) direction from the 3D simulation in Figure 6.19(c).	145

6.21 Schematic of direct laser acceleration within a channel, the electron path is shown as a black dashed line in each panel. (a) The laser E_y field travelling through the channel at ν_{ph} the electron is trapped within the influence of the laser by the quasi-static E'_y field in (b). At each turning point the electron falls in phase with the laser field ($R < 1$) and the electron is accelerated forward. 147

6.22 Peak intensity from the simulation within the capillary target during the simulation. No evidence of significant self-focusing of the laser. 148

6.23 Variation of scale length simulation results. E_y field averaged over 10 laser cycles for (a) 5 μm and (b) 2 μm scale lengths, and (c) $0.05n_c$ pre-filled capillary with 0° incident angle. Electron acceleration with varying scale length. (d) The density profile at the beginning of the simulation. (e) Accelerated spectra for the three conditions simulated. 149

6.24 Electron trace throughout the simulation. (a) The longitudinal electric field (E_x) profile (red-blue colour scale) acts to continuously accelerate the electron (scatter plot) forward; the energy is shown by a secondary colourbar. (b) Similar trace to (a) but for the transverse field (E_y) structure, arrows in each indicate the direction of force for the quasi-static fields reinjecting electrons back into the channel. (c) The macro-particle energy and R value as it transports through the target. During each crossing of the channel the electron drops further below $R = 1$ and is subsequently accelerated. The field in (a) and (b) is normalised to the laser electric field $E_0 = \sqrt{\frac{2I_L}{cn\epsilon_0}}$ 150

6.25	Electron energy distribution as a function of capillary length. (a) Electron spectra for 50 (blue), 100 (black), and 200 (red) μm capillaries. (b) Maximum energy as a function of capillary length, demonstrating an almost linear scaling.	151
7.1	Schematic for x-ray absorption radiography of a sample with internal structure. X-rays illuminate the target, and as they are highly penetrative, variations in the density can be probed. Radiography from Brenner <i>et al.</i> [10].	154
7.2	Targets used in the Experimental campaign, (a-b) foil targets, (a) top view with laser incidence highlighted (b) front view, (c) side view of wire target.	157
7.3	Focal spot measurements for the experimental campaign. (a) Focal spot image, an average of five 1 ms exposures, (b) horizontal and vertical lineouts of the spot with associated FWHM, (c) the encircled energy as a function of spot radius - within the FWHM $\sim 37\%$ of the energy was contained.	158
7.4	Schematic of the primary imaging diagnostics, setup is the same as the one in Chapter 6. Main image shows the emission line, with penumbral foils and X-ray spectrometers included. The inset is an expansion of the penumbral foil setup, the grey cone represents the forward x-ray emission from target. Magnets, blue in the figure, are required to remove the escaping electron population from the target. All distances in mm measured from target position. The chamber port attenuates the emitted x-ray spectra.	159

7.5	Critical detected energy as a function of target thickness for gold. Determined as the peak x-ray energy detected assuming a Boltzmann distribution of 200 keV and target attenuation from half the target thickness, using the NIST data tables [15].	160
7.6	Penumbral radiograph and lineout for (a) foil, and (b) wire target. The dashed line in each radiograph is where the lineout is determined. In the top panels the lineout is in black and the gradient in orange.	161
7.7	Spatial measurements taken from the penumbral foils. (a) Vertical and horizontal source from target types and materials measured by the penumbral foils, (b) are normalised lineouts (black) and gradients (orange) from a thick, thin, and a wire target. . . .	162
7.8	Spectral measurements taken from hard x-ray spectrometers 11° from target normal, single shot measurements made in parallel to source size measurements. (a) is the flux on the first crystal per incident laser Joule, (b) is the temperature of the x-ray emission inferred via the technique outlined in Rusby <i>et al.</i> [26]. . . .	163
7.9	Results from PIC simulations. (a) Electron density (red scale) and E -field (blue scale) spatial maps for the foil simulation at 500 fs. (b) same as (a) but for wire simulation, E -field is limited to $X > 7 \mu\text{m}$ to show the pre-plasma on the surface of the wire. (c) Cumulative on-axis electron density over the entire simulation. 0 μm indicates front surface for each target, (d) Refluxing electron spectra with a two-temperature distribution (dashed lines), see Table 7.2 for values.	166

- 7.10 Pathlength of electrons inside the target. (a) Diagram of additional R for foil targets, at the boundary the propagation angle θ_e is calculated from the electron momentum this gives the additional pathlength of electrons not simulated. (b-c) The fraction of total electron population, as a function of energy, that has an internal pathlength, R , of (b) $R > 2l$ and (c) $R > 4l$, where l is the target thickness (or wire diameter). 167
- 7.11 Plot of percentage of target surface covered with a $E_{sheath} > \alpha_\phi$ as a function of time for each target geometry. Where (a) $\alpha_\phi = 1$ TV/m, (b) $\alpha_\phi = 2.5$ TV/m. The dashed lines are fits to the data. 168
- 7.12 Output from the visualisation of GEANT4 simulation for (a) Wire and (b) Foil geometry. The red lines are electron trajectories and the green x-ray. From this visualisation the lateral expansion in the foil is clear. 169
- 7.13 Spatial output from the GEANT4 simulations (a) source location of detected x-rays within a 25 μm wire target. (b) Same as (a) but for a foil target. (c) Horizontal line out of each source with the FWHM displayed as text. (d) Horizontal source size as a function of target thickness showing a similar trend to Figure 7.7(a). In plots (c-d) red is used for the wire targets, and blue the foil. 170
- 7.14 Spectral output from the GEANT4 simulations (a) Emitted x-ray spectra using the simulated temperatures from EPOCH, temperature fits shown with a dashed line. K- α line in gold shown with a black dot line. (b) X-ray temperature as a function of target thickness showing a similar trend to Figure 7.8c). 171

7.15	Spectral output from GEANT4 simulations with EPOCH electron spectra. a) The emitted x-ray spectra for 1 MeV Maxwellian distribution in each target configuration b) Emitted x-ray spectra using the simulated temperatures from EPOCH with the foil spectra in the wire and wire spectra in the foil geometry.	172
7.16	Demonstration of the reduced source size from narrow wire targets, (a) is heavily processed XRT imaged acquired over several shots, (b) a single-shot acquisition from a 100 μm foil target, and (c) a single-shot acquisition from 100 μm wire target. (d) is the edge-spread-function (ESF) taken at the edge of the penny for both the foil and wire targets.	173
7.17	100 keV spectral shape for Al (black) and Au targets in the contrast model.	177
7.18	Parameter phase-space for x-ray temperature and flux using a high-Z spectral shape. The solution to Eq. 7.3 for the uranium sample outlined in Section 6.1.1 for different detectors (a) SR image plate, (b) 10 mm LYSO Scintillator. For $C > 0$ the image is resolved with $C \rightarrow 1$ producing the optimal image.	178
7.19	(a) Schematic of standard NWB from international standards document [27, 28]; 5 mm cylinder of U-238 to demonstrate transmission, grout interior is made from concrete and the barrel is modelled as iron. (b) Eq. 7.3 for a standard NWB, dashed line indicates a total x-ray energy of 0.1 J.	179

7.20 (a) Radiograph of the fanblade from Brenner *et al.* [10] shown with (b) lineout and contrast of the feature. Hexagonal pattern from the interior is a titanium mesh in place to provide structural support without adding significant mass to the fanblade. (c) The phase-space (determined by Eq. 7.3) for the fanblade and an image plate detector, dashed line indicates a total x-ray energy of 0.1 J, and the red asterisk shows the estimated conditions from the experiment. 180

7.21 Most transmissive photon energy and associated attenuation cross section coefficient for varying atomic number. This demonstrates that the most transmissive energy decreases with increasing Z . 181

7.22 Scattered transmission ratio as a function of Z and photon energy. Simulations were conducted at $Z = (6, 13, 22, 26, 50, 73, \text{ and } 92)$ for 100 logarithmically spaced energies between 10 keV and 100 MeV, the results were then interpolated via a Gaussian fitting function to produce to full parameter space. 183

8.1 Target schematic demonstrating the tapered capillary. The opening aperture is as large as the spatial jitter of the laser; the closing aperture is smaller than the initial spot to drive an increase in intensity. Black bars on the exterior surface are a high- z material to increase the generation of bremsstrahlung. 190

8.2 Source size required for phase-contrast imaging with respect to different object distances, calculated using Eq 8.1. 192

A.1	Radiography and model results from 2013 experiment. (a-c) radiographs for Best focus, -100 μm , and -200 μm defocus respectively. Lineout was taken at the edge of the feature averaged over 50 pixels (px). (d) Normalised lineouts for the image. (e) Model results for experimental conditions in (a-c), demonstrating a peak between 100 – 200 μm defocus where the best lineout was observed experimentally.	194
A.2	Model comparison with escaping electron data from Rusby <i>et al.</i> [17]. Black - model predictions for escaping electron number $E > 1$ MeV. Red - measured electron number from wraparound diagnostic.	195
A.3	Visual demonstration of the parameter C from Eq. 7.2 with lineouts.	197
A.4	(a) Schematic of a lens field of view from a scintillator. (b) QE curve for an AVT Manta Camera. Data taken from AVT Website: https://www.alliedvision.com/en/products/cameras/detail/Manta/G-1236.html	198
A.5	The relative x-ray yield for electrons in a gold target, computed from Kramers Law Eq. A.2 [29].	199
B.1	Comparison of scale between conventional RF accelerators and laser-wakefield interactions. (a) A schematic of the Diamond Light Source at RAL (b) shadowgraph of a plasma channel in a laser-wakefield gas cell, edited from Cole [30].	201

- B.2 (a) Leap-frog calculations of field and momenta in EPOCH - equations are taken from Arber *et al.* [31]. (b) Schematic of macro-particle operation within PIC simulations; the macro-particles are the large red circles with a gradient fill demonstrating the relative particle density at the limits of the macro-particle volume, the black and blue dots at fixed cell positions represent the current density and field calculation points respectively 204

List of Tables

4.1	Image plate composition for TR and SR types, schematic diagram included for clarity.	70
5.1	EPOCH simulation parameters. ^a front surface is at $X = 0 \mu\text{m}$. . .	110
6.1	EPOCH simulation parameters. Capillary starts at $4 \mu\text{m}$ to prevent the laser clipping as it enters the simulation.	141
7.1	EPOCH simulation parameters. ^a limited to $X = +7 \mu\text{m}$ for the wire. ^b values in parenthesis indicate wire simulation.	165
7.2	EPOCH and GEANT4 simulation results, N_γ for the wire simulations is normalised to the foil results.	171
B.1	Summary of laser parameters for each target area in the Vulcan laser system. For both areas the primary wavelength is $1.054 \mu\text{m}$. The shot rate is one per 20-45 minutes, some amplifiers are shared between the areas requiring delay between TAP and West shots.	203

Chapter 1

Introduction

This thesis encompasses experimental and numerical investigations conducted by the author into laser-plasma interactions, examining in detail the resultant x-ray emission. The escaping x-rays can be utilised as both an indicator of internal electron behaviour [17, 32–34] and as a potential source for industrial radiography [10, 35–39]. Herein the x-rays are used as a method to determine the hot electron properties and their application to radiography is discussed.

1.1 Historical context of the research

The ‘laser’ itself was first conceived by Albert Einstein in 1917 [40], the name being an acronym that outlines the foundational process: Light Amplification by Stimulated Emission of Radiation. The principle of the laser can be outlined as follows:

- The gain medium is initially in a ground state of E_1 .
- A majority of the atoms are excited to a long lifetime higher state E_2 .
- Incident photons then perturb the electrons and *stimulate* decay to E_1 .
- The excited atoms *emit* photons with energy $E_\gamma = E_2 - E_1$

Whilst the laser was theoretically outlined in the early 20th century it took another 50 years for experimental demonstrations to be completed; first with a

'MASER' (microwave, instead of light) by Shawlow and Towns [41] in 1958 and then Maiman with an optical demonstration in 1960 [42]. Since then, development in new laser technologies has been rapid. Techniques such as Q-switching and mode locking prompted a surge in laser intensities as controlled short pulses became attainable. However, the development of the chirped-pulse-amplification (CPA) technique in 1985 [43], for which half of the 2018 Nobel Prize was awarded [44], resulted in a renewed surge of advances in high-power short-pulse laser intensity. This transition over time is outlined in Figure 1.1. Throughout this research the author used the Vulcan laser system for the majority of the experimental campaigns. Vulcan is a petawatt class laser based at the Central Laser Facility in the Rutherford Appleton Laboratory at Harwell Campus in Oxfordshire.

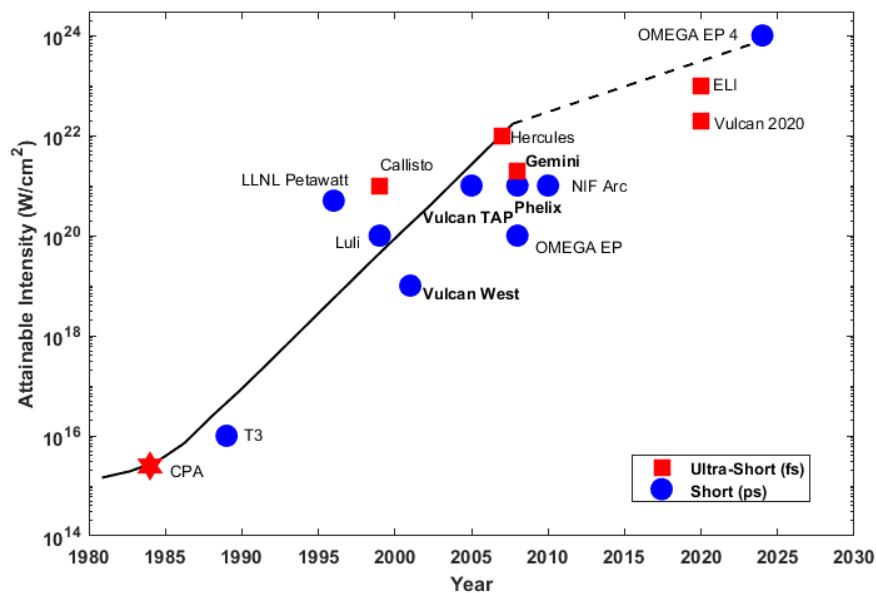


Figure 1.1: Plot of achievable short pulse laser intensity since the invention of CPA, with notable laser facilities marked including three future facilities designed to reach higher intensities. Trend taken from [1], commissioning date and peak laser intensity collated from references [2–9].

Plasma, or at least understanding of plasma, dates back to 1928 with the name and concept of plasma being formalised by Langmuir [45]. The definition of a plasma Langmuir gave was as follows: “*We shall use the name plasma to describe this region containing balanced charges of ions and electrons.*” when discussing the region of ionised gas near an electrical cathode. Plasma has since been named the “fourth state of matter”, and is assumed to account for a significant fraction of matter in the universe since both stars and the interstellar medium can be described as such. Its high electrical conductivity, and controllable recombination characteristics have made plasmas a highly useful state of matter.

The inevitable overlap of these two scientific fields quickly followed the creation of the first laser. Dawson [46] published an article reviewing the practicality of using lasers to create plasmas from solid and liquid targets with laser powers of 10^{10} W only a few years after Maiman demonstrated an optical laser experimentally [42]. Several early publications in laser-plasma studies note the generation of a variety of radiation from these interactions with energetic electrons [47, 48], ion emission [49], and x-ray emission [50] all being recorded. In 1979, the first proposal of using these interactions as an accelerator was put forward by Tajima and Dawson [51], they outlined the principles behind laser-wakefield acceleration and stated a need for intensities in excess of 10^{18} W/cm² in order to achieve this. At the time intensities of that scale were unattainable. However, as laser technology advanced and peak intensities grew (see Chapter 4), relativistic electron energies became readily attainable.

Laser-solid interactions are now an established source for a wide range of different radiation species. Whilst this thesis focuses on x-ray production from solid targets, there is significant attention from the wider field to use high intensity lasers with solid targets to produce energetic protons [52–55] and heavy

ions [56], thermal and epithermal neutrons [10, 57], and radiation across the electro-magnetic spectrum with particular focus on XUV [58–61] and, more recently, THz [62, 63]. In general these sources emit from small ($< 100 \mu\text{m}^2$) areas, are typically as short as the laser pulse ($\sim\text{ps}$), and high flux [10, 64–66].

1.2 Applications of laser plasma interactions

There are three prominent potential application areas for laser-plasma interactions; hadron-therapy, using ions to treat cancer [67], inertial confinement fusion (ICF), using lasers to compress and ignite a fusion reaction in a DT capsule [68, 69], and non-destructive testing, using laser plasma interactions as the source for radiography or inspection [10]. The following section outlines ICF and the principles behind laser driven x-ray radiography, hadron-therapy is discussed in these more focussed on ion acceleration [16, 70, 71].

1.2.1 Inertial Confinement Fusion

A significant motivator for initial research into laser-plasma interactions was using laser drivers to achieve controlled fusion reactions as a means to generate power. This involves fusing two light nuclei into a heavier, and more stable, nuclei. The difference in rest mass between the initial and final products is released as energy. This is similar in principle to fission except nuclei are combined rather than split to extract the difference in rest mass. The challenge is to provide the initial light nuclei with sufficient energy to overcome the electrostatic repulsion between them. Early theoretical work by Kidder [72] and Nuckolls [73] outlined how lasers could be used to do this by heating and compressing fuel target to ignite a fusion reaction.

The initial proposal envisioned using the laser to heat the outer surface of

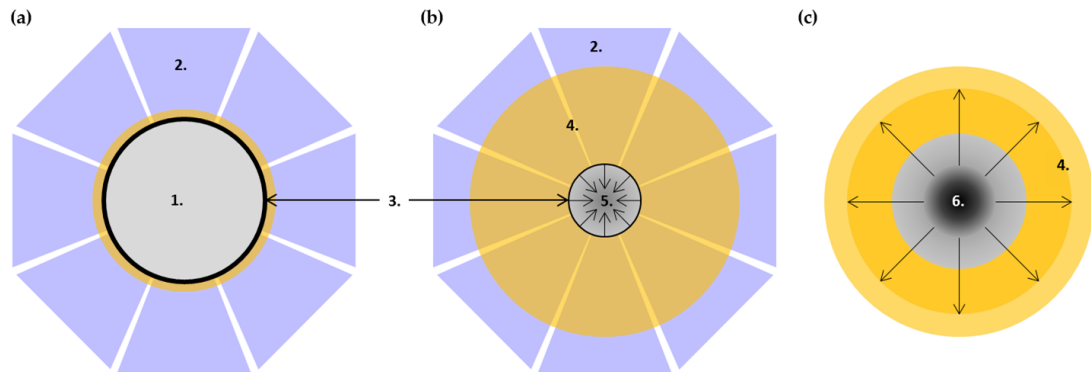


Figure 1.2: Laser driven fusion as an energy source. (a) laser heats the outer shell of the fuel capsule, (b) core compresses and heats until (c) the core ignites and re-expands. In this schematic; 1. Cold uncompressed fuel, 2. Incident laser pulses, 3. Outer shell, 4. Ablated plasma, 5. Imploding core, 6. Hot spot ignition.

the gas cell. The resultant ablation pressure would drive an increase in density and temperature in the centre of the core. The inertia of the heated outer layer acts to confine and compress the remaining fuel in the cell, this process is known as Inertial Confinement Fusion (ICF). There are two primary avenues of research towards ICF, the first is direct drive where the lasers directly irradiate the outer layer of the fuel capsule to drive the compression. The second method requires an exterior hohlraum to be irradiated by the laser. This laser interaction generates x -ray emission from the hohlraum walls, which in turn irradiates the fuel capsule. This drives a similar ablation pressure to the direct laser drive, albeit indirectly hence the name Indirect-Drive. Given the potential impact of this application it has seen significant research and attention; a detailed review of indirect drive ICF processes and difficulties has been published by Lindl *et al.* [74], similarly Craxton *et al.* [75] recently published a review of direct drive.

1.2.2 Laser Driven X-ray Radiography

The principle motivation behind this thesis and the body of work it represents is to develop and better understand laser driven sources of x-rays for the purpose of radiography. Fundamentally, the idea of non-destructive testing is to determine information about an object without requiring it to be altered. This principle can be applied to identify internal structure of manufactured items, a schematic of the operation is shown in Figure 1.3. Due to the small emission area, brightness, temporally short pulse, and *relatively* low footprint, lasers offer a clear opportunity for industrial partners to house their own inspection units.

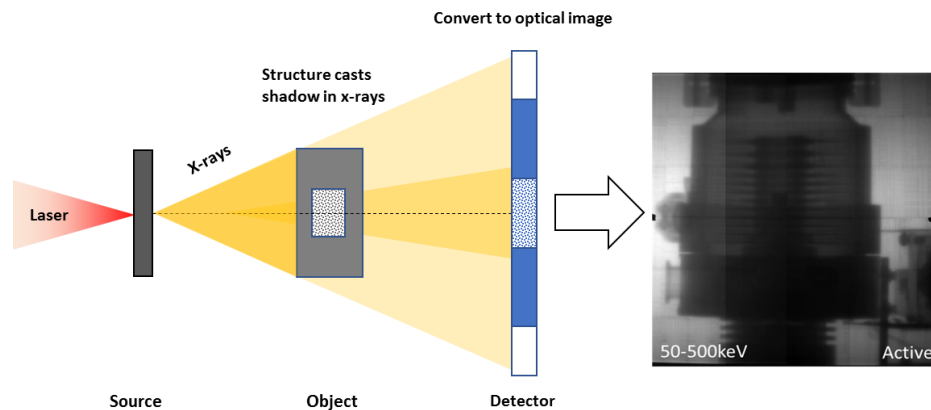


Figure 1.3: Schematic for x-ray radiography of a sample with internal structure. Laser accelerates electrons through a target, these electrons generate x-rays as they interact with the target. These x-rays illuminate the object, and as they are highly penetrative, variations in the density can be probed. Radiography from Brenner *et al.* [10].

Several demonstrations of x-ray radiography have been performed, from industrial objects [10, 35–39, 65, 76, 77] through to using the x-ray sources as a backlighter for ICF research [78–80]. Using the multi-modal nature of the interaction has also found use, proton probing of electromagnetic fields during laser interactions is used to monitor the \sim picosecond evolution of TV/m elec-

tric fields that occur during laser interactions. Fast neutron radiography and inspection from a pitcher catcher target design, where the laser accelerates ions from one target into a secondary converter, has been demonstrated by several groups [10, 57, 81–83].

1.2.3 Manufacture and inspection

Laser systems with high-energy pulses, such as the Vulcan laser system at the CLF used throughout the research presented in this thesis, are able to deliver > 100 J of laser energy onto target. The resulting x-ray emission is sufficiently bright to perform single shot radiography of a wide range of objects [10]. Currently, lasers of this scale are only able to fire once or twice an hour to allow for sufficient cooling of the laser medium. However, new laser systems using diode-pumped amplifiers are able to operate at Hz to kHz repetition rates [84] enabling industrial applications to be realised.

DiPOLE is a recent high energy demonstration of diode pumped laser technology [84]. A DiPOLE laser system has recently been developed by the CLF and delivered to HiLASE to perform laser processing such as laser-peening for industrial, and research, partners. The high-energy (100 J) and high-repetition (10-100 Hz) rate of the DiPOLE laser makes it an ideal candidate for laser-peening. In peening, the aim is to apply surface stress to a material in order to extend the lifetime of machine components, e.g. fanblades, welding joints, and others. Conventional "shock" peening techniques use ballistic ball bearings to apply the necessary stress to the material. Each impact dents the surface material and compresses the interior layers increasing the effective hardness of the material and extending the lifetime of the component. Laser peening, instead, ablates a sacrificial layer on the surface of the material, forms a plasma, and drives a shock into the material with pressures in excess of gigaPascals [85, 86].

This process is able to apply stress at greater depths than regular peening and in a controlled manner, compared to the inherently random nature of ballistic ball bearings.

A laser such as this could also be used to drive an x-ray source capable of performing non-destructive testing to ascertain the level of peening *in-situ*. The bandwidth of DiPOLE would facilitate compression to ~ 10 ps [?], the throughput of compressors is typically between 60-80 %. A final focusing optic of F3 would make the expected spot size ~ 5 μm . The intensity of the resultant laser pulse would be on the order of 10^{19} W/cm^2 , which is sufficiently intense to drive relativistic electron beams (see Chapter 2 for scaling and in-depth discussion of the mechanism at work) that are in turn capable of generating highly penetrative x-ray beams suitable for probing the density variation in components.

This section is included to highlight the flexibility of modern laser drivers, and how - with continued research and development - there could be novel and advantageous applications for laser driven x-ray sources.

1.3 Thesis Outline

This thesis reports on experimental investigations exploring the role of laser and target parameters that can be used to optimise the emission of x-rays from a solid target. The outline for the remainder of the thesis is as follows:

- **Chapter 2:** *Laser-Plasma Physics*

This chapter covers the background physics essential to the thesis, including laser driven ionisation processes and electron acceleration mechanisms.

- **Chapter 3:** *Fast electron transport and radiation*

Building upon Chapter 2, this focuses on exploring the mechanisms of electron transport and x-ray generation. A review of studies of electron divergence through solid targets is included.

- **Chapter 4:** *Methodology*

With the primary physics detailed, this chapter covers the methods and practices used in completing this research. An overview of high-power lasers, x-ray detectors, and simulation tools is given.

- **Chapter 5:** *Investigation of recirculating electrons in solid targets as a function of laser intensity for x-ray generation*

First of three results chapters, reporting on the investigation into the role of laser defocus on x-ray generation from solid targets through experimental measurements and an analytical model. 2D PIC simulations accompany the experimental data to further investigate the electron behaviour within the targets.

- **Chapter 6:** *Investigation of electron dynamics with laser-guiding capillary-targets*

The second results chapter, reporting on a study into the application of laser-guiding capillary-targets for increased laser absorption. Experimental results from a proto-type target are presented with 2D and 3D PIC modelling.

- **Chapter 7:** *Optimising x-ray source characteristics for large scale radiography*

This final results chapter reports on a mechanism to increase the flux of x-rays generated from laser-plasma interactions. Experimental results are presented, supported by 2D PIC and GEANT4 simulations. An analytical model for achieving better quality radiographs is also presented.

- **Chapter 8:** *Conclusions and future work*

A summary of the three results chapters and an overview of additional research avenues that can be explored.

Chapter 2

Intense laser interactions with over-dense plasmas

Laser plasma physics is a multidisciplinary field. It draws heavily on electromagnetic field theory and plasma physics, atomic and nuclear processes for radiation generation and nuclear activation, quantum mechanics for ionisation, and is also used to study laboratory astrophysics. This chapter discusses the foundational physics used throughout this thesis to describe laser-plasma interactions. It will then explore laser and electromagnetic fields, as well as the laws which govern their development, before going on to discuss how these fields interact with a single charged particle. The remainder of the chapter examines the underlying physics occurring during relativistic laser-plasma interaction. Ionisation and the formation of plasma is discussed and then the mechanisms by which laser energy is transferred into a population of hot electrons. The electron transport and subsequent radiation production and attenuation is discussed in Chapter 3.

2.1 Electromagnetic (EM) Fields

Electric (**E**) and magnetic (**B**) fields have distinct properties and evolve during the interaction with charged particles. There are five equations that describe the interactions between these fields and charged particles. The first

four are referred to as Maxwell's equations [87] and describe the way in which charges and currents drive electromagnetic fields, and how the fields evolve together.

2.1.1 Maxwell's Equations

Gauss's Law (Eq 2.1) states how the electric field, \mathbf{E} , is dependent on the charge density, ρ . Gauss's Law for magnetism (Eq 2.2) states that unlike for electric fields there cannot be a single unbalanced magnetic charge or monopole. Instead, magnetic field lines form as closed loops and so the total divergence for a magnetic field is zero. The Maxwell-Faraday law (Eq 2.3) states that the electric field of a loop is dependent on the temporal evolution of a magnetic field within the loop. The final Maxwell equation, Ampere's Law (Eq 2.4), links field evolution to the current density \mathbf{j} . It states that the magnetic field is proportional to both the electric current generating it and the temporal variation of the associated electric field.

$$\nabla \cdot \mathbf{E} = \frac{\rho}{\epsilon_0} \quad (2.1) \qquad \nabla \times \mathbf{E} = -\frac{d\mathbf{B}}{dt} \quad (2.3)$$

$$\nabla \cdot \mathbf{B} = 0 \quad (2.2) \qquad \nabla \times \mathbf{B} = \mu_0 \mathbf{j} + \frac{1}{c^2} \frac{d\mathbf{E}}{dt} \quad (2.4)$$

For each equation, ϵ_0 and μ_0 are the permittivity and permeability of free space respectively, and c the speed of light in a vacuum ($\simeq 3 \times 10^8$ m/s²). A charged particle within these fields will feel a force dependent on both the electric and magnetic field strength and the velocity of the charge. The equation for this is the Lorentz Force law;

$$\mathbf{F} = q(\mathbf{E} + \mathbf{v} \times \mathbf{B}) \quad (2.5)$$

where \mathbf{F} is the force on the particle, q the charge, and \mathbf{v} the velocity vector.

2.1.2 Laser Parameters

Lasers can be described by their wavelength λ_L and intensity I_L . The intensity of a laser is determined by the energy of the pulse E_L , the pulse duration τ_l , and the focused laser spot diameter ϕ_L . Eq. 2.6 describes the relationship between intensity and the electric field;

$$I_L = \frac{c\eta\epsilon_0}{2} |\mathbf{E}|^2 \quad (2.6)$$

where c is the speed of light and η the refractive index of the medium. From Maxwell's equations (Eq 2.1-2.4) the wave equation to describe field propagation can be derived as¹:

$$\nabla^2 \mathbf{E} = \frac{1}{c^2} \frac{d^2 \mathbf{E}}{dt^2} \quad (2.7)$$

The electric field is dependent on the medium that it is travelling in and the wavelength of light. The relationship between \mathbf{E} and \mathbf{B} can be shown, via Eq. 2.3, as:

$$|B_0| = \frac{1}{c} |E_0|. \quad (2.8)$$

From Eq. 2.8 it is clear that the effect of a magnetic field is significantly reduced when compared to the electric field. This relationship drives the emergence of several high intensity effects in which the corresponding magnetic field is sufficient to significantly alter the electron motion. The direction these waves oscillate in is known as the polarisation of the field. Relative to a target surface there are three distinct cases; S- and P- polarisation are two forms of linear polarisation where the E-field oscillates in a single axis. S-polarisation is where the field is orientated perpendicular to the plane of propagation and P-

¹Assuming a charge and current free system in vacuum, using the vector identity:

$$\nabla \times (\nabla \times \mathbf{A}) = \nabla(\nabla \cdot \mathbf{A}) - \nabla^2 \mathbf{A}$$

is parallel. The third case is elliptical polarisation wherein the two waves oscillate perpendicular to one another with some phase or amplitude difference (in the case where amplitude and phase are matched it is known as circular polarisation).

2.2 Single particle motion

2.2.1 Quiver Velocity

The force acting on an electron in a laser field is described by the Lorentz equation (Eq. 2.5). For cases where the magnetic field is negligible this reduces to:

$$\frac{d\mathbf{p}}{dt} = e\mathbf{E} \quad (2.9)$$

where \mathbf{p} is the momentum of the electron. From this, it can be shown that the electron quiver velocity v_q is;

$$v_q = \frac{eE_0}{m_e\omega_L} \sin(\omega_L t) \quad (2.10)$$

where E_0 is the magnitude of the laser field, m_e is the rest mass of an electron, and e is the elementary charge constant ($\simeq 1.6 \times 10^{-19}$ C). As the E-field increases in amplitude so to does the classical quiver velocity. The dimensionless parameter, a_0 , defines the intensity at which the quiver velocity of an electron becomes relativistic, this is known as the normalised laser potential and can be expressed as:

$$a_0 = \frac{eE_0}{m_e c \omega_L} \approx 0.85 \sqrt{I_{18} \lambda_\mu^2} \quad (2.11)$$

where λ_μ is the wavelength of the laser in μm , and I_{18} is the intensity of the laser in units of 10^{18} W/cm². In a 1 μm laser system $a_0 \approx 1$ at intensities of

$\sim 10^{18}$ W/cm². If the magnetic field is no longer negligible then the second term of Eq. 2.5 must be considered:

$$\frac{d\mathbf{p}_b}{dt} = e(\mathbf{v} \times \mathbf{B}) \quad (2.12)$$

$$\frac{dv_d}{dt} = \frac{e}{m_e c} v_q E_0 \cos(\omega_L t) \quad (2.13)$$

$$v_d = \frac{e^2 E_0^2}{4m_e^2 c \omega_L^2} \cos(2\omega_L t) \quad (2.14)$$

This results in a secondary force term which, since v_q follows the direction of the electric field and the magnetic field is perpendicular, acts in the direction of the laser travel. The drift velocity, v_d , peaks at twice the laser frequency $2\omega_L$ when the electron quiver velocity, v_q is at its maximum. The quiver and drift velocity, shown in Eq. 2.10 and Eq. 2.14 respectively, can be expressed with respect to the normalised laser potential to provide two simple equations for the peak transverse and longitudinal electron velocity:

$$v_{\perp} \rightarrow v_q = \frac{a_0 c}{\gamma} \quad (2.15)$$

$$v_{\parallel} \rightarrow v_d = \frac{a_0^2 c}{4\gamma} \quad (2.16)$$

where γ is the Lorentz factor of the electron. It is clear from these two equations that for $a_0 < 1$ the transverse velocity (Eq. 2.15) will dominate but as the laser intensity is increased further beyond $a_0 = 1$ the magnetic component and the longitudinal velocity will dominate. Since the electron is not travelling at c it experiences peaks and troughs of a_0 , resulting in continuous acceleration up to the maxima and back to rest as the laser passes. This can be thought of as the electron *dephasing* with the laser. The maximum energy of an electron moving

within a laser field in vacuum is:

$$E_{max} = E_0 \frac{a_0^2}{2} \quad (2.17)$$

where $E_0 \approx 0.511$ MeV - the rest mass of an electron ¹. A derivation of the energy limit and electron dephasing is shown in the review paper by Arefiev *et al.* [11]. Figure 2.1 shows the expected maximum energy of electrons from the laser field scaling exponentially with the laser intensity.

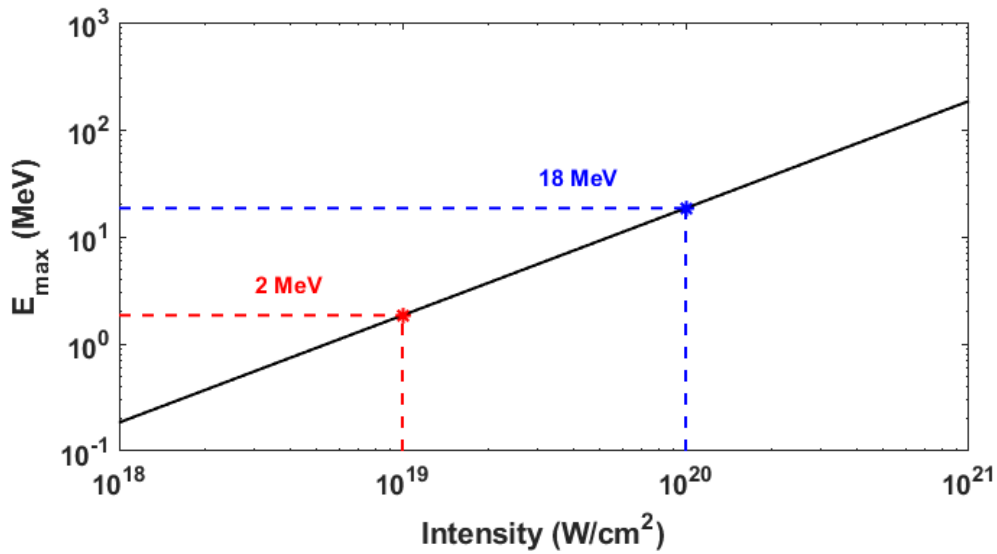


Figure 2.1: The peak energy as a function of laser intensity for a single electron. E_{max} at 10^{19} and 10^{20} W/cm² are shown in red and blue respectively [11].

Despite this being the maximum energy of an electron within a given laser field, energies above this limit are routinely measured in laser-plasma physics. The first reason for that is that electrons are not necessarily at rest when interacting with the laser, and a series of re-accelerations can occur during the interaction. One mechanism, a core focus of the wider field, is laser-wakefield interactions. Whilst outside the direct scope of this thesis, it is worth noting

¹Often expressed in terms of the γ -factor: $\gamma_e \approx 1 + \frac{a_0^2}{2}$ [11]

that the field structure established in a laser-wakefield can accelerate electrons beyond this limit, and is a prominent area of research within the field. A review article of the topic was published by Albert *et al* [65] that covers the process in detail, and a comparison to conventional accelerators is discussed in the appendices. The other primary mechanism relevant to this thesis is known as direct laser acceleration (DLA). If the electron is no-longer at rest and instead moving in the laser direction with some velocity it is able to be accelerated beyond this limit. This was succinctly expressed by Robinson *et al.* [88] as $R = \gamma_e - p_x/m_e c^2$, when $R < 1$ the electron is travelling with the laser potential and as a result can be accelerated beyond E_{max} .

2.2.2 Ponderomotive Force

In homogeneous fields the quiver velocity is oscillatory and the accelerated electron will return to its original momenta after a single field oscillation - also known as the Lawson-Woodward theorem. In reality, lasers have a non-uniform spatial intensity profile and are temporally finite, and as such are non-homogeneous fields. If the \mathbf{E} and \mathbf{B} now have a gradient the restoring force acting on a displaced electron is no longer the same as the initial force. The difference between these forces is known as the ponderomotive force and can be derived as:

$$\mathbf{F}_P = -\nabla\phi_{pond} = -\frac{e^2}{4m_e\omega_L} \nabla(E^2) \quad (2.18)$$

This force acts to drive electrons away from regions of high intensity, leading to a self-focussing effect as discussed in Section 2.4.2.4.

2.3 Ionisation

A plasma (discussed in more detail in Section 2.4) is ionised matter in *quasi*-neutrality. This state is achieved by the electrons gaining energy in excess of their binding potential and being freed from their orbitals. A myriad of ionisation processes occur as the intensity of the laser increases. In the simplest case of a hydrogen atom; an electron is in stable orbit with centripetal force, F_{ce} , counteracting the Coulomb force, F_{co} .

$$F_{co} = F_{ce} \Rightarrow \frac{m_e v^2}{r_o} = \frac{e^2}{4\pi\epsilon_0 r_o^2} \Rightarrow E_b = -\frac{e}{8\pi\epsilon_0 r_o} \text{ eV} \quad (2.19)$$

where r_o is the orbital radius of the electron, and E_b is the binding energy in eV. r_o can be substituted for the Bohr radius $\alpha_B = 5.291 \times 10^{-11}$ m for hydrogen, which gives the binding energy ≈ 13.6 eV. To ionise a hydrogen atom via the photo-electric effect it would require a single photon with a wavelength $\simeq 90$ nm, and whilst a laser with this wavelength is technically achievable it makes laser operation significantly more challenging since traditional optics can no longer be utilised. Instead, most high-intensity lasers operate at $\sim 0.2 - 10$ μm wavelengths and rely on additional processes to ionise media.

2.3.1 Multi-photon ionisation (MPI)

Electrons can be excited by photons of energy below the ionisation energy. For a short duration of time (relaxation time) they maintain that energy level before decaying and re-emitting a photon. If enough photons interact with the electron within the relaxation time it can gain sufficient energy to become free, a process known as multi-photon ionisation (MPI) [89]. For hydrogen, the electron requires 13.6 eV to be ionised from the ground state. A single 1 μm photon has 1.17 eV, therefore ~ 12 photons are needed to ionise a single electron. The intensity required to begin ionising matter via this process has

been shown experimentally to be $\sim 10^{10}$ W/cm² [90–92]. It is possible to couple more energy than the ionisation threshold via this process, which is known as Above-Threshold Ionisation (ATI) [93, 94]. In this case, the final energy of the electron is simply the sum of the absorbed photon energies minus the required ionisation energy:

$$E_f = n\hbar\omega - E_b, \quad (2.20)$$

where n is the number of photons absorbed by the electron. Evidence of the resulting quantised energies has been measured experimentally by several groups [95, 96].

2.3.2 Tunnelling Ionisation and Barrier Suppression Ionisation

The assumption for MPI is that the electric potential binding the electron to the ion is static, however, with increasing laser intensity this assumption is no longer valid since the laser electric field begins to suppress the binding potential. As the laser field suppresses the binding field, the chance for ionisation increases. The intensity threshold for this process can be determined by the intensity at which the electron potential is reduced to that of the binding energy [97]. The threshold intensity for barrier suppression ionisation (BSI) in hydrogen can be shown to be:

$$\begin{aligned} I_{BSI} &= cn\epsilon_0 \frac{E_b^4}{16Z^2e^6} \\ &\simeq 1.4 \times 10^{14} \text{W/cm}^2. \end{aligned} \quad (2.21)$$

This is two orders of magnitude above the threshold of MPI. In BSI the barrier is entirely suppressed and the electrons are able to freely leave. The distinction for tunnelling ionisation is that the electrons are able to quantum

mechanically tunnel through the partially suppressed potential with some finite probability, resulting in a portion of the electron population escaping from the potential [1]. A schematic of MSI, BSI, and Tunnelling Ionisation is shown in Figure 2.2.

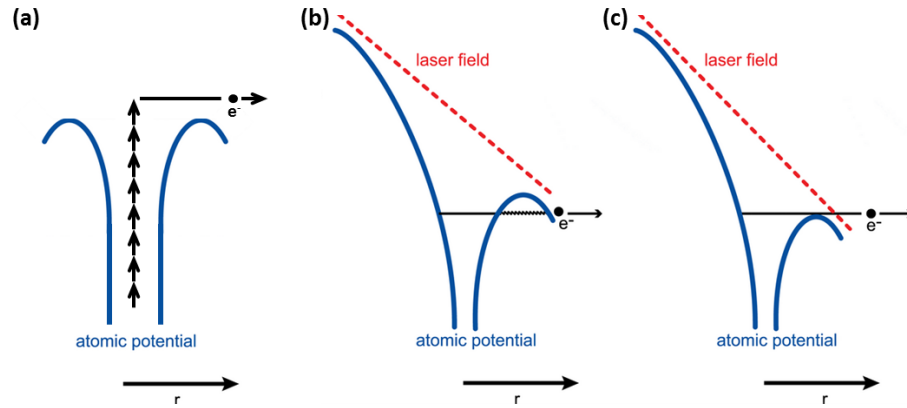


Figure 2.2: Schematic of ionisation mechanisms. (a) multi-photon ionisation, (b) tunnelling ionisation, and (c) barrier suppression ionisation. Figure adapted from Reference [12].

2.3.3 Collisional Ionisation

An electron freed by an excitation process is then able to potentially cause further ionisation by interacting with the surrounding atoms. The freed electron has kinetic energy, either through the laser field directly or from ATI processes, and can collide with other bound electrons. This process can cause a cascade of ionisation with each free electron having the potential to ionise others in the vicinity. The ionisation rate, ν_C , of these free electrons is dependent on their kinetic energy and the background electron density (n_e) and temperature (T_e) [56]:

$$\nu_C = 4\pi n_e \sqrt{\frac{2E_f}{m_e}} \alpha_b \frac{E_{hy}^2}{E_b k_B T_e} \ln \left(\frac{k_B T_e}{E_b} \right), \quad (2.22)$$

where E_{hy} is the binding energy of hydrogen. Since this process is dependent

on already freed electrons, it can occur outside of the laser field and it dominates within the target, causing ionisation beyond the skin depth of the laser (discussed again in Section 2.4).

2.3.4 Field Ionisation

The final process to consider is field ionisation in which the field intensity exceeds the binding potential and the electron is freed from its orbital. From the Bohr radius, the atomic electric field strength is:

$$\begin{aligned} E_F &= \frac{e}{4\pi\epsilon_0\alpha_B^2} \\ &= 5.1 \times 10^9 \text{Vm}^{-1}. \end{aligned} \tag{2.23}$$

and therefore the intensity required is $I_F \simeq 3.51 \times 10^{16} \text{ W/cm}^2$ (via Eq. 2.6). Whilst these intensities are now routinely available, the intensity threshold for other processes are significantly lower. As such field ionisation (unlike the other processes mentioned) dominates at the rear of a solid target due to the large electro-static field produced as the electrons leave the target. This field is discussed again in Chapter 3 as it also drives a recirculating population of electrons within the target and is one mechanism by which ions are accelerated.

2.4 Plasma

In contrast to the three traditional states of matter, plasma consists of a population of ions and unbound electrons. This state has been referred to as the *fourth state of matter* [98] due to the further increase in energy required to achieve the state compared to that of a gas.

Collisions and interactions between neutral particles in gases occur as discrete events between two particles under the Van der Waals force (r^{-6}). In

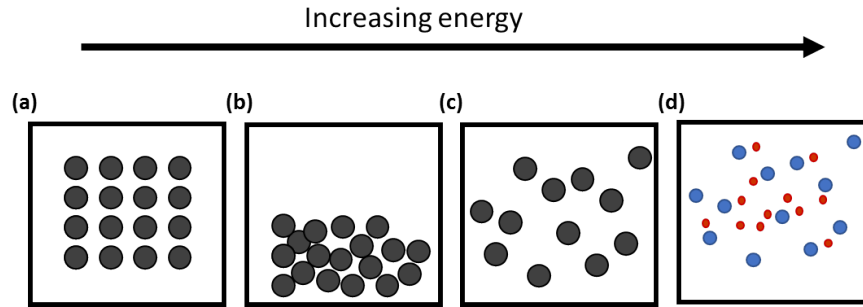


Figure 2.3: Schematic of the four principle states of matter, each transition requires additional energy to break bonds between the molecules or, for plasma, free the electrons via ionisation. (a) Solid, (b) liquid, (c) gas, and (d) plasma. Grey circles represent neutral atoms, the red and blue circles in (d) represent electrons and ions respectively.

a plasma, since the particles are charged, the Coulomb force (r^{-2}) dominates resulting in interactions involving a large number of other particles [99], and thus collective effects play an important role in plasma behaviour. An ideal plasma consists of a *quasi*-neutral population of electrons and ions. From a macroscopic perspective, a plasma has no overall charge yet substantial field growth and charge separation is possible as the populations of electrons and ions have collective electromagnetic effects. The presence of both electron and ion populations distinguishes plasma from an ionised gas due to the collective effects that emerge as a result.

2.4.1 Plasma Parameters

In order to describe and quantify different plasmas, there are several parameters routinely used. Two such parameters are the energy of the plasma (or temperature) and the density of the plasma. Combined, these can quantify additional relationships and parameters that describe plasma states in more detail.

2.4.1.1 Definitions

The degree of ionisation, Z^* , quantifies the average ion charge within the plasma. The density refers to the number density of the ions and electrons within the plasma (referred to as n_i and n_e respectively), and is typically expressed in units of cm^{-3} . It can be calculated from the mass density of a material by assuming an ionisation state of all atoms per unit volume:

$$n_e = \frac{Z^* \rho N_A}{A} \quad (2.24)$$

where ρ the mass density of the material, A is the atomic mass number of the material, and N_A is Avagadros number. The temperature is an expression of the kinetic energy the electron/ion distribution has and is typically expressed in Boltzmann form (i.e. $k_B T$) in units of eV.

2.4.1.2 Debye Length

The Debye length is the characteristic length over which the electric potential from a charged particle drops by $1/e$. Unlike free charges in a vacuum, charges within a plasma experience screening from other charges as a function of their number density. For a plasma with a Boltzmann temperature distribution, $k_B T$, the Debye Length is;

$$\lambda_D = \sqrt{\frac{\epsilon_0 k_B e^{-2}}{n_e T_e^{-1} + \sum_i Z_i^{*2} n_i T_i^{-1}}} \quad (2.25)$$

where Z_i^* is the effective ionisation for each ion species (for fully ionised plasmas $Z^* = Z$), and T_e, T_i are the temperatures of the electron and ion distribution, respectively. Typically, the ion presence in this equation can be neglected since over the time scale of the interaction (\ll nanoseconds) the bulk ion pop-

ulation does not move. This reduces Eq 2.25 to:

$$\lambda_D = \sqrt{\frac{\epsilon_0 k_B T}{n_e e^2}} \quad (2.26)$$

A plasma is also defined by the degree to which collective effects dominate. This is expressed by the plasma parameter (Λ) and the coupling parameter (Γ). Λ defines the number density of electrons in a given Debye sphere (volume of space in the plasma with a radius of λ_D). A higher plasma parameter means that there are more electrons able to interact with each other. Γ is the relationship between the potential energy in the plasma (Coulomb attraction between the species) and the kinetic energy of the particles. $\Gamma < 1$ indicates that electrons are sufficiently energetic to escape the plasma, leading to dispersion and a short plasma lifetime. Combined, the two dimensionless parameters and Debye length can be used to define and characterise different plasmas.

$$\Lambda = 4\pi n_e \lambda_D^3 \quad (2.27) \quad \Gamma = \frac{E_{co}}{E_{kin}} = \frac{e^2}{4\pi\epsilon_0 k_B T_e} \sqrt[3]{\frac{4\pi n_e}{3}} \quad (2.28)$$

2.4.1.3 Wave Equation

The freely moving charges within a plasma act upon one another despite the overall *quasi*-neutrality. When an electron is displaced there is a net restoring force established to return it to equilibrium. When this effect is considered over a large population of charges, the displacement and return becomes the oscillating frequency of the plasma. For a simple 1D case, the frequency of the plasma can be derived as follows. If a population of electrons are offset by a distance, x , the field established between the now separated charges is defined by Eq. 2.1 to be:

$$E = \frac{en_e x}{\epsilon_0} \quad (2.29)$$

This in turn sets a restoring force ($F = -eE$) and therefore the equation of

motion for these two populations is described by:

$$\frac{d^2x}{dt^2} + \frac{e^2 n_e x}{m_e \epsilon_0} = 0. \quad (2.30)$$

This equation is that of a simple harmonic oscillator¹ and the fundamental frequency of that oscillator can be shown as:

$$\omega_p = \sqrt{\frac{n_e e^2}{\epsilon_0 m_e}} \quad (2.31)$$

by substituting in $x(t) = A \cos(\omega_p t)$, where ω_p is the frequency of the plasma oscillation. It is important to note that whilst this fundamental frequency is independent of the plasma temperature, however as the temperature increases and the relativistic mass of the electrons becomes a factor, the frequency does reduce.

2.4.2 Laser propagation in Plasma

2.4.2.1 Dispersion relation

The interaction between the laser wave equation and the plasma wave equation is key to the propagation of the EM fields in the plasma medium. The dispersion relationship for a EM field and plasma can be expressed as:

$$\omega_L^2 - \omega_p^2 = k^2 c^2 \quad (2.32)$$

The derivation of this is shown in the appendices. In the case where the plasma frequency exceeds that of the incident light frequency, the wave-vector must become imaginary to satisfy the dispersion relationship, which leads to an effervescently decaying EM field. The extent of this decay is known as the col-

¹Equation for a simple harmonic oscillator: $\ddot{x} + \omega^2 x = 0$

tionless skin depth, δ ;

$$\delta = |k^{-1}| = \frac{c}{\sqrt{\omega_p^2 - \omega_L^2}} \quad (2.33)$$

2.4.2.2 Critical Density

From the dispersion relationship (Eq. 2.32), in the case where the plasma frequency matches the laser frequency (ω_p and ω_L respectively), the wavevector must reduce to zero and as such the laser can no longer propagate. The density at which this occurs is known as the critical density, and by substituting ω_L into Eq. 2.31 can be shown as:

$$n_{crit} = \frac{\epsilon_0 m_e}{e^2} \omega_L^2 \quad (2.34)$$

As the electron relativistic mass increases so does the critical density of electrons, allowing for increased propagation of the laser to higher density. This process, in which the entire target can become transparent to the laser, is known as relativistically induced transparency. The non-relativistic critical density for a laser with a 1 μm wavelength (such as the Vulcan laser used throughout this work) is $n_{crit} \approx 1.1 \times 10^{27} \text{m}^{-3}$. As an example, the density of a fully ionised aluminium target, Eq. 2.24 with $Z^* = 13$, has a density of $n_{Al} \approx 770 \times 10^{27} \text{m}^{-3}$ or $n_{Al} \approx 770 n_{crit}$.

2.4.2.3 Scale Length

Laser pulses used experimentally are not delta-functions or perfect Gaussians, instead they typically have a long (ns) pedestal preceding the main pulse. In modern high intensity laser systems where the main pulse is $I > 10^{19} \text{W/cm}^2$ this pedestal can be in excess of 10^{12}W/cm^2 and, therefore, sufficiently intense enough to ionise the front surface prior to the main pulse arriving. This ionisation causes an expansion of the front surface which leads to a decaying

density profile, known as the pre-plasma, with the form:

$$n_e(z) = n_0 \exp(-zL_s^{-1}) \quad (2.35)$$

where $L_s^{-1} \sim \frac{1}{n} \frac{dn}{dz}$ is the characteristic scale length¹ and n_0 is the target density. The extent of this pre-plasma is a key concern during interactions since it effects the coupling efficiency between the laser and the hot electrons [52, 100], the divergence of the accelerated electron beam [101, 102], and the accelerated spectra [77, 103]. The scale length can be measured experimentally by sending a short-pulse probe beam across the target surface [104, 105].

2.4.2.4 Refractive Index

The refractive index of a medium alters the phase velocity of light propagating through it $\eta = c/v_p$. In the case of a plasma, it is first useful to define the relative permittivity as:

$$\epsilon = \frac{\epsilon_p}{\epsilon_0} = 1 - \frac{n_e e^2}{\epsilon_0 m_e \omega_L^2} = 1 - \left(\frac{\omega_p}{\omega_L}\right)^2 \quad (2.36)$$

This unit-less parameter is used to quantify the refractive index, $\eta = \sqrt{\epsilon}$, which leads us to consider what happens as the incident laser frequency exceeds the plasma frequency. The phase and group velocity can be derived from the dispersion equation (Eq. 2.32) to show that:

$$v_p = \frac{c}{\sqrt{1 - \left(\frac{\omega_p}{\omega_L}\right)^2}} \quad (2.37) \quad v_g = c \sqrt{1 - \left(\frac{\omega_p}{\omega_L}\right)^2} \quad (2.38)$$

The equations above imply that for $\omega_L > \omega_p$ the speed of light in the plasma will exceed the speed of light in a vacuum. Although the phase velocity, i.e.

¹the length over which the density drops to $1/e$

the peaks and troughs of the EM wave in the plasma, travels at $v > c$, the group velocity, and therefore information, travels at $v < c$. Since the refractive index is dependent on the electron density ($\omega_p \propto \sqrt{n_e}$, from Eq. 2.36), the laser will experience a change of refractive index as it propagates through the pre-plasma. From Snell's law:

$$\frac{\nu_{p,in}}{\nu_{p,out}} = \frac{\sin(\theta_{in})}{\sin(\theta_{out})} \quad (2.39)$$

where $\theta_{in,out}$ is the angle of propagation with respect to the target normal for two different plasma densities. It is clear, from Eq. 2.39 that a laser will experience deviation from the original trajectory unless it is incident normal to the surface, this effect is demonstrate in Figure 2.4.

The ponderomotive force (Section 2.2.2) demonstrates that electrons in high intensity regions will be expelled at a higher rate than low intensity regions. As a result of this effect, the lower intensity regions will see a higher refractive index than the centre and consequently the plasma can alter the propagation of the electric field to focus the light. The power of the beam at which this effect is significant, is known as the critical power;

$$P_{crit} \approx 17.5 \left(\frac{\omega_L}{\omega_p} \right)^2 \text{ GW} \quad (2.40)$$

derived in References [106–108], this effect is known as 'self-focusing' in the plasma. This can also occur as the γ -factor of the electron increases due to the laser intensity, which results in a change of refractive index $\eta = \sqrt{1 - \frac{\omega_p^2 \langle \gamma_e \rangle^{-1}}{\omega_L^2}}$ [109].

2.5 Absorption

During a laser interaction, energy is transferred from the high-intensity pulse into the plasma via several absorption mechanisms. Each dominate in specific conditions, typically with increasing intensity there is a shift from one mechanism to another. The mechanisms here can be separated into two distinct categories; collisional and collisionless. The former describes where electrons interact with the surrounding ions during oscillation and thus lose energy and coherence with the laser. The latter however rely on a density gradient in the plasma profile that extends beyond n_{crit} of the laser, electrons that are driven beyond the critical surface cannot be restored by the laser field.

2.5.1 Inverse Bremsstrahlung

A free electron (as discussed in Section 2.2) oscillates with the electric field, gaining and releasing kinetic energy as it experiences the laser field. Inverse Bremsstrahlung, in which an electron collides with a nearby ion and deposits some energy into the ion, is one process to transfer laser energy to the hot electron population. It is more effective with high-density low-temperature conditions since the chance of collisions between the two species is higher. Numerically the rate of electron-ion collisions (ν_{ei}) can be shown as [110, 111]:

$$\nu_{ei} \propto \frac{n_e Z^*}{T_e^{\frac{3}{2}}}. \quad (2.41)$$

Inverse bremsstrahlung dominates at intensities between 10^{12} and 10^{15} W/cm² before the efficiency reduces.

2.5.2 Vacuum Heating

Consider a 1D capacitor model similar to the one described in Section 2.4, which has an electron and ion population with some predefined density (n_e

and n_i) at $x > 0$ and vacuum at $x < 0$, with a laser incident on the system at some angle, $\theta_L > 0$, to ensure that a component of the laser oscillates in the X-direction. As the laser field in the vacuum oscillates it will draw electrons from the $x > 0$ into the vacuum, thus establishing a field charge ΔE ;

$$\Delta E = 4\pi en_e \Delta x, \quad (2.42)$$

where n_e is the number density of displaced electrons drawn into the vacuum and Δx is the distance they are displaced. This displacement results in a restoring force from the ion population, and when returned to their original position the electron population will have gained a velocity $v_d \simeq 2v_q \sin(\theta_L)$.

2.5.3 Resonance Absorption

Instead of a step-like density profile consider a scale length, $L_s > \lambda_L$, from the target surface of increasing plasma density. As the laser propagates further through this under-dense region, the background electron density is increasing and changing the laser wave vector as it does so. The dispersion relationship (Eq. 2.32) between the laser and plasma is modified to include the angle of incidence and the varying laser wave vector:

$$\omega_L^2 (1 - \sin^2 \theta_L) = \omega_p^2 + k_x^2 c^2. \quad (2.43)$$

Rearranging this and considering the critical density (Eq. 2.34), k_x reduces to zero (and therefore the beam is reflected) at $n_e \simeq n_{crit} \cos^2 \theta_L$. Electrons that are driven by the electric field at this surface are able to propagate further into the plasma, oscillating at the same frequency as the laser and driving a resonant wave at the critical surface, where $\omega_p = \omega_L$. As the laser decays effervescently beyond this point, there is a weaker restoring field to draw the electrons back out of the plasma. The efficiency of this process is dependent on both the scale length L_s and the angle of incidence θ_L . This has been tested theoretically

and experimentally by several groups over the years [13, 112–115].

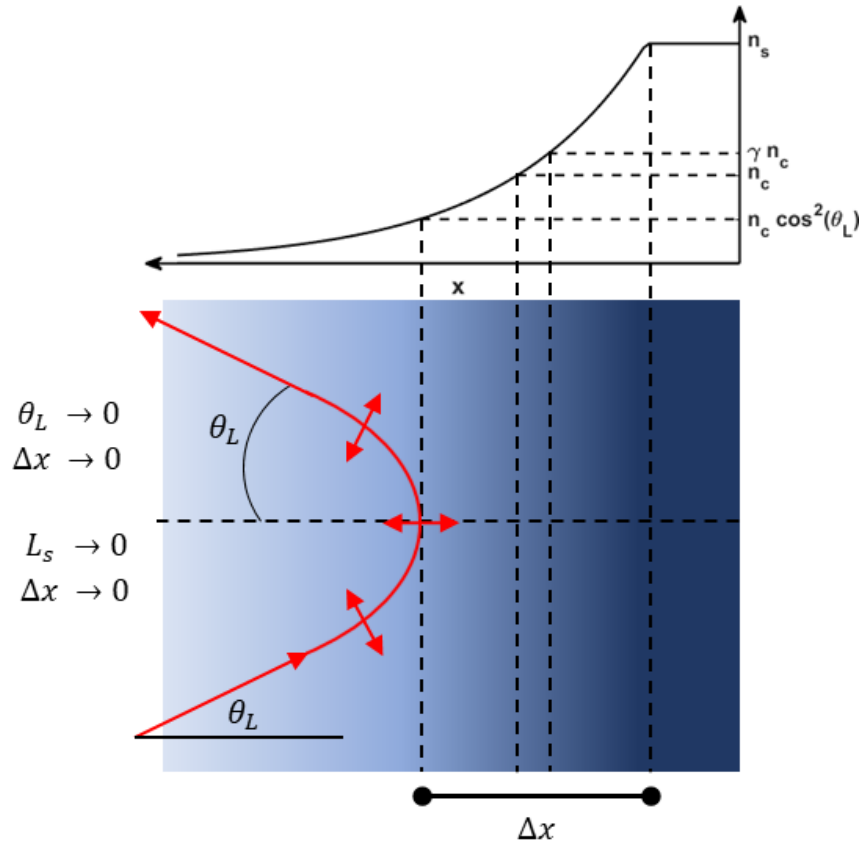


Figure 2.4: Schematic of a P-polarised laser pulse travelling through a pre-plasma with the scale length L_s . Red line indicates the path the laser takes, refracting away from the critical surface as the density increases. The dashed lines represent different densities within the pre-plasma; the turning point $n_c \cos^2(\theta_L)$ (Section 2.4.2.4), the critical density n_c , the relativistic critical density γn_c , and solid density n_c at the target surface [13].

The laser refracts as it travels through the underdense scale length as a function of the angle of incidence, shown in Figure 2.4 as a red line. The laser penetrates up until the point of reflection $n_c \cos^2(\theta_L)$ (Section 2.4.2.4), the distance Δx between this and the solid target vary as a function of L_s and the angle of incidence.

2.5.4 $\mathbf{j} \times \mathbf{B}$ Heating

As discussed in Section 2.2, for high intensity laser pulses the magnetic component of the Lorentz equation (2.5) becomes dominant. The quiver velocity of electrons increases under the effect of the electric field, therefore increasing the $\mathbf{v} \times \mathbf{B}$ component of the force. The increase in this term leads to an absorption mechanism known as $\mathbf{j} \times \mathbf{B}$ heating. Kruer and Estabrook [116] showed that the total force, for linear polarisation¹, from this mechanism can be derived as:

$$\mathbf{F} = -\frac{m_e}{4} \frac{dv_q^2(x)}{dx} (1 - \cos(2\omega_L t)) \quad (2.44)$$

This force demonstrates the two important effects of the $\mathbf{j} \times \mathbf{B}$ mechanism. The first term of the equation is dependent on the spatial variation in the electron quiver velocity and so, like the ponderomotive force, acts to push electrons away from high intensity regions. Since the force is dependent on the electron quiver velocity, it peaks at twice the laser frequency which is expressed by the second term $(1 - \cos(2\omega_L t))$. Resonance absorption and Brunel heating both drive electrons predominantly along the target normal axis as the laser field acts perpendicularly to the critical surface. With electrons oscillating in the electric field and the magnetic field acting perpendicular to the electric field, electrons are forced forwards in the direction of the beam. This distinction allows for $\mathbf{j} \times \mathbf{B}$ and the other mechanisms to be isolated experimentally by angling the target to the incident beam.

2.6 Electron Spectra

The laser and target parameters dictate which absorption process will dominate and experimental measurements of scale length and emission direction

¹In circularly polarized cases, the force equation reduces to the ponderomotive force as there is no longer a significant oscillatory component of the electron velocity

(target normal for resonant and vacuum heating, laser axis for $\mathbf{j} \times \mathbf{B}$) can be used to verify this. Experimentally, measured values of absorption are a convolution of all processes. Davies [19] presents an overview of absorption measurements inferred from several experimental methods and finds an intensity dependence of:

$$f_{abs} = \left(\frac{I\lambda_L^2}{3.37 \times 10^{20} \text{ Wcm}^{-2} \mu\text{m}^{-2}} \right)^{0.1958} \quad (2.45)$$

for $I\lambda_L^2$ values between 10^{18} and 10^{20} W/cm². The measurements in Reference [19] were obtained using a laser with a peak intensity of 10^{20} W/cm² and varied the energy from 0.02 J to 20 J to complete the scan. Whilst this is simply a fit for measured experimental values, it has proven useful throughout the field as an initial estimate of absorption values.

2.6.1 Distribution

Energy from the laser pulse is distributed to a population of electrons via the absorption processes detailed before. Overall these processes form a Maxwellian distribution of electron energies [117] (or Maxwell-Juttner for high intensity beams [118]), where the temperature of the distribution increases with intensity and the total flux increases with energy absorbed. The distribution functions for each are displayed below (Eq. 2.46 and Eq. 2.47), and how this looks spectrally is plotted in Figure 2.5. For a Maxwell distribution of particle energies in an idealised system, the temperature of the system, $k_B T_h$, defines the slope of the spectra and the modal particle energy at $E_{mean} = 0.5k_B T_h$:

$$f(E_h) = N_e \sqrt{\frac{4E_h}{\pi(k_B T_h)^3}} \exp\left(-\frac{E_h}{k_B T_h}\right) \quad (2.46)$$

where E_h is the hot electron energy in the distribution and N_e is the total number of accelerated electrons. For highly relativistic cases this expression is no

longer valid since the relative particle mass has increased as its velocity approaches c . The following expression can be used instead, with respect to the Lorentz factor of the electron, γ :

$$f(\gamma) = N_e \frac{\gamma^2 \beta}{\xi_T K_2(\xi_T^{-1})} \exp\left(-\frac{\gamma}{\xi_T}\right), \quad (2.47)$$

where ξ_T is the normalised temperature $k_B T_h / m_e c^2$, β is the normalised electron speed v/c , and K_2 is a modified Bessel function of the second kind. Whilst the modal energy is not as trivial to express, it can be shown to satisfy

$$k_B T_h = 0.511 \left(\frac{\gamma^3 \beta^2}{2\gamma^2 - 1} \right) \text{ for temperatures exceeding 1 MeV.}$$

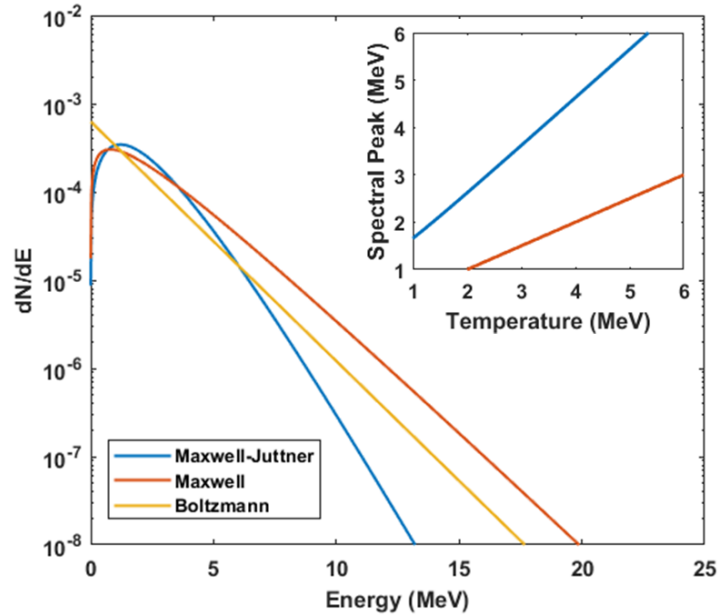


Figure 2.5: Electron distributions of the form Eq. 2.46 - 2.47 and a Boltzmann distribution for a 1 MeV electron temperature. The inset shows the relationship between spectral peak and temperature for each distribution.

2.6.2 Electron Temperature

Understanding how the laser intensity determines the properties of the internal electron population is crucial to the field due its effect on the secondary

sources (discussed again in Section 3.2). Since the majority of these electrons do not escape the target (see Section 3.1.4), it is difficult to accurately measure the hot electron population directly. Instead secondary processes, such as x-ray generation (Section ??) and ion acceleration (Section 3.1.4), or simulation results must be relied upon to determine the properties of the internal electron distribution. Several scaling laws have been developed through experimental measurements and analytical modelling to provide an estimate of the internal electron temperature. Whilst many exist [18, 114, 119–127] the two scaling laws that have been found to be the most applicable to the interaction conditions studied in this thesis are outlined here. Each takes a different approach to determine the relationship between intensity and electron temperature. The first is the scaling introduced by Beg *et al.* [18]:

$$T_{hot} = 0.215(I_{18}\lambda_{\mu}^2)^{1/3} \text{ MeV} \quad (2.48)$$

which was determined from a series of experimental results measuring the x-ray emission from a target. In the data collated by Beg *et al.*, the majority of experiments were conducted with a fixed laser energy ($< 30 \text{ J}$) and the intensity varied between 1×10^{18} and $1 \times 10^{19} \text{ W/cm}^2$ by changing the pulse duration of the laser. Therefore, caution should be applied when using this scaling to compare with data where the laser energy or spot size is varied. In contrast to the experimental findings, Wilks *et al* derived a scaling law based on the ponderomotive potential of the laser [121];

$$T_{hot} \approx m_e c^2 \left(\sqrt{1 + a_0^2/2} \right) \text{ MeV.} \quad (2.49)$$

where a_0 is the normalised laser potential described above¹. Both of these scaling laws are used in models and analysis presented throughout this thesis,

¹This equation is valid for linear polarisation, in the case of circular polarisation the term reduces to be $\propto \sqrt{1 + a_0}$.

henceforth Eq. 2.48 will be referred to as Beg scaling law and Eq. 2.49 as Wilks scaling law.

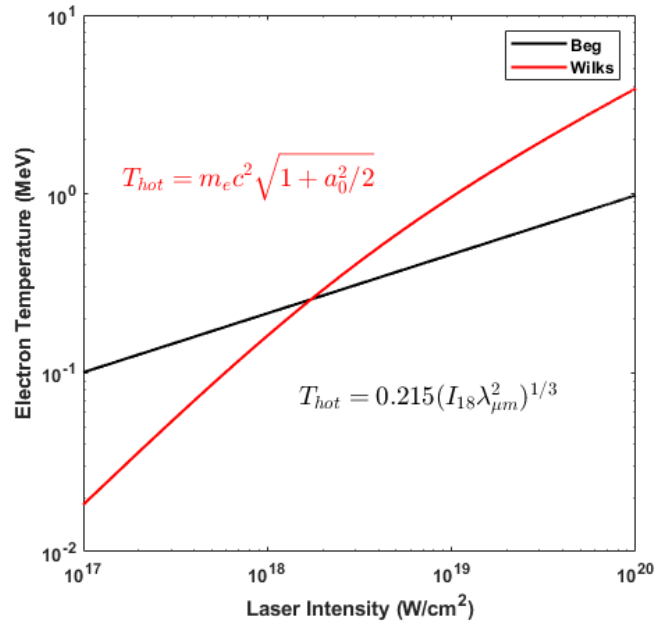


Figure 2.6: Electron temperature (in MeV) for different laser intensities as calculated by Beg (Eq. 2.48) and Wilks (Eq. 2.49) scaling laws.

2.7 Summary

The physical processes described in this chapter will be referred back to in later chapters, with particular emphasis on the electron spectrum and temperature. The scaling laws discussed in section 2.6.2 are used to develop a model of electron recirculation in Chapter 5. The propagation (and subsequent processes) that occur to this energetic electron current are discussed in the following chapter along with a review of electron transport studies.

Chapter 3

Electron transport through solid targets and radiative mechanisms

Chapter 2 provides an overview of energy exchange and absorption mechanisms between a high-intensity laser pulse and the plasma electrons on the front surface of solid targets. The accelerated “hot” electron population then travels through the solid target emitting radiation as it travels. This chapter explores the processes involved in hot electron transport through the target and the field growth and subsequent radiation emission (both EM and particle) that occurs. A review of relevant literature is also conducted looking at the role of K-alpha and bremsstrahlung in experimentally determining the electron transport.

3.1 Electron Transport

Ampere’s Law Eq. 2.4 states that a current density, \mathbf{j} , has a magnetic field associated with it. Alfven [128] and Lawson [129] explored this relationship to determine the limit at which the magnitude of the induced \mathbf{B} field becomes inhibitive to the transport of the current. As the azimuthal \mathbf{B} field increases, the Lorentz force pinches the beam and can turn the electrons around halting the propagation. The Alfven-Lawson current limit (the current at which this

force stops the propagation) is defined by:

$$I_A \simeq \beta\gamma mc^3/e \quad (3.1)$$

where β is the electron velocity divided by the speed of light for an infinitely wide current. In high intensity laser interactions the expected *accelerated* electron current can be calculated in excess of megaAmperes [130], however the limit expressed in Eq. 3.1 is $I_A \approx 50$ kA for 1 MeV electrons.

3.1.1 Return Current

Therefore, there must be a mechanism that reduces the local current to below the Alfvén limit to enable transport of the electron population into the target [131, 132]. Bell *et al* [130] suggested that there is a counter-propagating (return) current which is able to partially negate the otherwise inhibitive field growth, and maintain a current below the Alfvén limit. The return current is sourced from the colder, higher density, background electrons of the target [133]. This condition can be expressed as:

$$\mathbf{j}_{hot} + \mathbf{j}_{return} < \frac{I_A}{\pi r_e^2} \quad (3.2)$$

where \mathbf{j}_{hot} and \mathbf{j}_{return} are the current densities for each electron population, and r_e is a radius of the electron beam at any given point. Typically, this is expressed as a neutrality where $\mathbf{j}_{hot} + \mathbf{j}_{return} \simeq 0$. However, there are additional effects of this current to be considered which make it more intuitive to consider it as an inequality rather than a neutrality, these are discussed in the following sections. As an overview the schematics in Figure 3.1 outline the various mechanisms that are discussed in the following sections, (a) shows the factors affecting the electron divergence through the target, (b) highlights the different current densities that result from electron transport, and (c) shows the resulting fields that emerge.

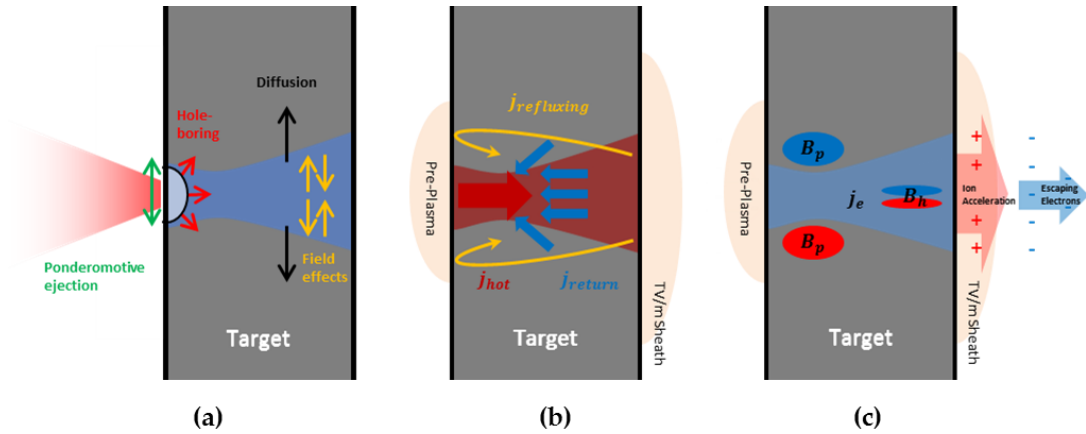


Figure 3.1: Schematic of the mechanisms discussed in the following sections acting throughout a solid target. (a) Factors affecting the effective divergence of the electron beam. From left to right, ponderomotive ejection, hole-boring, collisional scattering, and field effects. (b) Electron current motion, depicting the major components of electron travel; hot, return, and recirculating/refluxing. (c) Field components inside the target and the sheath formation on the rear surface accelerating ions. During transport, magnetic field growth happens azimuthally to the beam resulting in hollowing (B_h) and pinching (B_p) magnetic fields.

3.1.2 Electron Divergence

The divergence of electrons through solid targets has been studied by many groups [20, 101, 134, 135] as it affects many areas of the research field; including proton acceleration [136–138] and fast electron transport [139–141]. It requires further study to fully understand all parameters influencing the effective hot electron divergence, however, there are some core aspects that are discussed here. The initial conditions are vital to the final transport properties of the beam and the collective electron divergence is the result of many expansive and restrictive factors. The ponderomotive force acts on the electrons to drive them away from the more intense regions of the beam. For a centrally peaked intensity distribution this results in a divergence in the hot electron population. It can be shown, by assuming the electron is at rest before the laser arrives, that

the ejection angle relative to the propagation of the laser is [1]:

$$\cos \theta_{div} = \sqrt{\frac{\gamma - 1}{\gamma + 1}} \quad (3.3)$$

where γ is the Lorentz factor for the accelerated electron - for a 1 MeV electron this equates to $\sim 40^\circ$ - due to the variation in the longitudinal and transverse velocities (Eq. 2.16 and Eq. 2.15 respectively). Several studies have used this calculation (or variants of), to calculate electron divergence [142, 143], including a study by Meyerhofer in 1997 [144] that demonstrated its effectiveness at predicting the *peak* divergence angle of electrons with varying energy. Laser interactions can also deform the target surface, altering the effective target normal and driving electrons into the target at a more divergent angle [145, 146]. Electron collisions with the target material then act to widen the beam through scattering. Lawson presented the following scattering relationship:

$$F(l, \theta_s) = \frac{E_h^2}{440\pi l} \exp(-E_h^2 \theta_s^2 / 440l) \quad (3.4)$$

where θ_s is the scattering angle for the electron of energy, E_h , through a target of thickness l . Expressed in units of the radiation length:

$$l = A / \left(4\alpha N_A Z^2 r_0^2 \ln 183Z^{-0.33} \right) \quad (3.5)$$

where A is the atomic mass number, Z the atomic number, $\alpha \approx 1/137$ the fine structure constant, N_A is Avogadro's number, and r_0 the classical electron radius [147].

3.1.3 Internal Field Growth

This internal field growth significantly affects the propagation and divergence of electrons, and is dependent on the initial conditions of the interaction. The magnetic field growth is due to local variations in the current den-

sity within the target. From Maxwell's equations the temporal evolution of the magnetic field can be shown to be:

$$\frac{\partial \mathbf{B}}{\partial t} = \eta_e (\nabla \times \mathbf{j}_h) + \nabla \eta_e \times \mathbf{j}_h \quad (3.6)$$

where η_e is the resistivity of the plasma, and the higher order terms of the equation, such as magnetic diffusion, are negligible. Plasmas intrinsically have very low resistivity. However, since this typically scales as a function of temperature ($\eta_e \propto k_B T_h^{-3/2}$), cooler regions within the target will have a higher resistivity and therefore affect the field growth more.

Two components of field growth can be explored from this equation. Filamentation acts to modulate the beam as it transports through the target and scales with the electron density that has been accelerated. The spatial gradient of the current density (LHS of Eq. 3.6) causes a pinching (or hollowing depending on the sign of the gradient) magnetic field to occur. Since this is dependent on the current density this scales with changes in n_h . This acts to pinch the beam, which becomes a self-sustaining effect and filaments in the beam confine themselves further as they propagate. Silva *et al.* [148] conducted a thorough study on the rise of field driven instabilities during electron transport. They presented a threshold hot electron density at which filamentation would occur during transport with respect to the background return current density as:

$$n_h/n_r > \gamma_h \theta_{div}^2, \quad (3.7)$$

where γ_h is the Lorentz factor of the electrons and n_r the return current density. Modelling the internal field growth analytically relies on a well understood divergence angle to determine the current density deep within a target [134, 149].

The exploitation of resistivity changes has been explored by many groups as a way to narrow the divergence of the beam or structure filamentation within the electron channel [143, 150–153]. A magnetic field is generated from the temperature gradient in the target (or resistivity gradient $\eta_e \propto k_B T_h^{-3/2}$) and acts to both restrict and expand the beam depending on the sign of the gradient, RHS of Eq. 3.6. Scott *et al.* [154] used this experimentally to generate an azimuthal magnetic field and restrict the electron beam expansion. They demonstrated that by using an initial pre-pulse to seed magnetic field growth in the target it is possible to optimise this magnetic channel and narrow the electron beam expansion injected from the main pulse. Kar *et al.* [155] used layered targets to ensure resistivity changes surrounding the beam limited the lateral expansion of relativistic electrons. Measurements and simulations conducted by Kar *et al.* show a clear restriction in the lateral expansion of the electron beam. In standard foil targets McKenna *et al.* [156] demonstrated that the variation in resistivity laterally through the target impedes the expansion of the electron beam during recirculation. Experimental investigations by Maclellan *et al.* [152] demonstrate an annulus structure emerging in the transport of electrons through a silicon target. This structure is explained by a non-linearity in the resistivity curve. At ~ 3 eV there is a reduction in the resistivity of the target as electrons have enough energy to enter the conduction band of the target but not enough to cause electron-ion collisions. This non-linearity, despite the low temperatures at which it is important, dominate the overall transport as the resultant dip in the resistivity gradient (RHS of Eq. 3.6) causes a hollowing effect within the beam that drives electrons into the collimating field surrounding the main channel. Maclellan *et al.* [157] followed this work with a thorough simulation study investigating the effects of different laser parameters on the annulus characteristics showing that, via incident laser conditions, the resistivity gradients through the target could be controlled to elicit changes in the annulus structure.

Experimental measurements and simulations of the field effects on fast electron transport have been demonstrated by numerous groups [20, 101, 158, 159]. Measurements by Green *et al.* are of particular relevance given the similar laser conditions to those studied in this thesis. They found that with reduced on-target intensity the divergence of the electron beam narrows. A simple analysis of Eq. 3.3 would imply the reverse, with lower laser intensity driving a lower temperature fast electron beam having a large divergence from the ponderomotive force (as the electrons forward momenta is reduced). Green *et al.* [20] concluded that in the ideal case, as γ and n_h both scale with the laser intensity, the divergence should be independent (Eq. 3.7 $\rightarrow \theta_{div}^2 \propto n_h/\gamma$). However, the inclusion of many lower energy electrons (i.e return current, or accelerated by the laser pre-pulse) accelerated by the laser results in the average γ remaining effectively constant for the entire population of electrons over the range of intensities. Since the total number of electrons still increases with intensity (Eq. 2.45) the divergence of the electron population is observed to increase. This indicates that the field growth within the target (dependent on n_h) is dominating compared to the ponderomotive ejection at acceleration when determining effective electron divergence.

3.1.4 Sheath Development

The hot electrons generated in high-intensity laser plasma interactions typically have a mean free path much longer than the target thickness in most studies. At the rear target surface there is no longer a return current to be drawn and the electron propagation is inhibited. A small fraction of the hot electron beam escapes the target and propagates into the vacuum, known as escaping electrons. This loss of charge from the target results in strong electrostatic field growth on the rear surface of the target, which acts to return later electrons back into the target. This process is repeated on the front surface of

the target, resulting in recirculation through the bulk of the target material, as electrons reflect due to these fields [160]. The strength, and the lateral and transverse extent of this sheath field is an important factor in both electron recirculation and subsequent ion acceleration. The longitudinal extent of the field, assuming negligible ion expansion over the duration ($<ps$), can be approximated as the Debye length, λ_D [161, 162]. The lateral expansion can be described as a function of the initial laser spot size (and therefore hot electron generation area) and average electron divergence through the target. At the interface between target and vacuum the peak electric field can be approximated to scale [161]:

$$E_{\max}(z = 0) = \frac{\sqrt{2}k_B T_e}{e\lambda_D} \quad (3.8)$$

however, since λ_D is a function of electron density, this can instead be expressed by the radial divergence of the electrons, θ_e , the incident laser spot size ϕ_L , and the peak intensity on a target of thickness d [138, 163]:

$$E_{\max} \approx \frac{\phi_L}{\phi_L + d \tan(\theta_e/2)} I_{18}^{7/8} 5.2 \times 10^{11} \text{V/m} \quad (3.9)$$

This is a simplified expression; over the course of the interaction the size of the sheath will expand as electrons spread laterally through the target and reduce the peak strength. Dubois developed a model [164] that estimates the temporal evolution of the sheath by taking into account electron diffusion in the target and the reduction in rear surface density as electrons diffuse through collisions. Solving Eq. 3.8 for typical parameters ($k_B T_e \approx 1 \text{ MeV}$ and $\lambda_D \approx 1 \mu\text{m}$ [162]) leads to a peak field strength of $E_{\max} \approx 1.5 \text{ TV/m}$. Electrons arriving after this sheath has formed would have to have enough energy to overcome this potential in order to escape, if not, the electrons would recirculate within the target.

The escaping population is typically a small fraction ($< 5\%$) of those initially accelerated [8, 21, 38, 160, 165]. Electrons in this population come primarily from two mechanisms; as part of the plasma expansion, or highly energetic and able to overcome the sheath potential. Electrons in each population have interacted with the sheath field to some extent, and, as a result, measurements of escaping electrons must consider this effect when drawing conclusions about the accelerated population. Link *et al.* [166] explored the effect of proton acceleration on the escaping electron population, determining that as the sheath field increases, and the target charges, part of the escaping spectrum is cooled significantly. Measurements of escaping electrons should, therefore, be approached with care since they can be misleading if this effect is not accounted for. Grismayer *et al.* [167] developed an analytical model for the spectral cooling that occurs when electrons interact with an evolving sheath field. Rusby *et al* [168] demonstrated, via numerical simulations, that electrons escaping the target can be significantly de-accelerated as they overcome the sheath.

In summary, electrons are accelerated into the target and experience a multitude of transport effects. Their initial divergence is the result of intensity gradients at the front surface. The high current that propagates means a large return current must be drawn to offset inhibitive field growth. Despite this return current, local field growth acts to pinch, filament, and expand the beam as it propagates. Electrons within the target medium scatter as a result of collisions with the background atoms. If they are able reach the rear surface, large charge separation can occur instilling a TV/m electro-static field at the target boundary which acts to trap electrons and recirculate them through the target. A schematic of the transport mechanisms described in the prior sections (Return Current - Section 3.1.1, Electron Divergence - Section 3.1.2, and Field Growth - Section 3.1.3) is shown in Figure 3.1.

3.1.5 Target Normal Sheath Acceleration

The sheath field can be sufficiently strong to fully ionise the rear surface (Section 2.3) and then accelerate ions. For PW scale laser facilities peak energies in excess of 50 MeV are now routinely accelerated with a total flux of $\sim 10^{13}$ protons across the entire spectrum [169, 170]. These protons, found in the containment layers of a target, are more favourably accelerated due to their high charge-to-mass ratio compared to other ions. However, multiple ion species and charge states (sourced from containment and target ions) can also be accelerated by the same mechanism, depending on the skin depth of the sheath field and the ions in the vicinity. This process is known as Target Normal Sheath Acceleration (TNSA) and has been an area of study for many years; with the full extent of the process being the subject of many detailed investigations [121, 138, 161, 165, 171, 172]. TNSA is the culmination of many physical processes; the population of accelerated electrons, their subsequent divergence and structure through the target, the distribution on the rear surface, and the temporal evolution all influence the beam parameters of the accelerated ion beam. Several models have been developed and used throughout the community in order to account for different aspects of the interaction and provide some prediction as to the maximum acceleration. One of the most commonly used models is the plasma expansion model by Mora [161]. This model is a 1D analytical approach to the sheath field formation at a plasma boundary in terms of the initial electron temperature. It is used by the author in Chapter 5 to develop a model for the recirculation of electrons. Fuchs *et al.* [173] applied this model, and an approximation of the acceleration time, τ_{acc} , to estimate the maximum proton energy as:

$$E_{\text{proton}} \approx 2Zk_B T_e \left[\ln \left(\tau_{\text{acc}} + \sqrt{\tau_{\text{acc}}^2 + 1} \right) \right]^2 \quad (3.10)$$

ω_{pi} here is the ion plasma frequency. In reality, the acceleration time is finite

and τ_{acc} needs to be given in order to determine the maximum proton energy. The acceleration time has been shown to be bounded to the order of the laser pulse, $\tau_{\text{acc}} \approx 1.3\tau_{\text{laser}}$ [173] for picosecond laser durations and significant pre-plasma formation. Brenner *et al.* [170, 171] presented a model for calculating the acceleration time which incorporates the ion expansion rate and the transverse electron transport time for ultra-thin targets and femtosecond laser durations.

3.2 X-ray Generation

The accelerated electrons are able to emit radiation across the EM spectrum. This section encompasses the primary mechanisms involved in x-ray generation - focusing on bremsstrahlung and line emission from targets. Whilst this is an incomplete picture of the photon generation processes that occur in laser plasma interactions - in particular THz [62, 63, 174] and (X)UV [58, 59, 175, 176] - it encompasses the key aspects of physics which are relevant to the work present herein.

A key mechanism for the generation of x-rays is derived from the acceleration of electrons; when changes in energy occur the difference is emitted as radiation. This is described mathematically by Larmor's formula. The power emitted by an accelerating particle can be expressed as:

$$P = \frac{e^2 a^2}{6\pi\epsilon_0 c^3} \quad (3.11)$$

where a is the acceleration of the particle [177, 178]. The schematic in Figure 3.2 demonstrates the origin of this radiation. As the particle accelerates, a "break" in the field lines emerges at distance $r = ct$. Since field lines must be

continuous, a perpendicular component of the field emerges as a result:

$$E_{\perp} = \frac{qa \sin \theta}{rc^2} \quad (3.12)$$

Unlike the typical radial charge, which is proportional to $1/r^2$, this field has a $1/r$ dependence resulting in only this field contributing at large distances - i.e. it is radiated.

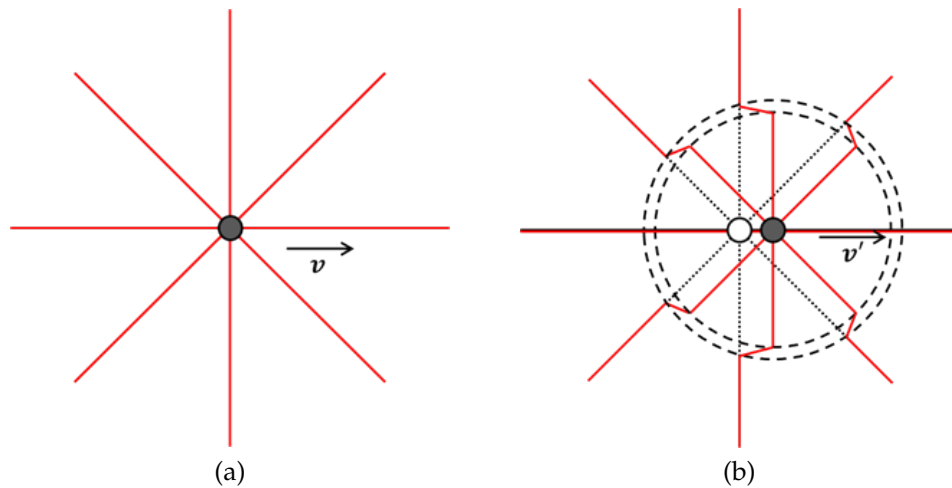


Figure 3.2: Field lines of a charge in a travelling frame at v , (a) Field lines at t_0 , (b) Field lines at t_1 after charge has accelerated to v' , where $v' > v$. Radius of the inner circle is $r = ct$.

3.2.1 Bremsstrahlung

The German root for bremsstrahlung is "braking-radiation"; since this emission is determined by electrons losing energy as they interact with fields within an atom, the difference between the incident energy and the final energy is emitted as a photon. The emitted x-ray spectra from laser plasma interactions is typically dominated by a continuum of photon energies generated by bremsstrahlung up to several MeV in energy. This process is an extension of Larmor's Law (Eq. 3.11). In the case of bremsstrahlung the acceleration, a , for

an electron is described by Coulombs law:

$$F = ma = -\frac{Ze^2}{4\pi\epsilon_0 r^2} \quad (3.13)$$

where r is the distance between the electron and the ion. The important distance, and therefore force, is the closest approach - or impact factor - b . The time of the interaction is $\Delta t \approx 2b/v$ where v is the speed of the incident electron and the ion is considered stationary for the duration. The energy is therefore a combination of Eq. 3.11 and Eq. 3.13:

$$P\Delta t = \Delta E = \frac{4Z^2e^6}{3m_e^2c^3} \frac{1}{b^3v} \quad (3.14)$$

For the total internal spectra of electrons there are a range of energies (and therefore velocities v), and a range of impact parameters. In a plasma, the maximum interaction range of concern is the Debye length, with the the minima set as the De Broglie wavelength [179], $b_{max} = \lambda_D$, $b_{min} = \lambda_B = h/p$. Integrating over the possible interactions distance and the number density of ions gives the energy radiated per electron as:

$$\frac{\Delta E}{\Delta t} = \frac{4n_i\pi}{3} \frac{Z^2e^6}{m_e^2c^3} \frac{1}{v} \left[\frac{1}{\lambda_D} - \frac{1}{\lambda_B} \right] \quad (3.15)$$

To include the energies: the spectra of hot electrons inside the target, $f(E_h)$ (Eq. 2.46) is used, leaving the total power emitted per volume for the accelerated spectra, W_B as:

$$W_B = \int_0^{v_{max}} \underbrace{\frac{4n_i\pi}{3} \frac{Z^2e^6}{m_e^2c^3} \frac{1}{v} \left[\frac{1}{\lambda_D} - \frac{1}{\lambda_B} \right]}_{\text{Per Collision}} \overbrace{N_e \sqrt{\frac{4E_h}{\pi(k_B T_h)^3}} \exp\left(-\frac{E_h}{k_B T_h}\right)}^{\text{Spectra}} 4\pi v^2 dv \quad (3.16)$$

$$W_B \approx 1 \times 10^{-21} Z n_e^2 \sqrt{T_e} \left[\exp \left(- \frac{h\nu}{k_b T_e} \right) \right] \frac{\text{MeV}}{\text{cm}^3 \text{s}} \quad (3.17)$$

This derivation is taken from the discussion by Giulietti and Gizzi [179] but converted into appropriate units and with certain steps reduced in order to provide clarity. Whilst the convolved energy equation results in a complicated expression, the single interaction model is simple to understand. When the electron is deflected by a nearby nucleus it emits radiation equal to the energy it is losing as a result of Larmor's formula, Eq. 3.11. A schematic of this process is shown in Figure 3.3.

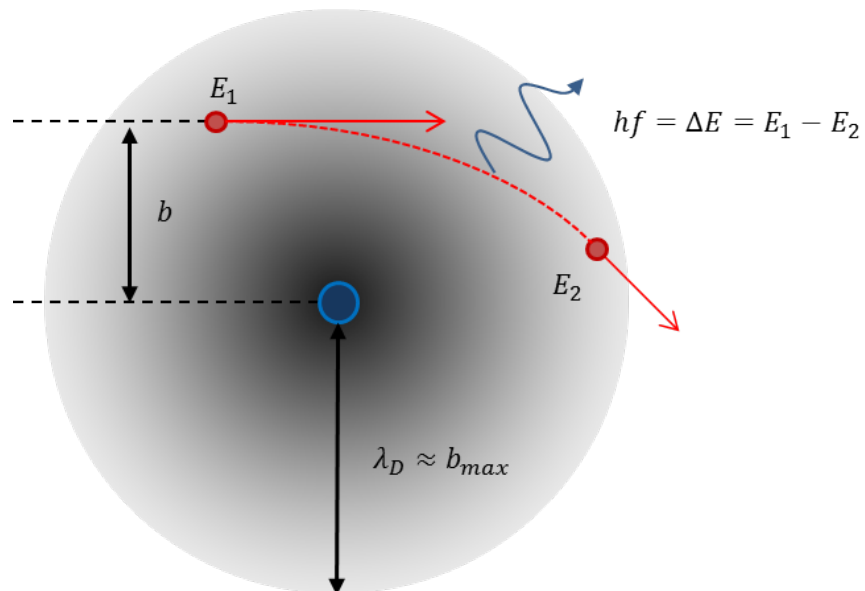


Figure 3.3: Bremsstrahlung is generated as the electron decelerates in a field. The energy of this photon is dependent on the approach distance b and the energy of the incident particle.

3.2.1.1 Line Emission

Energetic electrons travelling within a material have the chance to ionise atoms by colliding with the surrounding bound electrons. Lower-shell elec-

trons can be excited and ionised by these collisions resulting in higher-shell electrons decaying to the lower energy shell and, as a result, the atom emits a photon with characteristic energy to compensate. The most common of these (for typical interactions where $k_B T_e \approx 1$ MeV) is a K-alpha emission where the inner most electron (and therefore lowest orbital energy) is ejected, and an electron from the orbital shell above (L-shell) then decays. The emission is typically very narrow-band with significant variation being an indication of strong external fields [180], or hollow-ions where both electrons in the K-shell are ionised changing the transition energy from the L-shell [181–183].

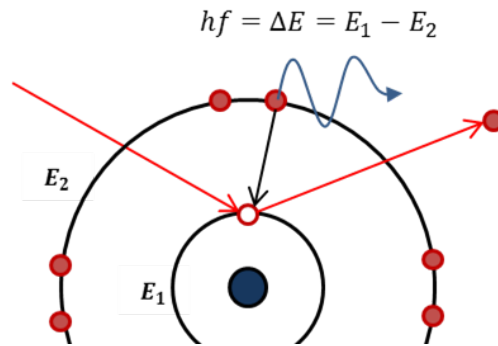


Figure 3.4: Line emission is typically a by-product of collisional ionisation; as the lower electron is ionised through collisions and higher orbital electrons then decay to the lower levels emitting characteristic energies. The most common of these transitions is from the L (E_2) shell to the K (E_1) shell resulting in a K-alpha x-ray being emitted.

This process is dependent on the number of travelling electrons present and the cross-section of collision between the accelerated electrons and orbital electrons:

$$N_k = \eta_r N_e \omega_k n_{Cu} \underbrace{\int_0^\infty f(E_0) dE_0}_{\text{Spectra}} \underbrace{\int_0^{s(E_0)} \sigma_k [E(E_0, s)] ds}_{\text{Cross Section}} \quad (3.18)$$

where σ_k is the interaction cross-section, E_0 is the energy of the electron, N_e is

the number of electrons, and ω_k is the branching ratio between K-alpha (L-K transition) and K-beta (M-K transition). Low energy, and more collisional, electrons are more likely to cause ionise the inner-electron and cause line emission, as a result the collisional return current that is established by the fast electron beam can be a source of this radiation.

3.2.1.2 Emitted Spectra

The combination of these processes inside a target results in a broad spectra extending up to the peak energy of the electron spectra (tens of MeV). The overall spectra is dominated by the broad continuum emitted via bremsstrahlung, with peaks from pair production and line emission at characteristic energies.

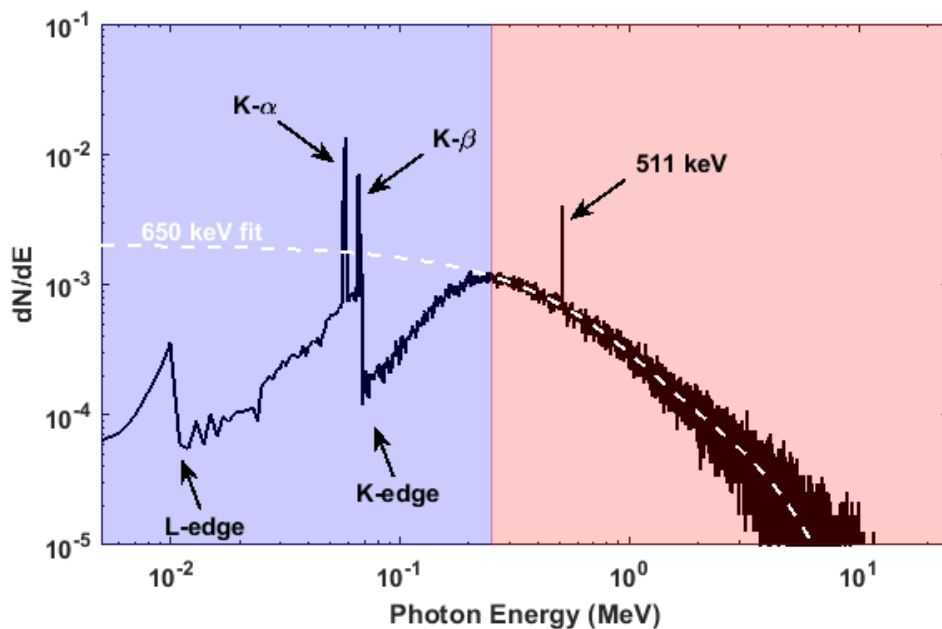


Figure 3.5: Total x-ray spectra from a 1 mm Ta thick target (black) 2.5 MeV temperature incident electron beam, modelled in GEANT4 assuming a single pass through the target. Single temperature fit is shown by a dashed white line. The shaded areas correspond to the two primary spectra regions, low energy (blue) dominated by target attenuation and the high energy (red) dominated by the Bremsstrahlung continuum.

Figure 3.5 shows a spectra generated for a single temperature electron beam

through a 1 mm thick Ta target. The spectra is effectively split into two regions: the lower energy (blue in Figure 3.5) is dominated by self-attenuation as the x-rays are generated and subsequently attenuated within the target (see section 3.4), and the high energy region (red in Figure 3.5) is dominated by the bremsstrahlung continuum and extends up to the peak energy in the electron spectra. A simplified expression for the emitted x-ray spectra can be attained by convolving a single Boltzmann distribution with the form $I = I_0 \exp(-E/k_B T)$ with the attenuation function of the target material.

3.3 K-alpha and bremsstrahlung emission

K-alpha emission has been used in many studies to date [20, 143, 184–189] to monitor the electron distribution. Its comparatively high yield and relatively low energy mean that it can be spatially and spectrally isolated via Bragg crystals or Ross-Pair filters [190, 191]. However, this technique is not without its shortcomings. The two primary stopping processes for electrons can be considered as collisional; interacting with atomic electrons in the material causing ionisation as a result of the collisions, or radiative; where the electron interacts with the atomic field and decelerates resulting in bremsstrahlung emission. The first case causes line emission in targets and is dominant at low electron energies, as shown in Figure 3.6, while at high energies the radiative stopping begins to dominate. These attenuation processes are dependent on the target material, and give rise to an attenuation length (λ_{att}) where the initial population of electrons has fallen to $1/e$.

Therefore, measurements made at higher energies - with bremsstrahlung emission rather than K-alpha - ensure that the bulk of the production is coming from the energetic tail of accelerated electrons, rather than colder electrons that could be from secondary processes such as collisional ionisation.

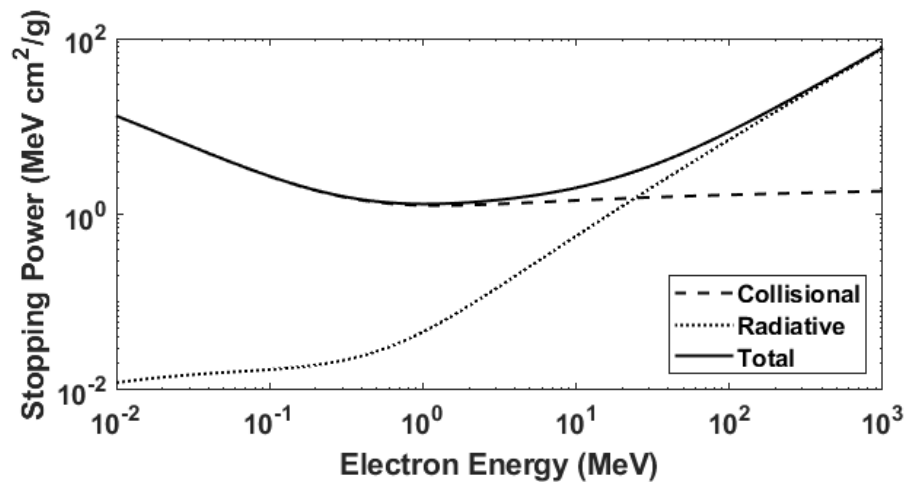


Figure 3.6: Electron stopping power in copper. The solid line is the collective stopping, dashed is collisional, and dotted is radiative. K-alpha emission is caused by the first process and bremsstrahlung by the second. Cross-sections from the NIST ESTAR database [14].

Another population of electrons to consider here is the return current. Typically this is a cold (10 – 100 eV) population of electrons, though there are conditions under which this cold background can increase in temperature. Recently, Compant La Fontaine published a study into the time evolution of the return current [192], and its effect on the target resistivity and x-ray generation, concluding that the Ohmic heating induced by the return current could reduce the x-ray signal by up to 40% for a tantalum target. At short distances into the target, the return current temperature was shown to rise to \sim keV energies, therefore introducing uncertainty in the origin of K-alpha sources. Spatially, the return current will occupy a similar volume as the accelerated current [130], however, unless factored in, the flux contribution by this population of electrons could lead to misleading measurements of the accelerated population.

Higher energy x-ray measurements preclude the chance of contribution from the return current. An effect to consider as a result of this is the angular emis-

sion of bremsstrahlung radiation; K-alpha emits in all directions but the angle of emission for bremsstrahlung is dependent on the incident electron energy (and momenta). The distribution of bremsstrahlung emission angle can be expressed as a function of the electron energy E by [147]:

$$F(\theta_\lambda) = \frac{1}{\left[1 + \left(\frac{E}{E_0}\theta_\lambda\right)^2\right]^2} \quad (3.19)$$

where E_0 is the rest mass of the electron, and θ_λ is the x-ray emission angle from the electron's direction of travel. For electrons greater than ~ 250 keV, the half angle of emission is less than 45° and therefore x-rays emitted from recirculating electrons will be detected primarily on every other pass of the target.

3.4 X-ray Attenuation

Attenuation of x-ray signal generated by electrons within the target decreases the flux of x-rays detected experimentally. The lowest x-ray energies are attenuated most strongly, resulting in a *quasi-top hat* distribution. There are various mechanisms behind the attenuation of x-rays which are key in understanding x-ray detection. The transmission of x-rays can be described through the Beer-Lambert law:

$$I = I_0 \exp(-\rho l \sigma) \quad (3.20)$$

where I_0 and I are the intensity of the x-ray signal before and after transmission respectively, ρ is the mass density, l is the length of transmission, and σ is the attenuation cross-section for that energy x-ray and material. There are three primary attenuation mechanisms to consider; absorption, where the incident photon is absorbed and the energy deposited in the target, scattering,

where the photon is deflected away from its initial trajectory, and pair production, where the incident x-ray seeds the creation of an electron-positron pair which then annihilates some time later to produce two 511 keV photons.

The photo-electric (PE) effect governs the losses for low energies. The x-ray deposits its energy into an electron, causing it to become ionised and able to deposit its energy elsewhere in the target. This is dominant at energies < 100 keV. The extent of the spectra that this dominates over is dependent on the Z of the material:

$$\sigma_{PE} \propto Z^n E_\gamma^3 \quad (3.21)$$

where E_γ is the energy of the incident x-ray and n is a scaling factor dependent on the material [193]. The atomic number dependence is a result of the increased density of high- Z materials and, therefore, a higher number of electrons that can be interacted with in a given volume.

At higher energies, the photon can be re-emitted from the electron with some fraction of its initial energy at a different angle. This scattering process can occur in two ways: either the photon energy is maintained (elastic/Thomson scattering) or photon energy is reduced (in-elastic/Compton scattering). In each case the incident photon interacts with bound electrons and is re-emitted. For Thomson scattering, the electron is excited by the photon electric field and, from Lamor's equation for radiated power (Eq. 3.11), an equal frequency photon is emitted at an angle dependent on the polarisation angle of the incident x-ray. This is an infrequent process with the majority of scattering being dominated by Compton scattering [194]. The incident photon must have sufficient energy to excite, and ionise, the electron. The electron carries away a portion of the incident energy and the rest scatters with the photon.

The cross-section for each Thomson and Compton are [195, 196]:

$$\sigma_{TS} = \frac{1}{3} \left(\frac{2e^2}{\epsilon_0 m_e c^2} \right) \quad (3.22)$$

$$\sigma_{CS} = \left(\frac{2e^2}{\epsilon_0 m_e c^2} \right) \left(\frac{1 + 2k + 1.2k^2}{3(1 + 2k)^2} \right) \quad (3.23)$$

where $k = E/E_0$. It is clear to see that for incident photon energies, where $k \rightarrow 0$, $\sigma_{CS} \rightarrow \sigma_{TS}$. The energy loss of the photon in Compton scattering is an important characteristic in x-ray attenuation since it can result in high-energy photons reducing in energy and becoming easier to detect. The energy of the scattered electron is dependent on the scattering angle of the photon:

$$E' = \frac{E}{1 + (E/E_0)(1 - \cos \theta)} \quad (3.24)$$

The final process is pair-production, in which photons with $E > 1.022$ MeV (the rest mass of an electron plus positron) travel within the field of a nucleus and a positron-electron pair is created. This must happen within an atomic field to maintain the conservation of momenta, and as such it scales with the relative size of the field. The cross-section is as follows [196, 197]:

$$\sigma_{PP} = \frac{e^6 Z^2 P(E, Z)}{64\pi^3 \epsilon_0^3 \hbar m_e^2 c^5} \quad (3.25)$$

where $P(E, Z)$ is a probability function dependent on the electron energy and atomic number.

The total cross-sections for materials are tabulated in databases such as XCOM from NIST [14]. The cross-sections for iron are outlined in Figure 3.7; the total attenuation cross-section being a summation of those described above $\sigma_x = \sigma_{PE} + \sigma_{CS} + \sigma_{TS} + \sigma_{PP}$ and dependent on the incident x-ray.

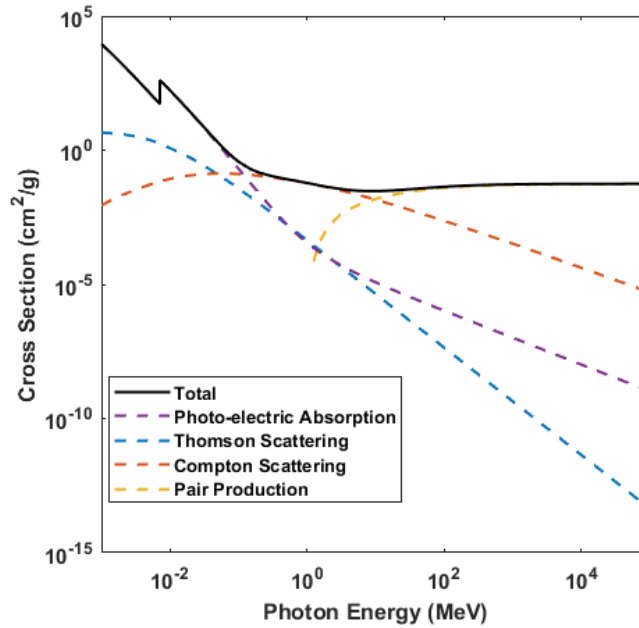


Figure 3.7: Cross-sections for the various processes occurring in x-ray attenuation for iron. Calculated from the NIST XCOM database [15]

3.4.1 Detected X-ray Emission

Detecting x-rays is a convolution of the emitted spectra, any additional materials the x-rays have to transport through, and the detector itself. Often, when using x-ray detectors, it is important to know what x-ray energy is most likely to be detected such that photon numbers can be estimated from the counts on the detector. This is referred to as the peak detected energy. The peak detected energy varies as a function of target thickness (ℓ), target material (ρ, Z), electron temperature (T_e) or the generated effective x-ray temperature (T_x), and the detector. For a fixed detector system, the experimental variables become the target and the electron/x-ray temperature. To explore the effect that each of these has a simple model can be constructed. Assuming a relativistic electron population $T_e \approx 1$ MeV and a thin target, such that $\ell < \lambda_{att}(T_e)$, x-rays will be generated fairly uniformly throughout the target in a continuum up to the energy of the incident electron and then attenuated by the remainder

of the target. In Figure 3.8(a) this process is drawn as a schematic, as electrons transport through each slice of the target they generate some x-rays. The emitted x-ray spectra is then a summation of each slice attenuated by the remainder of the target:

$$\gamma_x = \gamma_0 \sum_{n=0}^{n_t} \exp(-(\ell - (n - 1/2)d)\rho\sigma_x) \quad (3.26)$$

where γ_x, γ_0 is the x-rays created by the entire target and each slice respectively, n is the slice number and $n_t = \ell/d$, σ_x is the attenuation cross-section as discussed in the prior section. γ_0 can be calculated based on the electron radiative cross-sections, σ_e , from the NIST ESTAR database [15] similarly:

$$\gamma_0 = N_e(1 - \exp(-\ell\rho\sigma_e)) \quad (3.27)$$

where N_e is the number of electrons travelling through each slice. The peak detected x-ray can be calculated for a given x-ray temperature using these two equations. Figure 3.8(b) is the peak detected x-ray energy as a function of effective x-ray temperature for a 100 μm thick copper target detected in image plate through an 18 mm SiO_2 window. This configuration is used in the experimental discussion in Chapter 5.

This was determined using the cross-sectional data in the NIST ESTAR [14] and XCOM databases [15], and the 1D attenuation determined by Beers law (Eq. 3.20). However, this can be replicated in 3D using GEANT4 (a Monte-Carlo simulation toolbox discussed again in Chapter 4) to model the x-ray transmission. Firstly, a simulation was conducted with a 1 MeV electron spectra (nominal electron temperature for $I_L = 5 \times 10^{19} \text{ W/cm}^2$) incident on a copper target with $\ell = 100 \mu\text{m}$, electrons were propagated through and deflected by a magnetic field, any emitted photons detected on a layer of image plate

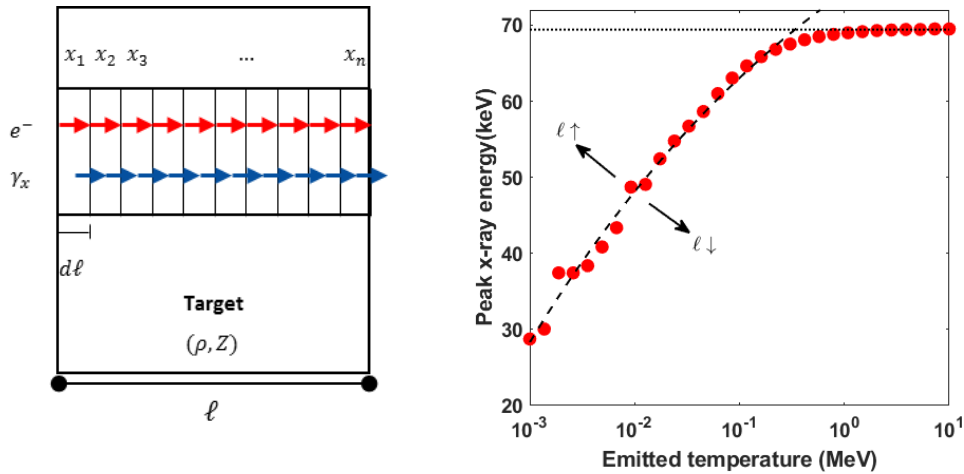


Figure 3.8: (a) Schematic outlining the production of x-rays throughout a target, each slice of the target is denoted by x_n , which has thickness $d\ell$. (b) Peak detected x-ray energy as a function of effective x-ray temperature, the peak signal approaches 70 keV as the effective x-ray temperature is increased $> \text{MeV}$. There is an increase in expected energy on the rising edge for increased target thickness as self-attenuation hardens the emission of x-rays.

and filtered by a 18 mm SiO_2 window, as before. The detected yield of x-rays as a function of their energy is shown in 3.9(a) with the effective temperature plotted as a black dashed line. The effective temperature from this configuration was $\sim 37\text{keV}$ and the peak is at $\sim 50\text{keV}$.

Additionally, the simulation can be used to determine the electrons responsible for generating the detected x-ray signal, shown in Figure 3.9(b) showing that the electrons most likely to generate the emission are from 1-3 MeV. The plot in Figure 3.10 shows how the responsible electron changes as a function of the electron temperature, calculated by assuming a Maxwellian distribution of electrons. This demonstrates that, by sampling these x-rays, the electrons are relativistic in nature and most likely from the hotter parts of the spectra due to their increased chance of radiation.

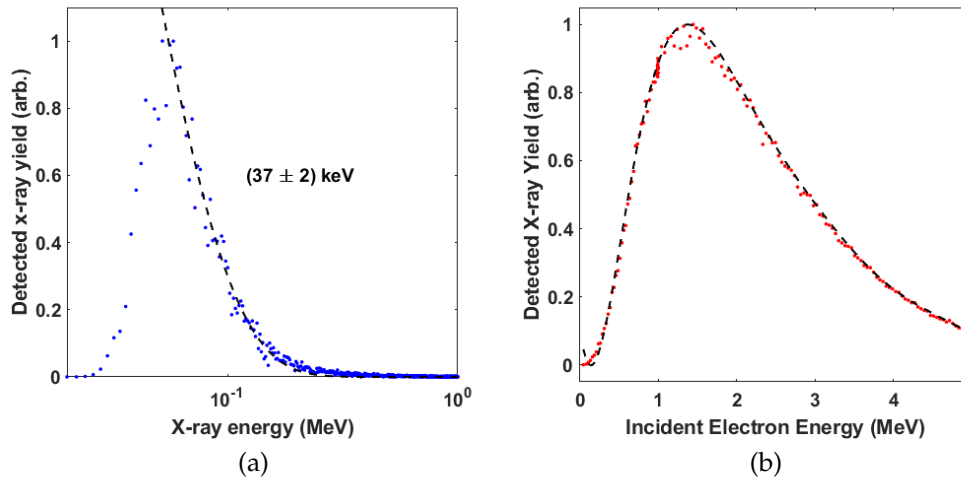


Figure 3.9: GEANT4 simulation results. (a) Number of detected x-rays as a function of their energy, an exponential fit of distribution is shown with an effective temperature of $\sim 37 \text{ keV}$. (b) The number of detected x-rays as a function of the incident electron energy.

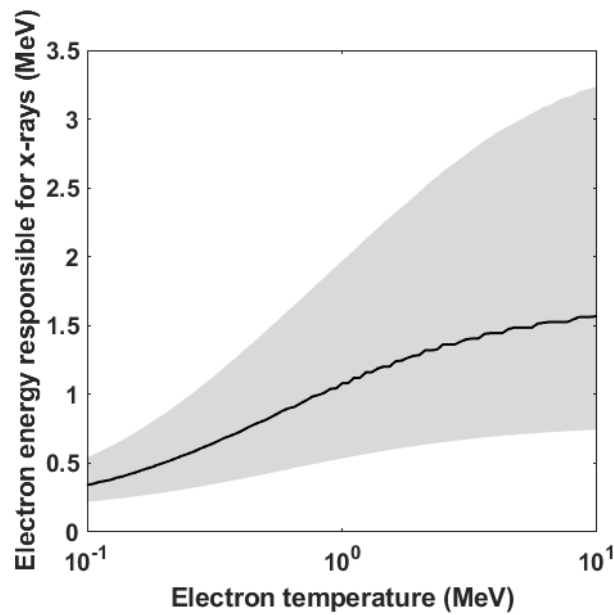


Figure 3.10: Primary electron energy responsible for x-ray generation in Figure 3.8 as a function of temperature, determined from the graph shown in Figure 3.9(b). Shaded region shows the area greater than 0.5 in Figure 3.9(b)

This is the response for a $100 \mu\text{m}$ copper target and is used to determine the peak energy for the detector system in Chapter 5 and the energy of electrons

most likely to generate those x-rays. A similar technique is used in Chapters 6 and 7 to determine the response for different target configurations. In the appendix a method to determine the responsible electrons from Kramer's Law is outlined.

3.5 Summary

Chapters 2 and 3 have covered the underlying physics relevant to the research presented in the thesis. The key concept to take from this overview is that the incident laser ionises and accelerates a broad spectra of electrons to relativistic energies into a target. These electrons collide with atoms within the target and produce a bright source of x-rays, which provide both a mechanism to diagnose the internal electron transport and beam characteristics, and the means to accomplish radiography of dense objects. As the electrons reach the rear surface, a large electro-static sheath field builds in response to the charge separation that drives a population of ions to be accelerated - a core focus for the field. The electrons that remain are recirculated back into the target, continuing to radiate as they propagate. The next chapter will discuss various methods applied throughout the thesis, including a description of the lasers that enable this work, and the detectors used to measure and characterise emitted x-rays.

Chapter 4

Methodology

The essential methods underpinning the experimental research is discussed herein. High intensity laser systems are introduced, covering the generation of the main pulse and the pedestal. The application and utility of numerical simulations is addressed with particular focus on GEANT4 and EPOCH, for their use in data analysis and designing diagnostics. The mechanisms and specifics of x-ray detectors are covered and particular attention is paid to the development of a high energy penumbral foil detector, to diagnose x-ray source size and relative flux that was developed by the author and used on numerous experimental campaigns.

4.1 High intensity lasers

The primary technique that allowed lasers to reach relativistic intensities ($> 10^{18}\text{W}/\text{cm}^2$) was CPA [43]. As the laser developed over time, the intensities reached *during* amplification were sufficient that non-linearities would build through optical mediums and significantly distort the beam. This leads to the requirement of either keeping beams under vacuum at all times, or lowering the intensity during amplification. One method used was to increase the diameter of the beam. Whilst effective, this quickly becomes expensive and untenable. CPA is the practice of stretching the pulse temporally rather than spatially, reducing the intensity during amplification.

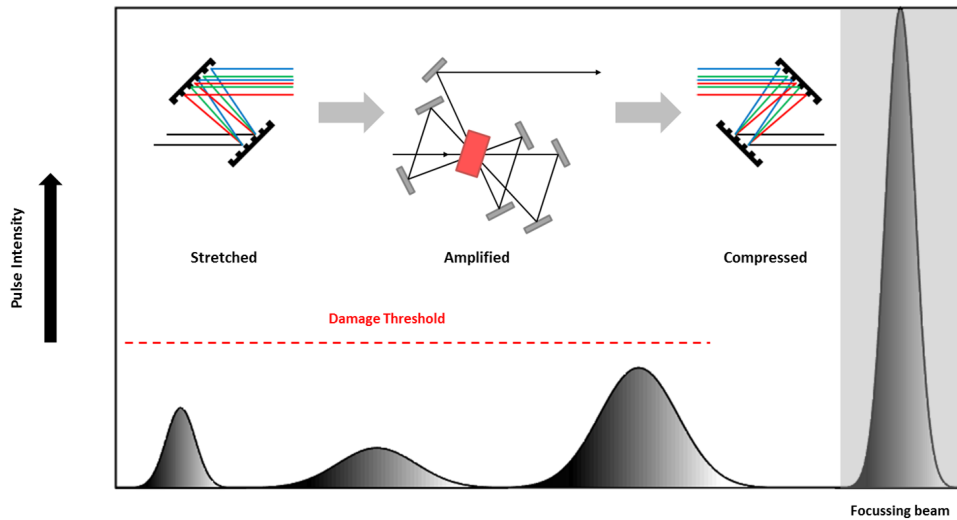


Figure 4.1: Chirped pulse amplification. *From left to right*: initial short pulse, stretched pulse, amplified stretched pulse, re-compressed pulse. Damage threshold is indicated, compression only occurs under vacuum with minimal remaining optics in path. Schematics for each stage are shown above the pulse shape.

The laser pulse is stretched using a pair of gratings, positively dispersed, to provide a longer path length for short wavelengths and vice versa. The distribution of wavelengths, or bandwidth, of the pulse is set by the lasing medium and optical properties of the laser. This now stretched pulse can be amplified without significant intensity dependent aberrations. The pulse is then re-compressed, using a second set of gratings, to a higher peak power.

4.1.1 Amplified Spontaneous Emission

The process of amplifying the primary laser pulse introduces a background signal to the entire chain via spontaneous emission from the gain medium. In a typical optical amplifier, the medium is excited microseconds before the seed pulse arrives, and electrons in the medium are excited to meta-stable states

with relatively long lifetimes. However, these electrons are able to spontaneously decay over the entire lifetime introducing a background signal to the laser chain. This emission is random and emitted in 4π with only a small percentage travelling down the remaining laser chain seeding further emission and thus amplification. The result is a lower-intensity, longer pulse duration pedestal that precedes the primary pulse - see Figure 4.2. The ratio between the intensity of this pedestal and the primary pulse is known as the intensity contrast of the laser system. Optimising this ratio is a key concern as often the pedestal is sufficiently intense to begin forming a plasma on the target surface ahead of the main pulse interaction. In thin targets, this can result in the bulk of the target being ablated before the main pulse arrives. This drives a pre-plasma on the front surface of the target leading to a change in the absorption or field growth [52, 100].

Various laser techniques are deployed to improve the temporal contrast of the system; alternative amplifier schemes¹ can be used to deliver amplification without contribution to the ASE due to the process requiring both the seed and pump laser to be matched [198]. It is also possible to exploit intensity dependent processes to improve temporal contrast. Frequency doubling crystals are significantly more efficient at high intensities ($\eta_0 + \eta_2(I) \propto I^2$) thus increasing the contrast of the peaks at the expense of total energy in the beam. This technique is used in major laser systems, such as LMJ [199].

4.1.2 Plasma Mirrors

Another mechanism to improve the contrast of lasers systems is to utilise a plasma mirror. These operate like a fast optical switch capable of isolating the main pulse from the preceding ASE pedestal. The mirror is typically a material that is initially transparent to the laser wavelength. The beam is directed

¹Optical Parametric Amplification (OPA), see discussion in reference [16]

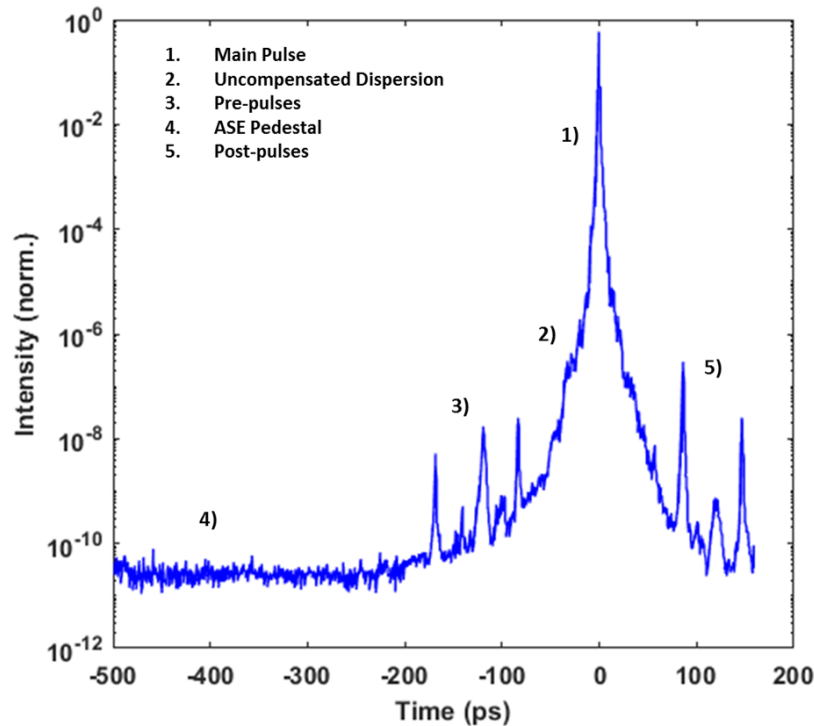


Figure 4.2: Laser temporal contrast. Contrast trace for Vulcan Petawatt, key features of the pulse are identified [16].

onto the surface such that only during the rising edge of the main pulse does the surface begin to ionise and create an over-dense plasma that reflects the remainder of the beam. The unwanted pedestal of the pulse is transmitted through the plasma mirror and away from the target leaving the main pulse to be focused onto the target surface.

Plasma mirrors increase the contrast preceding the main pulse (items 2-4 in Figure 4.2), typically reducing the pedestal level by \sim two orders of magnitude > 100 picoseconds before the main pulse and $\sim 10^3$ a few picoseconds before [200, 201]. Significant study has been conducted throughout the field on the operation of plasma mirrors, increasing the reflection efficiency [22, 23, 202], developing refocusing plasma mirrors to increase the intensity of the beam

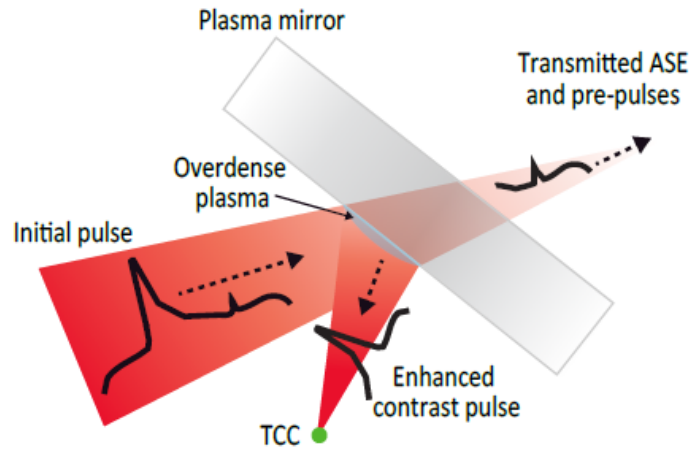


Figure 4.3: Plasma mirror operation, demonstrating the optical switching allowing transmission of the ASE and reflection of the main pulse. Image from Wilson [16]

[203], and cleaning the temporal profile enough to irradiate nanometre scale targets [54].

4.1.3 Laser Facilities

Whilst advancements in cost and scale have been made (ultra-)relativistic lasers (10^{20} W/cm²) more available, they are generally still out of reach of university facilities. Instead, national and international support is required to fund and develop the institutions. In this research, one facility was primarily used, the Vulcan Laser System at the Central Laser Facility, Harwell, UK. A review of the parameters and amplification process is contained in the appendix of this thesis. Throughout the thesis, relevant laser parameters are provided as part of the experimental discussion.

4.2 Detectors

Laser plasma interactions are capable of generating high-energy radiation. It is, therefore, necessary to have detectors able to characterise and compare the emission. Throughout the field of laser plasma accelerators there are many types of detectors commonly used. There are four features that can be used to categorise detectors; their repetition rate, their energy sensitivity, their resolution, and their dynamic range. Ideally a detector would excel at each of these features, however in reality one, or more, is traded in exchange for another.

There are numerous individual detectors within each of the categories outlined in Figure 4.4. The following two sections discuss a passive detector, image plate, and scintillators in general. Both have been used extensively throughout the research presented in this thesis. Although others are not discussed at length it is worth mentioning them in brief. Photo-nuclear processes, shown as (γ, X) in the figure, refers to the nuclear activation between a high energy (> 8 MeV) photon and the nucleus of various materials. This technique is employed within plasma physics extensively to detect very high energy photons with a high degree of certainty [77, 204]. X-ray film is another passive detector has been used for decades in radiography and laser-plasma interactions. Whilst image plate (IP) is considered the successor to x-ray film, the significantly higher spatial resolution means that x-ray film is still used. Phosphor Film is considered a successor to image-plate, at least to the medical community, owing to the fact that unlike IP (and x-ray film) it is an active diagnostic meaning it does not have to be manually reset after each exposure. The *slight* reduction in spatial resolution and dynamic range diminish the advantage and the long repetition rate of most high-energy laser systems means that IP being passive is not inherently an issue. CCDs are cameras that can be used to either directly detect incoming x-ray photons or, more commonly, are

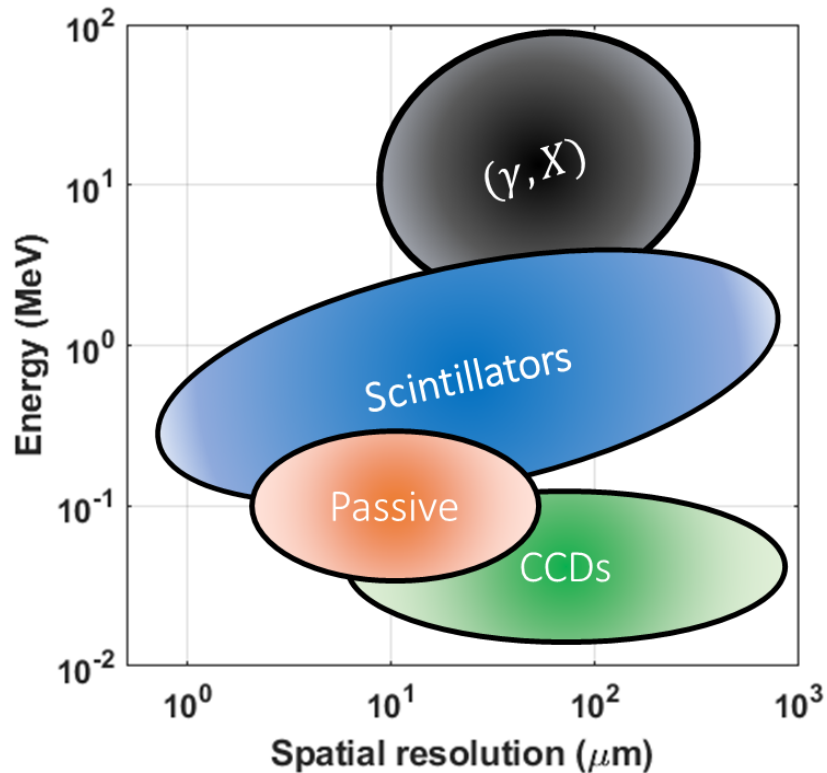


Figure 4.4: Summary of detectors with respect to their x-ray energy sensitivity and resolution. The circles indicate categories of detector and their working ranges. ‘Passive’ detectors are primarily single shot, or require significant time between exposures. (γ, X) detectors are limited by the radioisotopes half-life (seconds-hours), and the spatial resolution comes from imaging the decay signal using a secondary detector. CCDs and scintillators can operate at many Hz repetition.

coupled (via a lens) to a scintillator to monitor the optical emission instead. In certain set-ups the scintillator can also be directly mounted on the CCD using a fibre-optic plate to provide a significantly higher collection efficiency from the scintillator [205].

4.2.1 Image Plate

Image plate (IP) was developed as a multiple use equivalent to x-ray film. It has been characterised extensively [191, 206, 207], has high dynamic range, and

is able to be used to detect multiple radiation species (protons [137, 156, 171], electrons [208, 209], x-rays [191, 210, 211] etc.).

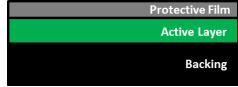
Compound	TR		SR		
	Thickness	Density	Thickness	Density	
Protective Layer (CH)	-	-	9	1.64	
Active Layer (BaFBr:Eu)	60	2.61	112	3.07	
Backing (CH + Fe2O3)	307	1.82	307	1.82	

Table 4.1: Image plate composition for TR and SR types, schematic diagram included for clarity.

The exact make-up of IP varies between models, however, the base recipe is the same. An active layer (typically a BaF compound) is supported by a magnetic substrate and protective coating. Energy deposited into the active compound excites electrons into a metastable state. To retrieve the information the IP is exposed to a blue laser, which de-excites the atom to emit radiation. The location and intensity of the emission is then detected to form an image from the absorbed x-ray energy. The variation in active layer and protective coating changes the sensitivity of the detector. A thicker protective layer will attenuate low energy signal, of x-ray and charged particle alike, before reaching the active layer. TR has no protective coating and is therefore ideally suited for low energy K-alpha detection. A thicker active layer, however, provides increased attenuation to incident radiation making it more sensitive. The main advantage of IP, however, is the large dynamic range it has compared to CCDs and x-ray film [212]. High dynamic range is vital in imaging to discern information from surrounding noise/background and to set a limit in spatial resolution.

Due to its versatility IP is used in various diagnostics, from bremsstrahlung cannons [191, 210, 211], to thomson parabolas [137, 156?], to electron spectrometers [208, 209], and as the detector stack for the penumbral foil detector described in section 4.3.2. As such the community has extensively characterised IP and its response to each incident species. For calculations in this thesis the author used modelling by Meadowcroft *et al.*, Maddox *et al.*, and Bonnet

et al. to determine the response of the respective image plate [191, 206, 207].

4.2.1.1 IP Resolution

In practice, IP resolution is a function of both the detector lattice structure, and the scanner used to digitise the data. The scanning laser diffuses through the detector layer to prompt re-emission the scattering throughout this process blurs the signal over a larger emission area [213]. By taking a known edge spread function (ESF) we can reconstruct the image and mitigate the effects. Whilst this is not important for spectral measurements, this is vital for spatial diagnostics that require maximum resolution.

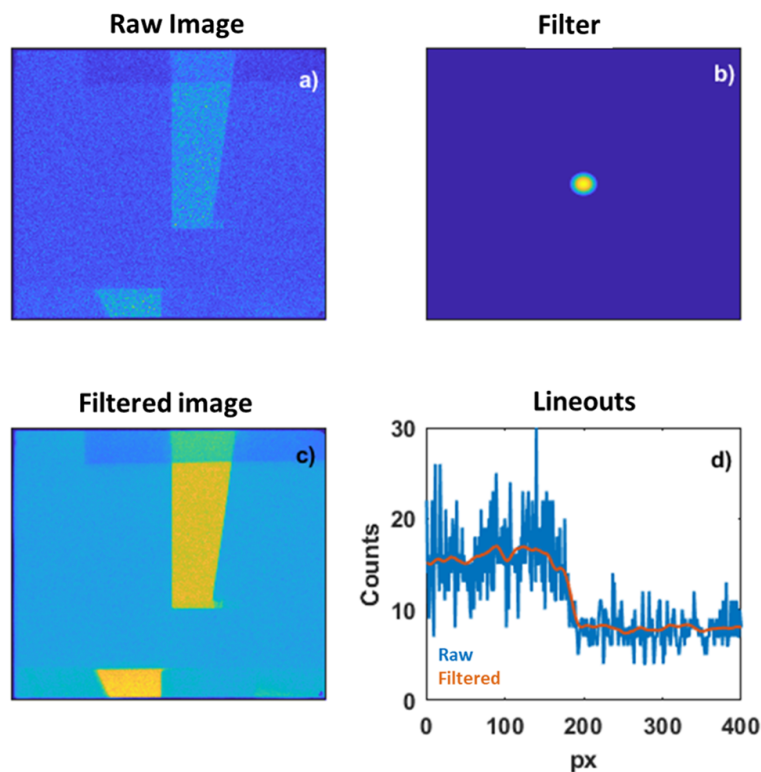


Figure 4.5: (a) raw image, (b) de-blurring function, (c) Gaussian-filtered image, (d) lineouts across each image at the transition from light to dark.

Throughout this research a Gaussian filter with the ESF for TR and SR IP, as measured by Fiksel *et al* [213], is used. With a known ESF, the source image can

be retrieved by dividing the Fourier transform of the image and ESF, and computing the inverse transform of the result. Figure 4.5 shows the a radiograph of the penumbral foils outlined in Section 4.3.2, this figure demonstrates the steps for deconvolution, with a comparison between the measured image and the deconvolved source. In Section 4.3.2 this technique is expanded to include the additional spreading introduced by filtering and the penumbral foil deployed in experimental campaigns, by a simple “sum-of-squares” calculation to determine the joint contribution from each source of ESF.

4.2.2 Scintillators

Scintillators are able to convert incident x-ray (and other energetic radiation) into readily detectable optical photons. In inorganic scintillators (CsI, LYSO) the incident photon is absorbed by the material, exciting an electron. This electron typically has many times the energy required to free it and it travels through the scintillator crystal freeing more electrons through collisions. With time these electrons will decay, via an intermediary energy level caused by impurities in the crystal, emitting photons within a spectrum characteristic to the material. These impurities are known as activators and increase the efficiency of the scintillator. A schematic for this mechanism is shown in Figure 4.6. Electrons in an organic scintillator (such as hydrocarbons and benzene compounds), however, use transitions between internal energy states to scintillate. Photons excite electrons in high energy levels, these then decay directly (fluorescence) or via a triplet state decay significantly later (scintillation). Each process is inherently reversible, with the excited electrons eventually decaying back to ground in order to emit light, this happens in nano-microseconds depending on the material without the need for intervention from operators - this is referred to as an active detector compared to a passive detector (which requires intervention to be reset).

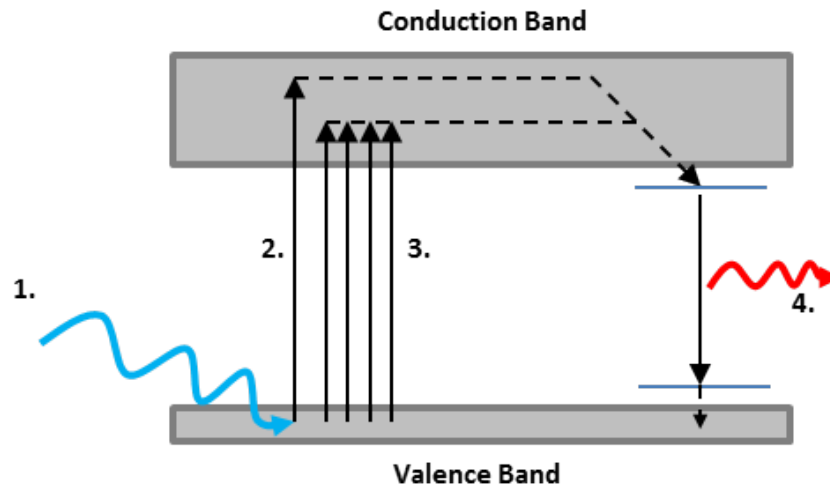


Figure 4.6: Inorganic scintillation schematic, the incident photon (1) excites the electron to the conduction band (2) with many times the binding energy, it collides with many other atoms in the crystal causing further excitation (3), these electrons eventually decay through the presence of activator crystals (4)

4.3 Measuring X-ray Source Size

Determining the distribution and area over which x-rays are emitted during a laser-plasma interaction is key for characterising the emission as a potential source for industrial radiography applications. There are various techniques applied throughout the field for determining spatial information about the x-ray emission. Three techniques are addressed here and a discussion of a high resolution, high energy, penumbral foil that the author designed during this research. The techniques addressed are; using crystal diffraction, pinhole-cameras, and the penumbral imaging. Each has its advantages, however using the latter technique it is possible characterise > 100 keV x-rays.

4.3.1 Low energy (< 50 keV techniques)

X-ray imaging crystals rely on Bragg diffraction. X-rays interact with the crystal lattice and are reflected. At discrete intervals, dependent on the inter-atomic separation d_s and the angle of incidence for the x-ray, the reflected x-rays constructively interfere and produce a bright diffraction peak. At other angles the phase shift between the reflected x-rays cause destructive interference. The path difference between the crystal structure causes peaks in signal to occur at:

$$2d_s \sin(\theta) = n\lambda_\gamma \quad (4.1)$$

where λ_γ is the wavelength of the incident x-ray, d the inter-crystal spacing, and θ the incidence angle, outlined in Figure 4.7. This process is inefficient and limited in energy range by the crystal structure. Typically these are applied to 1 – 40 keV K-alpha x-ray emission where the flux at the specific bandwidth is typically orders of magnitude higher than the continuum. Crystal diagnostics exist that are designed to work with hard x-ray emission, however, they intrinsically have a low efficiency due to the cross-sections of interaction to coherently scatter x-rays [214, 215]. Using spherical crystals the same technique can be used to form an image of the x-ray emission area on a detector plane, this technique has been used extensively in the field, particularly with Cu K-alpha emission at ~ 8 keV [20, 184, 216].

Pinhole cameras project an image of the source onto a detector plane, exactly the same as *camera-obscura* using for optical light - Figure 4.8 is a schematic outlining the process. The pinhole is made from a thin high-density material with a hole smaller than the source, this is normally placed close to the target source allowing ample magnification to the detector. Whilst widely used throughout the field [217–219], pinhole cameras are prone to low collection ef-

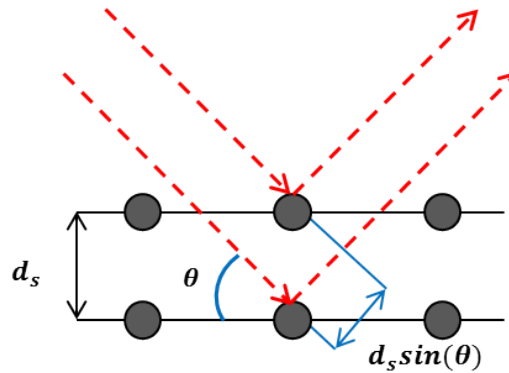


Figure 4.7: Bragg diffraction in crystals. Grey dots indicate the lattice structure of the crystal, and the red dashed line indicates the path of x-rays reflecting off the lattice structure.

efficiency and signal to noise issues. Charged particles emitted from the target can contribute to the detected signal, even when isolated from the detector via magnetic fields, through collisions with the pinhole substrate and housing. In thin targets, this can be a significant factor as the necessary areal density of a pinhole could result in the pinhole substrate being a more effective x-ray converter than the target. The diameter, d , of the pinhole needs to be smaller than the lateral extent of the source to provide a measurement.

Penumbra imaging measurements are the simplest of the three techniques, involving placing a dense object between the source and the detector. This creates a non-transmitting object from which the source characteristics can be determined. When illuminated with a non-point source this will create a transition region in which the x-ray signal changes gradually. The single edge reduces the contribution from diffraction by several orders of magnitude relative to pinholes. Measuring higher x-ray energy can be achieved by varying the areal density of the edge. The issue with this becomes the overall alignment. Unless the object is directly perpendicular to the source the transmission length experienced will be non-uniform leading to a blurring of the penumbra

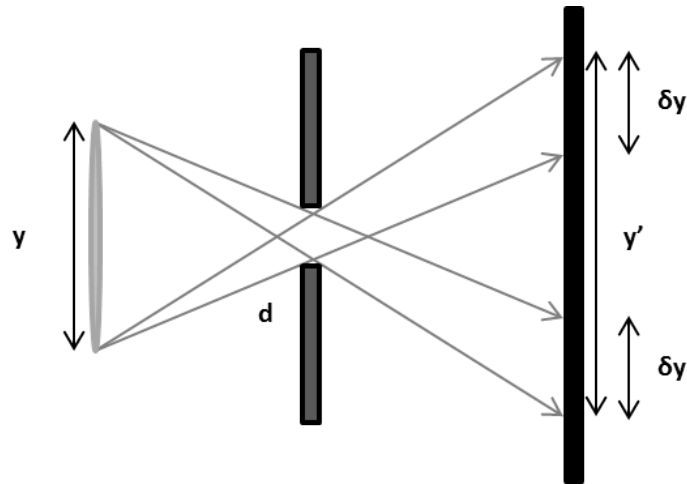


Figure 4.8: Pinhole camera schematic, the hole - smaller than the source - projects an x-ray image onto the detector plane.

on the detection plane [77, 220–222]. Colloquially this technique is often referred to as ‘knife-edge’ measurements as a sharp metal object neatly meets the criteria for operation at soft x-ray energies.

4.3.2 High-energy, high resolution, approach

Inherently all of these methods become less effective at higher x-ray energies as the materials are less efficient at attenuating or diffracting the incident photon. To address this issue the author designed a curved penumbral foil that presents a uniform transmission edge, and is effective to energies in excess of 500 keV (before scattering dominates the signal). This diagnostic applies the penumbral or knife-edge technique to cast a shadow, the transition between light and dark on the detector plane is correlated to the profile of the x-ray emission. The drawbacks of the standard penumbral technique at high energies is demonstrated by Figure 4.9; with increasing energy the thin barrier becomes transmissive and increases the background on the measurement; increasing the barrier thickness to overcome this introduces non-uniformity in the transmission.

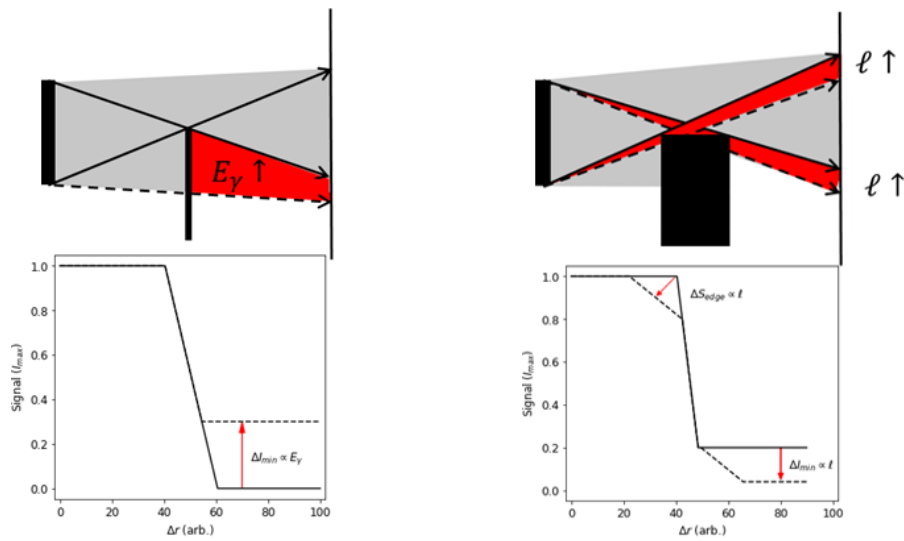


Figure 4.9: Schematic of issues with the standard penumbral technique at high energies. LHS shows increasing energy for a thin foil, RHS shows that increasing the foil thickness to offset the increased transmission introduces a different error.

The schematic of this design is shown in Figure 4.10. The curved edge ensures that at small depths ($< 10\text{m}$) into the foil there is significant attenuation of $>100\text{ keV}$ x-rays. The curved edge also means that there is a large field-of-view that the detector is sensitive to.

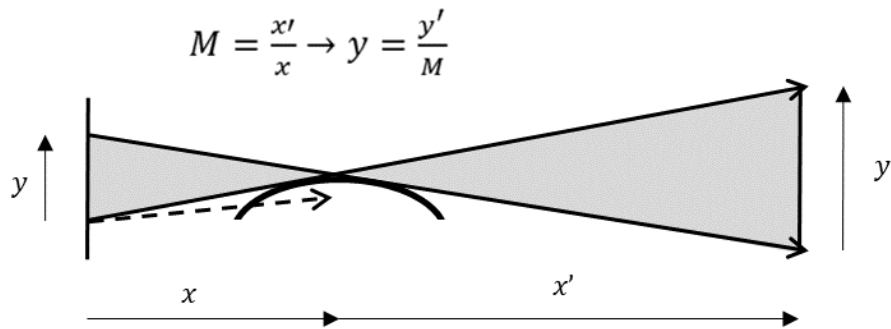


Figure 4.10: Penumbral imaging x-ray measurement. The transition region between signal and dark is a projection of the source profile.

4.3.2.1 Penumbra Foil Characterisation

The penumbral foil was designed with the aim of achieving 75% attenuation for x-rays up to 500 keV at small depth into the foil. The chosen foil was tungsten due to its high density and ease of handling ($Z=79$, $\rho=19.91 \text{ g/cm}^3$). To minimise the size, and weight, of the diagnostic we can create the desired spherical properties by simply bending a foil to the desired radius. In the final design a $300\mu\text{m}$ thick foil was selected and curved to a 152 mm radius of curvature.

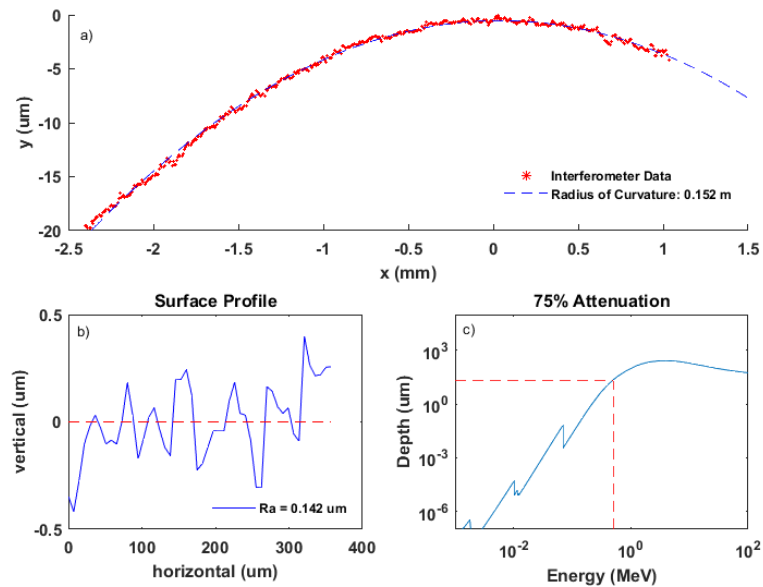


Figure 4.11: (a) Profile. (b) surface roughness, (c) is a convolution of the x-ray transmission and segment length through the determined radius of curvature to determine the depth at which 75% of the x-rays are attenuated.

The foils used for the research presented within this thesis had an unpolished surface on the primary edge, which effects the transmission and point-spread-function (PSF) of the foil. The surface was characterised to provided an absolute radius of curvature, Figure 4.11(a), and surface quality, Figure 4.11(b), such that we can determine the effect on the signal. As Figure 4.11c) demon-

strates, this translates to 75% attenuation at $20\mu\text{m}$ into the foil. The large radius of curvature also increases the field of view of the diagnostic, this simplifies the alignment procedure and allows emission from the entire target to be measured.

Determining the achievable accuracy possible with the penumbral foil is key for high accuracy measurements. Using GEANT4, the PSF can be generated for the penumbral foil and the detector stack in question. The supports and magnet, typically used in experimental setups, were excluded from the model for simplicity. A 18 mm silicon window was included to determine the PSF relevant to measurements made in Chapters 5, 6, and 7. 10^6 x-rays were simulated at 500 energies between 1 keV and 10 MeV to produce the PSF for the penumbral foil. The layout of the simulation is shown in Figure 4.12(a). The simulation recorded the positions of x-rays crossing before and after the laser window in order to determine the scattering that it caused in the detector. Figure 4.12 shows the results from the simulation, (b) is a histogram from the 400 keV simulation and lineout across penumbral edge. Figure 4.12(c) shows the PSF as a function of energy. A schematic of the setup in the simulation is sho

With an ideal detector this diagnostic could operate at 1 MeV with $< 5 \mu\text{m}$ spreading, shown in black in Figure 4.12(b). Uncertainty in measurements with the penumbral foil are a convolution of both the PSF - dominated by x-rays scattering through filter materials - and the spatial resolution of the image plate detector (discussed in Section 4.2.1.1). These factors are independent of one another, and thus can be combined simply using the sum-of-squares formula:

$$\sigma_{sys} = \sqrt{\sigma_{scatter}^2 + \sigma_{detector}^2} \quad (4.2)$$

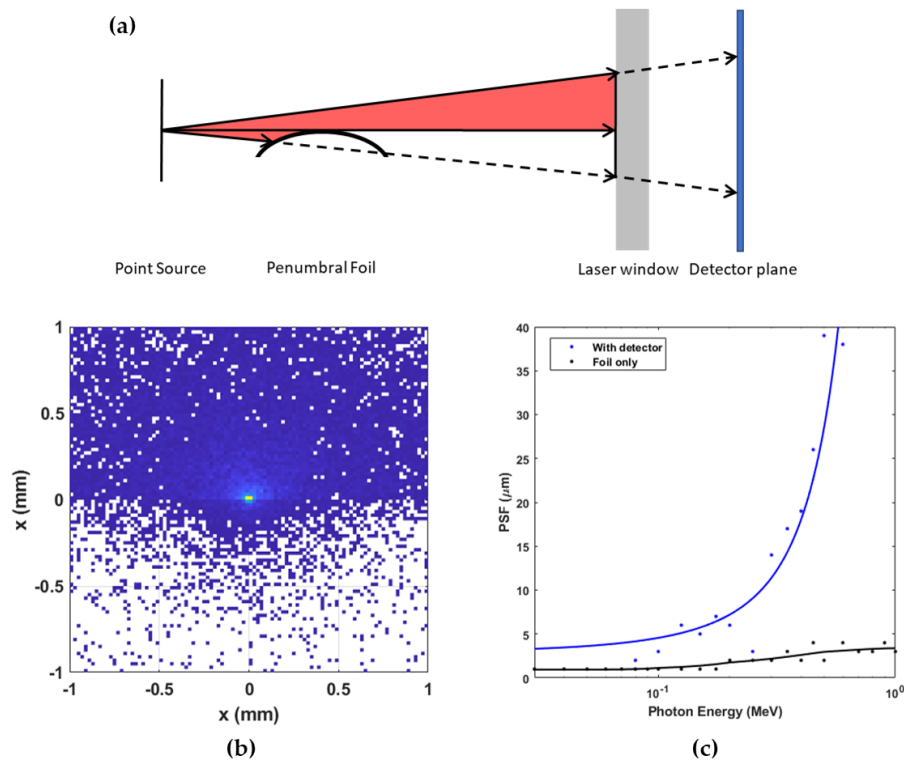


Figure 4.12: PSF Simulation. (a) Schematic of GEANT4 simulation, red represents the x-rays emitted from a point source, (b) Histogram of x-rays recorded in the detector plane for 400 keV x-rays. (c) PSF as a function of x-ray energy for detector and just considering the foil (black).

Determining the emission area of x-rays from the penumbral foil requires measuring the transition between signal and background, as shown in Figure 4.10. In solid targets the emission area was often more complex than this schematic suggests. The transition between signal and background indicated two sources of different brightness, each producing a significant fraction of the total signal. A schematic of a two source structure is shown in Figure 4.13. This is discussed at length in Chapter 5, and as such, the deconvolution method for both sources is outlined here.

Figure 4.13 demonstrates how two regions of a x-ray source with different brightness interact to form a penumbral measurement, the brighter - red - source is smaller but is significant brighter than the grey region expressed by

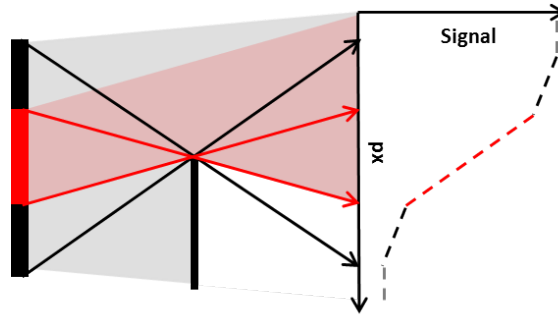


Figure 4.13: Schematic outlining the expected response from a two source x-ray signal, red is the brighter central region surrounded by a larger substrate source (grey).

the increase gradient in the transition. Isolating these two sources allows the relative flux and source size from both to be retrieved. To do this; first the peak gradient and its full-width-half maximum (FWHM) is determined, the next point of inversion in the gradient is considered the boundary of the central source. The contribution and size of this source is recorded, and then removed from the lineout. The process is then repeated - without the bright contribution from the central source - with the substrate as the primary, its width and contribution can be determined. The individual steps of this are shown in Figure 4.14. This technique is used at length in Chapter 5 to determine effects of refluxing electrons in solid targets.

4.4 Characterising emitted x-ray spectra

X-ray spectrometers, these are typically limited in their spatial resolution in favour of improved spectral resolution, examples of these vary from single photon detectors coupled to scintillators [223] to large area arrays [224]. Crystal spectrometers are also used throughout the field and are able to spatially resolve information [214], although this is typically reduced to one spatial dimension. Absorption filters have long been a mechanism to determine emitted spectra, for all manner of particles. In scintillators, the detecting medium

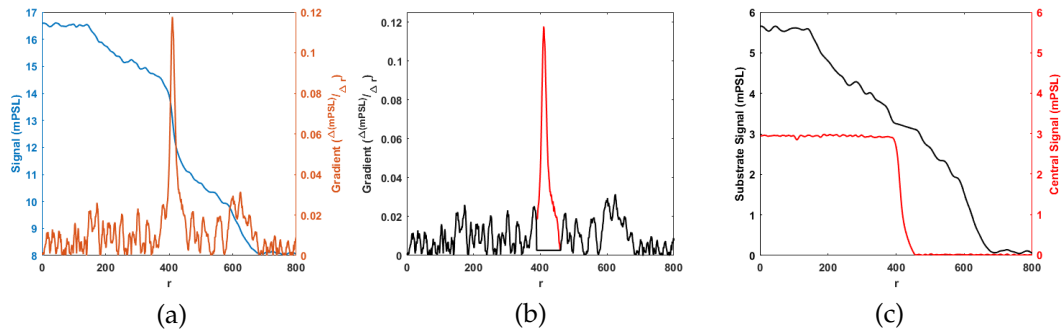


Figure 4.14: Isolating the central source from a full penumbral lineout. (a) Raw lineout (blue) with the gradient (orange) from the lineout, (b), highlighted gradients of the central (red) source and substrate (black) (c) isolated source profiles and flux contributions.

is multi-use and effective over a wide range of energies making them ideally suited for absorption spectrometers, they can act as both the filter and the detector [225]. The design discussed here was developed with Rusby *et al* [17], and a deconvolution technique for retrieving x-ray temperatures is outlined.

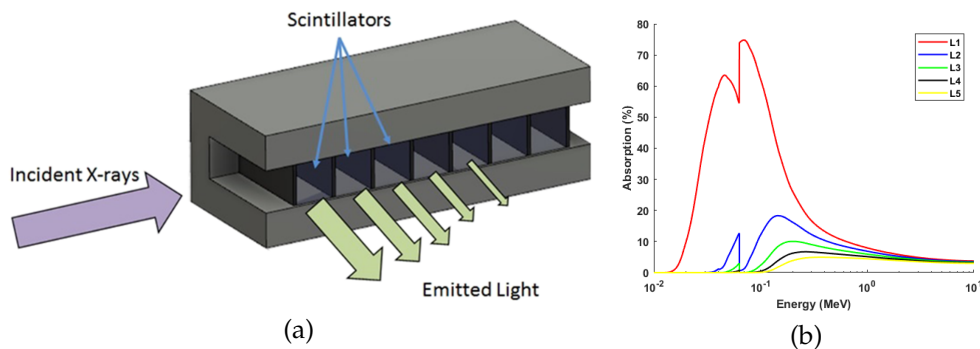


Figure 4.15: LYSO scintillator design. (a) Schematic of design, edited from Rusby *et al.* [17], (b) spectral response from fielded diagnostic, calculated using the NIST cross-section database [15]

The design is a series of 2 mm LYSO scintillators, with black plastic spacers to ensure the bins are kept visually separate on camera, housed inside a Pb frame that doubles as an aperture and shielding. This is used as a high energy x-ray spectrometer with the electrons swept away by a strong magnetic field.

However, due to the sensitivity of scintillators to energetic particles it could readily be used as a spectrometer for other species. Each layer attenuates the signal for the next layer resulting in a reduced low energy response the deeper into the spectrometer - figure 4.15, this alters the incident photons arriving at each layer and therefore the deposited energy. To reconstruct the incident spectra (S in Eq. 4.3) from the measured results, Monte-Carlo modelling is used to establish the response matrix, R in Eq. 4.3, for varying incident x-ray energy:

$$R * S = L$$

$$\begin{bmatrix} R_{E_1, L_1} & \dots & R_{E_1, L_N} \\ \vdots & \ddots & \vdots \\ R_{E_N, L_1} & \dots & R_{E_N, L_N} \end{bmatrix} * \begin{bmatrix} \frac{dN}{dE_1} \\ \dots \\ \frac{dN}{dE_N} \end{bmatrix} = \begin{bmatrix} L_1 & \dots & L_N \end{bmatrix} \quad (4.3)$$

where L is the output from the scintillators. To deconvolve the spectra a ‘trial’ method is used, outlined by Rusby *et al.* [17, 21]. A test spectra is assumed to have a Boltzmann distribution with a set temperature. The temperature is then varied and the ‘best fit’ is found by minimising the difference between the test spectra and the measured output. This method is reasonably tolerant to noise and most effective when the incident spectra is a single temperature. Chen *et al.* [226] demonstrated a trial method with a two-temperature distribution highlighting the non-unicity of solutions when considering the possibility of numerous spectral shapes. This single temperature fit is used in each of the data chapters to determine the effective x-ray emission temperature.

4.5 Numerical Modelling

The measurements made with diagnostics is often the convolution of countless particle and field interactions that happen on sub-femtosecond time scales.

Numerical models provide a way to explore these processes as they are occurring rather than the integrated measurements provided by the majority of diagnostics. Both, EPOCH for PIC modelling [31], and GEANT4 for Monte Carlo modelling [227–229], were used extensively by the author throughout this research. There are significant differences between each package and the following sections detail the benefits of both. However, it should be noted that in practice GEANT4 is run on a personal desktop linux computer and is able to complete simulations of 10^8 particles in a matter of hours, allowing in depth material and particle studies to be completed in days. For EPOCH the author often used 100-200 CPUs for days at a time to finish a single simulation, owing to the particle density and resolution of the simulation parameters.

4.5.1 Monte Carlo Codes

A Monte-Carlo code does not explicitly simulate plasma interactions instead relying on random numbers and a large number of particles to obtain results to stochastic processes. This is an ideal methodology to determine the bremsstrahlung production from a hot electron population or x-ray attenuation in detectors given the multitude of variables that determine the creation or attenuation of x-rays (see Section ?? and Section 3.4). GEANT4 is a Monte-Carlo package designed for particle and nuclear physics, containing “physics lists” for a wide range of particles and energies (ranging from tens of eV to tens of GeV). From a practical perspective it simulates a particle moving through a system, plotting trajectories and energy loss based on scattering with the surrounding particles. Interaction cross-sections are interpolated from experimental data, theoretical simulations, and analytical solutions. GEANT4 is a mature code package with details of the main libraries are reported in several papers, see References [227–229] for a more thorough review.

4.5.2 PIC Codes

Kinetic approaches provide information on the particle dynamics within an interaction, instead of assuming fluid like behaviours or omitting collective effects entirely as is the case with hybrid and monte-carlo simulations respectively. Particle-in-Cell codes, like the name implies, rely on particles moving between cells and calculating the effect that this motion has on the surrounding fields.

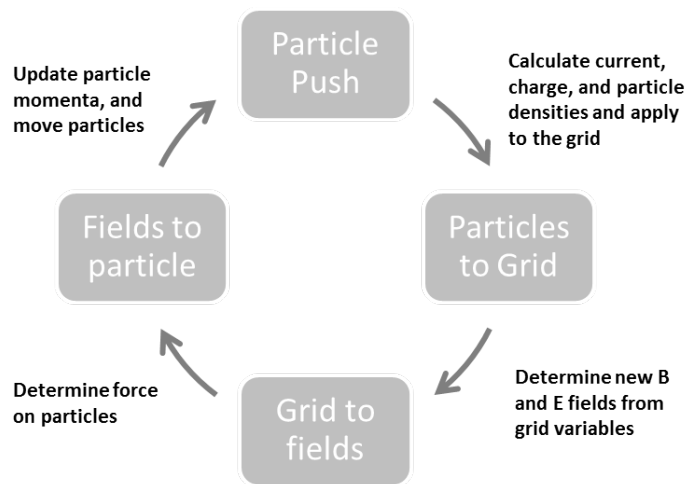


Figure 4.16: Generalised process for PIC simulations, this cycle is completed numerous times for each population over the lifetime of the simulation.

The PIC cycle is shown in Figure 4.16, it demonstrates the computational order in which PIC simulations evolve. First, the field structure in the grid is determined (either through initial conditions or the particle distributions from the previous cycle). Second, the local field values for each particle are then interpolated from the grid to ensure a higher order accuracy between the discrete field values and the continuous particle position. Third, the particles are then moved according to the local fields and residual momenta (again either from initial conditions or the previous time-step), and finally, these new particle positions then determine the particle distributions on the grid which

in-turn determine the field structure in the first step.

4.6 Summary

This chapter covered the methods and diagnostics applied throughout this work. The following chapters will discuss the application of these methods and techniques to investigate areas of x -ray generation within laser plasma interactions. Where applicable, the following chapters will refer back to techniques mentioned here and expand on sections where additional detail is necessary.

Chapter 5

Investigation of recirculating electrons in solid targets as a function of laser intensity for x-ray generation

At the rear-surface of targets, accelerated electrons fall into two categories; either they escape the target, or they recirculate until they have lost their energy. Recirculating electrons can be sufficiently energetic that on the initial and subsequent passes of the target they are able to generate x-rays (line emission and bremsstrahlung) as they interact with the target ions. In this chapter, the spectral properties of recirculating electrons are studied by determining the spatial profile of the internal electron current via hard x-ray measurements. The physical processes that govern the spatial evolution are dependent on the electron divergence and transport through the target, and interactions with the sheath field. This chapter reports on an investigation into the effect of laser defocus on the recirculating electron population. Spatial measurements of the x-ray source are presented from an experimental campaign using the Vulcan laser system, and an analytical model is used to describe the extent to which the recirculating electron population is reduced with increased laser spot size.

5.1 Introduction

An intense laser field accelerates a multi-megaampere current of relativistic electrons into the target [1, 18, 64]. Energetic electrons can produce broadband bremsstrahlung radiation with energies up to tens of MeV as they propagate [10, 230]. The incident laser pulse drives the electron population with some initial divergence into the target. As the electrons travel through the target, internal magnetic field growth causes filamentation, hollowing, and confinement of the electron beam [154, 231] and the mechanisms that alter the propagation are discussed in Chapter 3. As electrons reach the rear target surface they typically establish a (>1 TV/m) sheath field over the emission area [56, 121, 138, 161, 165, 171, 172, 232]. This field can cause them to reflect, forming a recirculating (or refluxing) electron population between the surfaces of the target that continues to expand laterally as it travels [233, 234]. Measuring this sheath directly is difficult, however, it can be measured from the deflection of charged particles [235–237], or inferred from the accelerated ion emission [238]. In lieu of those methods, Mora [161] presents a simplified plasma expansion model that can be used to estimate the sheath strength based on the incident laser conditions. The 1D model presented posits a sharp boundary of ions with a population of electrons expanding with a Boltzmann distribution into the vacuum, the field established between the escaping electrons and the static (under the time frame considered) ion population can then be determined as:

$$E_{sheath} = \frac{\sqrt{2}k_B T_e}{e\lambda_D} \quad (5.1)$$

where $k_B T_e$ is the hot electron temperature, e the electron charge, and λ_D the Debye length of the plasma (discussed in Chapter 2) [161]. For example, $k_B T_e \approx 1$ MeV and $\lambda_D \approx 1$ μm , this equates to $E_{sheath} \approx 1$ TV/m. Electrons

accelerated later in the pulse must therefore overcome this in order to escape, or they are reflected back into the target where they can continue to propagate ballistically and generate bremsstrahlung emission as they do so. While this is a 1D model, the divergence of the electron beam can be incorporated into the calculation of E_{sheath} . The divergence through the target determines the rear surface electron density which in turn determines λ_D .

5.1.1 X-ray production for recirculating electrons

The population of electrons recirculating due to the sheath can be a large fraction of the initial beam [8, 160] and, as they still carry significant energy, these electrons are able to generate x-rays as they interact with the bulk of the target [38]. Since the electrons are initially accelerated in a forward cone, it is reasonable to suggest that two spatial regions would emerge as the electrons recirculate through the target. A central region, in which the majority of electrons travel through, is defined by the electron divergence through the target. A second, broader region would then emerge as a fraction of the central electrons recirculate and maintain their lateral momentum and spread away from the central channel - this will henceforth be referred to as the substrate source. Since the recirculating population can be a significant fraction of the initial beam under suitable conditions [8, 160] then it is reasonable to suggest that the substrate source could be a dominant source of x-rays as the electrons recirculate.

There are two loss mechanisms to consider that will factor into the development of these two sources. Electrons travelling through the target are attenuated, losing energy to heat target atoms and ions or radiated via bremsstrahlung. If they were sufficiently low energy to begin with, these electrons will not be able to reach the rear surface and, as such, cannot recirculate. On the other

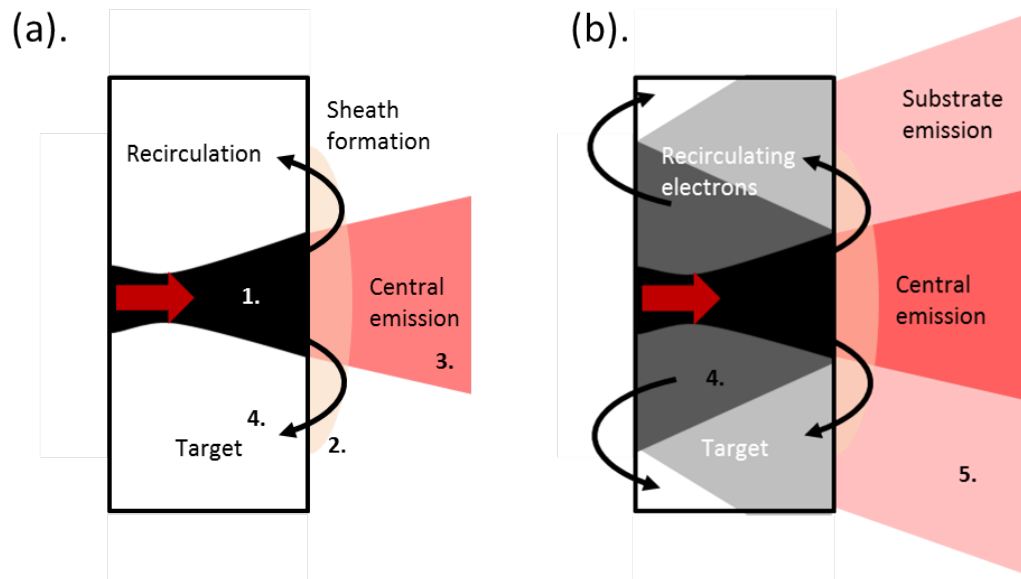


Figure 5.1: Two source components for x-ray emission, (a) first pass of electrons through the target, (b) subsequent electron recirculation. The main channel of accelerated electrons (1) which travel through the target generating x-ray radiation (3). At the rear surface, electrons with energy lower than the potential are reflected, those with more energy can escape and cause the formation of the sheath field (2) through charge separation. Electrons can then recirculate the target due to this sheath field (4) and spread laterally through the target. These electrons can still have significant energies, \sim MeV, and thus still generate bremsstrahlung (5) as they continue to travel through the target.

hand, electrons with sufficient energy to reach the rear surface and overcome the sheath, by definition are not recirculating. Electrons that are neither fully attenuated on the initial pass of the target nor overcome the sheath potential, are therefore able to recirculate the target until they too are attenuated, or escape. This process is shown schematically in Figure 5.1.

Lateral expansion of the electron beam is an area of much study. Quinn *et al.* [185] developed a recirculation model to investigate K-alpha emission in targets with a limited amount of recirculation (controlled via a CH layer on the rear surface), predicting that electrons recirculating the target could drive

a 200 μm K-alpha source from a 20 μm thick Cu target. This is mirrored by results from Compant La Fontaine *et al.* [221] that demonstrated an increase in x-ray source size when reducing the target thickness from 100 μm to 20 μm . Concluding that as the refluxing electrons are trapped in the target, lateral scattering increases the size of the emission area. Neumayer *et al.* [189] quantitatively measured the K-alpha generation in thin targets (using an Al substrate to control the recirculation) showing, via PIC simulations and analytical modelling, that $\sim 95\%$ of K-alpha is generated by the recirculating electron current for high intensity lasers.

The aim of this chapter is to understand the change in the spatial profile of the emitted x-ray signal as a result of reduced hot electron temperature due to decreasing laser intensity. Measurements show that a two source structure is typically present in bremsstrahlung x-ray sources; each of which responds differently to changing laser conditions. The discussion of these findings is supported by an analytical model which considers the role of the sheath field in the recirculating electron population. PIC simulations are also presented exploring the development of each source region via the electron density.

5.2 Experimental Investigation

5.2.1 Layout

An experiment was conducted using the Vulcan laser [3], delivering a laser pulse duration of (2.0 ± 0.6) ps, with an on-target energy of 80 J, and a spot size (at best focus) of (4.1 ± 0.8) μm , providing a peak intensity of $\sim 8 \times 10^{19}$ W/cm² [239]. Copper target foils, 3×7 mm in size and 100 μm thick, were positioned relative to best (smallest spot diameter) focal position referred to as ΔZ . Electron measurements were made using a fibre based Cherenkov detec-

tor (details of which are in Liu *et al.* [240]), providing a flux measurement of the escaping electrons with energies greater than 1 MeV. The x-ray source profile was characterised using a penumbral technique discussed in the Chapter 4.

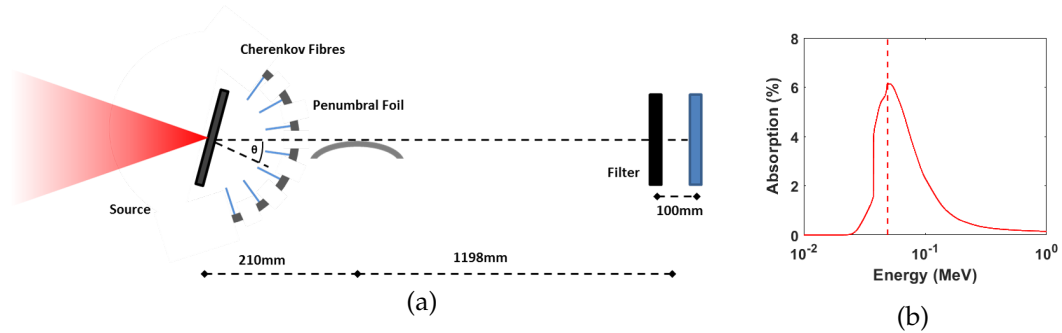


Figure 5.2: (a) Top view of the experimental layout, showing the distances to the penumbral foil and detector stack, and the positioning of the Cherenkov diagnostic. θ is 15° , denoting the angle of the target from laser axis. Between the detector and the source is an 18 mm SiO_2 filter. (b) Absorption as a function of energy for the x-ray detector. Dashed line highlights peak response x-ray energy, ~ 50 keV.

5.2.2 Focal Spot

The laser spot was increased in size by moving the parabola toward and away from the target normal. The defocus distance is referred to as ΔZ and was measured by the micrometer stages of the parabola in the target chamber, for $\Delta Z < 0$ the laser is converging onto the front surface. The target was moved up to $350 \mu\text{m}$ from best focus to increase the spot diameter to $\sim 150 \mu\text{m}$. The focal spot was characterised via a $\times 20$ magnification focal spot camera at regular intervals between best focus and $500 \mu\text{m}$ to determine the scaling of the spot size. It is worth noting that the beam has a *quasi-top hat* profile and is a square beam as it enters the chamber, hence the square profile in Figure 5.3(d).

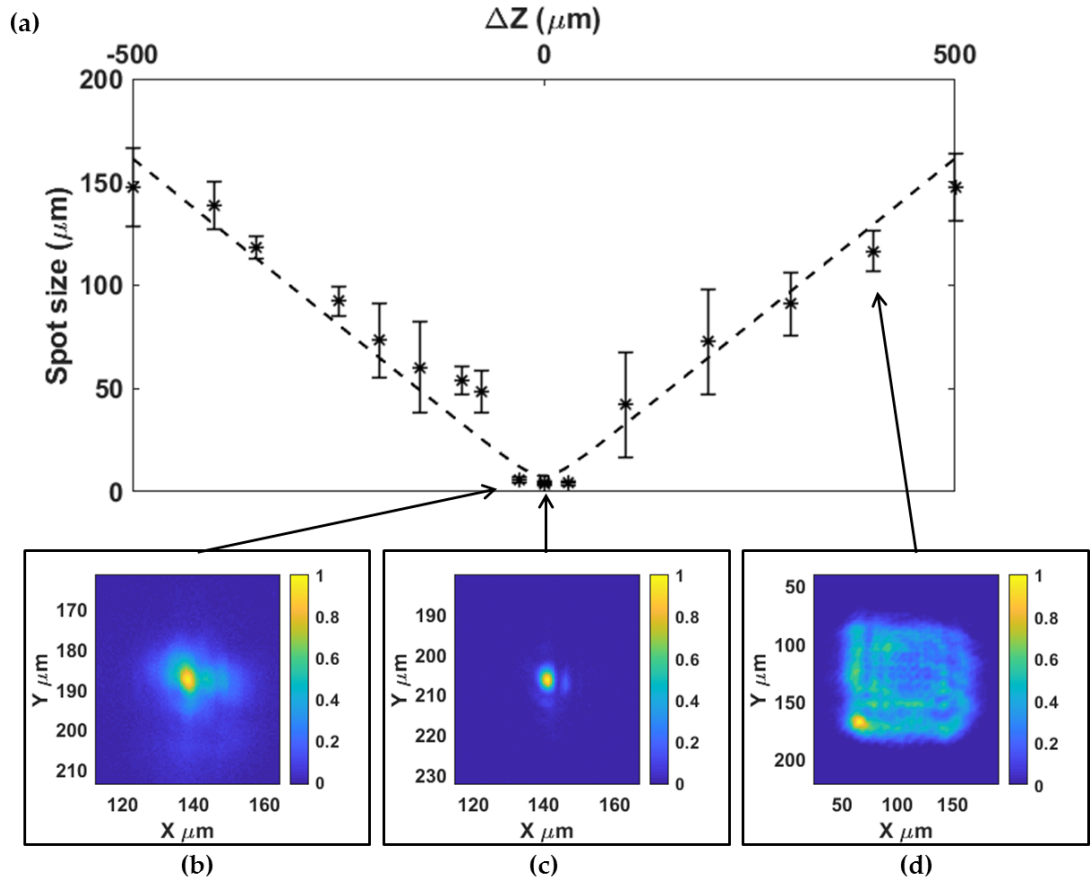


Figure 5.3: Focal spot from the experimental campaign measured from images taken with the CW laser. (a) Width of the focal spot, ϕ_L , as a function of defocus, ΔZ , the dashed line is a fit with Eq. 5.2. (b-d) normalised images of the spot at $\Delta Z = -50, 0$, and $400 \mu\text{m}$, respectively.

The width of the beam was determined from the FWHM of the spot profile. For positions outside of the Rayleigh range ($> 50 \mu\text{m}$) the beam is square, as such the width of the beam was determined from horizontal and vertical linouts rather than radially to prevent bright spots of the image artificially reducing the apparent spot size when significant energy is still contributed by a larger spot. The results of this analysis and examples of the focal spot at three positions are included in Figure 5.3. Due to the *quasi*-top hat profile, the beam does not follow a Gaussian width expansion, instead scaling directly with the

defocus:

$$\phi_L = \sqrt{(2.44\lambda_L F_{\#})^2 + \left(\frac{\Delta Z}{F_{\#}}\right)^2} \quad (5.2)$$

where the focal length of the parabola is $F_{\#} = 3.1$, and the wavelength of the laser $\lambda_L = 1.054 \mu\text{m}$. For the scan, the maximum defocus considered was $350 \mu\text{m}$ from best focus, delivering an intensity of $\sim 10^{17} \text{ W/cm}^2$.

5.2.3 Penumbra Measurements

Using the technique outlined in Chapter 4, any present two-source structure can be deconvolved from the penumbral image. The lateral size and flux of both sources can be determined by first isolating the bright central emission. In doing so, each region can be studied independently with respect to the laser defocus. The flux from each region is presented first, compared to the total escaping electron emission - measured by a Cherenkov fibre array [240] - as a function of defocus. The spatial measurements of the sources are then presented, with each source demonstrating an independent scaling with laser defocus position, ΔZ .

5.2.3.1 Flux measurements

Figure 5.4(a) shows the normalised total x-ray emission flux record on the penumbral detector, and number of escaping electrons, from the Cherenkov detector, as a function of laser defocus. The number of incident x-ray photons (N_{γ}) is determined via the equation presented by Bonnet *et al.* [207], and transmission calculations are determined via the NIST (XCOM) database [15] and the method discussed in Chapter 4. Figure 5.4(a) indicates to a first order approximation that as the laser is defocused, and the on-target laser intensity reduced, the number of accelerated electrons travelling within the target (cre-

ating bremsstrahlung as they travel) and escaping from the target are remain relatively constant over the range of intensities - albeit a reduction of $(25 \pm 5)\%$ at large defocuses compared to best focus.

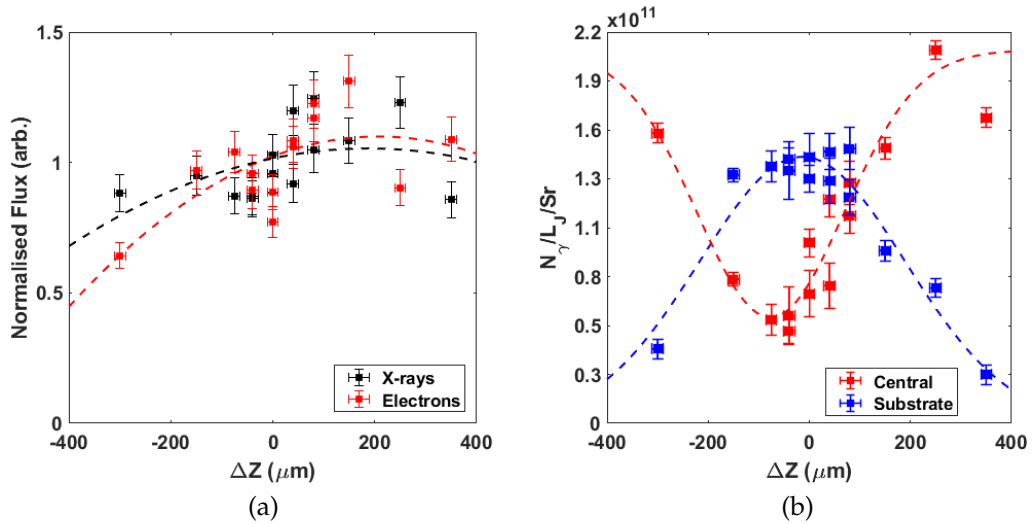


Figure 5.4: X-ray and electron flux for varying focus position. (a) Total X-ray flux (black) and escaping electron (red) number per laser Joule, each are divided by the mean of the data to allow direct comparison. (b) X-ray flux at 50 keV contributed by each source, central (red) and substrate (blue) - origin of which is shown in Figure 5.1. Lines of best fit (dashed) are included as a visual aid.

This relatively flat response for total x-ray over two orders of magnitude intensity is consistent with K-alpha measurements made by Reich *et al.* [241] for copper targets irradiated at similar laser intensities. Riley *et al* [242] also measured a similar response for titanium targets irradiated by ultra-short (~ 45 fs). Measurements made using a low energy (~ 1 J) laser by Nilson *et al.* [243] demonstrate reasonable agreement between $5 \times 10^{17} - 1 \times 10^{19}$ W/cm². These K-alpha measurements suggest a similar scaling with intensity must also be true for the internal electrons. This result can be explained by considering the established scaling laws for hot electron temperature [18, 121] and absorption [19, 244, 245], for an electron distribution $f(E_h)$ where E_h is the electron

energy. The electron temperature of the distribution scales as $I_L^{0.33-0.5}$ [18, 121] whereas the absorption scales as $(I_L \lambda_L^2 / A)^P$ where P is dependent on the interaction conditions with values in the literature ranging from 0.1 [245]¹ to 0.26 [19]. In measurements, the absorption has been shown to scale slower than the temperature; it is therefore possible for lower intensity beam to accelerate a *larger* number of electrons than a high intensity beam. This can occur since the average energy of each electron will be sufficiently reduced in the former case and, therefore, the total energy absorbed will be lower. Figure 5.5 demonstrates the scaling graphically for $P = 0.2$ - whilst the total energy in the electron beam (orange, determined by $\sum f(E_h) * E_h$) is reduced, the number of electrons (blue, determined by $\sum f(E_h)$) is increased as the intensity decreases.

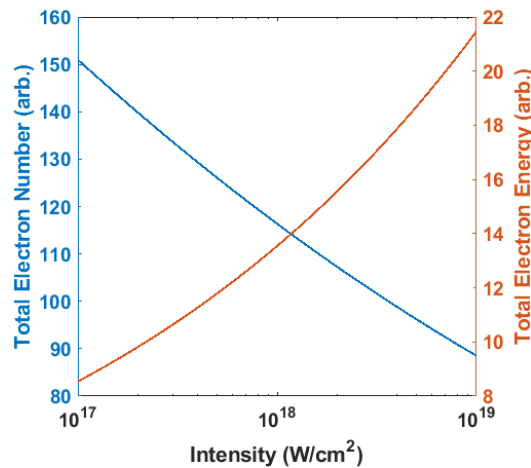


Figure 5.5: Electron number $\sum f(E_h)$ (left axis) and total energy $\sum f(E_h) * E_h$ (right axis) as a function of intensity. Calculated using the Beg scaling law [18] and the absorption results by Davies [19] for a Maxwellian distribution of electrons.

However, if each region is considered independently - Figure 5.4(b) - there is an increase in x-ray flux from the central source for larger defocus. The values in Figure 5.4(b) are normalised to the incident laser energy to account for

¹Scaling from Figure 2 in [245] dataset 3.

shot to shot variation. More pertinently, the ratio between the central and substrate source shifts significantly in favour of the central source at a defocus of 100-200 μm - Figure 5.6. At the maximum defocus tested there is a $\times(10 \pm 2)$ increase in the ratio between the two source components compared to best focus. As $I_L \rightarrow 10^{17}$ due to the increasing spot size, the temperature ($E_h = k_B T_e$) of the fast electron population decreases. This results in the associated attenuation length¹ ($\lambda_{Att.}(E_h)$) of the mean electron energy approaching the target thickness in copper - i.e. the probability of an electron with $E = k_B T_e$ reaching the rear of the target, due to collisional losses, has reduced to $\sim 36\%$. In the inset of Figure 5.6 this is expressed with respect to the defocus. To calculate the $\lambda_{Att.}(E_h)$, the intensity at each defocus position is determined using a spot defined by Eq. 5.2, from this the temperature of an electron beam is calculated using the Beg [18] and Wilks [121] scaling laws (Eq. 2.48-2.49). With this temperature $\lambda_{Att.}(E_h)$ can be interpolated from the NIST (ESTAR) database [14]. As can be seen in the inset of Figure 5.6, for each scaling law, the attenuation length of the expected fast electron temperature with copper approaches the target thickness at $\sim 150 \mu\text{m}$ defocus.

This is the same defocus that the central source begins to dominate in flux contribution. This implies that the central source is dominated by electrons on their first pass of the target, and that by contrast, the substrate source must be generated by either a subset of highly-divergent fast electrons, or electrons that are recirculating through the target. The latter is known to be a significant fraction of the accelerated electron population [38, 233, 234], and therefore will be considered here. The recirculating fast electron population is dependent on the sheath field established on the target rear surface, which stops many electrons escaping on the first pass of the target.

¹or mean-free-path

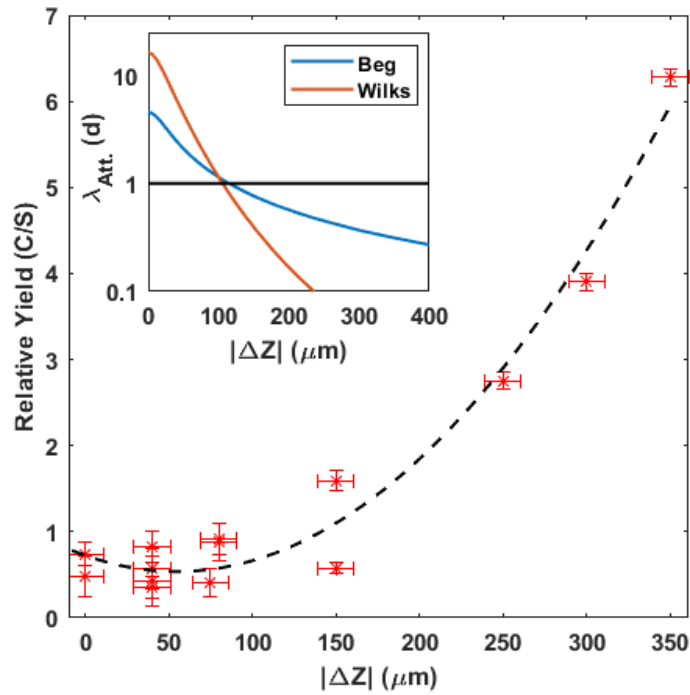


Figure 5.6: Comparison between the x-ray flux in each region of the x-ray source for varying focus position. Ratio of the central source to the substrate source, more flux is contributed by the central source for increasing defocus. Inset shows the attenuation length, $\lambda_{Att.}$, normalised to the target thickness, d , for electrons with energy $E = k_B T_e$ in a copper target for Wilks (orange) and Beg (blue) scaling law as a function of defocus position.

5.2.3.2 Spatial X-ray Measurements

The results above suggest a mechanism to improve x-ray radiography by reducing the flux from the larger substrate source. Figure 5.7(a-b) are plots of the lateral size of both the central and substrate source as a function of defocus position. The central source increases as the laser is defocused, from an optimum of $\sim 84 \mu\text{m}$ to $> 120 \mu\text{m}$ at largest defocus. This scales more slowly than the laser spot size and, therefore, cannot be expressed by a single divergence through the target - as expected due to the change in laser intensity [20, 101]. This is shown in Figure 5.7(a) by the dashed lines, which are determined by assuming the source expands with a fixed divergence from the laser spot (from

Eq. 5.2). The substrate source, however, decreases with the laser intensity from ~ 1.8 mm at best focus to $\simeq 1$ mm at large defocus. A lineout of the penumbral edge at best focus and largest defocus is presented in Figure 5.10 to demonstrate the difference at each limit.

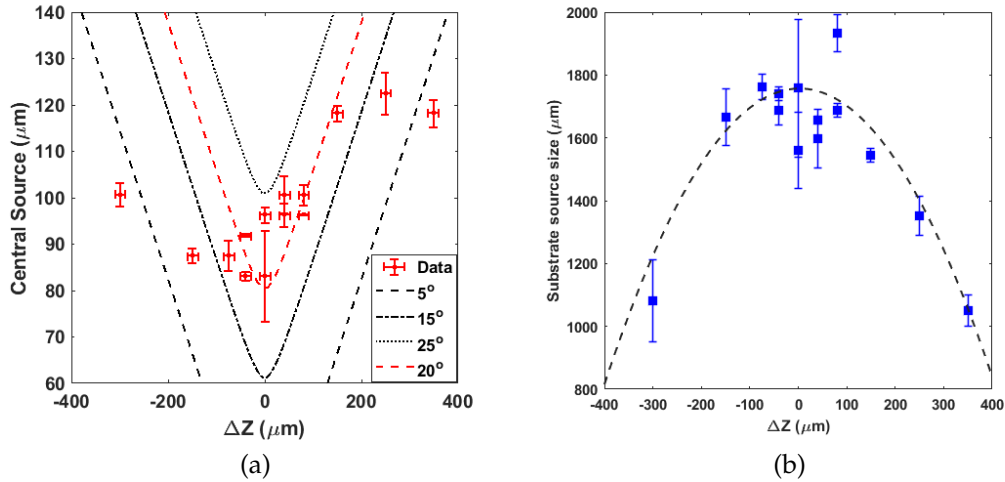


Figure 5.7: Central and substrate x-ray source size as a function of defocus. (a) Central source size as measured (red), with the expected size from a simple geometric expansion for different electron divergences also shown (black dashed lines). (b) Source size for substrate x-ray source as a function of defocus position.

The divergence of the electrons through the target can be inferred from the central measurement and laser spot diameter. There is reasonable agreement with the divergence measurements made by Green *et al.* [20] over the tested intensity range, Figure 5.8, however the inferred divergence measurements stop increasing significant beyond $\theta_{div} \sim 20^\circ$ (red dashed line in Figure 5.7(a)). This plateau suggests that there is some collimation of the beam occurring as the fields develop within the target - similar to what Yuan *et al.* [136] observed in thicker targets. As Green *et al.* [20] did not measure a similar effect from the K-alpha emission it can be assumed that this is only occurring in the higher energy electron population, and that the higher divergence that they measured is

a convolution of both central and recirculating electrons. As $I_L \rightarrow 10^{17} \text{ W/cm}^2$ the measured electron divergence drops to almost zero, i.e. a collimated beam through the target. This result is likely due to the laser beam profile at large defocus accelerating the electrons responsible for generating the x-rays ($\sim 1 \text{ MeV}$, see Figure 3.9(b)) from a smaller area than the total spot area.

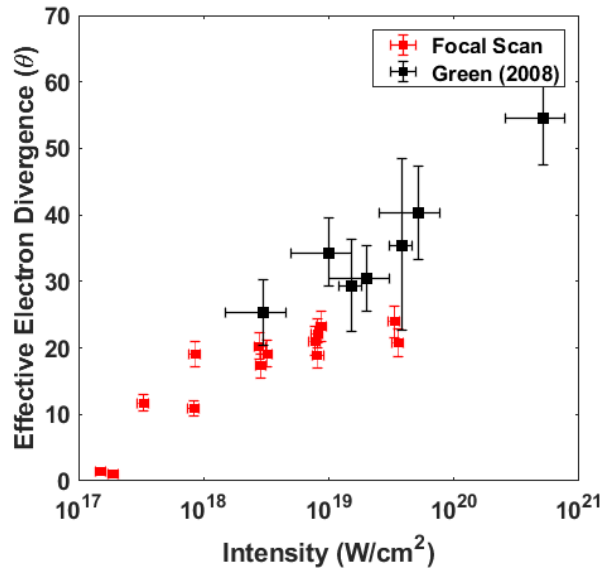


Figure 5.8: Electron divergence as a function of on target intensity, calculated from the central source measurements. Measurements from this experiment (red) extend the trend seen in numerous experiments collated by Green *et al.* (black), references of each in [20].

The increase in the central source can be explained by the increasing laser focal spot and reduced electron divergence [20]. However, the decreasing size of the substrate source (Figure 5.7(b)), the reduction in substrate x-ray flux (Figure 5.4(b)) and the change in the ratio (Figure 5.6) is indicative of a lower total number of recirculating electrons. This suggests that there is additional physics to consider. For instance, several groups have demonstrated that the divergence-intensity relationship is not necessarily causal and that a varying scale length is a significant factor in electron beam divergence [101, 125].

Changing the on-target intensity for a fixed scale length was shown to have little effect on the electron divergence between $10^{19} - 10^{21}$ W/cm² with a reduction occurring below 10^{18} W/cm². Ovchinnikov *et al.* did not simulate intensities lower than this, however, it would be reasonable to suggest that the reduction seen between 10^{19} and 10^{18} would continue as the ponderomotive ejection angle would reduce considerably as the intensity drops further below 10^{18} . The divergence remains approximately constant for intensities greater than 5×10^{18} W/cm² and significantly reduces at lower intensities, which suggests that these conditions are similar to the simulations conducted by Ovchinnikov *et al.*, where there was a near constant scale length with $L_s > \lambda_L$. The scale length was not experimentally measured, however, prior hydrodynamic simulations on similar laser systems [52, 100, 246] demonstrate that the scale length reduces as the laser pedestal intensity is reduced.

5.2.4 Spatial Contrast Improvement

The spatial resolution of a radiographic system is dependent on the size of the source emission area and the resolution of the detector. As such, decreasing the size and flux contribution of the substrate source is beneficial to radiography as it removes the larger blurring factor on the image. The increase in central source size, whilst detrimental to the smallest resolvable feature, is paired with an increase in the x-ray flux, resulting in a brighter source for increased defocus, shown in Figure 5.9.

The increased contrast between the central and substrate source causes greater spatial contrast of the x-ray emission and the reduction of the secondary source removes the majority of the background signal. When the ratio between these two sources is at its greatest (i.e 300 μ m defocus from the experimental scan), the image quality is at its best. An example of this can be seen in the radiographs in Figure 5.10. Since the central source size increases as a function of

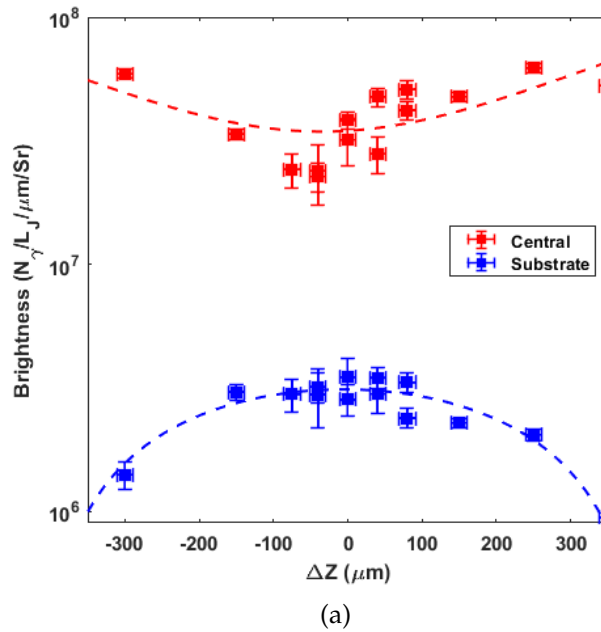


Figure 5.9: Brightness of the central and substrate sources as a function of defocus position showing an increase in central brightness as the laser is defocused.

defocus, radiography should aim to use an intensity that delivers a small central source yet does not introduce a large blurring substrate source.

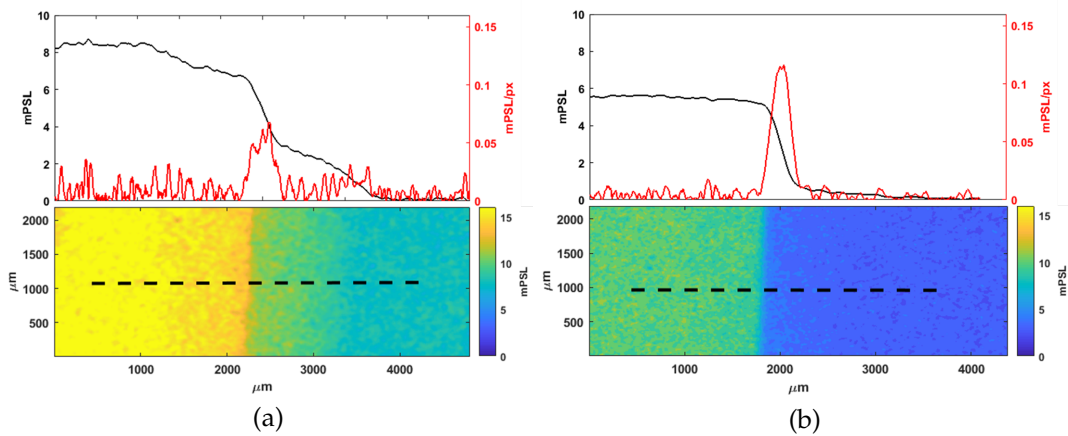


Figure 5.10: Comparison of varying defocus in radiographs, (a) target at best focus, (b) target at $-300 \mu\text{m}$ defocus. The significant image contrast improvement by reducing, or removing, the secondary source is clear.

While the radiograph of the penumbral edge can be considered as a simplified - almost ideal - example, the increase in contrast is clear. Objects with features smaller than the substrate source could be blurred by its contribution. For more complex radiographs, where the spectra of emission must be considered, this might not be as simple and a compromise between reducing the contribution from the substrate source and maintaining a sufficiently energetic electron beam to produce x-rays of the required energy might have to be made.

5.3 Analytical Modelling

The flux variation between the central and substrate sources, and the resultant image contrast improvement, can be explored analytically by what fraction of fast electrons *only* travel in the central channel, and what fraction recirculate or escape the target. From established scaling laws the intensity and fast electron relationship scales as, $I^a \propto (k_B T_e)$, where $k_B T_e$ is the hot electron temperature and a varies from 0.33 [18] to 0.5 [121]. As discussed at the beginning of this chapter, the population of electrons that do not recirculate are either attenuated on the first pass of the target or are able to overcome the sheath potential. Mora [161] presents a 1D isothermal plasma expansion model that can be used in calculations of the sheath potential. The peak electric field (Eq. 5.1) scales as with the electron temperature, $k_B T_e$. The extent of the sheath field at the rear target surface is λ_D , as such the energy of electrons able to escape the target can be approximated to:

$$U_{esc} \simeq E_{sheath} \lambda_D \simeq k_B T_e \quad (5.3)$$

Electrons with more than this energy typically can escape the target on the first pass and as such only contribute to the central source of x-rays. The other sub-population to consider is the low energy electrons, those that would typi-

cally lose their energy through collisions with the bulk target in a single pass. This limits low energy electrons from reaching the rear surface based on the target material and thickness, with the transmission function, ζ , defined as: $\zeta(E_h, \rho, l) = \exp(-l\rho\sigma(E_h))$, where $\sigma(E_h)$ is the attenuation cross section for an electron of initial energy E_h , ρ and l are the target density and thickness respectively. The remaining electrons contribute to the substrate source and blur the final image. This can be expressed as a ratio between electrons that contribute only to the central source and those that contribute to the substrate. This ratio can be expressed as, η_R :

$$\eta_R = \frac{N_c + N_e}{N_h} = \frac{\int_0^\infty (1 - \zeta) f(E_h) dE_h + \int_{k_B T_e}^\infty f(E_h) dE_h}{\int_0^\infty f(E_h) dE_h} \quad (5.4)$$

where N_e , and N_c , are the populations of escaping electrons, and electrons lost through collisions in the targets respectively. N_h is the total number of accelerated electrons calculated from the laser intensity by assuming a Maxwellian distribution of the form:

$$f(E_h) = A \sqrt{\frac{4E_h}{\pi(k_B T_e)^3}} \exp\left(-\frac{E_h}{k_B T_e}\right) \quad (5.5)$$

where A is the conversion efficiency calculated from the equation presented in Davies [19] (Eq. 2.45), and $k_B T_e$ is the electron temperature for the given laser intensity. This equation is integrated with respect to energy to determine the total number of possible accelerated electrons. N_e , and N_c , are calculated with respect to N_h . The number of collisional electrons, N_c is determined by applying a transmission function, $\zeta(E_h, \rho, l)$, to the initial spectrum to determine how many are able to reach the rear surface. The number of escaping electrons, N_e assumes electrons with energy greater than U_{esc} (Eq. 5.3) are able

to escape which sets the lower limit of the integral. At the higher intensities considered in the experimental results ($I_L > 10^{19}$ W/cm²) a relativistic Maxwellian distribution [118] was also considered. The maximum energy in a Maxwell-Juttner distribution is lower than a Maxwell-Boltzmann distribution of the same temperature (see Figure 2.5) and, as a result, this distribution predicts a higher number of recirculating electrons for the same conditions. In the following results a Maxwell-Boltzmann distribution is used, however, for $I_L > 10^{19}$ W/cm², the results from a Maxwell-Juttner distribution are included to demonstrate this increase.

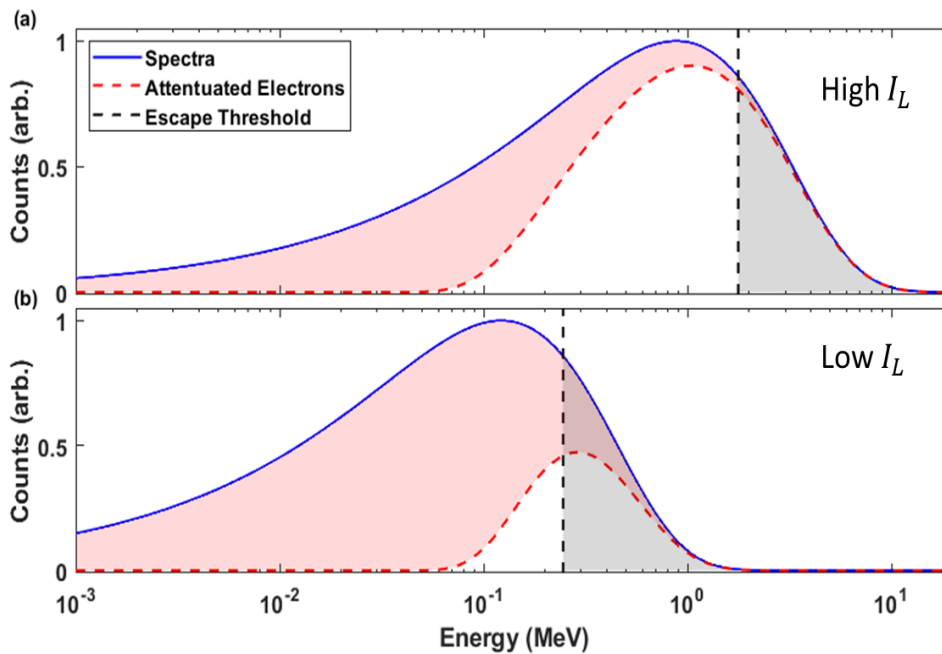


Figure 5.11: Maxwellian distribution for electrons with temperature $k_B T_e$ at two different laser intensities, (a) High $I_L = 1 \times 10^{20}$ W/cm² and (b) Low $I_L = 4 \times 10^{18}$ W/cm², this correlates to the laser at best focus and 150 μ m defocus. The red dashed line indicates electron transmission through the target, black dashed line is the escape energy cut-off. The population of electrons between these two lines contributes to the substrate source (unshaded), the other two (red - collisional, grey - escaping) can only contribute to the central source.

Figure 5.11 shows these for a typical spectra for a high intensity laser. The

difference between the total number accelerated and those that escape or collide through the target are the recirculating electrons. In order to maximise the central source of x-rays N_c and N_e need to be significantly greater in number than the recirculating electrons. This model is calculated from peak laser intensity and so does not include considerations of the temporal effects that occur during an interaction. For example, electrons accelerated during the rising edge of the laser pulse are less energetic than those from the peak, and the sheath field increases as more electrons reach the rear surface. These effects are known to alter the sheath development [161, 171, 173, 247]. An optimum intensity would be expected when varying either energy or pulse duration, occurring when the sheath field and electron attenuation result in the lowest recirculating population.

This model gives us a method to optimise the electron temperature as a function of the target thickness, maximising the central source distribution and therefore the final image quality. The equation presented above, Eq. 5.4, can be solved for the experimental conditions to explore the role that the recirculating electron population has. The intensity was calculated for 80 J in a spot defined by Eq. 5.2 with a 2 ps pulse duration - matching the nominal experimental conditions. The results and the expected ratio between the two sources is shown in Figure 5.12(b), the results from the experimental campaign also plotted. The ratio of x-ray yields is calculated from the electron populations by the ESTAR radiative stopping power tables [14], with the recirculating population contributing on every other pass of the target to account for the directionality of the emission.

The ratio of x-ray yields is calculated from the electron populations using the ESTAR radiative stopping power tables [14], with the recirculating population contributing on every other pass of the target to account for the direction-

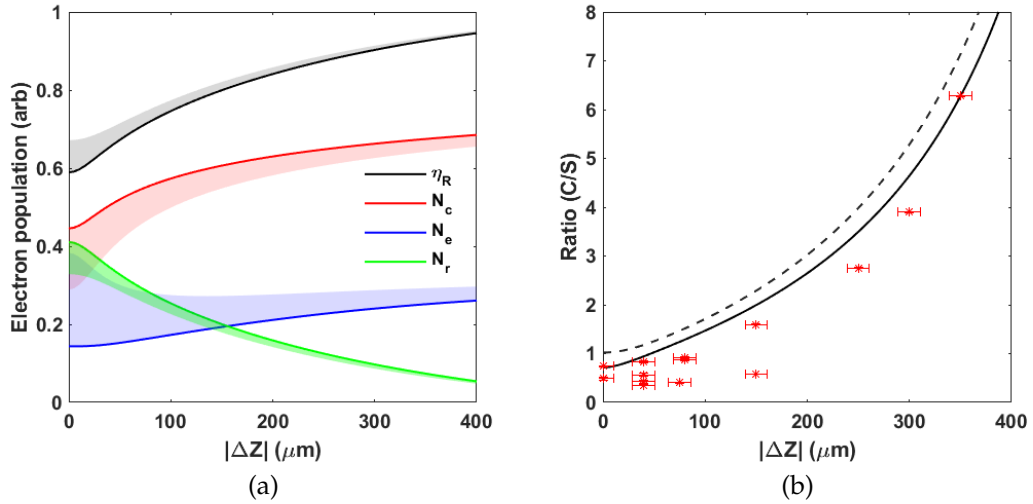


Figure 5.12: Results from the analytical model. (a) Population of electrons that contribute only to the central source, Eq. 5.4 (black) as a function of defocus, the percentage of the electron spectra that are collisionally attenuated on the first pass (red), escape the target (blue), or recirculate the target (green). The relativistic correction from Maxwell-Juttner distribution is shown by the filled area for each population. (b) is the ratio of the central to the substrate source calculated as $\eta_R/2(1 - \eta_R)$, to account for the directionality of bremsstrahlung, for a Maxwell distribution (solid) and a Maxwell-Juttner distribution (dashed) with the experimental data in red, the model uses laser conditions from the experiment and Beg scaling to determine the electron spectra [18].

ality of the emission. The dashed lines in Figure 5.13 show the curves for tantalum (dashed) and aluminium (dot-dash) targets at 100 μm thickness peaking at different intensity regions compared to the copper target. The model peaks, marked in blue in Figure 5.13, at $\sim 300 \mu\text{m}$ defocus for copper targets, agreeing with the experimental data presented in Figure 5.4(a).

The penumbral measurement of the x-ray source from the experiment is unable to reveal much information about the spectral nature of the two sources, however, from this model some conclusions can be drawn. The maximum energy of the substrate emission should be limited to the temperature of the elec-

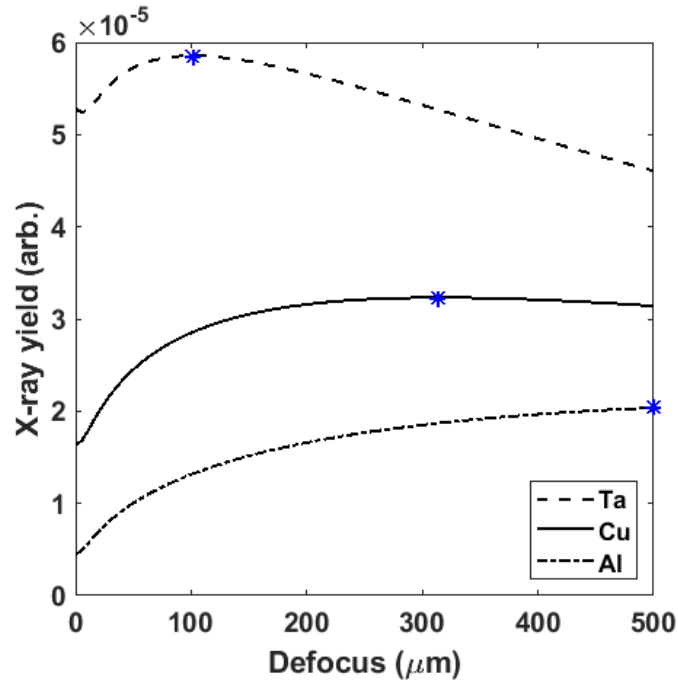


Figure 5.13: Calculations using the analytical model. The central x-ray flux calculated for various targets: copper - solid, tantalum - dashed, and aluminium - dot-dash, the peak flux shown with a blue asterisk.

tron beam for a Maxwellian distribution. At best focus, $\sim 1 \times 10^{20} \text{ W/cm}^2$, the modal generation should be similar as both the recirculating and single pass spectra peak at $E_h \approx 1 \text{ MeV}$. As the intensity is reduced, the recirculating electrons are *on average* more energetic than the first pass population as collisional losses are most effective at lower energies, this would suggest the substrate source would have a harder x-ray emission spectra. To determine this in detail however, the energy loss of the electron population though collisions and interactions would have to be considered.

The absorption in the model was assumed to scale with intensity by the equation presented by Davies [19] to account for the reduced absorption at lower intensity. However, a recent study by Gray *et al.* [245] posited a succinct model for *re*-acceleration of electrons with larger spot sizes, exploring the role

of electrons recirculating back into the laser field and gaining additional energy from the laser. In thin targets, where this re-acceleration is most effective, this would act to increase the brightness of the substrate source and effectively blur the central source further. In thicker targets however ($> 50 \mu\text{m}$) the increase in energy through this effect can be considered negligible due to the number of passes occurring within the pulse duration.

5.4 PIC Simulations

The analytical model presented in the previous section relies upon a simple assumption about the escaping electron population and cannot explore the divergence of electrons. In reality, the sheath will evolve over time and the initial escaping electron population could be below the $k_B T_e$ threshold used in the model. To explore this more thoroughly, the interaction conditions were modelled in 2D using EPOCH [31], and the electron population tracked throughout the simulation.

5.4.1 Simulation Parameters

The PIC simulation parameters, outlined in Table 5.1, were set to provide similar conditions to the experimental investigation. However, aspects were reduced to keep the simulations computationally viable. The intensity was set at a peak of $5 \times 10^{19} \text{ W/cm}^2$. The beam energy and pulse duration was maintained and intensity lowered by introducing curvature to the phase of the beam and defocusing from the front of the target. The phase of the beam is given as:

$$\varphi = -\frac{-k_L x^2 - k_L y^2}{2Rc(x)} + \arctan\left(\frac{x}{RR}\right) \quad (5.6)$$

where k_L is the wavenumber of the laser, the Rayleigh range of the beam

$RR = \frac{\pi}{\lambda}(2.44\lambda F_{\#})^2$, $Rc(x)$ is the radius of curvature at x , where x is the propagation vector of the beam [17]. The pulse duration, τ_l , was set to 250 fs and the target thickness, l , was reduced to 25 μm to compensate for the reduced pulse duration and ensure that $\tau_l > 2l/c$. This was set to maintain the experimental conditions ($l = 100 \mu\text{m}$ and $\tau_l \sim 2 \text{ ps}$) as Gray *et al.* [245] demonstrated that, under similar conditions, there was additional laser absorption into the electron population as it recirculated and re-experienced the laser field. The laser was defocused by up to 300 μm onto the target surface using Eq. 5.6. To minimise variation between the simulations and directly probe the effect of the sheath field and recirculation, the scale length was fixed to 2 μm . This length was selected to match prior measurements made using the Vulcan laser system. Santala *et al.*[102] measured a 2.6 μm scale length and McKenna *et al.* [156] measured two distinct regions in the pre-plasma including a sharp primary scale length of 1 μm .

Intensity	$5 \times 10^{19} \text{ W/cm}^2$		
Scale Length	2 μm		
Density	77 N_c		
Particles per cell	30		
X(min,max,dx)^a	-7 μm	43 μm	10 nm
Y(min,max,dy)	-25 μm	25 μm	10 nm

Table 5.1: EPOCH simulation parameters. ^a front surface is at $X = 0 \mu\text{m}$.

5.4.2 Sheath Field Strength

The model put forward in the previous section is based on the sheath field strength decreasing as the laser intensity is reduced. The validity of this statement can be verified using the PIC simulations by determining the peak field strength beyond the rear surface of the target as a function of time. The separation between the sheath and target can be determined to provide an estimate

on the energy required to escape. Figure 5.14(a) shows the peak field strength as a function of defocus. In Figure 5.14(b) the distance, in X , between the peak of the sheath field and the target is used to calculate the potential that electrons would have to cross as a function of the electron temperature.

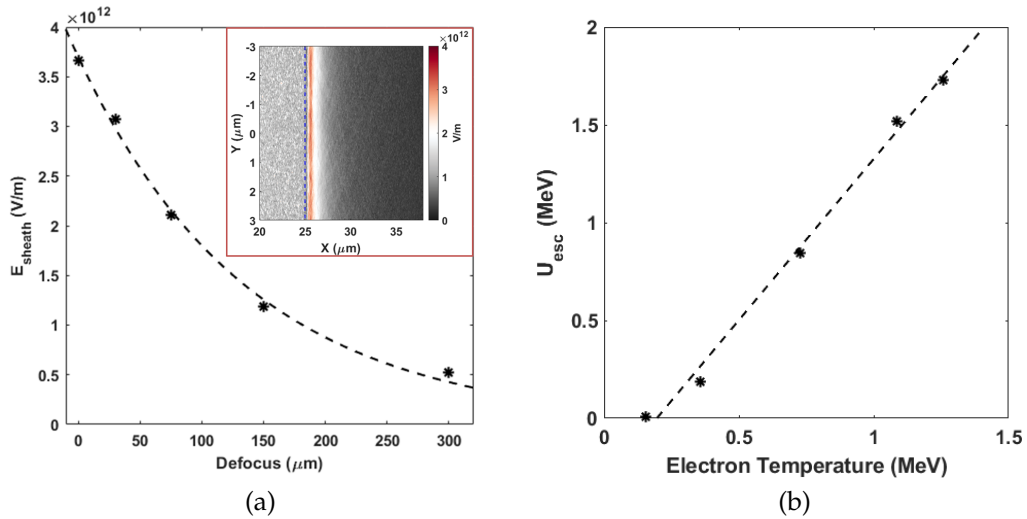


Figure 5.14: Sheath field from EPOCH simulations. (a) Peak field strength as a function of defocus, inset shows a figure of the sheath for the best focus simulation at 425 fs. (b) Sheath field potential as a function of mean electron temperature, in agreement with the model this potential scales linearly with electron temperature. The temperature was calculated at 425 fs.

The temperature was determined at $t = 425$ ps for electrons with $E > 250$ keV and $X < 25$ μm by using a simple Boltzmann fit of the form $N = N_0 \exp(-E/k_B T_e)$. This time step was the maxima of the sheath for all but the largest defocus. The electron spectra in the simulations had multiple temperature components, as noted in Figure 5.15, the average of these was used in Figure 5.14. The scaling between the determined electron temperature and the field potential is linear, in agreement with Mora *et al.* [161] and the model in the previous section [248].

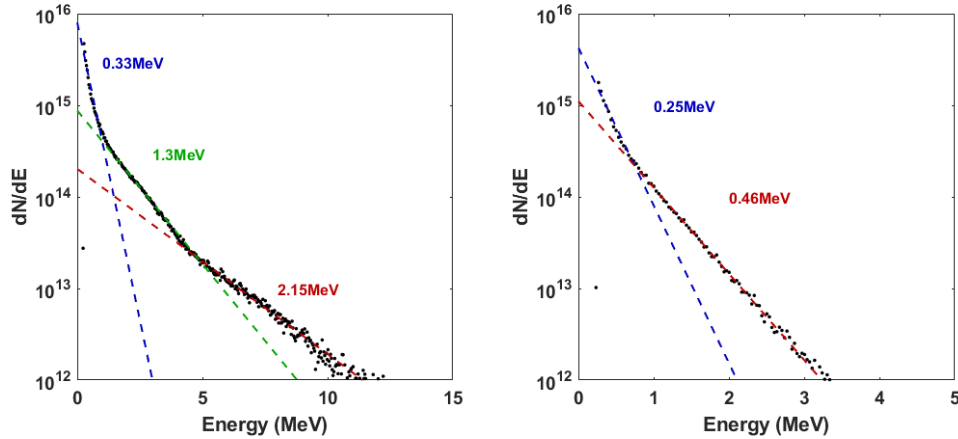


Figure 5.15: Electron spectra from EPOCH simulations (a) best focus and (b) 150 μm defocus. The multiple temperature distribution are shown as independent fits with the corresponding temperature shown.

5.4.3 Divergence

In order to assess the spatial evolution of the electron channel the phase space of the electron population was analysed as the simulation evolved. Divergence through a target for a fast electron beam is a manifestation of many individual processes, Green *et al.* [20] demonstrated experimentally the link between intensity and effective electron divergence through a target, and later Ovchinnikov *et al.* [101] explored the effect that the pre-plasma can have on the divergence, concluding that it has a strong influence over the effective electron divergence. Debayle *et al.* [134] explored the role of field growth via PIC simulations and determined that there were two competing effects at work. The first, generated in the pre-plasma as initial electron acceleration sets up magnetic fields that filament the beam, and the second is from the ponderomotive force on electrons, where electrons at the highest intensity of the spot are driven away. In Figure 5.16 the electron density at $t = 425$ fs is plotted with front and rear surface forward travelling electron density lineouts. The lineouts are calculated by determining the average electron density travelling with $+ve$ x-momentum in the first and last 4 μm of the target.

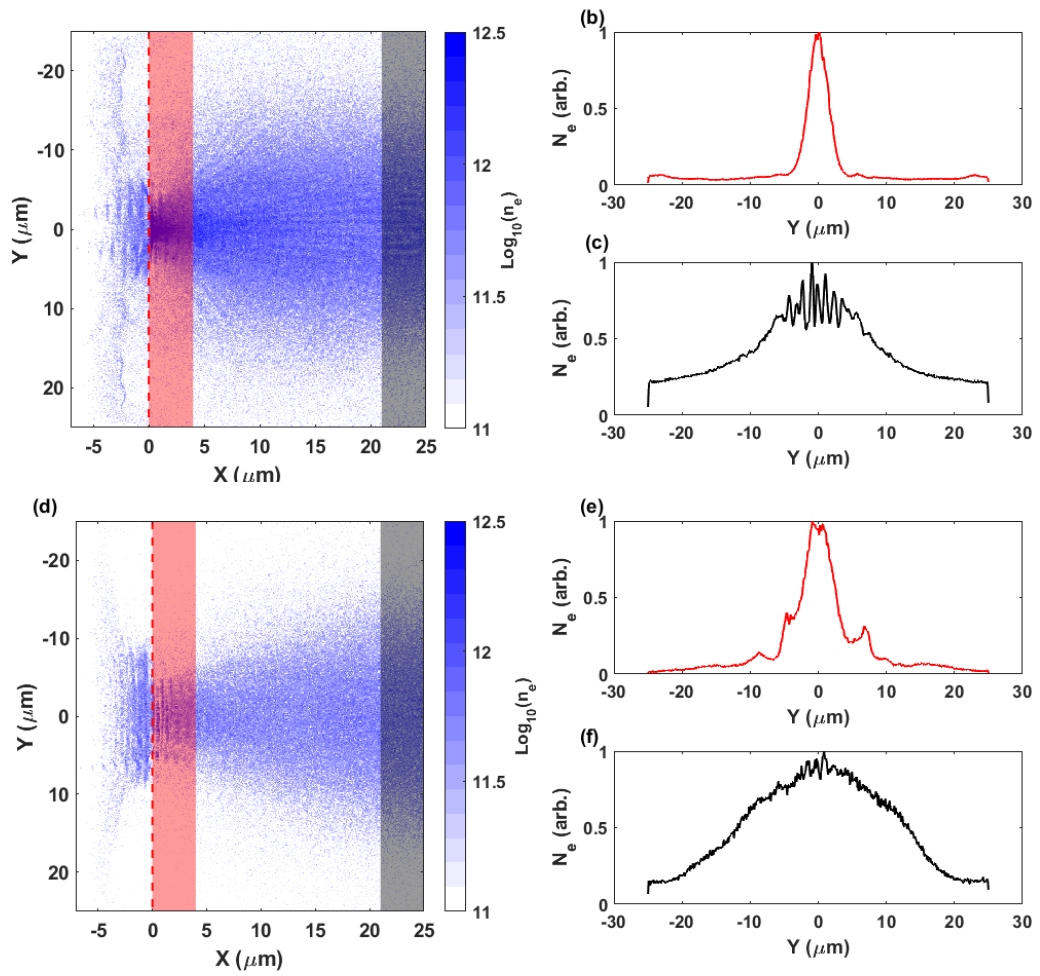


Figure 5.16: Electron density at best focus. (a) Electron density at 425 fs, front target surface is indicated by the dashed line at $X = 0 \mu\text{m}$. (b-c) Lineout of electron density at front (b) and rear (c) surface - averaged over the corresponding shaded region in (a). (d-f) is the same as (a-c) for the $-75 \mu\text{m}$ defocus simulations.

The change in electron density at the front and at the rear surface, shown in Figure 5.16, demonstrates the divergence through the target. The lateral expansion of electrons can be probed in two different ways. First, the effective electron divergence, calculated from the front and rear surface electron density lineouts in Figure 5.16, is used to determine what the lateral size of the electron density would be for a $100 \mu\text{m}$ target.

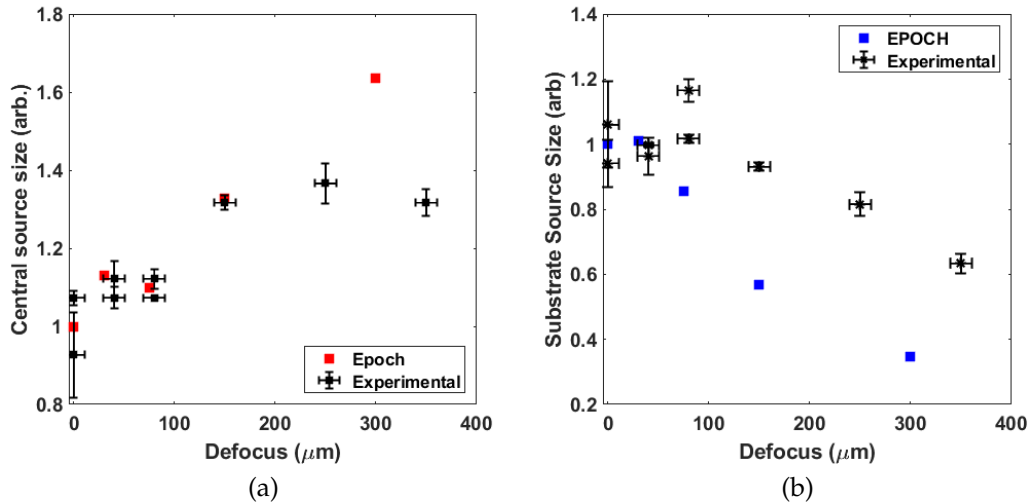


Figure 5.17: X-ray emission area for central and substrate sources inferred by the hot electron divergence and the total stopping range for the accelerated electron population. Experimental and simulation results are normalised to best focus. a) central source, b) the substrate source.

Since the x-ray emission area will follow the same expansion of the electrons this can be used to determine the central source, the results of this analysis is shown in Figure 5.17(a). The measured substrate source during the experiment was > 1 mm in size, if the expansion happened at $v_{\text{exp}} \approx c$ this would take ~ 3.3 ps to fully establish - making both the size and time required outside of the scope of this simulation. The stopping power of the electron population is considered to determine the extent of the electron expansion during the electron lifetime. The CSDA range of the average electron energy, calculated from the ESTAR data tables [14], is used as an indicator for the total x-ray size, plotted in Figure 5.17(b). Despite the absolute values being reduced compared to the measured results, there is some agreement between the trend of expected substrate source size inferred from the electron temperature and the measured x-ray size. The effective electron divergence inferred from the x-ray measurements, scaled slowly with intensity beyond 5×10^{18} W/cm² reaching $\sim 20^\circ$ as the intensity was increased further. For the highest intensity simu-

lations ($\Delta Z = 0, 30, 75 \mu\text{m}$) the divergence of hot electrons rapidly rises with the rising edge of the laser pulse and then plateaus at $\sim 20^\circ$ the same as the integrated measurements shown in Figure 5.8.

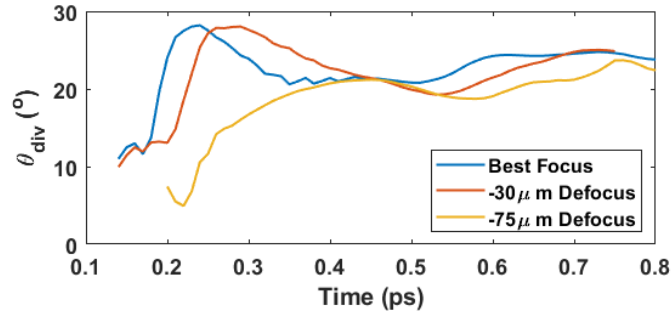


Figure 5.18: The divergence of hot electrons as a function of time calculated from the electron momenta during the simulation.

5.5 Conclusion

The x-ray spatial profile from a high intensity laser-solid interaction results in a two source structure. The central channel dominated by electrons on their first pass through the target and a larger substrate source from recirculating electrons spreading laterally through the target. Experimental results demonstrate a $\times(10 \pm 2)$ increase in the flux ratio of these sources is obtained by simply defocusing, suggesting a way to increase the quality of any radiograph by optimising this ratio and the flux. By defocusing the laser there would be an increase in the minimum resolvable feature, however this is offset by the contrast gain achieved by removing the majority of the substrate source. Through analytical modelling the relationship between escaping, attenuated, and recirculating electrons can be probed and optimum laser intensities for varying target parameters presented. The model is in good agreement with the experimental data, both the ratio between central and substrate flux and the total central flux produced. PIC simulations are then used to explore the

dispersion through the target. There is evidence of two components that effect the x-ray source profile; the first establishes over the duration of the simulation, whereas the substrate source is a result of the remaining energy in the recirculating electron population.

Chapter 6

Investigation into fast electron dynamics and laser propagation within laser-guiding capillary-targets

Planar targets have a single discrete interaction between the laser and target, typically accelerating electrons along the laser-axis and/or the target normal; by opting for a more complex target surface, there is the potential for multiple interactions that each accelerate electrons. In this chapter, a novel capillary target is explored experimentally and a simulation study, comprising both a geometrical model and PIC modelling. The capillary design captures the reflected laser light within the hollow centre of the target, changing the interaction conditions from a single point of acceleration as the laser travels through the capillary. The conversion efficiency and intensity of each subsequent interaction is reduced; however, the numerous interactions with the target prompt higher overall conversion efficiency from the laser to electrons compared to a single interaction with a foil. The experimental data examined in this chapter demonstrate an increase in x-ray yield compared to similar solid wire targets. An analytical model is presented exploring the effect of glancing angle interactions within a capillary, and numerical simulations in EPOCH 2D and

3D are used to explore the individual processes that result in a brighter x-ray source. The simulations in EPOCH suggest that the measured increase is due to a combination of both the number and energy of electrons accelerated by the *quasi*-static fields building in the capillary.

6.1 Complex Target Structure

Chapter 2 outlined several absorption mechanisms by which laser energy is converted into hot electrons. In each instance, only a single interaction between the laser and target is considered. The capillary target design explored in this chapter results in numerous interactions between the laser and target, driving a near continuous source of electrons along the target inner wall whilst channelling the remaining laser energy forwards.

Using complex targets for laser-plasma interactions is not a new idea. In one notable example, cone structures have been used in fast ignition experiments [249]. A gold cone inserted in to the shell which contains tritium and deuterium is used to enable electrons to be injected directly into the core. The intent of the cone structure is to guide the laser light, and subsequent fast electron acceleration, as close to the core as possible, such that they create a hotspot within the compressed fuel and ignite the fusion reaction. Without the cone, plasma expansion from the fuel can mitigate the laser propagation and reduce the overall energy deposited into the centre. This technique has seen a myriad of developments over the years [141, 153, 249, 250]. Kodama *et al.* [249] demonstrated that significant electron energy was "wasted" through TNSA acceleration of protons on the outer surfaces of the cone, diminishing the eventual delivery of the electrons, and concluded that approximately 25% of 100 kJ of laser energy would need to be coupled to the electrons in order to

facilitate the necessary conditions for ignition. Cone-wire geometries, where a large aperture cone is affixed to a thin wire, have been used to explore fast ignition principles [153, 251–253]. Green *et al.* [251] measured significant heating on the surface of wires from the cone-wire geometry, due to the inhibitive magnetic fields that occur on the surfaces. The connection between the cone and the wire caused filamentation and beam breakdown as the electrons cross the interface. They concluded that, with an increased wire diameter and minimal resistivity change at the interface, a significant increase in electron density could be driven.

Complex target surfaces have also been used to increase absorption between the laser and the electron population [254–256], or shape the transporting electron beam [257–261]. Kemp *et al.* [124] demonstrated that structures on the scale of the laser wavelength can increase the energy of the accelerated electrons through the generation of magnetic fields along the surface structure, which trap electrons and re-inject them into the laser field to be re-accelerated. Recent work by Jarrett *et al.* [262] demonstrated that the diffraction from sub-spot structures could be used to infer the interaction conditions. While both of these targets are significantly different from the design explored in this chapter, the mechanisms at work here are critical in enabling us to interpret the results observed for capillary targets.

6.2 Capillary target design

The target design explored in this chapter is a hollow micro-fibre, positioned along the laser propagation axis. A schematic is shown in Figure 6.1, which outlines the basic concept of the capillary target combined with a collimated laser beam in (a) and the propagation of modes within the capillary in (b). The laser is initially incident with a glancing angle onto the internal

walls of the fibre, this then ionises and reflects a portion of the remaining laser energy towards the other side of the capillary. Each interaction accelerates electrons into the capillary walls. The inner wall is a pulled glass fibre, coated on the outside with gold to increase x-ray conversion.

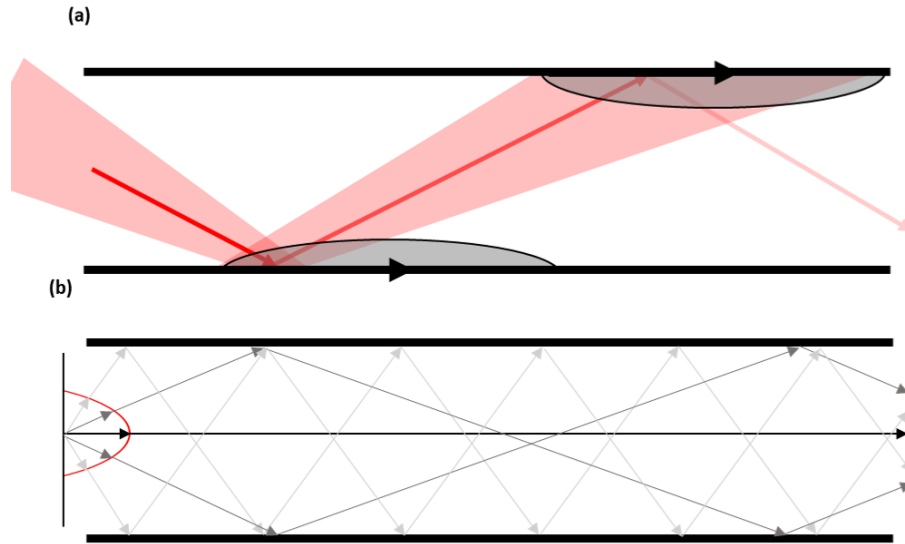


Figure 6.1: Schematic showing laser interaction with a capillary target. (a) Demonstrates the single ray approximation that will be explored again in Section 6.3.1, (b) Demonstrates the various modes that will develop as the beam defocusses into the capillary.

However, the focussing laser beam will produce a series of modes within the capillary as the wings of the beam propagate at a different angle to the central axis. These modes will alter the amount of energy able to propagate through the capillary - this is discussed again in section 6.3.2. For the following experimental section, the capillary length ℓ_c was 2 mm long with a 20-80 μm aperture, $2r_w$. Each target had a slight ellipticity due to the manufacturing process. Figure 6.2 shows a schematic of the design and a picture of one of the targets shot during the experimental campaign. The target inner wall was 5 μm glass coated in 5-20 μm of gold. As shown in Figure 6.2(b), the surface of

the gold was irregular as a result of the manufacturing process. The laser is focused to the inside edge of one wall. The inner edge ionises under the rising edge of the pulse to form a plasma which, ideally, reflects the remainder of the laser, allowing it to interact again on the other wall. The subsequent interactions boost the overall absorption of laser energy into the target and enhance fast electron generation along the length of the capillary.

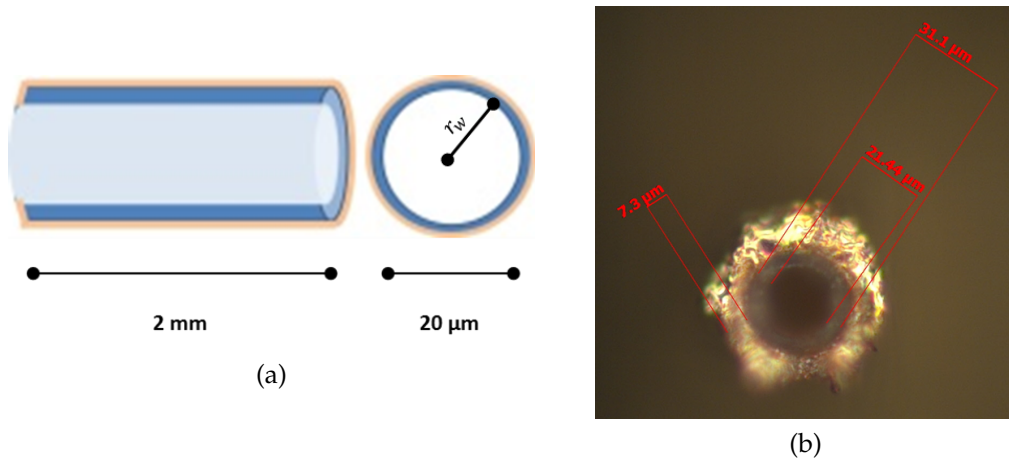


Figure 6.2: Prototype capillary targets. (a) Schematic outlining the key target measurements; (b) image and measurements of one of the targets shot during the experimental campaign.

6.2.1 Experimental Investigation

This capillary target design was trialled during an experiment using the Vulcan laser system. Although a prototype, the results demonstrated the effectiveness and potential of targets like this. The capillary targets were compared to wire targets in both a horizontal and vertical orientation. The primary material of the wire was gold for each target type, with the appropriate dimensions (radius and length) maintained between targets. A schematic of each target geometry is shown in Figure 6.3.

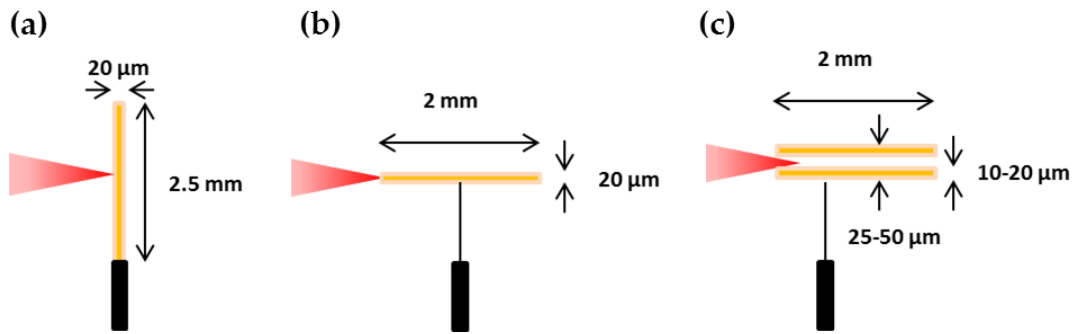


Figure 6.3: Schematic of the targets with key dimensions labelled. Solid wire targets (a) Vertical and (b) Horizontal orientation. (c) Capillary target. In each case the primary material is gold, capillary targets have a inner layer of glass.

The experiment was conducted with the nominal laser parameters of ~ 200 J on-target energy and a pulselength of ~ 14 ps FWHM. The peak intensity of the laser at best focus was $\approx 10^{19}$ W/cm². The expected intensity due to a 5° glancing angle of the capillary is $\approx 10^{17}$ W/cm² - Figure 6.4(b) shows the intensity as a function of glancing angle for the first interaction.

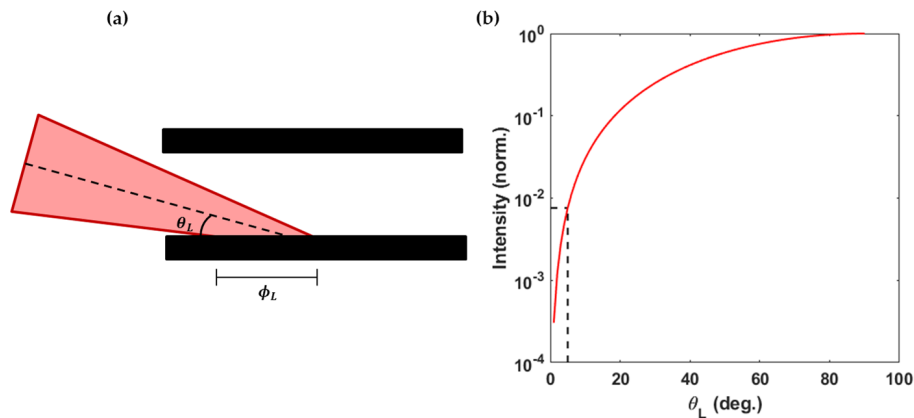


Figure 6.4: Initial laser conditions with target geometry. (a) Schematic of the spot size due to glancing angle, (b) calculation of peak intensity as a function of angle (dashed line is 5° glancing angle).

Figure 6.5 shows the experimental layout of the final laser optic and the main imaging line. The source profile was characterised via a set of on-axis

penumbral foils, with the design as discussed in Chapter 4. One foil is positioned to measure the vertical source (V-Foil) and one the horizontal source (H-Foil). The set-up shown in Figure 6.5 ensures a magnification of $\times 17.5$ for the horizontal axis and $\times 13.4$ for the vertical axis. The x-rays were detected using layers of Fujifilm SR image plate, filtered by 2 mm of aluminium and any escaping electrons are deflected by a 0.6 T magnet.

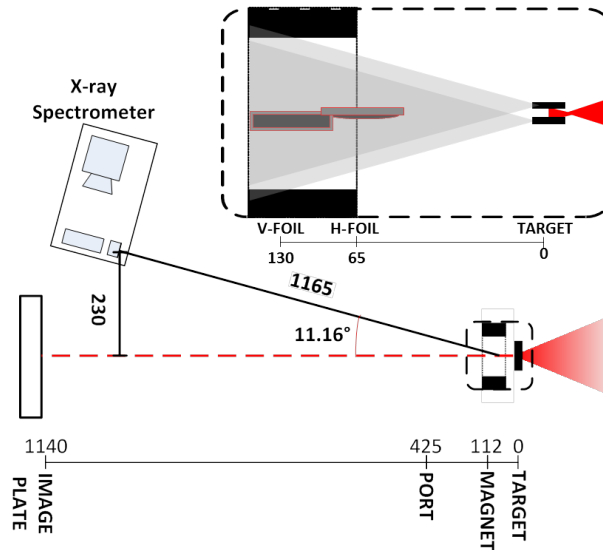


Figure 6.5: Schematic of the primary imaging diagnostics. The set-up is the same as in Chapter 7. The main image shows the penumbral foils and X-ray spectrometers. The inset is an expansion of the penumbral foil set-up, with the grey cones representing the forward x-ray emission from the capillary walls. Magnets are required to remove the escaping electron population from the target. (All distances in mm measured from target position).

The response function of the detector is shown in Figure 6.6(a) for a uniform x-ray signal. However, as highlighted in Figure 6.1, electrons can be accelerated along the target and generate x-rays continuously. In order to determine the effective spectra that is emitted from the target, the variable attenuation length of the capillary targets must be considered. A Boltzmann distribution of x-rays is attenuated by some fraction of the total target length to provide a spectrum similar in shape to those measured in GEANT4 (Figure 3.5). Both the

effective temperature and the attenuation length are unknown, and so the entire parameter space must be tested to explore the effective x-ray energy. This was completed by varying an x-ray spectrum of the form:

$$N_\gamma(E_\gamma) = \exp\left(-\frac{E_\gamma}{T_\gamma}\right)\zeta(E_\gamma, l, \rho) \quad (6.1)$$

where $\zeta(E, l, \rho)$ is the transmission of each photon energy E_γ through a material, with density ρ and length l , determined from the NIST XCOM database [15]. The length is varied between 10 μm and 2 mm, and the temperature T_γ is varied from 50-500 keV - the approximate scaling for the electron temperature between intensities of 10^{15} and 10^{19} W/cm². The results from this parameter scan are shown in Figure 6.6(b). The peak response for the entire parameter space is (59 ± 9) keV. For the lower intensities expected at a glancing angle, the peak response is closer to the barium edge of image plate at (39 ± 2) keV. This number is important when calculating the number of photons emitted from the target, due to the non-uniform response of image plate to higher energy x-rays. For vertical and horizontal solid wires the response is clear, since the electron/x-ray source is attenuated by a fixed amount of target.

The spectral emission from each target was characterised by an off-axis hard x-ray spectrometer shown in Figure 6.5. Using the spectrometer design mentioned in Chapter 4, the effective temperature of the x-ray emission is inferred via the technique discussed in Rusby *et al.* [26, 263]. In addition to these x-ray measurements, the front surface interaction was imaged using a high-magnification backscatter camera. The reflected laser light can be measured via this diagnostic to compare a capillary interaction to that of a solid target, either horizontal or vertical wire. The backscattered light during the laser-solid interactions can be an indicator of the on-target intensity [264–266].

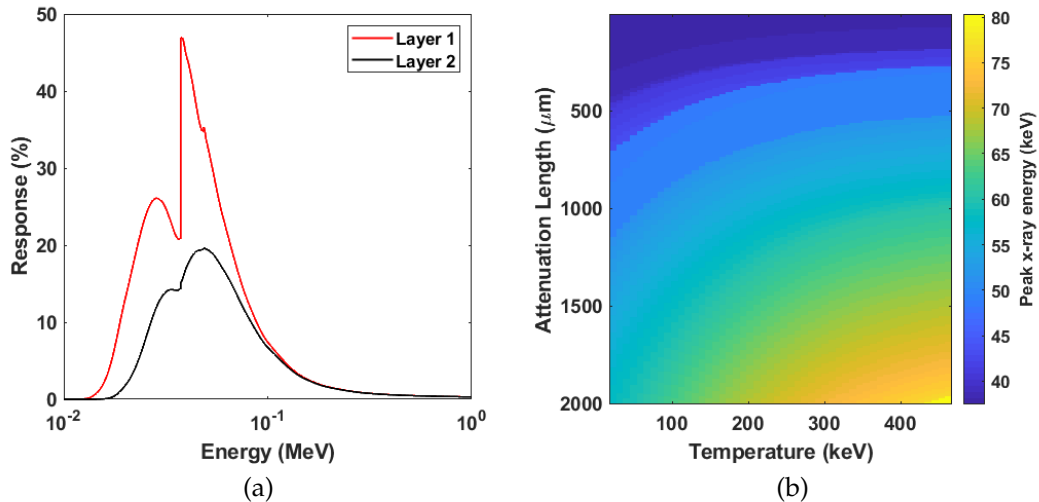


Figure 6.6: Detected x-rays in the experimental set-up. (a) Response curve for the image plate detectors through the chamber port, created from the NIST transmission tables [15]. (b) The peak x-ray energy as a function of x-ray temperature and attenuation length, at the low temperatures expected from the interaction with a capillary wall, the peak x-ray energy is at the K-edge of the barium in the image plate.

6.2.2 Experimental Results

Due to the complexity of these targets and the focal spot jitter of the laser, there was only a limited set of successful shots to compare with solid wire targets, one at full energy (~ 200 J) and two at quarter energy.

6.2.2.1 X-ray Measurements

The effective x-ray temperature in Figure 6.7(a) is determined via the technique discussed in Rusby *et al.* [26]. The much higher temperature for the horizontal wire demonstrates the effect of self-attenuation (or “beam-hardening”) in the full energy horizontal wire target shots. Self-attenuation refers to the process in which the x-ray spectrum generated by a target is reduced due to lower transmission at low x-ray energies. X-ray attenuation scales with energy and so the emitted spectra appear “harder” or more energetic than thinner

targets for the same laser conditions [38, 267]. The capillary target emits a significantly cooler effective x-ray temperature compared to a horizontal wire indicating that, as outlined in Section 6.2.1, the effective attenuation length is considerably lower. This is likely due to the continuous injection of electrons along the target as the laser transports through the capillary compared to the single injection point in a solid wire. The capillary target exhibits a similar effective temperature to the vertical 25 μm wire, and produces more forward going x-rays despite the expected reduction in on-target intensity due to glancing angle irradiation. At lower laser energies there is a significantly reduced photon number from the horizontal wire target, which could explain the limited beam hardening seen in Figure 6.7(a) compared to the capillary targets which emitted significantly more photon flux than the horizontal wire target under the same laser conditions.

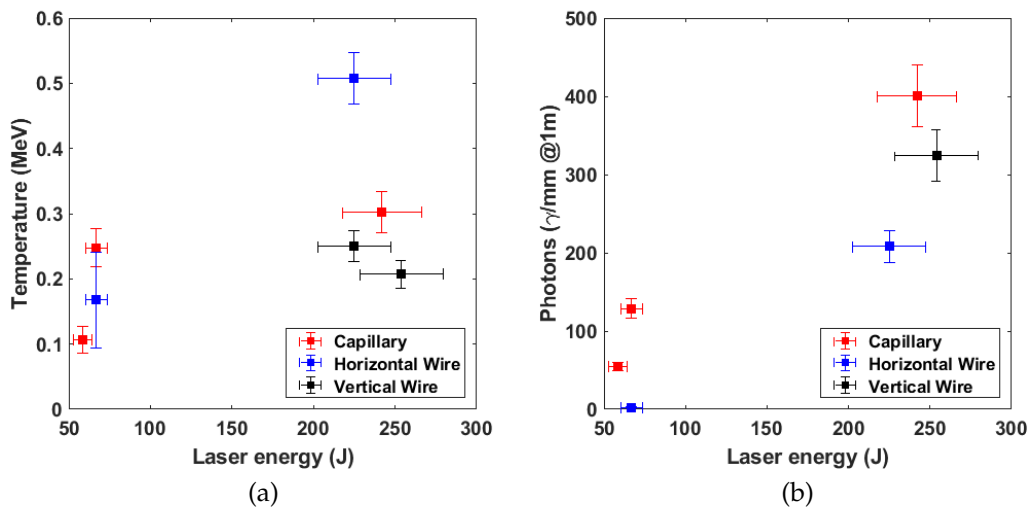


Figure 6.7: X-ray emission from each target measured by the gamma-spectrometers. (a) The effective X-ray temperature determined via the method outlined in Reference [21] and Chapter 4, (b) the first crystal flux converted into absorbed photons per mm.

Both the flux and the temperature demonstrate a slight increase for capil-

lary targets compared to the solid alternatives. The discussion in Chapter 7 demonstrates how the field structure on the surface of a vertical wire enhances the electron recirculation through the target, and therefore increases the x-ray generation. The further increase in x-ray signal observed for the capillary targets must therefore be due to more favourable electron conditions; either there are more electrons accelerated during the interaction, or the spectrum of the accelerated electrons is more likely to radiate x-rays.

The spatial measurements from the penumbral, for each target configuration, is shown in Figure 6.8. Both the capillary and horizontal wire targets seem to be slightly misaligned to the penumbral foils, with the source size being larger than the cross section should permit. This is due to the side of each target contributing to the source profile. At 2 mm in length, an offset of 1° to the penumbral foils would produce a source of $30\ \mu\text{m}$. Despite this misalignment, the capillary x-ray source size measures smaller than a vertical wire and produces a fairly symmetric source. The large errors shown on the horizontal wire measurements are due to the limited flux

Figure 6.9 shows the lineout from a penumbral measurement during one of the quarter-energy shots. The peaks of each wall are (31 ± 3) and (36 ± 3) μm in size for the left- and right-hand side respectively. The asymmetry and increase from the known $22\ \mu\text{m}$ size (shown in Figure 6.2(b)) implies that the capillary was angled towards the penumbral. The angle can be estimated as 0.5° from the penumbral plane, assuming that the full length of the wire is contributing to the measurement. The laser was aligned to provide the central axis of the beam with a 5° glancing angle interaction with the wall and an uncertainty in alignment of this magnitude is expected. The same feature is not present in the vertical penumbral, indicating that either the penumbral foil is significantly vertically offset and the edge feature is not being imaged,

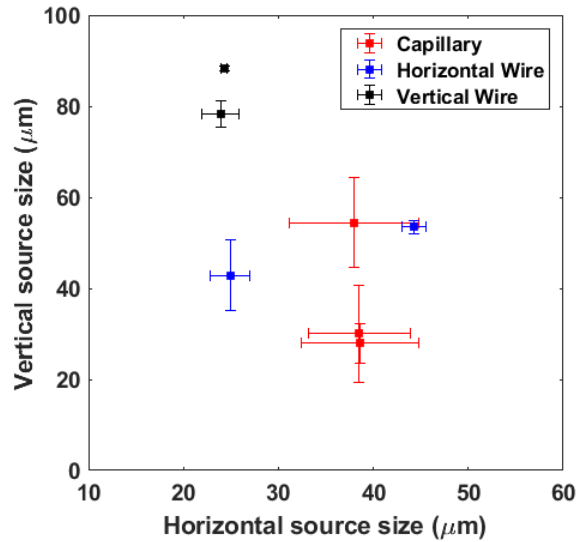


Figure 6.8: Vertical and horizontal source size for each target configuration.

or that electrons do not readily circulate the capillary azimuthally and instead are channelled along interior walls near their injection point. In simulations presented later in this chapter, the latter of these is explored via a 3D EPOCH simulation.

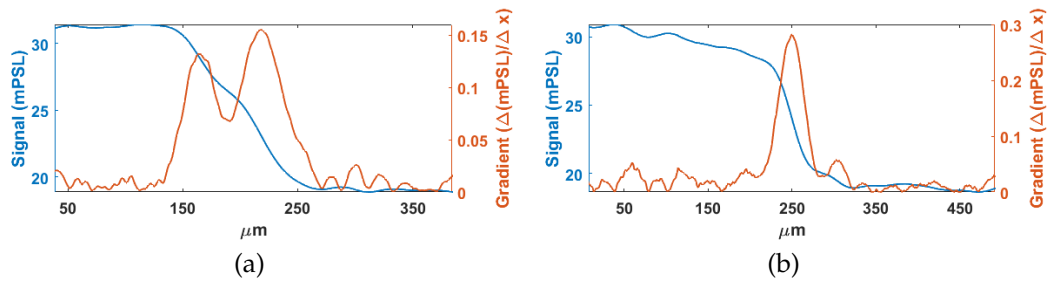


Figure 6.9: Penumbral profile from a capillary target from the (a) horizontal penumbral and (b) the vertical penumbral, demonstrating the source contribution from each wall is resolved in the horizontal axis. The walls measure as (31 ± 3) and (36 ± 3) μm FWHM - slightly larger than the actual profile of the walls as discussed in the text. In each graph, the signal across a transition is shown in blue, and the gradient in orange.

6.2.2.2 Probing the laser-interaction

Probing the laser-interaction is challenging, since the primary reflections are used for the secondary interactions. The expectation is that the capillary target design increases absorption, and this should decrease the amount of detected laser light measured via the high-magnification backscatter camera. The reflection conditions from each target are significantly different, with the solid wire backscatter only gathering a small percentage of the reflected light and the capillary primarily reflecting laser light forward away from the diagnostics. This means that the intensity of the backscattered light cannot be used as an indicator of the relative absorption.

University of Strathclyde – October 1, 2019

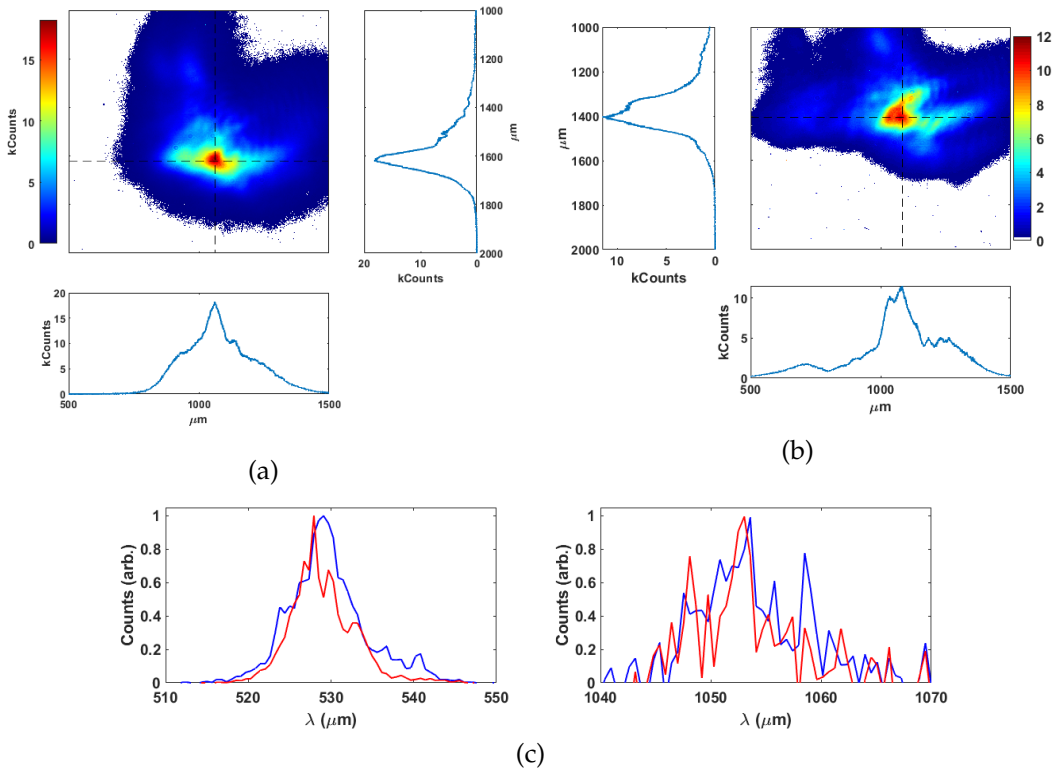


Figure 6.10: Data from the backscatter diagnostics. (a-b) Capillary and horizontal wire backscatter images; (c) backscattered spectrum for capillary (red) and horizontal wire (blue).

The results in Figure 6.10(a-b) show backscatter images for both the capil-

lary and horizontal wire targets with lineouts in both directions, and (c) shows the spectrum of each centred at $1\omega_L$ and $2\omega_L$. The geometry of the capillary target means that a quantitative comparison is unreliable; however, the results in Figure 6.10 show that the backscattered $2\omega_L$ is both broader and shifted for the solid target in comparison to the capillary. While these changes are slight results by Kalashnikov *et al* [268] and Zepf *et al.* [264] demonstrate similar changes for solid targets under equivalent laser conditions. This change in Doppler shift between the two targets demonstrates that the capillary was, likely, irradiated at a glancing angle because, if the front surface of the capillary had been hit, there should be a similar Doppler shift to that seen for the horizontal wire.

6.3 Discussion

The results presented in the previous section demonstrate an increase in measured x-ray flux from the capillary targets compared to similar size solid targets in vertical and horizontal geometry. The backscatter diagnostics indicate that the target was irradiated at a glancing angle and as such the laser was significantly less intense compared to the wire targets. The x-ray temperature showed that, compared to a solid wire, there is considerably less beam hardening for the emission. These results indicate that the target design allows laser energy to propagate through the capillary to some extent - measuring any transmitted laser light directly was not possible due to the x-ray diagnostics present in the imaging line - but determining physics occurring during the transport requires further exploration. This section considers the physical processes at work analytically, treating the propagation of the laser as a series of discrete interactions. A geometrical model of the laser reflection within the capillary is presented along with considerations of the glancing angle interac-

tion, and the effect that divergence will have.

6.3.1 Laser propagation model

A simple model can be constructed to investigate the role of laser incidence angle in electron absorption throughout the capillary; for a large angle of incidence the laser could interact many times within the capillary, conversely for a shallow glancing angle there will be fewer possible interactions. To explore the variation with different incident angles a collimated laser is considered - this is equivalent within the capillary to a laser focused with a large $F_{\#}$ optic. With a focussing laser a series of modes will establish as the beam propagates through the capillary - by limiting the discussion to a collimated beam reflecting through a cavity the idealised electron acceleration can be explored. The effect that the divergence and physics of a glancing angle interaction is then considered.

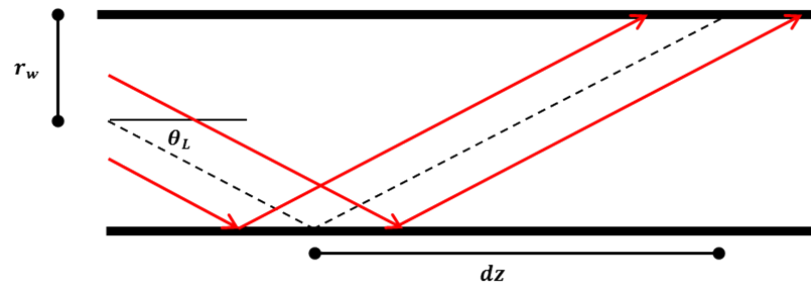


Figure 6.11: Schematic of collimated beam reflections through the capillary, the separation between the central axis of each interaction is shown.

The laser is incident onto the inner wall of the target and propagates through the capillary. The propagation of the central axis of the beam can be determined from the geometry to provide an estimate for the spot area. The propagation distance, dz , between each wall within the capillary can be determined

from the incidence angle as:

$$dz = \frac{2r_w}{\tan(\theta_L)}. \quad (6.2)$$

Assuming that the beam is incident at the opening aperture of the capillary, $z = 0$, the initial offset of the central axis can be calculated as half the spot diameter on the angled wall as:

$$z_0 = \frac{\phi_L}{2 \sin(\theta_L)} \quad (6.3)$$

therefore the propagation of the central ray is $z_L = \phi_L/2 \sin(\theta_L) + 2nr_w/\tan(\theta_L)$, where n is the interaction number and continues until z_L exceeds the length of the target. The wings of the spot are defined as $z_L \pm \phi_L/2 \sin(\theta_L)$ and used to calculate the intensity of the laser at each interaction. To determine the absorption, the plasma reflectivity curves published in the literature [22–24] are used, and the portion of the beam not reflected is assumed to be absorbed into hot electrons with the temperature determined by Beg's scaling law (Eq. 2.48). The peak laser intensity is set to 1×10^{19} W/cm², with ~ 200 J and a 14 ps pulse duration, and $\phi_L = 7$ μ m, to mirror the experimental parameters. The capillary radius was set to $r_w = 10$ μ m and the length set to 2 mm.

Figure 6.12 shows the published reflectivity results of Dromey *et al.* [23] and Zeiner *et al.* [22] in black for a 500 fs pulse. The intensity was varied between 10^{12} to 10^{16} W/cm² by changing the on-target spot size, as such this is a suitable starting point to explore the propagation with the capillary interaction. Subsequent experiments by Wilson *et al.* [203] demonstrated that these results are valid at significantly higher pulse energies. Streeter *et al.* [24], blue in Figure 6.12, published reflectivity measurements for intensities from 10^{17} to 10^{21} W/cm². As noted by Dromey *et al.* [23], the spatial quality in the reflected beam begins to deteriorate for $I_L > 10^{16}$ W/cm², and as such the subsequent intensity would be reduced for initial interactions higher than this. From these

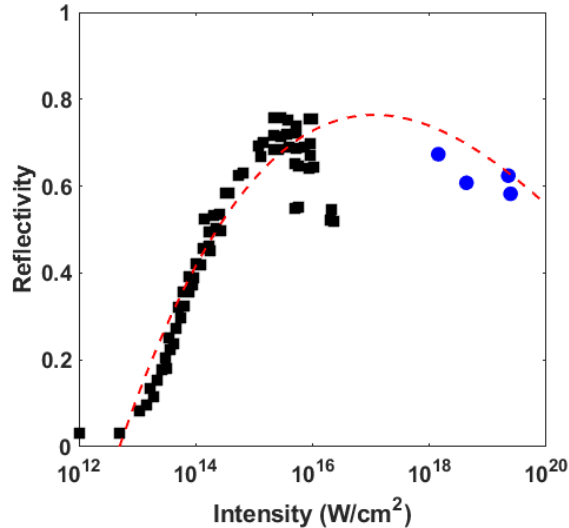


Figure 6.12: Reflectivity of plasma mirror compiled from the results by Ziener *et al.* and Dromey *et al.* (black), with high intensity values by Streeter *et al.* (blue) [22–24]. The fit is a polynomial and was used to interpolate the reflectivity in the discussion.

measurements it is clear that the first interaction (and as many subsequent ones as possible) should have an intensity of $\sim 10^{16}$ W/cm², where the reflectivity is optimum for transport of the laser down the capillary. This implies that the target needs to be set at a glancing angle of $< 20^\circ$ to ensure the correct spot diameter on the initial interaction. Zeiner *et al.* [22] varied the incidence angle up to 45° without significant change to the reflectivity; however, further considerations due to the glancing angle are discussed in the Section 6.3.3.

The plasma scale length affects the reflectivity of the inner wall and the conversion to hot electrons at each interaction. For simplicity, the scale length, L_s , is considered as constant throughout the capillary and set to $L_s \geq \lambda_L$. Since the duration of the laser pulse during the experiment (~ 14 ps) was fairly long, the scale length could also change during the interaction further altering the reflectivity. This is comparable to measured scale lengths from high power laser systems caused by the inherent pre-pulse [102, 156], and mitigates high ab-

sorption at glancing angles from vacuum heating [112, 115]. At each wall, the accelerated electron temperature, T_h , is calculated according to the Beg scaling law (Eq. 2.48) and absorption from the reflectivity results in Figure 6.12. The electrons then propagate through the inner wall, and the attenuation is determined by the Beer-Lambert law (Eq. 3.20) where the attenuation cross-section, σ , is the from the ESTAR database [14] for the electron temperature. Figure 6.13 shows the results from the model for incident angles of a,d) 15° , b,e) 5° , c,f) 2° , demonstrating the difference each geometry has on the propagation of the laser and the electron acceleration as a result.

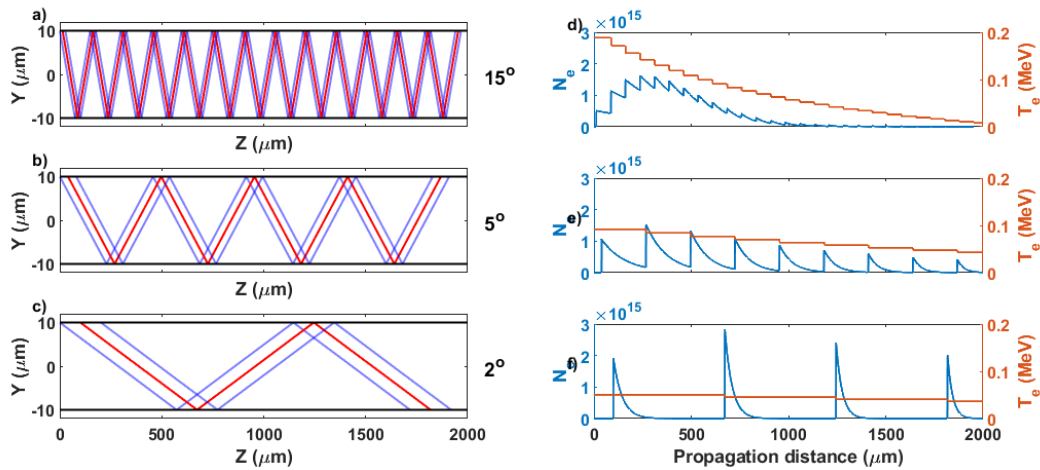


Figure 6.13: Laser interactions with the capillary walls for 3 different angles (a,d) 15° , (b,e) 5° , (c,f) 2° . (a-c) show the path for a collimated laser, red is the centre axis and blue the edge of the beam. (d-f) show the number of injected electrons and the temperature from each interaction.

At an incidence angle of 15° (75° from target normal), the laser interacts with the capillary many times, but the laser intensity and number of electrons quickly dissipates. At smaller incident angles, the number of interactions reduces, but so does the average temperature of the accelerated electrons. In the final case, a large number of electrons is still being injected at the final inter-

action, indicating that not all the energy has been converted into hot electrons and some laser energy has been wasted. The total electrons injected and their average temperature is of interest. Figure 6.14 shows that, with increasing θ_L , the number of injected electrons falls as the average energy of the electrons increases. For x-ray generation and electron transport down the capillary, this indicates some optimum condition where there are sufficient electrons at the right energy to propagate.

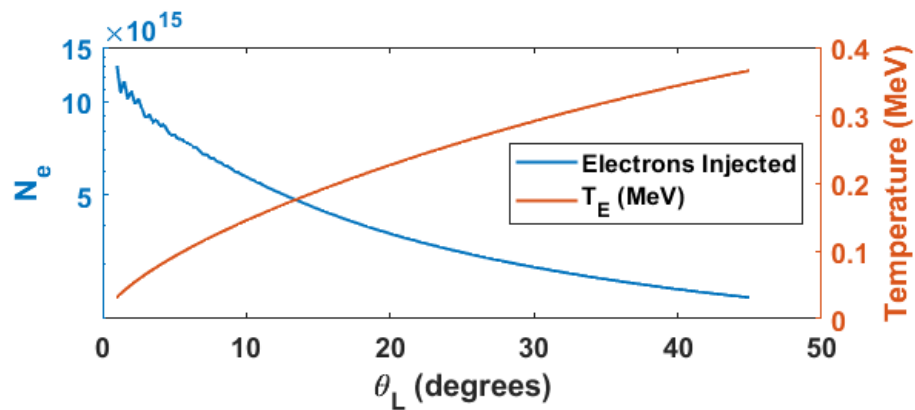


Figure 6.14: Number of electrons and average temperature accelerated at the capillary wall for varying incident angle. Capillary dimensions are fixed with a $20 \mu\text{m}$ aperture and 2 mm in length, each interaction is summed to determine the electrons injected.

A single interaction at 85° incidence (5° from normal), determined by the same model, would accelerated $\sim 4 \times 10^{14}$ electrons with a temperature of 400 keV. This demonstrates the additional acceleration expected for capillary targets compared to single interactions with solid targets.

6.3.2 Effect of laser divergence

Since the laser focuses into the capillary, rather than propagates as a collimated beam, the area illuminated by the laser will expand as modes develop in the laser propagation. The area of illumination is dependent on the length

of the capillary and, assuming that the incidence angle, θ_L , is less than the focusing angle ($\theta_f = \tan^{-1}(1/2F_{\#})$), can be calculated by:

$$A_c = \pi r_w \left(2\ell_c - \frac{r_w}{\tan(\theta_f - \theta_L)} - \frac{r_w}{\tan(\theta_f + \theta_L)} \right) \quad (6.4)$$

This equation is the lateral surface area of a cylinder segment using the propagation of each edge of the spot to determine the length of each side of the cut cylinder, a schematic of this is shown in Figure 6.15(a). In the initial interactions there will be limited loss from the exit of the aperture and so the intensity can be calculated using Eq. 6.4. For the experimental conditions $A_c \approx 3 \text{ mm}^2$ and therefore the intensity of this interaction would be $\sim 10^{16} \text{ W/cm}^2$. This intensity should cause significant reflectivity as the plasma is formed on the inner surface of the capillary from the values shown in Figure 6.12. Subsequent interaction conditions are less trivial to determine. Laser light will escape from the exit aperture after each reflection, diminishing the total energy in the pulse. For $\theta_L > \theta_f$, the area of illumination becomes a large ellipse, similar to the collimated model in Section 6.3.1, with the area expanding rapidly as the preceding edge of the pulse has a longer path length through the capillary, shown in Figure 6.15(b). The problem is compounded when considering the pulse duration is significantly longer than the travel time across the centre of the capillary, and, as such, the reflections will not be distinct. This means that under certain conditions ($\theta_L \approx \theta_f$), the trailing edge of the pulse is reflected several times before the leading edge has crossed the capillary once.

6.3.3 Glancing Angle Considerations

The effect of a laser at a glancing angle with the capillary wall is unaccounted for in this model. Several groups [269–273] have explored the physics that occurs at the target surface as the laser propagates. Chen *et al.* [271] simulated similar conditions to the capillary model above, using a laser with a

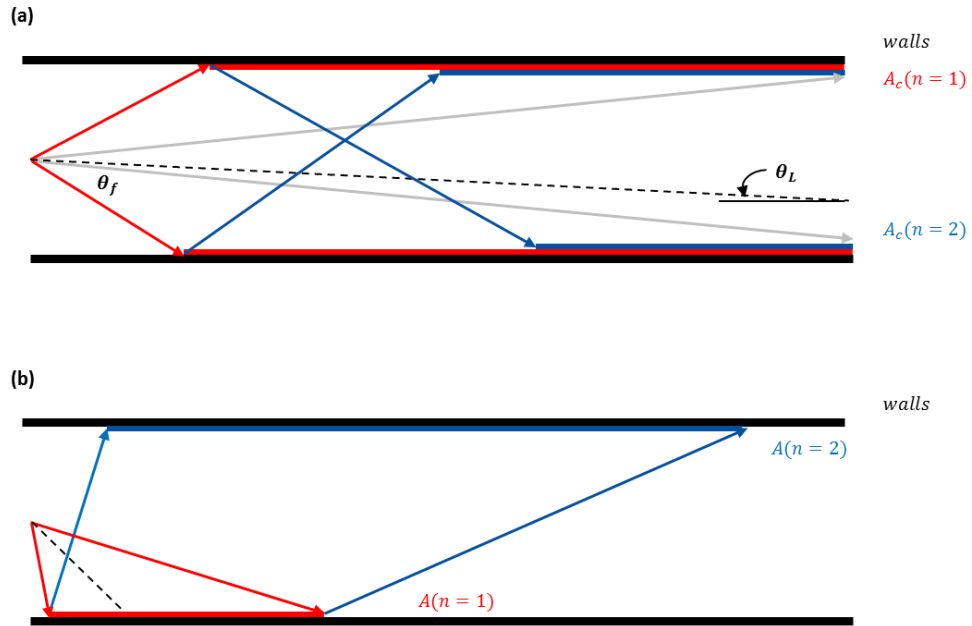


Figure 6.15: Schematic of laser light focusing into a capillary for (a) $\theta_L < \theta_f$, (b) $\theta_L > \theta_f$. The maximum surface area that can be illuminated is determined by Eq. 6.4. In both panels the first interaction area is shown in red and the second in blue. The grey arrows in (a) indicate the angular range of laser that escapes from the capillary before interacting with the walls.

University of Strathclyde – October 1, 2019

peak intensity of $a_0 = 2$ ($I = 5 \times 10^{19} \text{ W/cm}^2$) incident onto a target at 20° (70° from target normal). The results demonstrate that, as the laser reflects off the target surface, electrons from the wall are accelerated out and establish a *quasi*-static E_y field to complement the laser pulse. This E-field draws electrons back towards the target surface, and a secondary B_z field - that follows the return current in the target surface - forces them away again. Nakamura *et al.* [269] studied this analytically and showed that a critical angle exists at which this mechanism begins to dominate electron behaviour. This critical angle is $\sim 25^\circ$ from the target surface, considerably larger than the experiment above, however it shows that under intense laser conditions ($a_0 > 2$) the surface magnetic fields can be a significant fraction of the laser magnetic field strength - highlighting the importance of this mechanism. The combination of E- and B-fields that emerges on the target surface causes the electrons to oscillate near

the surface within the laser pulse. This oscillatory motion results in successive acceleration as the electron crosses the laser pulse, similar to the anti-*dephasing* mechanism discussed by Pukhov *et al.* [274] and Arefiev *et al.* [11] for direct laser acceleration.

Kluge *et al.* [25] demonstrated similar successive periods of acceleration using a conical target on the front surface of a foil. A glancing laser angle with the cone promotes significantly higher electron energy than that of a standard foil interaction. They also noticed that as the cone length was increased, the peak electron energy was increased. This trend was more pronounced for electrons being accelerated by the longitudinal fields, as they were able to spend more time in the accelerating gradient. A scaling can be inferred from Figure 6 in Kluge *et al.* [25]. Their paper did not focus on the increased length and instead discussed the effect on proton acceleration. The results for a laser of $a_0 = 8.5$ is shown in Figure 6.16 from their 2D LSP simulations. Since the peak energy from the cone, E_c , should correlate to the acceleration length of the electron, and the acceleration length (provided the electron cannot leave the influence of the laser) is dependent on the channel length, l , then it follows that the peak electron energy should increase as a function of the channel length, $E_c \propto l$. This scaling is shown in the graph by the dashed fit.

Gray *et al.* [275] demonstrated the surface transport of electrons with foil targets at glancing angles, showing a peak of electrons travelling laterally across the target for laser conditions similar to those used experimentally. This is in line with previous experimental results [156, 272, 273, 276] from different laser conditions, which demonstrate that a surface current of electrons is a robust mechanism expected to occur at glancing angles.

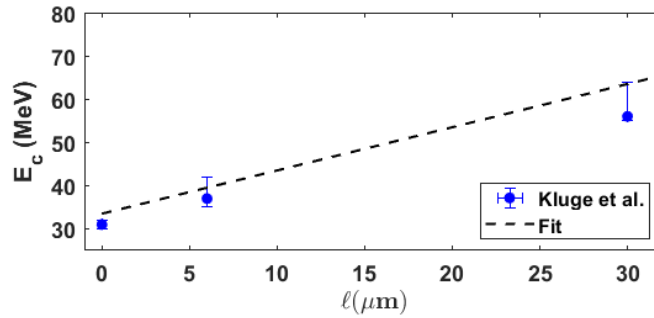


Figure 6.16: E_c as a function of channel length, l , taken from Figure 10 in Reference [25] at the point where N first drops to 1. Dashed line is a linear scaling of the form $E_c \propto l$.

6.4 Modelling

The simple model, presented in Section 6.3.1, agrees with the experimental results, showing that a glancing incidence angle causes a low intensity interaction on the inner walls that accelerates a large number of cooler electrons into the target. The x-ray flux emitted reinforces this idea, with a significant flux improvement from the capillary targets compared with other target geometries. The measured effective temperature of the x-rays, however, is comparable despite the capillary targets having a lower effective laser intensity, indicating that the electron acceleration is exceeding the standard Beg and Wilkes scaling law. This increase could be occurring due to either an increase of intensity within the capillary or the re-acceleration mechanisms, demonstrated in References [25, 271], are driving a more energetic spectra than the simple geometry model of Section 6.3.1 would predict.

To investigate this, 2D and 3D PIC simulations were conducted using EPOCH [31]. In each simulation, information about the E- and B- fields, the particle momenta, and particle position were output every half laser cycle (1.6 fs). The pulse duration was set to 250 fs FWHM with a Gaussian profile, and the spatial

profile of the beam was a super-Gaussian with a nominal width of $3\ \mu\text{m}$ and angled onto the inner edge of the capillary. While this is not a complete comparison to experimental conditions it captures several significant aspects; the pulse duration is long enough that interactions on each wall can happen at the same time, and the central radius of the spot is smaller than the capillary width and so regions exist outside of the direct influence of the laser. When comparing these results to the experimental measurements, the significant increase in pulse duration will be considered. The spatial resolution of the simulation was $10\ \text{nm}$ in x and $100\ \text{nm}$ in y , for a box size of $100\ \mu\text{m}$ by $12\ \mu\text{m}$. The density of the inner capillary wall was set to $10n_c$ and had 30 macro-particles per cell. The peak laser intensity is was set to $1 \times 10^{19}\ \text{W}/\text{cm}^2$. Electrons above $1\ \text{MeV}$ are tracked throughout the simulations since results shown in Chapter 3 highlight how the electrons primarily responsible for $50\text{-}100\ \text{keV}$ x-rays are typically more energetic than $1\ \text{MeV}$.

6.4.1 Effect of glancing angle interactions with the capillary walls

The interaction with the inner wall should result in a similar effect to that discussed in Section 6.3.3, with electrons trapped in surface fields and directed more readily along the capillary. The magnetic fields generated as a result of the electron acceleration should be equal to a significant fraction of the laser field [269]. To explore the effect of glancing angle within the capillary, simulations with an incidence angle of 30° , 15° , and 5° were conducted. A scale length is included on the inner surface of the capillary, to ensure similar conditions to the experiment it is set such that $L_s \geq \lambda_L$. Scale lengths of this magnitude have been consistently measured using similar laser systems [52, 102]. It is reasonable to suggest a similar scale length would form within the capillary,

an investigation into the effect of the scale length is shown in Section 6.5. The variable parameters for this simulation set are shown in Table 6.1.

Outer diameter	12 μm
Inner diameter	8 μm
Length	96 μm
Scale length	2 μm
Angle of incidence	0-30°

Table 6.1: EPOCH simulation parameters. Capillary starts at 4 μm to prevent the laser clipping as it enters the simulation.

Simulations above and below the critical angle, outlined by Nakamura *et al.* to be $\theta_c \approx 20^\circ$ [269], were conducted to investigate any enhancement in the accelerated electron spectra. The geometric model predicts more electrons as $\theta_L \rightarrow 0$ and studies into the glancing angle interaction predict a more energetic spectra. Figure 6.17 demonstrates both of these features. The time step, for each simulation, was chosen as the one with the highest number of accelerated electrons, this occurred at later times for the glancing angle simulations owing to the increased path length required to approach the critical surface of the target.

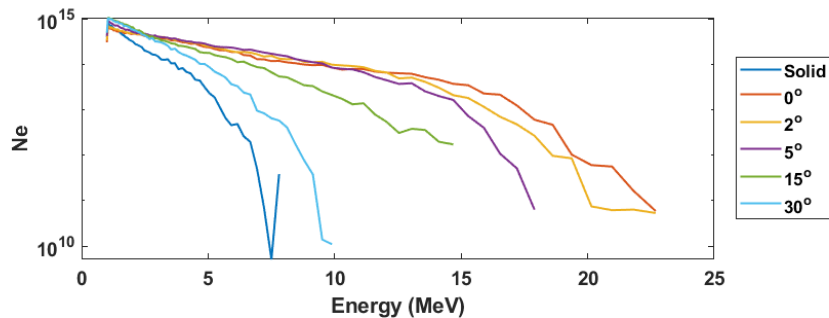


Figure 6.17: Electron spectra for each angle of incidence within the capillary. Spectrum was taken at the time step with the most accelerated electrons for each simulation.

As with the results by Nakamura *et al.* [269], the onset of the enhancement is between the 30° and 15° simulation where a clear change in the peak spectra is shown. The 30° simulation resembles a single acceleration point with a sharp increase in electron number initially that decays over time, by contrast the near 0° simulations demonstrate continuous increase in both number and temperature until the laser begins to leave the box, $t \approx 750$ fs. The temporal evolution of the spectra demonstrates that the laser-solid interaction initially accelerates more electrons than the capillary, as shown in Figure 6.18(a). However, as the pulse continues to propagate, the electrons within the capillary become more energetic and more populous than those in the solid target as the direct laser acceleration, discussed in Section 6.3.3, begins to take effect. Towards the end of the simulation, shown in Figure 6.18(c), the capillary still has a hotter electron spectra and a significantly higher population of electrons within the solid layers. The mechanism behind these electrons is explored more in Section 6.5.

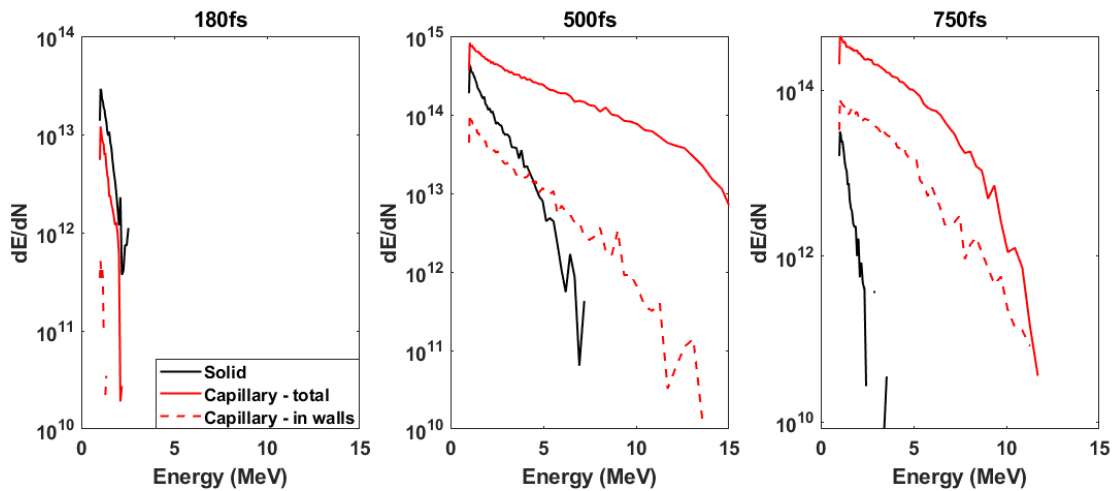


Figure 6.18: Spectra of electrons in the wall (red dashed) and in the capillary (red solid) at separate times throughout the 5° simulation. Compared to a solid wire (black) under the same laser conditions, the capillary quickly exceeds the total number and temperature. The temperature of the electrons within the capillary and within the walls is $k_B T_h = (3.5 \pm 0.3)$ MeV, compared to the solid target of $k_B T_h = (0.9 \pm 0.1)$ MeV at $t = 500$ fs.

Solid wire targets with similar dimensions promote the same directionality in the electron beam, with fields established at the outer diameter of the wire acting to limit the expansion of the electron beam [231]. However, in comparison to the capillary targets, they have a single high intensity interaction with the laser, promoting a single period of absorption from laser energy into hot electrons. The intensity from a single interaction at 5° from target normal with a solid target is two orders of magnitude higher than the glancing angle wall interaction in the capillary, and so one would expect a hotter temperature. Since there is no subsequent injections of electrons, the population should quickly diminish through the target. These simulations were conducted without collisions and so there would be an additional decay of hot electron population that scales as $e^{-(\rho l \sigma)}$ (density, ρ , length, l , and cross section for electron energy σ). This is also true for the capillary structure; however, as with the model in Section 6.3.1, due to the number of subsequent injections along the length of the capillary, n_s , the electron attenuation should scale as $e^{-(\rho(l-n_s \delta l) \sigma)}$ for each accelerated population.

6.4.2 Effect of laser polarisation on spatial electron profile

Figure 6.9 demonstrates a two source structure in the penumbral measurements only in the horizontal axis. This is evidence that the electron population predominantly travels along the length of the capillary, and that there must be additional interactions with the laser to accelerate electrons on either edge. If the latter was untrue, or the electrons readily circulate the channel, there would be a near continuous source at the end of the capillary. The lack of a two-walled structure in the vertical direction, therefore, implies that the electrons do not readily circulate the capillary walls azimuthally and evenly create x-rays - otherwise the vertical penumbral should also display a secondary feature. Therefore the evidence of a second wall must be the result of subse-

quent interactions within the capillary. While this cannot be directly confirmed from the time-integrated experimental data, simulations in 3D can explore the transport of electrons in and around the capillary. The 3D simulations were conducted with similar parameters as the 2D simulations but with the spatial resolution limited to 200 nm ($x = 0, 100 \mu\text{m}$, $y, z = -10, 10 \mu\text{m}$) to accommodate the extra dimension. The laser was set to focus at $5 \mu\text{m}$ into the capillary as an F3 beam, to match with the experimental parameters and see if there was significant electron circulation around the capillary.

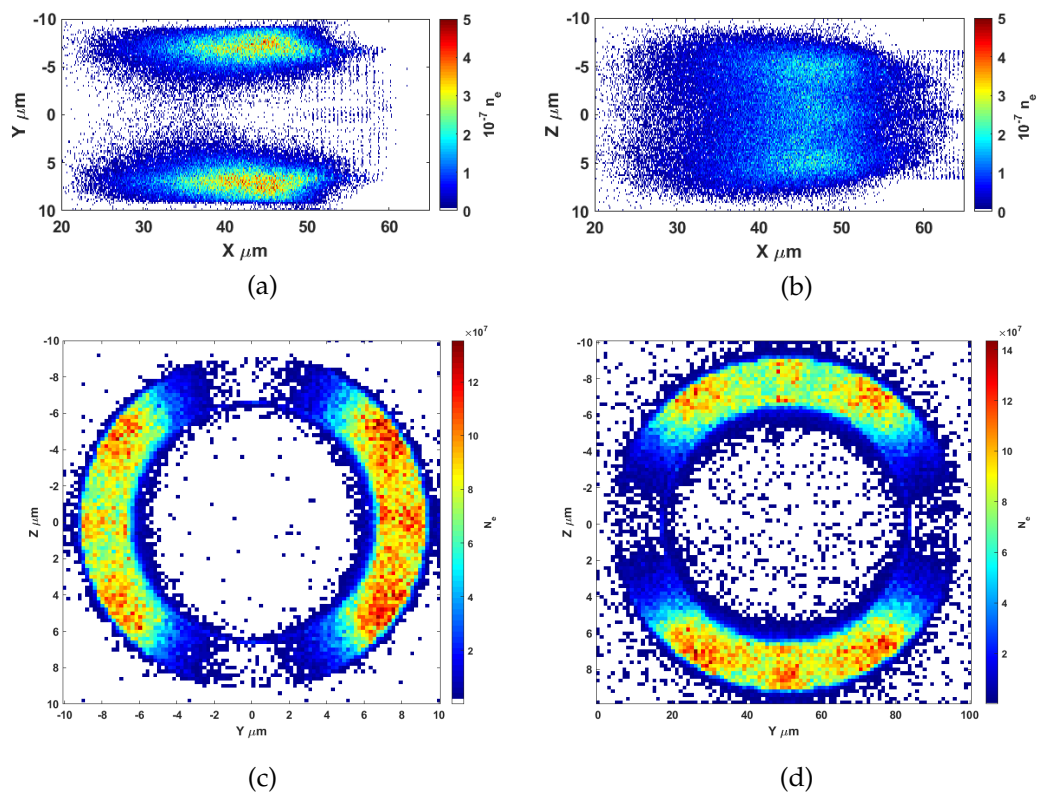


Figure 6.19: Hot electron density in 3D. (a) View from above demonstrating two lobes of electrons on either wall corresponding to the P-pol acceleration. (b) Side view of the target. (c) A cut through of the capillary showing the electron lobes emerging only in the horizontal axis for P-Pol and (d) the vertical axis of S-Pol. Each plot is taken at $t = 250$ fs.

The beam primarily deposits electrons within the horizontal axis of the cap-

illary. The electron density appears washed out from the side view, which agrees with the measurements made by the penumbral in Figure 6.9. The electron density shown in Figure 6.19(c) is integrated and shown in Figure 6.20 for a horizontal and vertical measurement; there is an increase in the width of each wall measurement due to the slight spreading of the electrons. The vertical measurement by comparison looks like a single source.

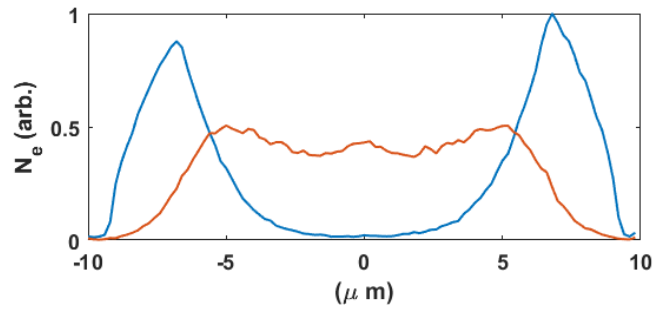


Figure 6.20: Integrated electron density in the horizontal (blue) and vertical (orange) direction from the 3D simulation in Figure 6.19(c).

6.4.3 Summary of simulations

The series of simulations reported here demonstrate critical aspects measured during the experiment. In the 3D simulations there is a clear increase in electron density along the angle of polarisation for the laser, the integrated electron density in Figure 6.20 demonstrates a similar spatial profile of electrons as measured by x-rays emission in Figure 6.9. The comparison between the capillary and solid targets show a significant increase in both number and temperature of the electron distribution, similar again to the measured flux and temperature increases seen from the x-ray diagnostics in Figure 6.7. Exploring the mechanism responsible for this increase requires additional detail, the following section reports on analysis that tracks macro-particles throughout the simulation.

6.5 Successive Acceleration

At the intensities within this study ($\sim 10^{19}$ W/cm², $a_0 \approx 2.7$), where $\mathbf{j} \times \mathbf{B}$ and the ponderomotive force dominate the acceleration mechanism, the maximum gain of a previously at rest electron from the laser field can be calculated. As outlined in Chapter 2, the maximum energy, E_p , of an electron moving within a laser field is:

$$E_p = E_0 \frac{a_0^2}{2} \quad (6.5)$$

where $E_0 \approx 0.511$ MeV is the rest mass of an electron. In the case of these simulations, $E_p \approx 1.7$ MeV which is significantly lower than the peak energies seen in both the solid target and the capillary (Figure 6.18).

This phenomena was explored by Sorokovikova *et al.* [277] for solid targets, demonstrating that, during the laser pulse, an electro-static field emerges in the pre-plasma as electrons are ejected by the ponderomotive force. Electrons accelerated later in the pulse then cross this potential well, gain energy, and therefore can exceed $E = E_p$. This effect, however, is dwarfed in comparison to the highly energetic tail seen in the capillary simulations (Figure 6.18). Electrons in these simulations were accelerated to energies significantly above this limit via *super*-ponderomotive, or direct laser, acceleration [11, 88, 278, 279]. By maintaining phase between the electron and the laser, the electron is pushed forward by the laser potential to energies greater than the typical oscillatory motion. This was succinctly expressed by Robinson *et al.* as $R = \gamma_e - p_x/m_e c^2$: when $R < 1$ the electron is travelling with the laser potential and as a result is accelerated beyond E_p . The walls of the capillary targets act to instil the *quasi*-static fields necessary to drive the *super*-ponderomotive acceleration. Particles well above E_p emerge following a series of successive interactions, instead of

a solitary moment of acceleration shown by Robinson *et al.* [88]. As the electrons fall into phase with the laser at the capillary edge where the quasi-static E_y field has emerged, they are reflected back across the path of the laser and thus accelerated. A schematic of this mechanism is shown in Figure 6.21.

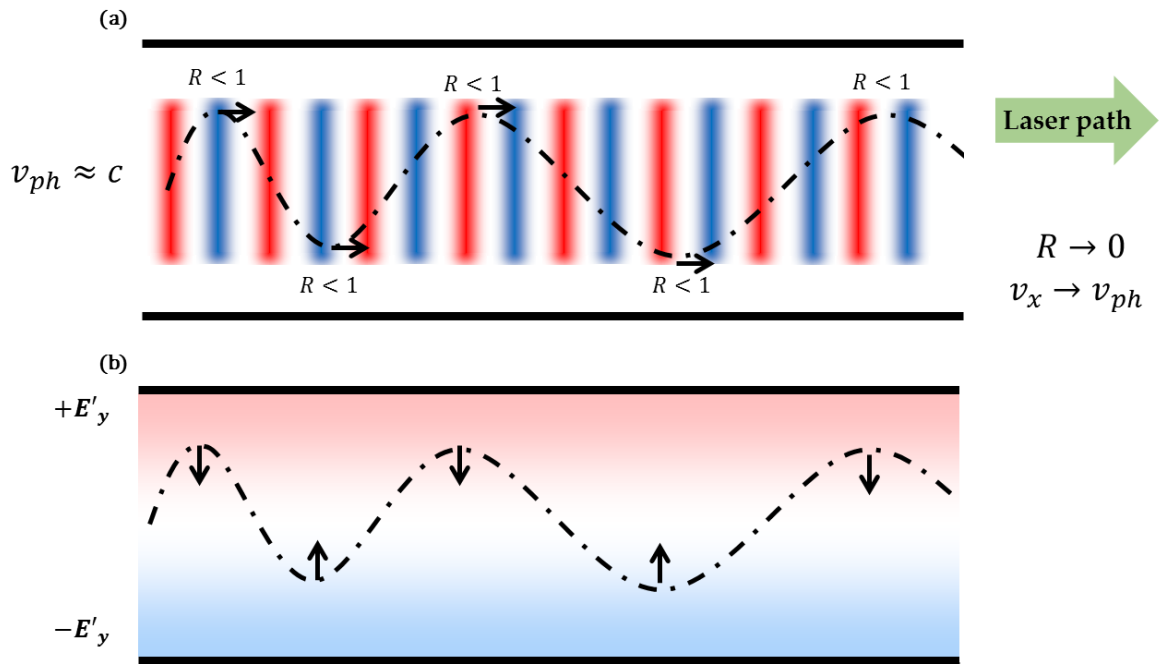


Figure 6.21: Schematic of direct laser acceleration within a channel, the electron path is shown as a black dashed line in each panel. (a) The laser E_y field travelling through the channel at v_{ph} the electron is trapped within the influence of the laser by the quasi-static E'_y field in (b). At each turning point the electron falls in phase with the laser field ($R < 1$) and the electron is accelerated forward.

The plasma density within the channel is important to consider, since it could induce self-focusing in the beam, and therefore be an explanation for the more energetic electrons. However, the maximum intensity of the laser, shown in Figure 6.22, peaks at $\sim 1 \times 10^{19}$ W/cm² as it travels through the plasma and is therefore not the cause of these energetic electrons.

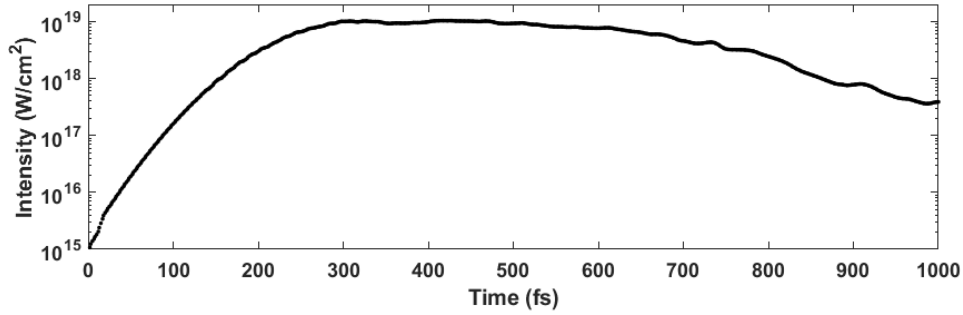


Figure 6.22: Peak intensity from the simulation within the capillary target during the simulation. No evidence of significant self-focusing of the laser.

The scale length within will effect the degree of self-focusing that the laser pulse experiences, and alter the formation of the quasi-static fields within the capillary. Higher plasma density within the capillary impedes the laser propagation and disrupts the growth of the *quasistatic* fields along the capillary as a result. A comparison of the E_y field is demonstrated in Figure 6.23 for simulations with a scale length of $5\ \mu\text{m}$ (i.e. larger than the capillary radius), and $2\ \mu\text{m}$ (used for the majority of the simulations) compared to an ideal case of an under-dense uniform plasma set at $0.05n_c$. The higher density electron background in the channel promotes significant non-linearity to emerge in the *quasi*-static fields, Figure 6.23(a-b). The uniformity of the fields in Figure 6.23(c) causes many more electrons to oscillate through the laser channel resulting in a significantly more energetic electron spectra.

Tracking individual macro-particles reveals that a population of electrons oscillate laterally throughout the capillary, causing them to re-interact with the laser and be accelerated to energies significantly above the ponderomotive limit (Eq. 6.5). Figure 6.24 is a trace of one of these particles from the under-dense uniform plasma simulation showing the successive acceleration points as the electron propagates through the capillary. The E_x and E_y fields are averaged over 10 laser cycles to highlight the *quasi*-static fields that emerge during

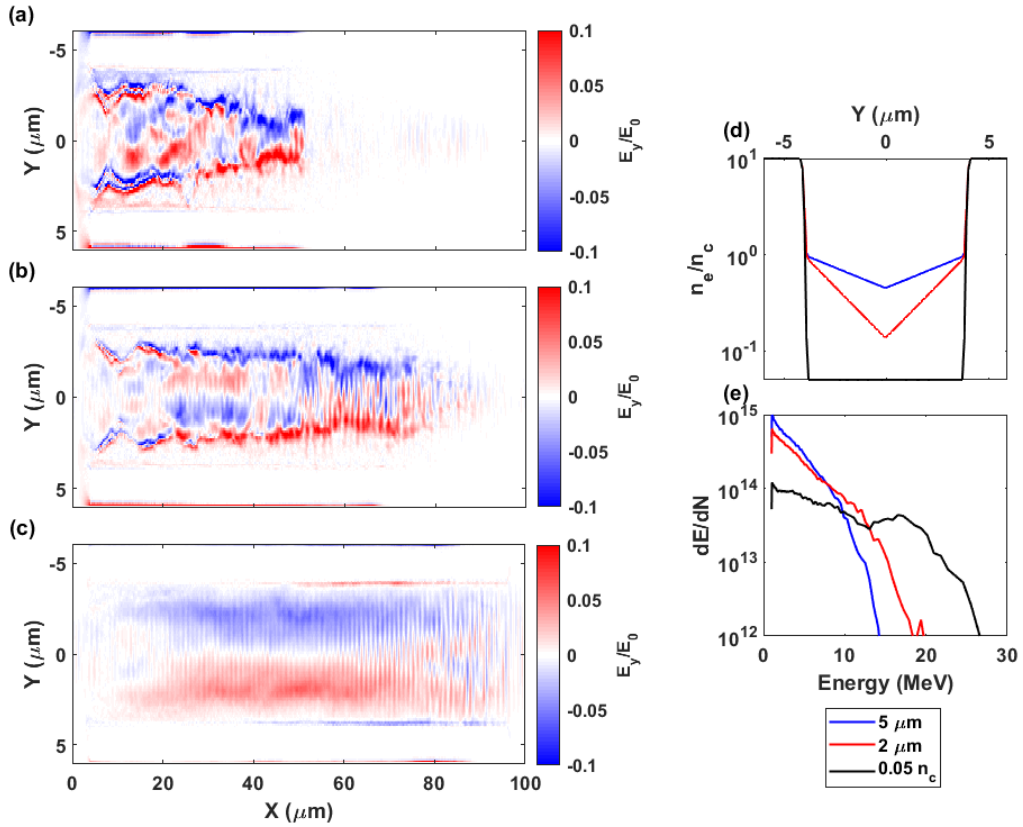


Figure 6.23: Variation of scale length simulation results. E_y field averaged over 10 laser cycles for (a) 5 μm and (b) 2 μm scale lengths, and (c) 0.05 n_c pre-filled capillary with 0° incident angle. Electron acceleration with varying scale length. (d) The density profile at the beginning of the simulation. (e) Accelerated spectra for the three conditions simulated.

the pulse. Each time it reaches the edge of the capillary, the E_y fields drive it back towards the centre of the channel. Crossing the channel causes the electron to dephase and loses some energy. Tracking these particles throughout the simulation demonstrates this oscillatory motion; the trace of one particle is shown in Figure 6.24. As the particle crosses the channel, its relative phase R drops below 1 and the electron experiences a greater acceleration from the laser. The electron then falls out of this mode at each wall as it is turned around by the fields.

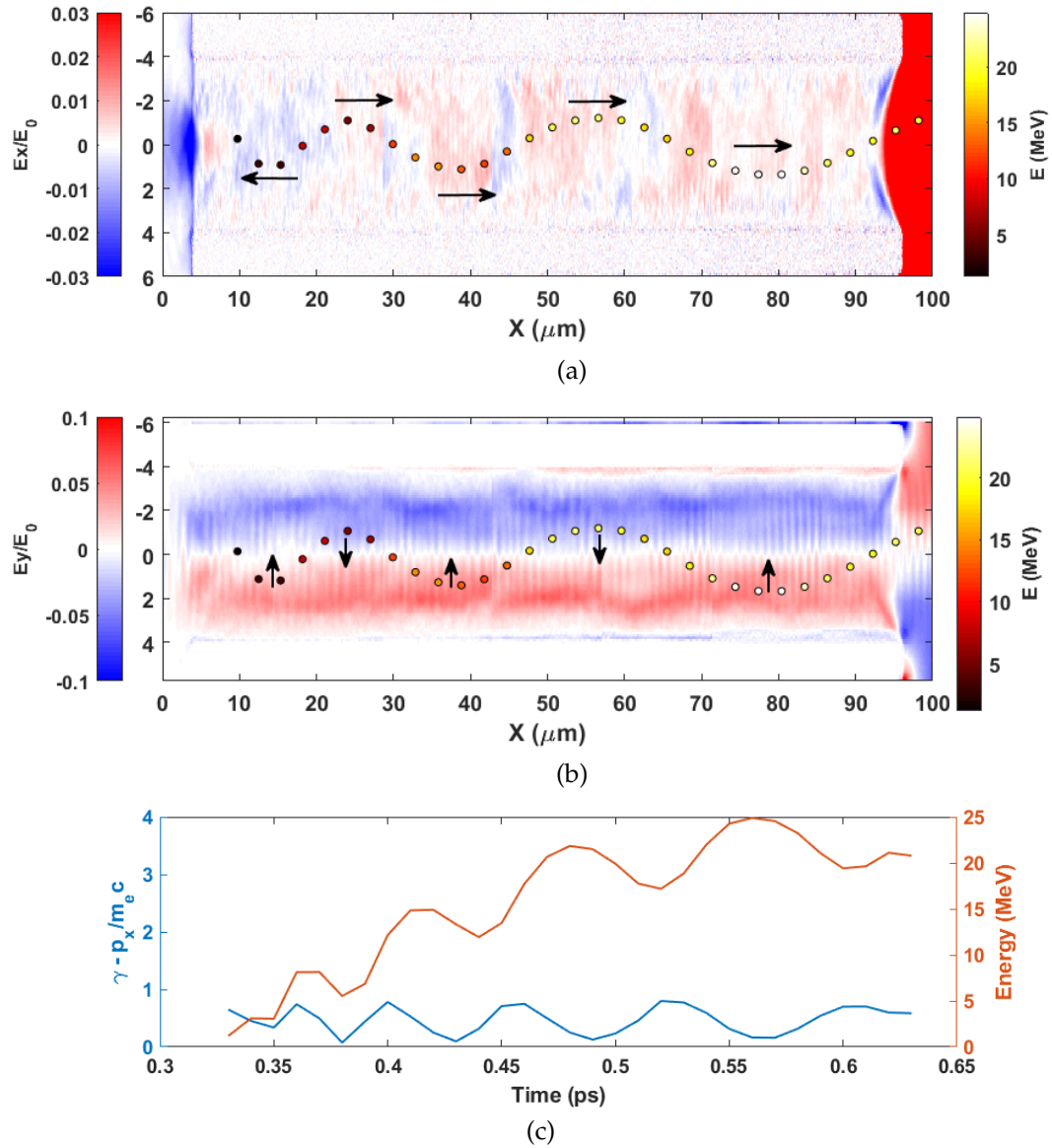


Figure 6.24: Electron trace throughout the simulation. (a) The longitudinal electric field (E_x) profile (red-blue colour scale) acts to continuously accelerate the electron (scatter plot) forward; the energy is shown by a secondary colour-bar. (b) Similar trace to (a) but for the transverse field (E_y) structure, arrows in each indicate the direction of force for the quasi-static fields reinjecting electrons back into the channel. (c) The macro-particle energy and R value as it transports through the target. During each crossing of the channel the electron drops further below $R = 1$ and is subsequently accelerated. The field in (a) and (b) is normalised to the laser electric field $E_0 = \sqrt{\frac{2I_L}{cn\epsilon_0}}$.

The traces in Figure 6.24(c) show that the electron does not experience continuous acceleration, but rather periodic - similar to results by Chen *et al.* [271]. These periodic points of acceleration occur throughout the capillary and therefore, by extending the capillary, there should be continued acceleration. Unlike Kluge *et al.* [25], the laser in this simulation was smaller than the capillary diameter, meaning the electron leaves the spot profile. The transverse fields return the electrons back to the influence of the laser field and promote successive acceleration. In principle, this should scale with capillary length (as shown by Kluge *et al.* [25] and Figure 6.16) and, as a simple demonstration, simulations of 50 and 200 μm capillaries were conducted with the same laser parameters. The spectra from each capillary length are shown in Figure 6.25: as expected, there is a continued increase in peak electron energy. The spectra is also significantly hotter than one might expect for the effective on-target laser intensities. The maximum energy increases slower than demonstrated by Kluge *et al.* however the trend is still approximately linearly with capillary length.

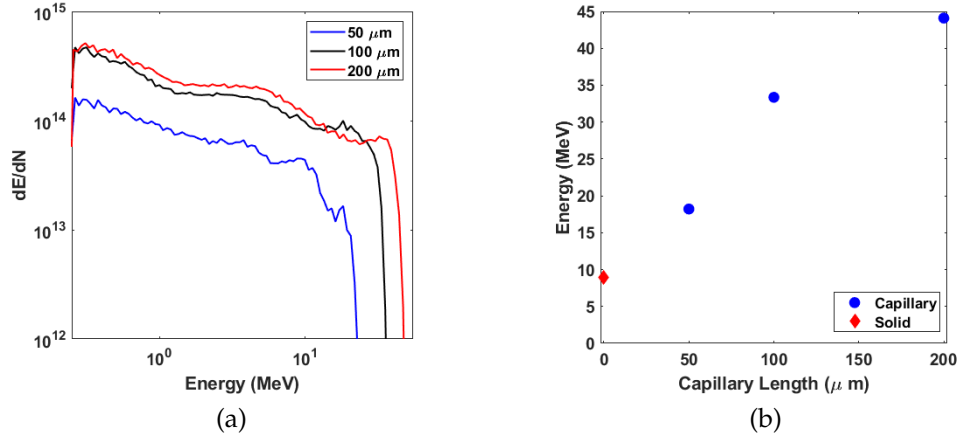


Figure 6.25: Electron energy distribution as a function of capillary length. (a) Electron spectra for 50 (blue), 100 (black), and 200 (μm) capillaries. (b) Maximum energy as a function of capillary length, demonstrating an almost linear scaling.

6.6 Conclusion

In this chapter, a novel target design is proposed and initial measurements made using a prototype design have been presented and discussed. The capillary shape establishes field structures that re-inject electrons back into the path of the laser, prompting successive re-acceleration of the electrons. This energetic source of electrons diffuses into a gold cladding layer and generates a bright source of x-rays. Additional study is required to optimise the electron transport through the surface layers and to explore the *super*-ponderomotive acceleration experienced in the sub-critical plasma channel that forms in the centre of the target. Experimental evidence and 3D PIC simulations demonstrate that the electrons do not readily circulate the capillary and are instead deposited primarily at the capillary walls.

Chapter 7

Optimising x-ray source characteristics for large scale radiography

Due to the range of size, density, and resolution demands associated with industrial x-ray radiography, there is not a source that is "one-size fits all". Compromises and optimisations have to be made depending on the object of study. For example, the x-ray source required to image a small biological sample is significantly different in both spectral and spatial demands to that for an aircraft weld. Both of these examples, however, are readily achieved with laser driven systems [10, 65, 76]. Altering the source characteristics to deliver what is needed requires continued study. In this chapter, the emission from spatially constrained targets is presented from both an experimental and modelling perspective to explore alternatives to conventional foil targets. The optimum parameters (flux and effective temperature) of an x-ray spectra for radiography samples is then explored via theoretical models and numerical simulations.

7.1 X-ray Radiography with laser driven sources

High intensity laser pulses rapidly ionise and accelerate electrons in laser-solid interactions, driving a multi-megaAmpere current of relativistic electrons into the target [1, 18, 130]. This electron current produces a bright source of bremsstrahlung radiation as it propagates, which has long been used as a source for radiography [10, 35–39] and diagnosis of the internal electron current [17, 32–34]. In contrast to conventional sources of x-ray radiation, laser-driven sources are able to deliver a broad (keV - tens of MeV) range of energies in a duration on the order of the laser pulse (\sim ps) from a small ($< 100 \mu\text{m}$) source [188]. High energy laser pulses ($> 100 \text{ J}$) offer the potential of single shot acquisition through larger industrial samples when combined with thick ($> 10 \mu\text{m}$) high-Z targets due to the high flux of energetic x-rays produced during the interaction. With the advent of high repetition rate high power lasers, commercial interest in using laser driven sources has grown [76, 84].

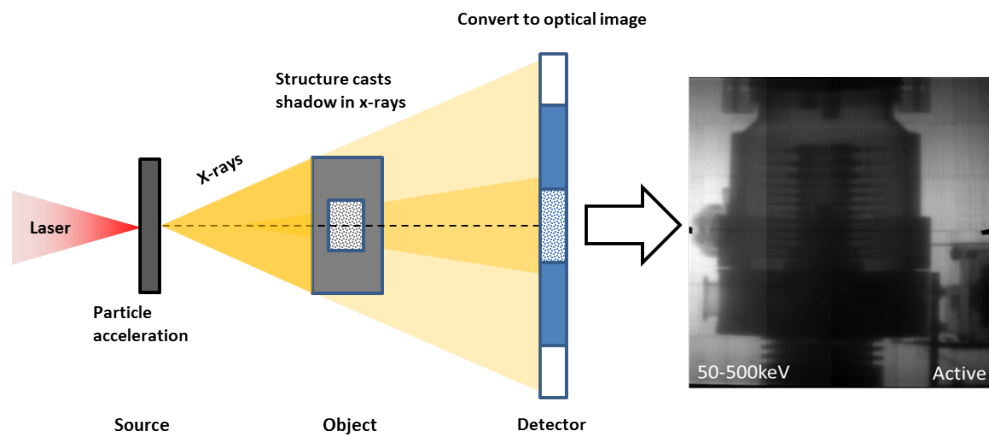


Figure 7.1: Schematic for x-ray absorption radiography of a sample with internal structure. X-rays illuminate the target, and as they are highly penetrative, variations in the density can be probed. Radiography from Brenner *et al.* [10].

X-ray absorption radiography is a simple process; x-rays are generated from a source, propagate through a sample with structure, and then are spatially resolved to determine any difference in the transmission of x-rays, which is dependent on the absorption of both the detector and the sample. The complexity lies in efficiently and effectively delivering a source that is able to probe the structure of a specific test sample. A high density object requires sufficiently high energy photons to ensure transmission. Observing slight changes in areal density across the object require high flux emission and a high dynamic range detector to ensure the contrast between each region can be detected. Small features require a smaller source and high spatial resolution on the detector. Samples in motion or those undergoing dynamic changes require a temporally short source. The field of x-ray radiography has long existed without using laser-plasma interactions as the source of the x-rays [280], most notably in the form of medical x-rays [281–283]. “Conventional” sources are typically table-top x-ray tubes - cathode tubes with a converter at the end to generate x-rays - or large scale linear accelerators and synchotrons [284–286]. Whilst these sources are effective and absolute calibration can yield clear radiographs through a range of samples, they are limited in flexibility and capability. A significant drawback of conventional sources is that more penetrative sources (high energy x-rays) typically have larger sources, limiting the ability to produce high resolution images of large, dense, samples. Using laser-plasma accelerators as the driver for the x-ray source is an established practice within the field and an emerging technology for industrial uses [10].

7.2 Spatially Constrained Targets

Chapter 5 demonstrated that defocusing the laser onto the target surface reduced the x-ray emission from the substrate of the target and increased the spatial quality of radiographs. In this chapter increasing the flux of x-ray sources

is investigated by using a wire target geometry, a comparison between 25-100 μm wires and 25-600 μm thick foil is shown. In thick targets, electrons are more likely to collide with the target material and emit bremsstrahlung prior to interacting with the sheath on the rear surface. When interacting with the sheath they typically lose energy [17, 166, 167] and subsequently recirculate through the target [160, 221, 234, 287]. However, upon circulation the source size typically increases, as the electrons continue to travel laterally through the target, and a large substrate source degrades the resolution of the image, as discussed in Chapter 5. These recirculating electrons still have significant energy enough to readily generate x-rays as they continue to circulate the target. Switching to a wire target geometry will, as a minimum, remove the flux produced from the substrate, in the transverse direction, as there is no material from which to generate x-rays.

Prior work has demonstrated that the spectral emission can be altered by varying laser and target conditions [34, 288, 289]. Courtois *et al.* demonstrated the effect that a large preplasma can have on the directionality and profile of an x-ray source [77]. They demonstrated that a large scale-length increases the absorption into hot electrons and therefore drives a greater production of high energy x-rays for the same target - applying a longer scale length via a controlled laser intensity contrast would, therefore, be one technique to change x-ray emission to optimise imaging of an object. Modifying the target shape provides a simple mechanism to restrict and confine the spatial source size. Using laser-driven x-ray sources as a backlighter in inertial confinement fusion has also been an area of study, where experimental investigations have demonstrated a *quasi*-monochromatic source with the side profile of the target as the source [79, 80]. Whilst this technique has achieved a source size of $(5.5 \pm 1.0) \mu\text{m}$, the flux of x-rays emitted from the target edge is significantly lower than on laser axis and target normal [290]. As demonstrated in

the previous sections, flux is typically a deciding factor in resolving features on a radiograph and so maximising the efficiency of the entire system is essential. Bremsstrahlung sources of $(30 \pm 10) \mu\text{m}$ have been demonstrated during laser-wakefield experiments using a bremsstrahlung converter positioned after the laser-gas interaction [220]. However, laser-solid interactions convert a significantly higher proportion of laser energy to hot electrons with a larger emitted beam divergence [19, 65], which is advantageous to industrial scale imaging requirements. Results from an experimental campaign using constrained targets to reduce the x-ray emission area are presented in the remainder of this chapter. Experimental results are supported by PIC and Monte Carlo simulations to demonstrate the underlying physics that occurs due to the wire target geometry.

7.2.1 Experimental Campaign

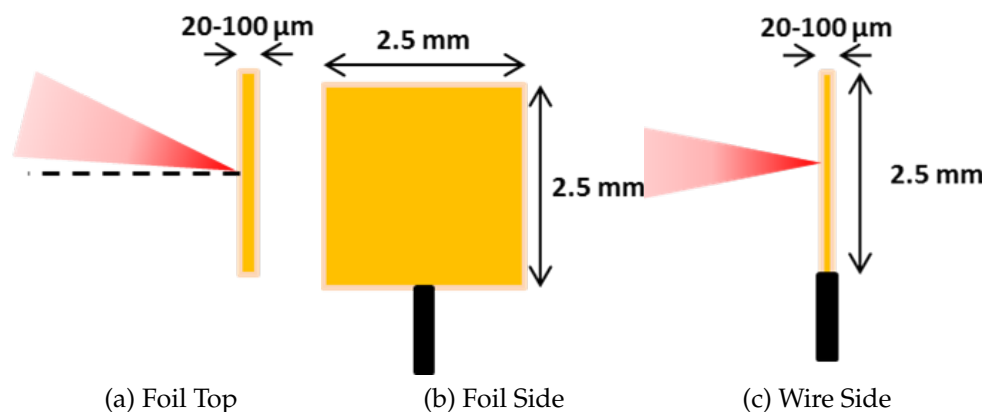


Figure 7.2: Targets used in the Experimental campaign, (a-b) foil targets, (a) top view with laser incidence highlighted (b) front view, (c) side view of wire target.

The experiment was conducted using the Vulcan laser [2]. The target variations are shown in Figure 7.2, foil and wire targets were irradiated independently with laser pulse parameters maintained for each target type. The laser

energy was ~ 200 J on-target and the pulse duration was ~ 14 ps. The incident angle for foil targets was fixed at 5° relative to the target normal. The focal spot was characterised prior to the experimental run using a low-power CW laser. The results of that analysis are in Figure 7.3, demonstrating a full-width-half-maximum of (6.4 ± 0.7) μm with 37% of the energy contained within the spot. This provided an on target intensity of 10^{19} W/cm² and, therefore, expected electron temperatures of $\sim 0.5 - 1$ MeV [18, 121].

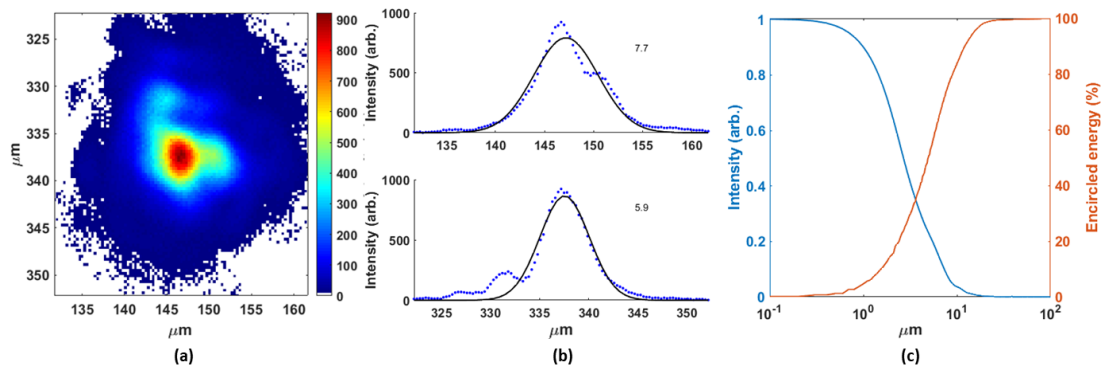


Figure 7.3: Focal spot measurements for the experimental campaign. (a) Focal spot image, an average of five 1 ms exposures, (b) horizontal and vertical line-outs of the spot with associated FWHM, (c) the encircled energy as a function of spot radius - within the FWHM $\sim 37\%$ of the energy was contained.

The experimental layout, Figure 7.4, provided sufficient magnification for the main imaging line. Primary diagnostics for the spatial and spectral measurements are penumbral foils and scintillator rails respectively. Imaging was conducted on a large (100×100 mm) sheet of IP with the penumbral foils removed. A 0.6 T magnet was positioned behind the target rear surface to ensure that charged particle emission did not contribute to the measured signal.

The x-rays were detected using layers of Fujifilm SR image plate (IP) for the improved spatial resolution over scintillators. Filtering from the 2 mm aluminium chamber port and the IP sensitivity provided peak absorption at ~ 35 keV. The peak absorption energy changes with both target material and

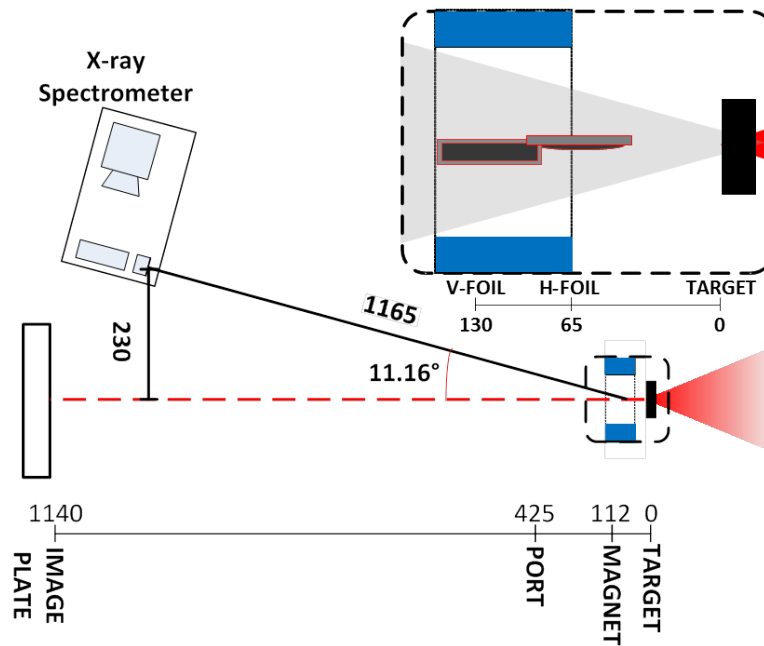


Figure 7.4: Schematic of the primary imaging diagnostics, setup is the same as the one in Chapter 6. Main image shows the emission line, with penumbral foils and X-ray spectrometers included. The inset is an expansion of the penumbral foil setup, the grey cone represents the forward x-ray emission from target. Magnets, blue in the figure, are required to remove the escaping electron population from the target. All distances in mm measured from target position. The chamber port attenuates the emitted x-ray spectra.

thickness - partially due to the K-alpha emission for gold being above 35 keV. Modelling of how this maximum energy changes with target thickness is shown in Figure 7.5, using the same technique as outlined in Chapter 6. For thicknesses below $\sim 20 \mu\text{m}$ the detector responds as expected with $\sim 35 \text{ keV}$ as the critical energy, however for targets thicker than this, the critical energy rises to the K-alpha of that material. The spectral shape of the emission is assumed to be a Boltzmann distribution with an effective temperature of 200 keV and the transmission through the target is calculated by half the target thickness. Half the target thickness is used as the expected electron temperature since the attenuation length¹ (or mean-free-path) of the 500 keV electrons in gold is

¹Material length at which attenuation reaches $1/e$, discussed in Chapter 4 and 5.

$\sim 160 \mu\text{m}$ [14]. This electron energy is, therefore, sufficient to generate x-rays quasi-uniformly throughout the target.

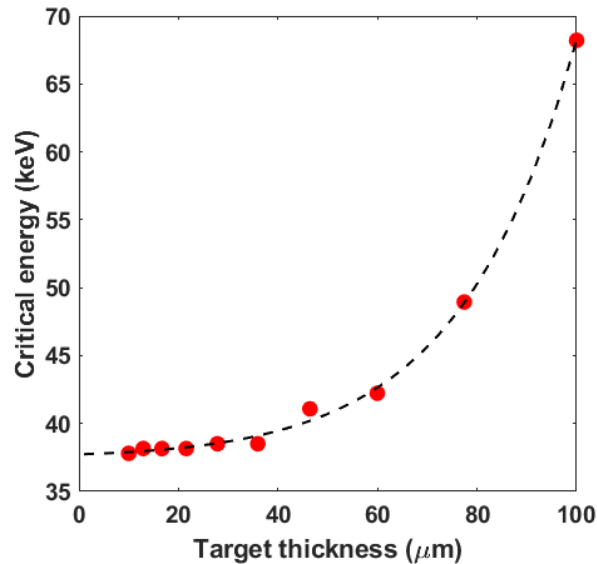


Figure 7.5: Critical detected energy as a function of target thickness for gold. Determined as the peak x-ray energy detected assuming a Boltzmann distribution of 200 keV and target attenuation from half the target thickness, using the NIST data tables [15].

7.2.1.1 Spatial x-ray emission profile

The x-ray source size was measured via a set of on-axis penumbral foils using the same technique outlined in Chapter 4. The penumbral foil set has $300 \mu\text{m}$ tungsten slabs curved to a radius of $(152 \pm 2) \text{ mm}$, one positioned to measure the vertical source (V-Foil) and one for the horizontal (H-Foil). The set-up, shown in Figure 7.4, provided a magnification of $\times 17.5$ for the horizontal axis and $\times 13.4$ for the vertical axis.

As demonstrated in Chapter 4 for a foil target the observed x-ray signal is a convolution of two sources; the first, a bright central source generated as

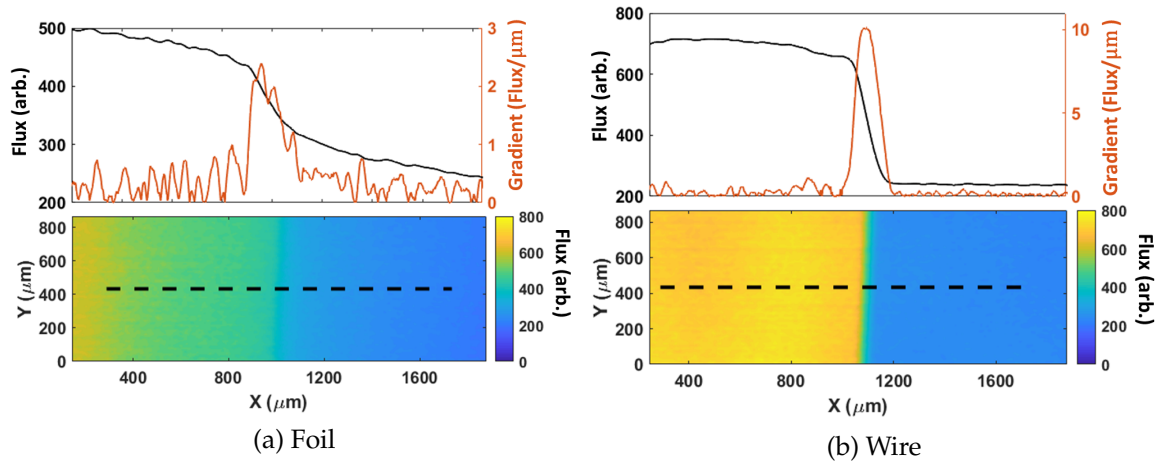


Figure 7.6: Penumbra radiograph and lineout for (a) foil, and (b) wire target. The dashed line in each radiograph is where the lineout is determined. In the top panels the lineout is in black and the gradient in orange.

the main electron channel propagates through the target, the second a diffuse source dominated by electrons recirculating through the target substrate after their first pass. The penumbra radiographs demonstrate the effect of switching from foil to wire targets, shown in Figure 7.6. The substrate feature from the foil introduces a large blurring function into radiographs by contributing similar levels of flux to the central source. When switching to a wire this substrate source is removed on the horizontal axis and all flux is contributed by the single source. As expected, the source is asymmetric for wire targets as electrons are free to expand vertically within the target. Figure 7.7(a) shows the horizontal axis measurement decreasing with reduced target thickness, but when measuring the vertical source contribution there is a flat response for targets that are less than $100\ \mu\text{m}$ thick. In the measured radiographs this presents as an asymmetric blurring function giving poorer resolution in the vertical axis than the horizontal. This effect is not present for foil targets as the horizontal and vertical sources are *quasi*-symmetric and instead both axes have similar blurring functions.

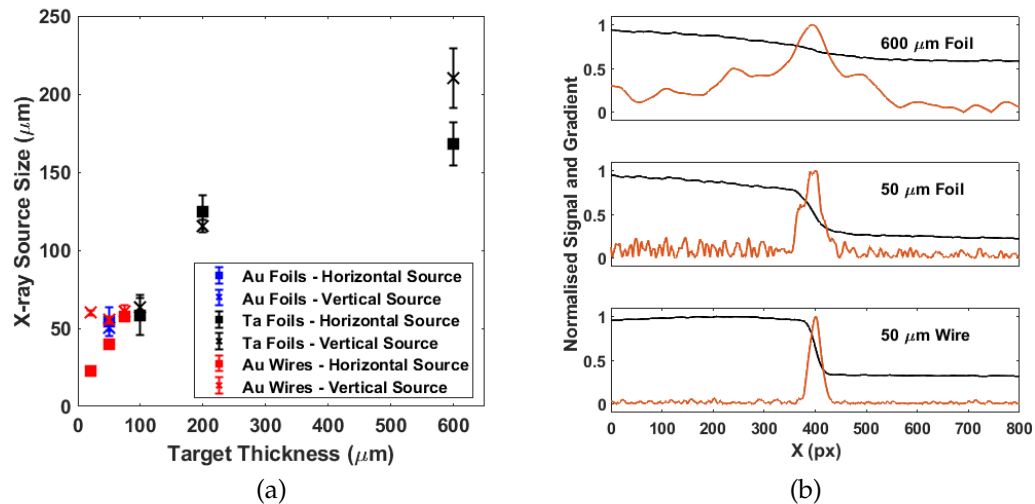


Figure 7.7: Spatial measurements taken from the penumbral foils. (a) Vertical and horizontal source from target types and materials measured by the penumbral foils, (b) are normalised lineouts (black) and gradients (orange) from a thick, thin, and a wire target.

7.2.1.2 Spectral x-ray characterisation

Using the imaging detectors and two off-axis scintillator-based hard x-ray spectrometers [26], the on-shot flux and effective temperature for each target configuration was measured. Figure 7.8 shows that the effective x-ray temperature for the wire and foil targets is similar, yet the flux contributed by wire targets is $\sim 50\%$ higher than foils of a similar thickness. Increasing flux and temperature with target thickness is expected, to a certain degree before self-attenuation dominates. Larger targets attenuate more of the soft x-ray emission and artificially harden the emitted spectrum. Also, the likelihood of electrons interacting with the background material - emitting bremsstrahlung - on their first pass through the target increases with target thickness. The temperature, Figure 7.8(b), is inferred via the technique discussed in the Chapter 4 and by Rusby *et al.* [26], by fitting to the response across the crystals in the spectrometer.

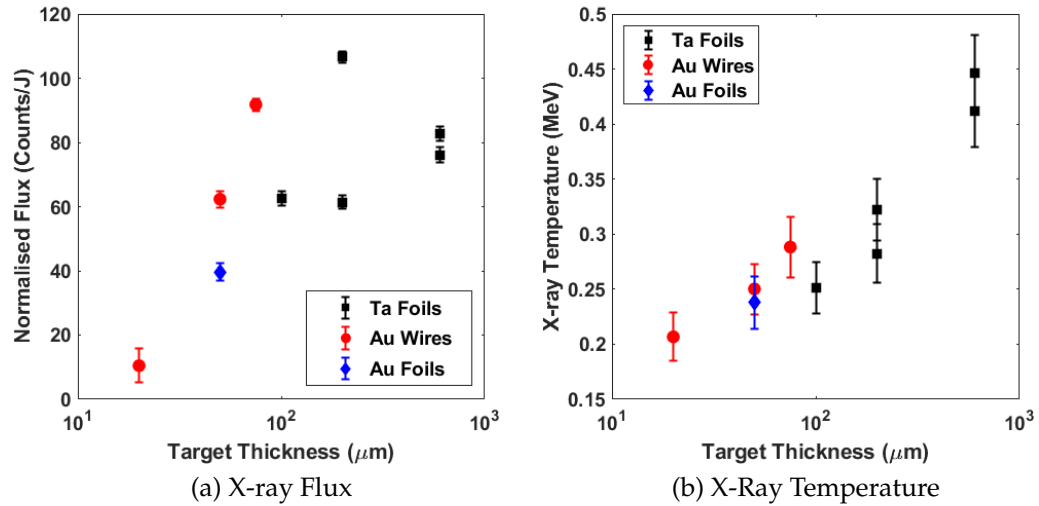


Figure 7.8: Spectral measurements taken from hard x-ray spectrometers 11° from target normal, single shot measurements made in parallel to source size measurements. (a) is the flux on the first crystal per incident laser Joule, (b) is the temperature of the x-ray emission inferred via the technique outlined in Rusby *et al.*[26].

To explain the increase in x-ray flux when the target geometry changes, the effect that the sheath is having on the internal electron population is considered. An electro-static field builds on target surfaces which is initially proportional to the number density of electrons that reach the surface. Therefore, if all else is equal, the relative strength is governed by the surface area over which electrons are spread. In foil targets, the total available surface area is $A_{foil} = 2(lh + lw + hw)$ where l, w, h is the target thickness, width, and height. In a wire this becomes $A_{wire} = 2\pi r(r + h)$ where r is the radius of the wire. In the case where $2r = l$ and $h > r$, it can be shown that for a foil target with $w > \frac{l(\pi-2)}{2}$ the surface area is larger than that of a wire - i.e the target is *at least* as wide as it is thick. The number density of electrons at the surface, and field strength, will therefore be lower for a foil than that of a wire. Electrons accelerated later in time are therefore more likely to recirculate in the wire, as the average field strength will be higher.

This explanation assumes that the conversion from laser to hot electrons remains similar despite the change in geometry. This assumption is valid when considering wires significant larger than the spot diameter but will become a factor as the wire size is reduced further. Considering the parameters explored in the experiment, the laser spot diameter was $(6.4 \pm 0.7) \mu\text{m}$, as shown in Figure 7.3, a wire of $25 \mu\text{m}$ diameter corresponds to a maximum displacement from a flat surface of $0.4 \mu\text{m}$ ¹. This deviation is negligible considering the surface roughness of targets is typically on a similar scale and therefore the accelerated electron population should be similar for similar laser parameters.

7.2.2 PIC Modelling

Particle-in-cell (PIC) simulations can be used to explore the effect that target geometry has on the hot electron transport. Due to the relatively long pulse duration used for the experiment it is not possible to directly simulate the experimental conditions, instead the focus of this section is to explore the role that the target geometry has. The simulations were conducted with EPOCH [31] in 2D, focusing a $5 \times 10^{19} \text{ W/cm}^2$ laser onto the front surface of a $25 \mu\text{m}$ thick target, to explore the effect that the target cross-section has on the sheath field. The pulse duration was 250 fs and the simulation conducted for 850 fs, the results shown in Figure 7.9(a-b) were taken at 500 fs where both the wire and foil target had their peak sheath field. The simulations compared, the effect of a standing wire and a foil to probe the difference in internal electron density, and therefore resultant x-ray emission as a result of the differing target cross-sections. Variation in the scale length has been shown to have a significant effect on the electron dynamics and resultant x-ray yield [101, 186], as such, in order to focus on the effect of the geometry, both simulations included a $2 \mu\text{m}$ plasma scale length on the front surface [52, 102]. The simulation pa-

¹Calculated from Pythagoras' theorem, valid for spot sizes smaller than the wire diameter.

parameters are listed in Table 7.1. The increased box size for the foil simulation compared to the wire is to maximise available lateral expansion for electrons in the target.

Intensity	$5 \times 10^{19} \text{ W/cm}^2$		
Scale Length	$2^a \mu\text{m}$		
Density	$77 N_c$		
Particles per cell	50		
X(min,max,dx)^b	-7 μm	43 (33) μm	10 nm
Y(min,max,dy)^b	-25 (-15) μm	25 (-15) μm	10 nm

Table 7.1: EPOCH simulation parameters. ^a limited to $X = +7 \mu\text{m}$ for the wire. ^b values in parenthesis indicate wire simulation.

There is a large increase in electron density within the wire target compared to the standard foil over the duration of the simulation. As expected, and shown in Figure 7.9(a-b), a stronger E-field is established at the surface of the wire target geometry compared to the foil. This change in field strength drives the internal electron density for each geometry, Figure 7.9(c). Absorption through the simulations were equal for both targets geometries. For the wire, as there is a higher potential field surrounding more of the target surface, more electrons are constrained within the target. As the electrons recirculate through the target their energy typically decreases and as a result the spectrum over the lifetime of the simulation varies for each geometry. In wire targets there is significantly more low energy electrons remaining within the target, whereas in the foil these same electrons would be able to escape laterally. This results in a cooler two-temperature distribution for the wire target, Figure 7.9(d).

The electron density results imply that there should be a brighter (more flux per area) source from the wire than for the foil, since the increased electron density, for targets of the same material, should produce a brighter source of

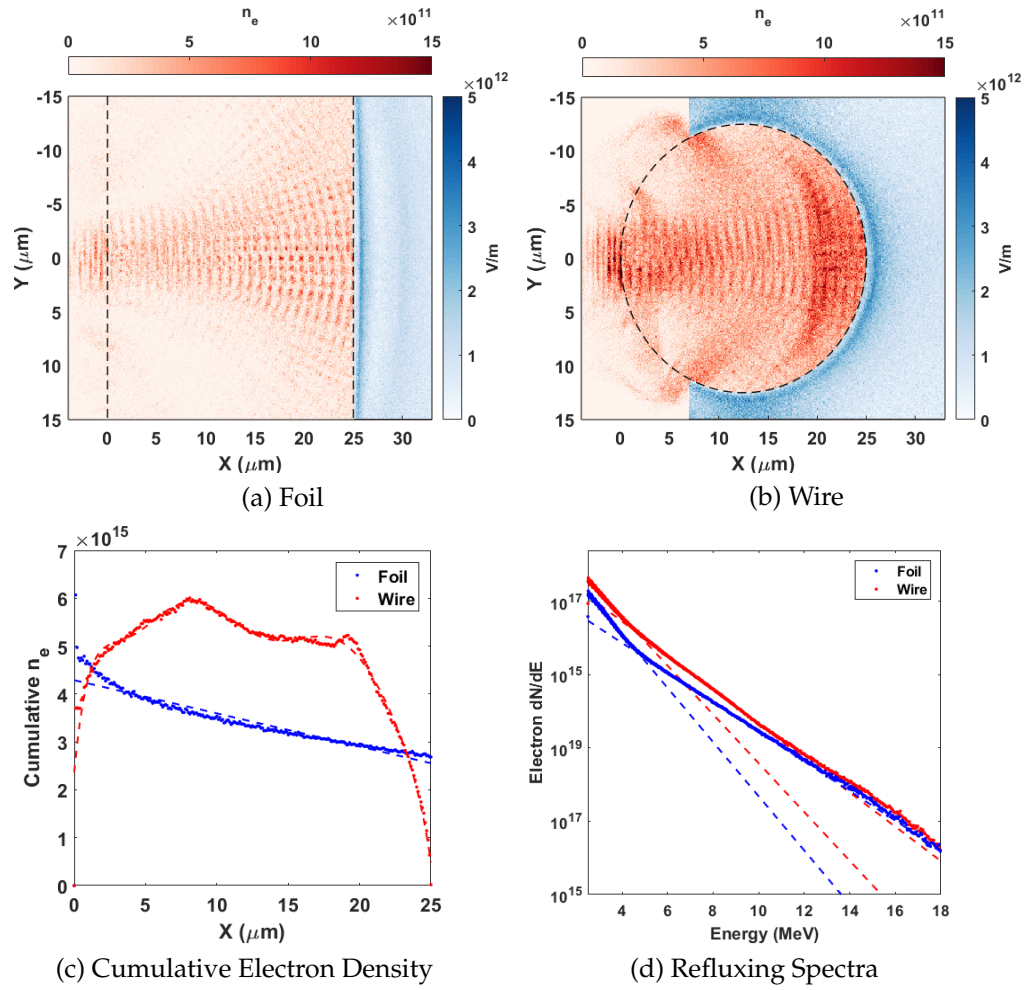


Figure 7.9: Results from PIC simulations. (a) Electron density (red scale) and E -field (blue scale) spatial maps for the foil simulation at 500 fs. (b) same as (a) but for wire simulation, E -field is limited to $X > 7 \mu\text{m}$ to show the pre-plasma on the surface of the wire. (c) Cumulative on-axis electron density over the entire simulation. $0 \mu\text{m}$ indicates front surface for each target, (d) Refluxing electron spectra with a two-temperature distribution (dashed lines), see Table 7.2 for values.

x-rays. Demonstrating that the total *flux* is higher however is less clear. To do so the individual electron pathlengths can be tracked to demonstrate the increased circulation that the wire geometry promotes. The reduction in surface area means that less particles need to escape to establish a field strength equiv-

alent to a comparable foil and as a result a higher population should circulate within the target for longer in the wire. The pathlength, R , of each electron was determined by tracking the individual macro-particles throughout the simulation at 10 fs resolution. In the foil target when an electron crossed the simulation boundary it was able to escape from the simulation despite not necessarily escaping the target. To account for this the propagation angle of the electron was used to determine where the electron would have escaped the target (in a larger simulation). A diagram of this is shown in Figure 7.10. The electron propagation angle is calculated at the boundary and used to approximate the additional R that the electron would have contributed in a larger simulation.

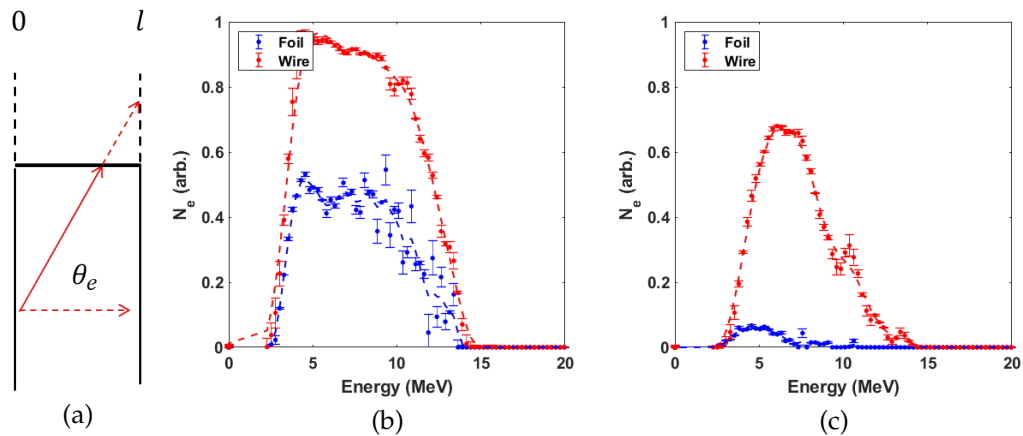


Figure 7.10: Pathlength of electrons inside the target. (a) Diagram of additional R for foil targets, at the boundary the propagation angle θ_e is calculated from the electron momentum this gives the additional pathlength of electrons not simulated. (b-c) The fraction of total electron population, as a function of energy, that has an internal pathlength, R , of (b) $R > 2l$ and (c) $R > 4l$, where l is the target thickness (or wire diameter).

As is clear from Figure 7.10 there is a significant increase in the fraction of electrons accelerated that experience a pathlength greater than the target thickness. This is due to the increased electric field surrounding the target for the wire compared to the foil target, the increased field strength traps and recirculates more of the electrons. The temporal evolution of the field can be demonstrated by setting a simple criteria and tracking over the duration of the simulation. Figure 7.11 is a plot of the percentage of the available target surface perimeter that has a sheath field of $E_{sheath} > 1 - 2.5$ TV/m. The wire geometry peaks at a higher % and reaches that maxima quicker, showing why the increase in electron density happens.

University of Strathclyde – October 1, 2019

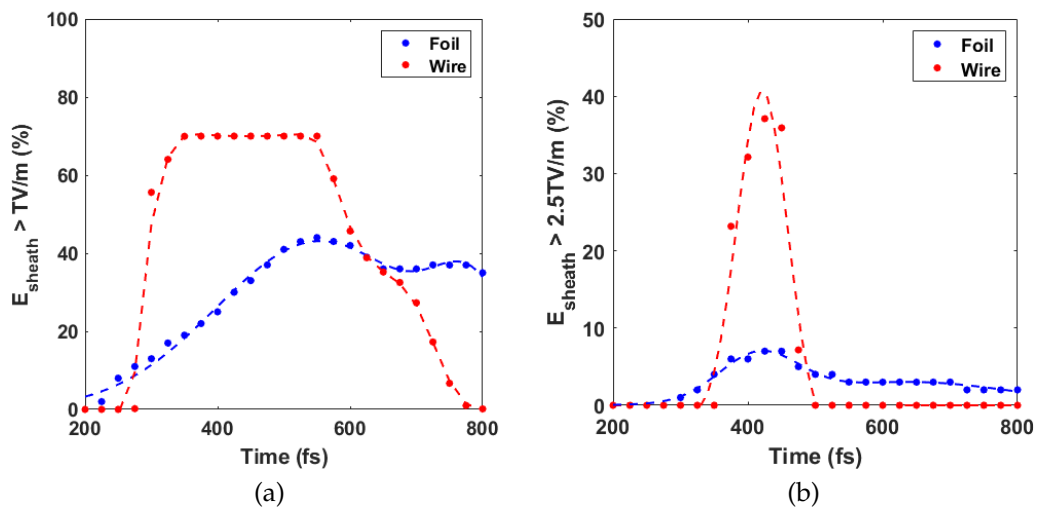


Figure 7.11: Plot of percentage of target surface covered with a $E_{sheath} > \alpha_\phi$ as a function of time for each target geometry. Where (a) $\alpha_\phi = 1$ TV/m, (b) $\alpha_\phi = 2.5$ TV/m. The dashed lines are fits to the data.

7.2.3 Monte-Carlo Modelling

Since EPOCH cannot intrinsically determine the x-ray radiation the internal electron spectra was used in a Monte-Carlo simulation with GEANT4 [227, 291] to determine the expected x-ray flux. In order to approximate the increase in path length for the recirculating electrons an electric field was applied to the target surfaces. The strength of the field was set to 4 TV/m, which was the peak field in the wire simulation. It is necessary to have the full spectra over the PIC simulation to account for the variation in energy of recirculating electrons that GEANT4 cannot simulate[38].

University of Strathclyde – October 1, 2019

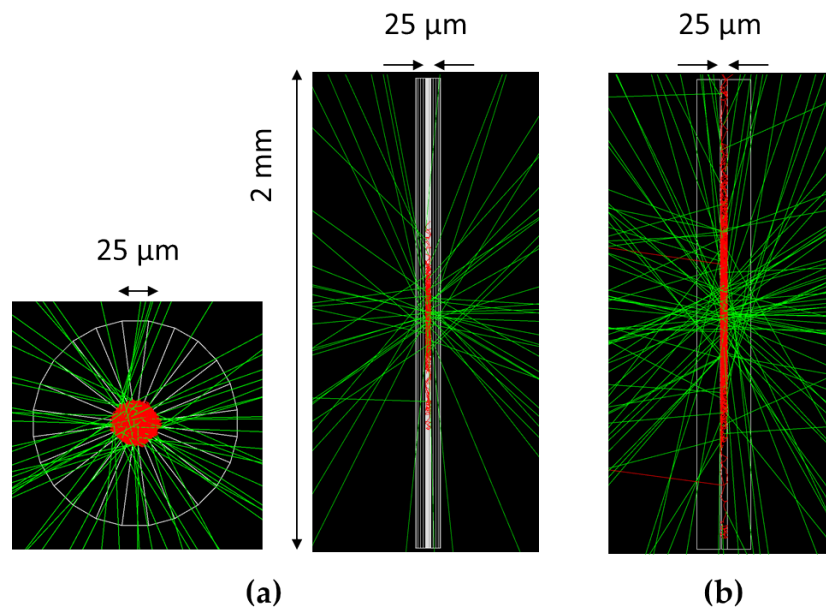


Figure 7.12: Output from the visualisation of GEANT4 simulation for (a) Wire and (b) Foil geometry. The red lines are electron trajectories and the green x-ray. From this visualisation the lateral expansion in the foil is clear.

10^6 electrons were passed through gold foils 25-500 μm thick and a gold wire 25 μm thick. In Figure 7.12 the effect of this electric field can be seen on both target configurations. The images are produced via GEANT4's internal

visualisation software, the red traces are electrons, and the green traces are x-rays, the wire frame is the boundaries of both the target and electric field. In the foil, these fields promote lateral scattering with electrons drifting far from the source point. In wires however it promotes a significant increase in electron density. The spatial distribution from the GEANT4 simulations is shown in Figure 7.13(a-b) for the foil and wire respectively. For the wire there is a clear asymmetry in the source with electrons being directed up and down the wire.

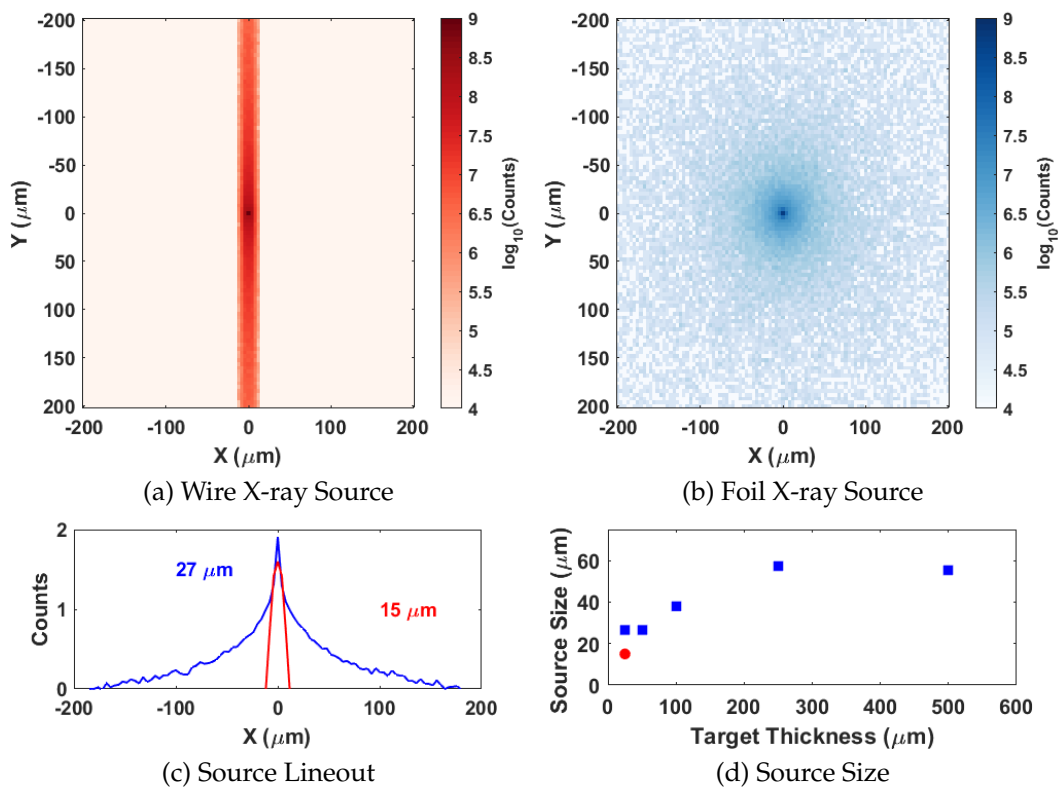


Figure 7.13: Spatial output from the GEANT4 simulations (a) source location of detected x-rays within a 25 μm wire target. (b) Same as (a) but for a foil target. (c) Horizontal line out of each source with the FWHM displayed as text. (d) Horizontal source size as a function of target thickness showing a similar trend to Figure 7.7(a). In plots (c-d) red is used for the wire targets, and blue the foil.

The simulation results, in Figure 7.14 and Table 7.2, demonstrate the in-

	Wire	Foil	
T_{hot}	1.9	2.1	MeV
T_{cold}	1.3	1.2	MeV
$N_{electron}$	5.7	3.7	$\times 10^{18}$
N_{γ}	2.4	1	arb.
$\eta_{e \rightarrow \gamma}$	9.66	2.7	%

Table 7.2: EPOCH and GEANT4 simulation results, N_{γ} for the wire simulations is normalised to the foil results.

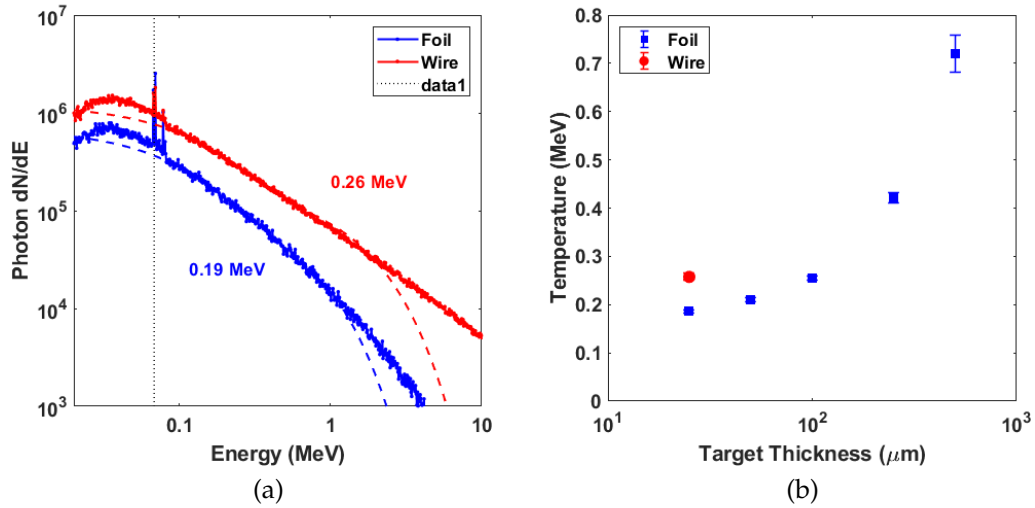


Figure 7.14: Spectral output from the GEANT4 simulations (a) Emitted x-ray spectra using the simulated temperatures from EPOCH, temperature fits shown with a dashed line. K- α line in gold shown with a black dot line. (b) X-ray temperature as a function of target thickness showing a similar trend to Figure 7.8c).

crease in overall flux for a wire target compared to an equally thick foil target. The increase in x-ray flux from the GEANT4 simulations is the result of the change in the two temperature electron distribution. The more populous high energy tail of the wire target, shown in Figure 7.9(d), generates bremsstrahlung more readily as it travels through the target resulting in the increase seen in Figure 7.14(a). The effective temperature of the simulated emitted spectra increases more than the measured results, Figure 7.14(b), indicating that the recirculating population has changed for the thicker foil targets. These results

likely underestimate the low energy x-ray flux as the EPOCH output does not include electron energies below 2.5 MeV - the significant increase in $N_{electron}$ for the wire target, however, suggests that the underestimation would favour the wire geometry.

To demonstrate the effect of the internal electron spectra, Figure 7.15 has the same target geometries with different spectra. In Figure 7.15(a) the targets each had the same input spectra of electron ($k_B T_e = 1$ MeV), for this condition the foil generates x-rays slightly more efficiently, and in Figure 7.15(b) the spectra from EPOCH simulations for the foil are used for the wire and vis-a-vis. The response, in Figure 7.15(b), is almost identical with a slight increase in the wire target again. Collectively, these two graphs demonstrate that both the spatial effects and the spectra effects that the sheath has on the recirculating electron population is important when considering the generated x-ray flux.

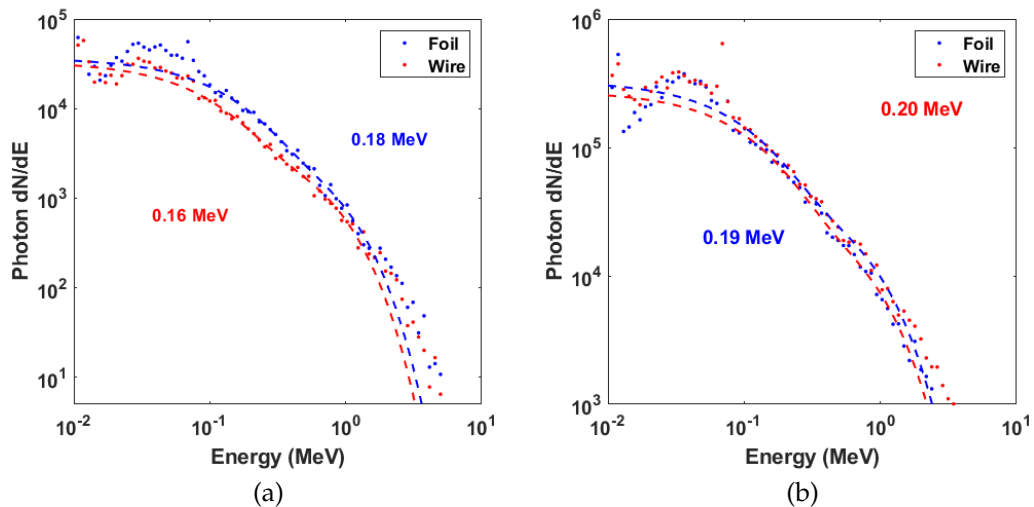


Figure 7.15: Spectral output from GEANT4 simulations with EPOCH electron spectra. a) The emitted x-ray spectra for 1 MeV Maxwellian distribution in each target configuration b) Emitted x-ray spectra using the simulated temperatures from EPOCH with the foil spectra in the wire and wire spectra in the foil geometry.

7.2.4 Radiographs

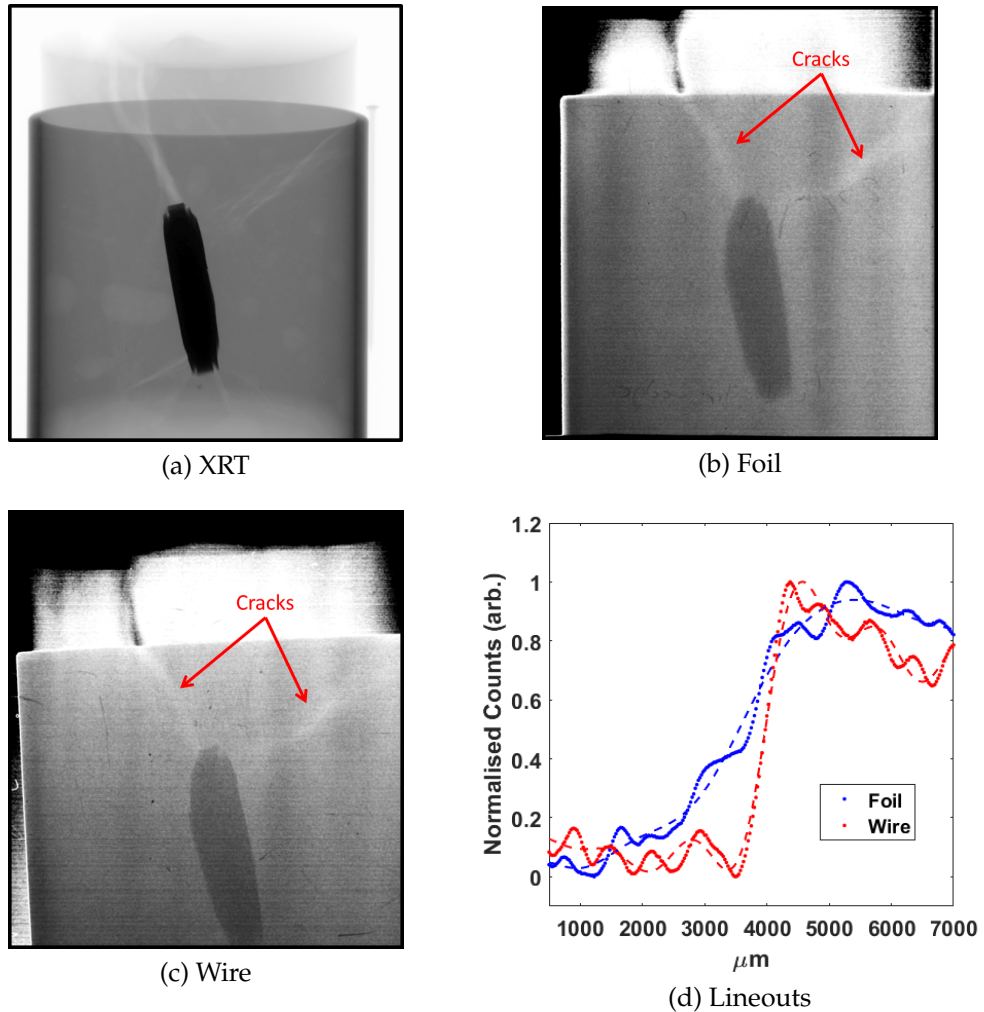


Figure 7.16: Demonstration of the reduced source size from narrow wire targets, (a) is heavily processed XRT imaged acquired over several shots, (b) a single-shot acquisition from a $100\ \mu\text{m}$ foil target, and (c) a single-shot acquisition from $100\ \mu\text{m}$ wire target. (d) is the edge-spread-function (ESF) taken at the edge of the penny for both the foil and wire targets.

Imaging and source measurements were made independently so as not to interfere with the image. The industrial sample is a scaled nuclear waste container. It consists of 5 cm diameter steel canister containing a uranium penny sample encased in grout. The sample has previously been characterised in a x-ray transmission (XRT) machine, Figure 7.16(a). The uranium underwent

controlled corrosion after being encased in grout resulting in expansion of the penny and cracks forming within the grout [292]. Figure 7.16(a-c) demonstrates that these cracks, which are indicators of containment failure, are resolved in both the heavily processed XRT image and the two single exposure laser-driven x-ray images, a key proof of concept for radiographic inspection. The difference in the edge-spread-function (ESF) for a wire and foil target is displayed in Figure 7.16(d). The FWHM of the ESF for the foil is ~ 2 mm and for the wire is ~ 0.8 mm at $\times 5$ magnification demonstrating a significant improvement in the quality of the image.

7.3 Forming an image

Increasing the flux of x-ray sources has obvious benefits when considering the role of laser-plasma interactions for industrial radiography. To explore the role of the spectrum and flux in imaging this section takes an analytical approach to explore the contrast of images. In order for a feature to be readily detected the difference in transmitted flux between the feature and its surrounding material must be larger than the sum of the squares of all sources of noise. This can be expressed by the following inequality:

$$|S - B| > \sigma_n \quad (7.1)$$

where S and B are the intensity of the image peak and background, and σ_n is the total contribution from noise and uncertainty - including spatial blurring from x-ray scattering and the detector. This can be used to provide a figure-of-merit for radiography, C :

$$C = \frac{|S - B| - \sigma_n}{S + B} \quad (7.2)$$

This equation provides a quantity to express the image contrast. A feature on the image can be resolved providing $C > 0$ and $C \rightarrow 1$ would be a perfect binary transfer. When $\sigma_n \ll S - B$ this reduces to a traditional contrast function. In situations with high noise compared to the difference in transmission, $\sigma_n \geq S - B$, this parameter would drop below zero indicating that it would be indistinguishable from the surrounding background. In an idealised system the dynamic range of the detector would be the limit on the contrast of images. However in reality, many factors must be considered before an image is formed. Assuming sufficient spatial resolution, i.e. that the source size is smaller than the feature of interest, and, for simplicity, scattering in the system small, there are three components involved in answering this question: the emitted spectra of x-rays, the transmission of an object, and the efficiency of the system to detect the transmitted x-rays. This discussion will be framed around two detector types; image plate (IP), and a 10 mm LYSO scintillator. Both are discussed in Chapter 4 of this thesis. The key point is that IP is thin and, therefore, inefficient at high energies (> 100 keV) with good spatial resolution, and that LYSO is highly efficient up to ~ 1 MeV but its increased thickness limits the spatial resolution.

The emitted x-ray spectra can be approximated by a single Boltzmann distribution convolved with the self-attenuation of the laser irradiated target. The effective temperature of the distribution can vary between tens of keV to tens of MeV depending on the interaction conditions. The self attenuation through the target reduces the flux of lower energy photons in the spectra resulting in a *quasi*-top-hat distribution (Chapter 2). The transmission of an object can be determined for a given spectra from the NIST transmission tables [14] and the Beer-Lambert Law (Eq. 2.78). The key to resolving the image however is to determine the transmission of both the feature and the surrounding area. In the sample used in Section 7.2.4 there is 5 mm of U238 through 45 mm of grout

contrasting with the transmission through 50 mm of grout. The final factor is the efficiency of the detector system, η , as a function of the incident energy of photons, and the distance from the source. The calculation of efficiency for each detector (IP and LYSO scintillator) is included in the Appendix; each are bounded to a maximum response to account for detector saturation. Each detector is set 1 m from the interaction. When all of these factors are considered together the following equation can be used to determine the effectiveness of the image:

$$C = \frac{|S - B| - \sigma_n}{S + B} \quad (7.3)$$

$$S = \frac{1}{r^2} \int \eta_\gamma(E_\gamma) f(E_\gamma) \left[\zeta(E_\gamma, O_S)(1 - \zeta(E_\gamma, d)) \right] dE_\gamma \quad (7.4)$$

$$B = \frac{1}{r^2} \int \eta_\gamma(E_\gamma) f(E_\gamma) \left[\zeta(E_\gamma, O_B)(1 - \zeta(E_\gamma, d)) \right] dE_\gamma \quad (7.5)$$

$$\sigma_n \approx \sqrt{S} + \sqrt{B} \quad (7.6)$$

where r is the distance to detector system and the energy dependent efficiency of each detector is $\eta_\gamma(E_\gamma)$. ζ is the transmission function for the x-ray energy E_γ , and the object in question - either for S and B or the detector d . In the case where only statistical noise is a concern, σ_n can be simplified to $\sigma_n \approx \sqrt{S} + \sqrt{B}$. $f(E_\gamma)$ is the emitted x-ray spectra from a given target which is assumed to follow a Boltzmann distribution attenuated at low energies - the attenuation is modelled by a decaying exponential from 50 keV for high-Z (i.e Au) targets, and 5 keV for low-Z (i.e. Al) to capture the softer emission. Figure 7.17 is the modelled spectra from both the high-Z and low-Z targets, the spectra are normalised and then multiplied by the desired photon number in the model.

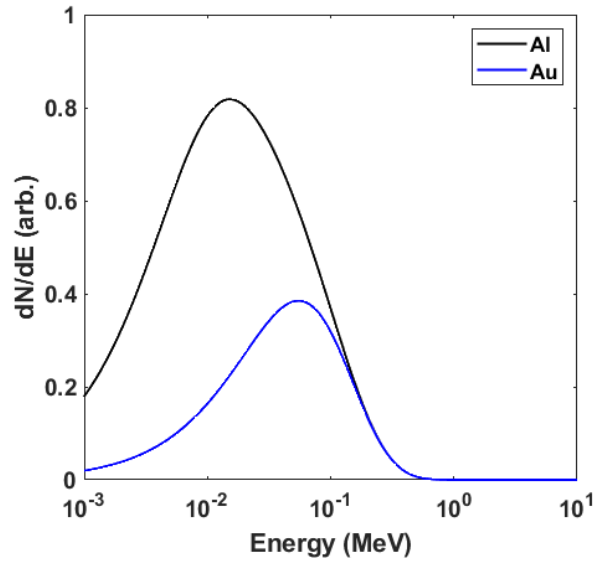


Figure 7.17: 100 keV spectral shape for Al (black) and Au targets in the contrast model.

Considering the question posed at the beginning of this section; Eq. 7.3 can be solved and used to investigate image contrast under different flux and temperatures of the x-ray emission. Figure 7.18 shows the result as a function of x-ray temperature and flux, with a high-Z target spectral shape. Maximum contrast is achieved with a high flux with an intermediate x-ray temperature. LYSO is able to deliver a resolvable feature over a significantly broader set of parameters than image plate.

7.3.1 Spectral optimisation for object and detector

In each case demonstrated in Figure 7.18, the optimum is found with an intermediate temperature and higher flux source of x-rays with this effect being more pronounced in image plate due to the small absorption length. This test case represents a near ideal object for radiography; a high-Z object buried within a low-Z container providing optimum contrast between the regions of the object. In cases where there is a less than ideal background differential,

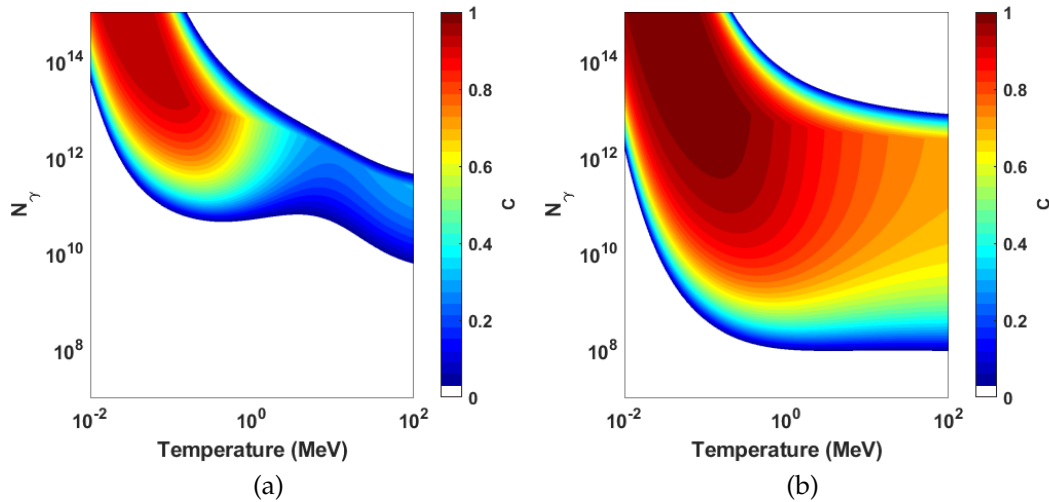


Figure 7.18: Parameter phase-space for x-ray temperature and flux using a high-Z spectral shape. The solution to Eq. 7.3 for the uranium sample outlined in Section 6.1.1 for different detectors (a) SR image plate, (b) 10 mm LYSO Scintillator. For $C > 0$ the image is resolved with $C \rightarrow 1$ producing the optimal image.

imaging is more challenging and requires different parameters to optimise the spectra. Scaling up to larger objects is of industrial relevance; a major challenge is increased flux required to produce a high contrast image. The standard nuclear waste barrel (NWB) is a 500 L drum with 5 mm thick steel walls filled with grout and the stored waste [76]. This is significantly larger than the test sample and the desired information from such a radiograph is the degree of deterioration (e.g. cracking or expansion) to the surrounding grout and to know if the uranium is corroding. Modelling this using Eq. 7.3 was completed by taking the background to be a line through this drum with 600 mm of grout and 10 mm of steel, and the feature of interest as 595 mm of grout, 10 mm of steel, and 5 mm of Uranium. This has significant attenuation due to the size and so the LYSO scintillator will be considered for this object. Figure 7.19 is the schematic of the drum and Eq. 7.3 solved for a 5 mm Uranium sample at the center of the barrel with the LYSO detector.

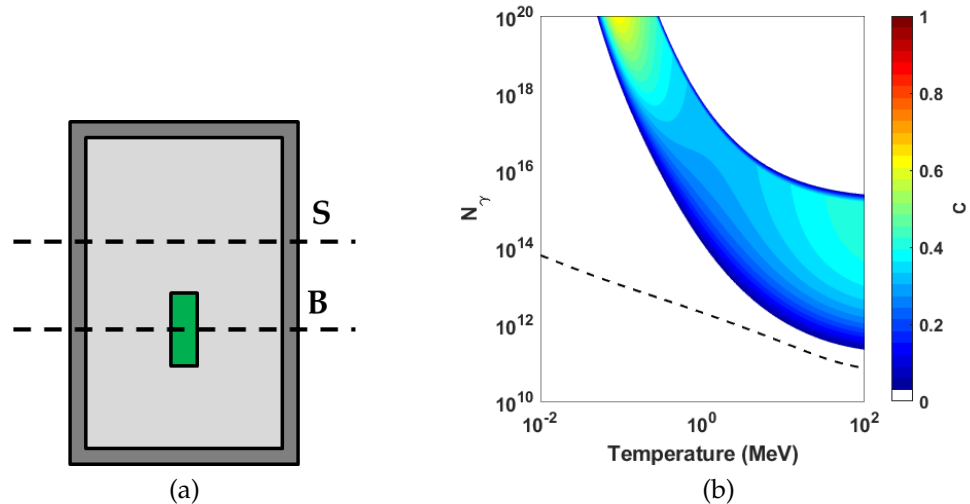


Figure 7.19: (a) Schematic of standard NWB from international standards document [27, 28]; 5 mm cylinder of U-238 to demonstrate transmission, grout interior is made from concrete and the barrel is modelled as iron. (b) Eq. 7.3 for a standard NWB, dashed line indicates a total x-ray energy of 0.1 J.

The parameter space shown in Figure 7.19(b) demonstrates the issues with this imaging challenge, only at the highest levels of flux, or very high temperatures, is an image formed. Park *et al.* [187] measured the conversion from laser energy to K-alpha emission as 10^{-4} for thick targets, using this as a foundation the laser energy required (assuming similar scaling across laser intensities) to image a NWB can be determined. In Figure 7.19(b) the dashed line indicates 0.1 J of incident x-ray flux, by the conversion determined by Park *et al.* this would require ~ 1 kJ of laser energy. To reach $C \sim 0.4$, the 'optimum' value shown in Figure 7.19(b), requires ~ 1 kJ of x-ray energy and, by the same scaling, ~ 10 MJ of laser energy to achieve. This simple model suggests that imaging a NWB is likely impractical for commercial lasers systems unless the conversion efficiency is increased, or the transmission length is reduced by imaging at the edge of the NWB.

The other challenge to consider is low-Z buried within high-Z, e.g. looking

for defects or crack formation within additively manufactured components or lightweight aeronautics. Successful imaging of one such object has been demonstrated with laser-solid targets by Brenner *et al.* [10]. The sample was a fanblade made from titanium alloy, consisting of 1 cm walls with a hexagonal mesh interior that provides mechanical strength but limited the overall mass of the fan blade. This results in a transmission line of 30 mm titanium next to 25 mm of titanium and 5 mm of low density foam (modelled as mylar). This requires significantly lower energy x-rays in order to ensure contrast between the two regions. Modelling this with Eq. 7.3 and a low-Z target assumption is shown in Figure 7.20. The change in emission requirements is clear, demanding a high-flux but low temperature source to produce any image, with higher temperatures producing an image with $C \sim 0$. In the experiment the measured contrast of this object was (0.21 ± 0.04) . In Figure 7.20(b) the red asterisk are the approximate laser conditions and emitted x-ray spectra (100 J laser with 100 keV x-ray spectra at 10^{-4} conversion efficiency [187]) from the Brenner experiment equal to $C \sim 0.18$.

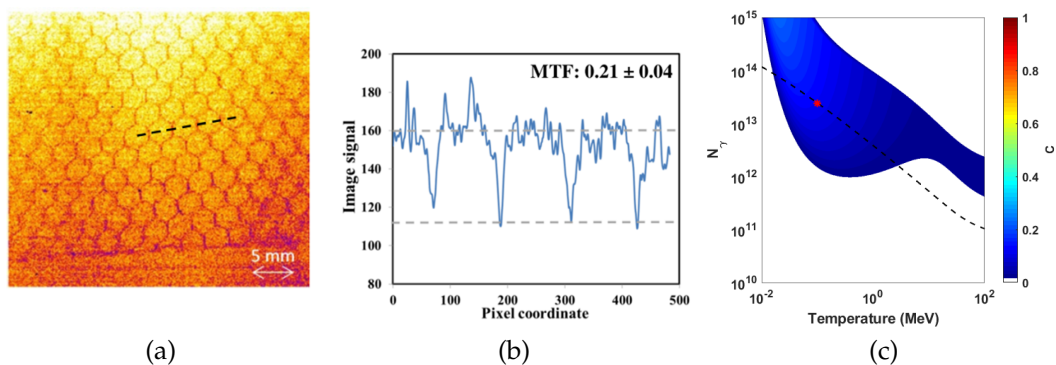


Figure 7.20: (a) Radiograph of the fanblade from Brenner *et al.* [10] shown with (b) lineout and contrast of the feature. Hexagonal pattern from the interior is a titanium mesh in place to provide structural support without adding significant mass to the fanblade. (c) The phase-space (determined by Eq. 7.3) for the fanblade and an image plate detector, dashed line indicates a total x-ray energy of 0.1 J, and the red asterisk shows the estimated conditions from the experiment.

7.3.2 Effect of atomic number

Attenuation through materials is dependent on both the energy of the incident photon and the target material, as summarised in Chapter 3. The photoelectric and scattering processes scale differently to one another resulting in shifting peaks in transmission. The model explored in Section 7.3 demonstrates that for optimum contrast between transmission relatively low x-ray energies are required. For large scale objects, such as Figure 7.19, the necessary flux is only achievable (with realistic laser parameters) at high temperature and so it is worth considering the scattering processes that dominate at these energies. Using the values in the NIST database [15], the most transmissive energy for different materials can be determined. Figure 7.21 demonstrates that as the relative Z of the sample is increased there is a reduction in what energy is the most transmissive for that material. This indicates that for high- Z materials increasing the energy beyond ~ 4 MeV will not enhance the transmission through the sample and instead increase the amount of scattered photons.

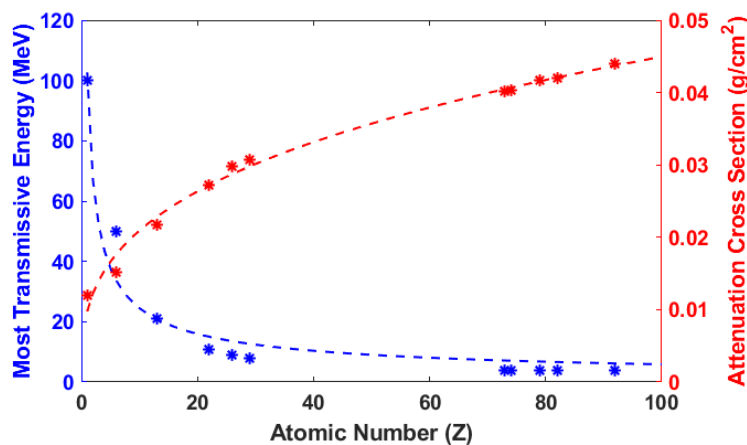


Figure 7.21: Most transmissive photon energy and associated attenuation cross section coefficient for varying atomic number. This demonstrates that the most transmissive energy decreases with increasing Z .

This is due to the fact that in higher- Z materials pair production becomes

a dominant factor at lower energies reducing the overall transmission of high energy photons. The majority of the photon energy is still transmitted through the object, however, many of the photons have been scattered from their original trajectory lowering the effective resolution for the image. Optimising the imaging contrast due to the transmitted photons requires minimising the scattering potential and increasing the contrast between low- and high-Z materials. These cross-sections only provide an initial estimate of the scattering as they are 1D approximations. Using GEANT4 [227], the full effect of this scattering can be explored. A simulation was conducted to determine the scatter from incident x-rays with energies of 10 keV to 100 MeV. These x-rays were simulated from $x, y, z = 0$ and propagated through materials of different atomic number with thickness matched to an areal density of 10 g/cm^2 (equivalent to $\sim 5 \text{ mm}$ of uranium). The ratio of scattered x-rays to unscattered was determined across these simulations by counting the number of photons that were detected at $x, y = 0$ as a fraction of the total detected, and used to create the parameter map in Figure 7.22.

In agreement with the solution to Eq. 7.3, Figure 7.22 suggests that the highest energy x-rays ($> 10 \text{ MeV}$) are, in general, less beneficial to imaging. From the GEANT4 simulations it is clear that higher energies introduce a significant proportion of scatter to the detected image and, therefore, increase the effective σ_n for the contrast. X-ray of energies $> 10 \text{ MeV}$ are also harder to detect reducing the efficiency for imaging. Relatively low energy x-rays ($< 100 \text{ keV}$) that are transmitted through the 10 g/cm^2 are readily scattered as a result of Compton scattering. However, the overall transmission at 100 keV for a 5 mm uranium object is $\sim 10^{-7}$ indicating that the increased scatter ratio seen in Figure 7.22 could be a result of the low number of transmitted photons.

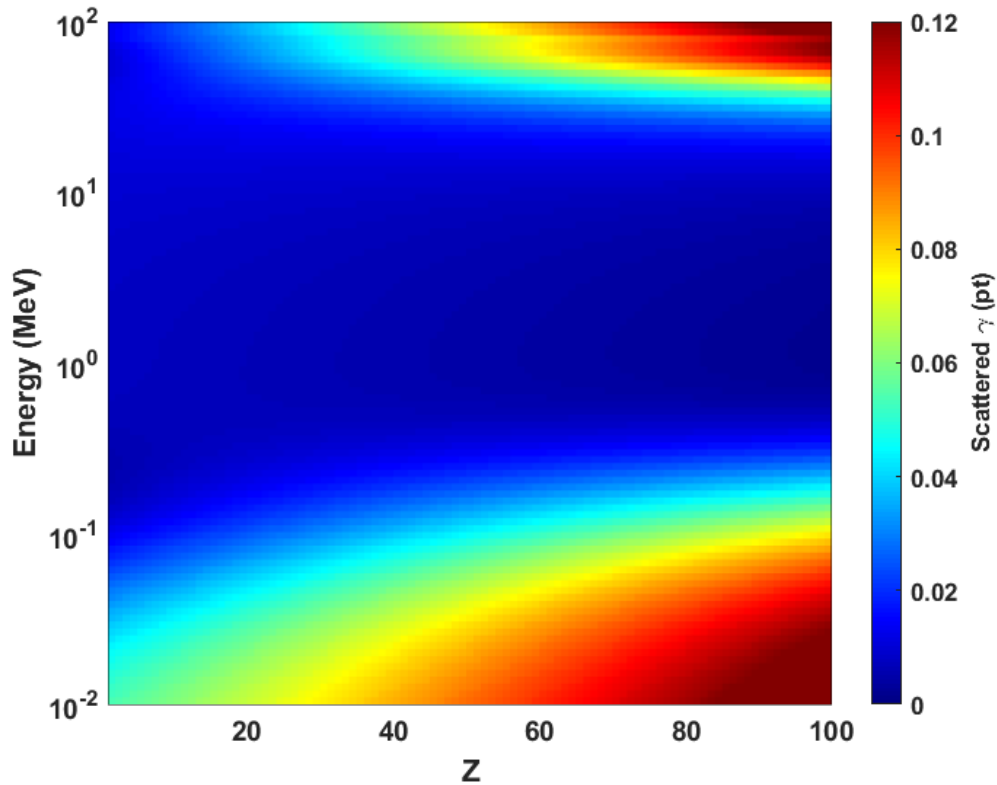


Figure 7.22: Scattered transmission ratio as a function of Z and photon energy. Simulations were conducted at $Z = (6, 13, 22, 26, 50, 73, \text{ and } 92)$ for 100 logarithmically spaced energies between 10 keV and 100 MeV, the results were then interpolated via a Gaussian fitting function to produce to full parameter space.

7.4 Conclusion

Radiography of industrial samples benefits from a flexible x-ray source to ensure that a wide range of objects can be imaged. This chapter has demonstrated methods to calculate the optimum spectra for an object through calculating the contrast parameter C (Eq. 7.3) for an object and a range of temperatures. The parameter space of this equation demonstrates the flux and that 100 keV to 1 MeV temperatures are generally more effective at imaging due to the contrast between different density materials that these spectra can offer.

Experimentally a method to improve the flux without significantly altering the temperature and maintain a small emission zone is shown. Changing from a foil target to a wire target constricts the electron expansion as the electric field on the rear-surface of the target builds rapidly and covers more of the surface area. The change in the sheath field results in a higher population and cooler recirculating electron population, which in turn results in an increase in the measured x-ray flux. Simulations using EPOCH in 2D show the sheath field developing faster on the wire target geometry, and by using the recirculating population outputted from EPOCH in a GEANT4 simulation, the increase in x-ray emission can be demonstrated by applying electric fields to the target surfaces. Wire, and constrained targets, also limit the material producing background x-rays which removes the second source discussed throughout Chapter 5, resulting in a clearer final radiograph. The demonstration of this effect is shown in Figure 7.16 where a x2.6 improvement in the image quality is measured for a scaled nuclear waste container.

Chapter 8

Conclusions and future work

The research presented in this thesis explores laser-solid interactions to enhance or optimise the radiography capabilities of x-ray sources. Experimental campaigns and simulation studies throughout this body of work have been conducted to better understand the physics at work as these high-energy, high-resolution, x-ray sources develop. This final chapter summarises the work presented and discusses the potential impact and areas for future work.

In short, each experimental chapter studies a different aspect of the emitted x-ray source. Chapter 5, focuses on optimising the internal electron population to the target parameters, to deliver a better spatial contrast of the x-ray source. Chapter 6, explores a capillary target design that could be used to generate electrons significantly more energetic than the ponderomotive limit via *direct-laser-acceleration* (DLA) occurring within the capillary. In the final experimental chapter, it is shown that a standard wire target reduces the escaping surface area of electrons and, therefore, increases the field strength and recirculating electron number. The spectral changes in the recirculating electrons promotes a brighter x-ray source that, due to the limited target size, emanates from a narrow lateral source. An analytical model was presented that explores the spectral demands for different radiography objects. The results indicated that while there is significant advantage in increasing the overall flux of x-ray sources, there is limited benefit in increasing the peak energy due to contrast, at

high energies, requiring significant differences in areal density before a change is observed. The remainder of this concluding chapter discusses the findings from each of the investigations, and considers what future work could be done to expand upon the research completed.

8.1 Investigation of recirculating electrons in solid targets as a function of laser intensity for x-ray generation

Measurements of x-ray sources from laser-solid interactions with a high intensity laser demonstrated a two-source structure; a bright central source on the order of 100 μm , and a larger substrate source on the order of millimetres. Within a few rayleigh ranges of focus position ($\pm 100 \mu\text{m}$ with an F3 parabola), the substrate source generated a similar flux of x-rays as the central source, introducing a large blurring function to the image. At large defocuses, the substrate source begins to diminish and flux ratio between the central and substrate source increases by $\times(10 \pm 2)$, resulting in significantly better image quality despite the slight increase in central source size.

This result was explored via an electron refluxing model that considered two populations of electrons - those that can only contribute to the central source and those that can also contribute to the substrate source. The sheath model, presented by Mora [161], was used to determine an escape energy for electrons, and the collisional losses within a target, calculated by the NIST transmission database [14]. Electrons that collide on the first pass of the target or are able to escape through the sheath can only contribute to the central source. The number of the central electrons to those that recirculated was demonstrated analytically to agree with the measurements of the x-ray source.

Using this model, it is possible to determine an optimum balance between the target thickness and the laser intensity, to minimise the central source, whilst keeping the ratio of the two sources favourable.

8.2 Investigation into electron dynamics with laser-guiding capillary-targets

Chapter 6 reported on an exploration into the use of a capillary target to channel the laser and provoke multiple interactions as it propagates through the capillary. Initial modelling suggested that there should be an increase in the number of accelerated electrons with a cooler overall temperature compared to a single interaction with a solid target. Experimental measurements demonstrated that there was indeed a significant increase in the number of electrons (measured via an increase in x-rays despite the limited target mass) without a significant decrease in the effective x-ray temperature compared to solid wires in vertical and horizontal orientations. Prior work by several groups [270–273] has demonstrated how a glancing angle interaction can cause a surface field effect, which further accelerates electrons and results in an increase in energy. Simulations demonstrate that electrons were not getting trapped in these surface fields; however the channel structure and the emergence of these fields resulted in electrons oscillating through the laser path several times. In so doing they were successively re-accelerated to *superponderomotive* energies, which could explain the increase in temperature. Comparisons to solid targets demonstrated that the flux of accelerated electrons within the capillary quickly exceeded that of a solid target.

Continued study is required to make the most of this promising target structure. Enhancing DLA mechanisms is an area of considerable interest for the community, due to the emergence of high flux high energy electron popula-

tions from relatively low laser intensities. One progression in this design is to taper the walls of the capillary to drive the DLA mechanisms, and also enhance the conversion of energetic electrons into x-rays. The bremsstrahlung converter on the exterior surface of the capillary could be spatially deposited, to further confine the source of energetic x-rays, using the bulk of the capillary target to capture the laser energy. In future experiments, the transport along the capillaries could be tracked directly with spatially resolved K-alpha imagers [214, 215] or additional penumbral foils, to monitor the electron transport through the capillary walls, similar to fast electron measurements made by Akli *et al.* [252].

8.3 Optimising x-ray source characteristics for large scale radiography

Chapter 7 discussed how to optimise the spectra of x-rays emitted from the target. A simple imaging parameter was constructed by considering the spectral transmission of different regions of an object with respect to the source and the detector in question. For each test case trialled, there was a clear advantage for high flux, but no significant benefit to increased temperature. Using wire targets demonstrated a simple and effective way to increase the flux without altering the laser parameters. This increase resulted from the sheath field building around the target over a smaller surface area compared to the foil, causing a higher population of electrons to remain within the target. In addition, the wire target, as with reducing the on-target intensity shown in Chapter 5, reduced the emission from the substrate of the target. Penumbral measurements and radiographs of samples both demonstrated the increase in image quality resulting from switching to a wire target. The increase in flux and the reduction of the lateral source width combined to deliver more favourable

imaging conditions.

8.4 Future work

The work presented in this thesis aims is at optimising laser-solid interactions for energetic x-ray sources. Numerous methods offer valid approaches to optimisation, and determining the optimum laser and target parameters for any potential object is a necessary step towards the commercialisation of these sources. Although the work presented here is not the final answer, it does present a significant step towards finding the optimum conditions.

The model presented in Chapter 7 offers a simple method of determining what laser parameters are needed in order to resolve certain features. Currently this model is a 1D approximation that only considers the spectral demands of an object; with further development, this model could be expanded to include spatial demands and incorporate more realistic spectra. The novel capillary targets presented in Chapter 6 offer an opportunity to deliver "coherent" sources of high energy x-rays due to the ability to tailor the final emission size. There is additional merit from the potential of direct-laser acceleration to readily generate ultra-relativistic electrons. As well as radiography, this source of high energy electrons, and the channelled electrons in the capillary, have potential for a wide range of applications, including fast ignition. The model in Chapter 5 effectively demonstrated a method to optimise the spatial profile of the x-ray emission by minimising the number of electrons that were able to recirculate the target. It is known from prior work [17, 161, 166, 167] that the recirculation population is more complex than the model assumes and incorporating these complexities into the model could improve results. The temporal evolution of the sheath will also impact on the energy of electrons, with higher energy electrons being generated at the peak of the pulse, typically, after the

sheath has been developed. Therefore lower energy electrons, accelerated by the rising edge of the pulse, will be able to escape as the sheath field is forming.

8.4.1 Tapered Capillary Targets

The experimental results demonstrate that capillaries are able to produce at least equal levels of flux to standard wire targets, while retaining a small horizontal and vertical source size. The horizontal source profile exhibits two peaked structures contributed by each side of the capillary, indicating that the reflected laser light from the first interaction is seeding subsequent acceleration in the target. In order to maximise the benefit of this subsequent laser transport, the target can be shaped to change the interaction as the laser propagates. One option is outlined in Figure 8.1: the tapered capillary has the same two-layered structure of the targets in Chapter 6, but the aperture is reduced from $30\ \mu\text{m}$ to $<2\ \mu\text{m}$ over $\sim 200 - 500\ \mu\text{m}$.

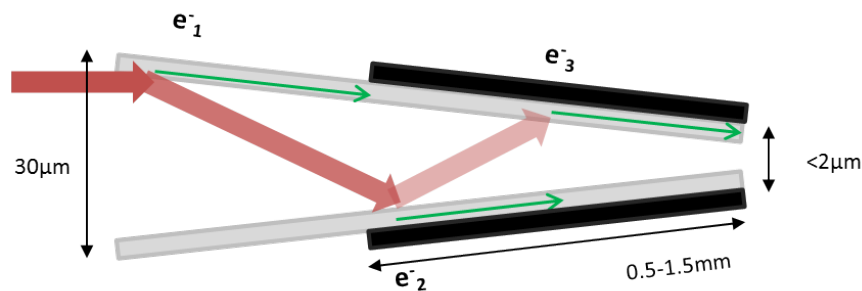


Figure 8.1: Target schematic demonstrating the tapered capillary. The opening aperture is as large as the spatial jitter of the laser; the closing aperture is smaller than the initial spot to drive an increase in intensity. Black bars on the exterior surface are a high- z material to increase the generation of bremsstrahlung.

These apertures are designed with the laser parameters in mind. For the Vulcan laser system, the pointing stability warrants a $30\ \mu\text{m}$ aperture to ensure that the spot is captured by the tube. The small aperture is then set

to be smaller than the laser spot to ensure laser absorption towards the end. This design takes a similar approach to Sentoku *et al.* in 2004; however, the long propagation distance increases the energy deposited by the laser over the course of the interaction. The benefit of such a design is two-fold: firstly the super-ponderomotive electrons accelerated within the capillary will be driven into the walls, guaranteeing conversion to x-rays; secondly the ultimate source of the x-rays can be reduced to below the spot size of the laser, and thus phase contrast imaging could be attainable at high x-ray energies. This latter benefit can be achieved by locally depositing the bremsstrahlung converter (shown as black bars in Figure 8.1) to a small region at the end, or along, the capillary.

8.4.1.1 Phase Contrast Imaging

One possible application of these capillary targets is to induce spatial coherence in the x-ray emission. By tapering the capillary, the available lateral area that x-rays can be generated from can be reduced, and, as such, spatial coherence can be achieved. The equation below [293] helps define the required experimental parameters:

$$l_c = \frac{\lambda_x R_1}{\sigma_s 2\sqrt{2 \log 2}} \quad (8.1)$$

where R_1 is the distance from the source to the object, σ_s is the lateral size of the feature from which to retrieve phase information, and λ_x is the wavelength of the x-ray. This defines l_c as the required source size and scales inversely with the x-ray energy as shown in Figure 8.2. Increasing the propagation distance also increases the limit on the source size, thus designing the geometry of the experiment will be necessary to ensure phase contrast radiography is viable.

For achievable experimental layouts, and significant magnification onto detectors, the object can be placed at maximum 1 m away from the interaction and allow ~ 5 m for magnification before a detector. With the gold struc-

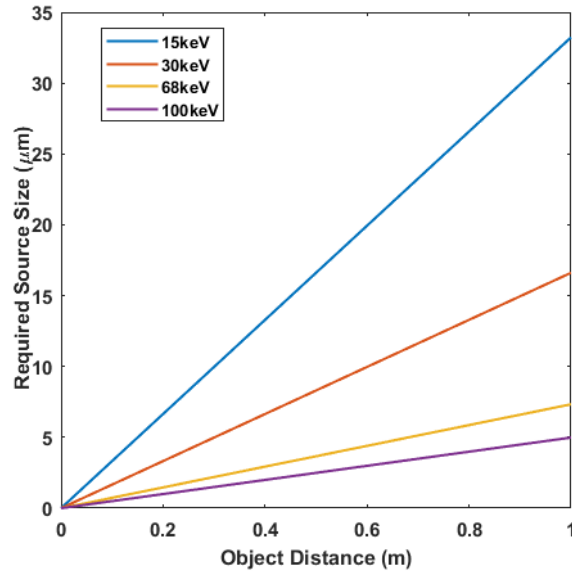


Figure 8.2: Source size required for phase-contrast imaging with respect to different object distances, calculated using Eq 8.1.

tured targets, the brightest single energy will *typically* be the K-alpha signal at ~ 68 keV, which is significantly higher than the currently utilised phase-contrast sources [294].

Appendix A

A.1 Considerations for the recirculation model in Chapter 5

The analytical model presented in Chapter 5 is based upon the 1D plasma expansion model that Mora posits in Reference [161]. A necessary step in making this model more thorough is to include spatial and temporal evolution of the sheath field during the interaction, as this will impact the population of electrons that recirculate the target. One method to address this could be to model the sheath potential by treating the target as a capacitor, similar to the model presented by Link *et al.* [166]. This would enable a temporal evolution of the sheath strength that could more accurately treat the recirculating population of electrons.

To test the effectiveness of the recirculation model, without the temporal considerations that could be added, it was compared to prior results with different laser and target parameters. The following section has two comparisons, the first using x-ray images and a defocused laser similar to the configuration explored in Chapter 5, and the second considers escaping electrons from a solid target.

A.1.1 X-ray radiography data

Experimental results from a higher energy laser experiment conducted in 2013 demonstrated an image contrast improvement as the laser was defocused.

The laser intensity varied from 5×10^{20} W/cm² at best focus, to a defocus position of -200 μ m and intensity of 2×10^{18} W/cm². The target was 100 μ m thick tantalum target. Radiography images of a steel machine part were recorded on SR image plate and presented in Figure A.1(a-c).

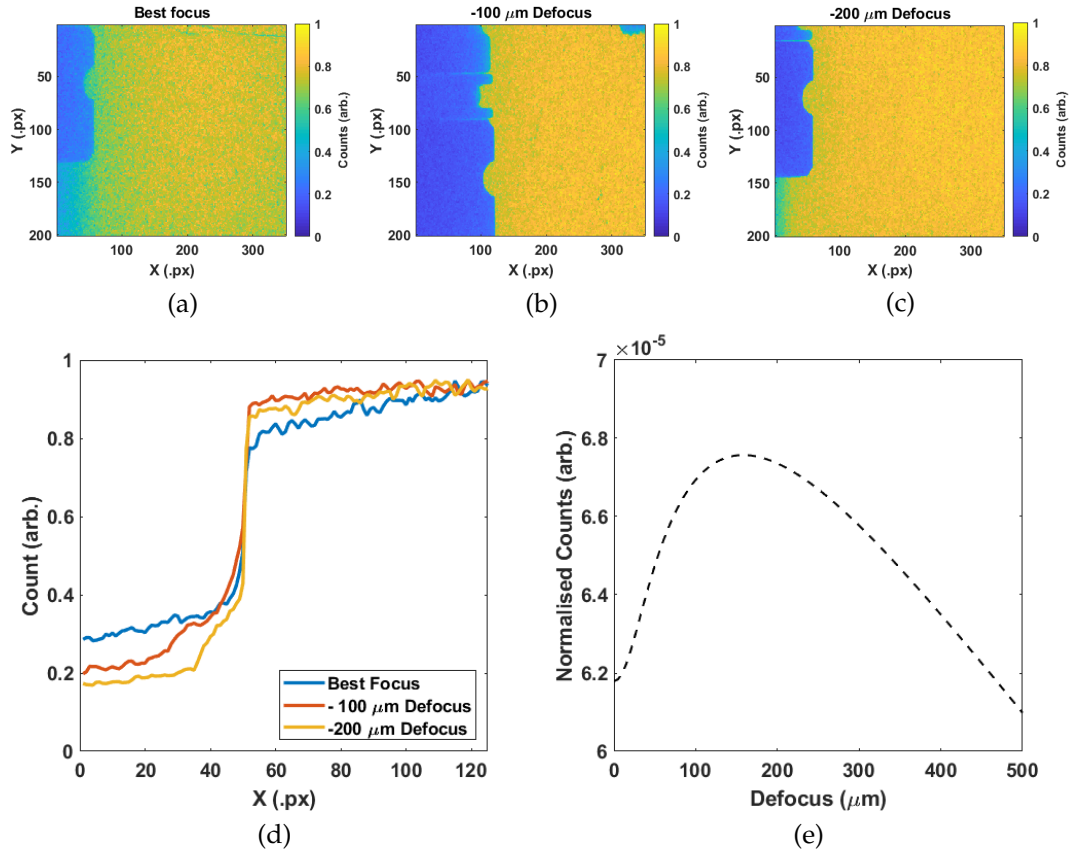


Figure A.1: Radiography and model results from 2013 experiment. (a-c) radiographs for Best focus, -100 μ m, and -200 μ m defocus respectively. Lineout was taken at the edge of the feature averaged over 50 pixels (px). (d) Normalised lineouts for the image. (e) Model results for experimental conditions in (a-c), demonstrating a peak between 100 – 200 μ m defocus where the best lineout was observed experimentally.

The transition across the edge of the sample is used to demonstrate the improvement from best focus to the optimum experimental defocus. Without penumbral measurements, it is not possible to accurately determine the substrate source distribution. However, the lineouts in Figure A.1(d) demonstrate the existence of a larger blurring function for best focus, but not at either 100 or 200 μm defocus. The results from the model are shown in Figure A.1(e) showing that the optimum for these conditions should exist at $\sim 150 \mu\text{m}$.

A.1.2 Escaping electron data

This model can also be used to explore the escaping electron number from target interactions. During an experiment on the PHELIX laser system in GSI, the escaping electron measurements from 100 μm thick copper targets were measured using a wraparound image plate detector for varying defocus. The laser parameters give an intensity range from $3 \times 10^{20} \text{ W/cm}^2$ at best focus to $4 \times 10^{17} \text{ W/cm}^2$ at maximum defocus. The experimental results presented by Rusby *et al.* [17] show a significant peak in the escaping electron number with defocus, and then a rapid fall off as the intensity is further reduced.

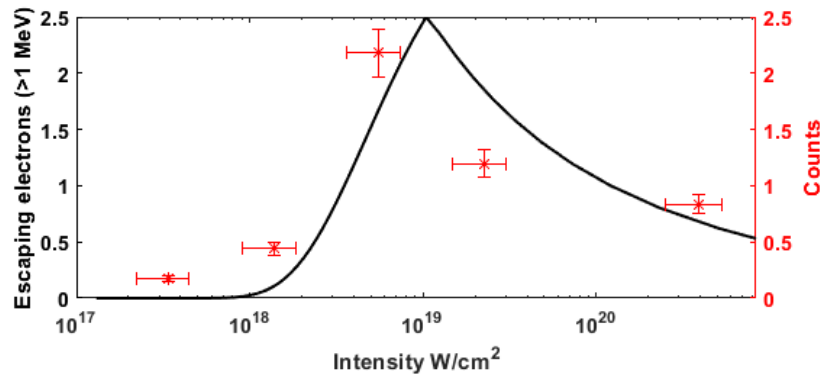


Figure A.2: Model comparison with escaping electron data from Rusby *et al.* [17]. Black - model predictions for escaping electron number $E > 1 \text{ MeV}$. Red - measured electron number from wraparound diagnostic.

This measurement can be explained by the balance explored in the analytical model presented in Chapter 5; as the intensity is reduced, the electron spectrum is optimised to drive more electrons above the escaping “threshold”. As the intensity is further reduced, attenuation through the target begins to dominate and significantly fewer electrons reach the rear surface. This result is emphasised by the ~ 1 MeV energy threshold for detected electrons. As shown in Figure A.2, the model (black) predicts a clear peak in the escaping electron signal at $\sim 10^{19}$ W/cm², which then decays slowly as the intensity is further increased - which is in broad agreement with the measurements made by Rusby *et al.* [17].

A.2 Considerations for the contrast model presented in Chapter 7

A.2.1 Demonstration of contrast

The final term in Eq. 7.2 factors in signal noise to the standard image contrast equation. As a result, negative values are possible when the summation of the noise is larger than the difference between regions. A demonstration of this unintuitive valuation is shown in Figure A.3. As the parameter C approaches 0 the square feature at the centre becomes less visible, however it is still discernable against the background until $C < 0$, shown in Figure A.3(f). This was made by creating two regions; one at a set value, S , and the other as a fraction of this value, $B = nS$, where n is between 0 and 1. Statistical noise is added used the random number function in Matlab, and the parameter C calculated using the equation presented in Chapter 7.

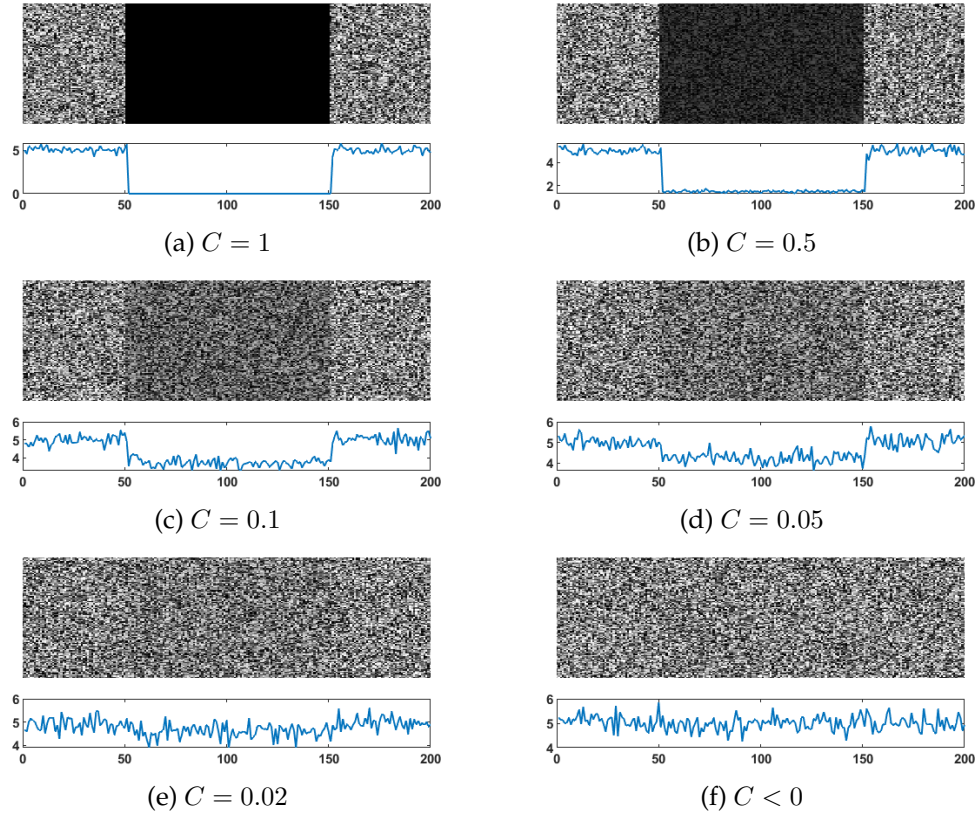


Figure A.3: Visual demonstration of the parameter C from Eq. 7.2 with line-outs.

A.2.2 Image Plate

The fractional absorption of the incident photons, and the response in photo-stimulated luminescence (PSL) is determined by the the equation outlined in Bonnet *et al.* [207]:

$$Y = \alpha_{part} E_{dep}^{eff} \quad (\text{A.1})$$

where the Y is the yield in PSL for energy deposited, E_{dep}^{eff} , within the image plate. The transmission tables in NIST [15] are used to calculate the relative absorption. The parameter α_{part} is a coefficient depending on the image plate type. In the case presented in Chapter 7, SR image plate is considered therefore; $\alpha_{part} = (3.3 \pm 0.7) \times 10^{-4}$. The minimum detectable change for image plate

is ~ 1 μ PSL per 25 μ m pixel, and the maximum is ~ 16 PSL per 25 μ m pixel.

A.2.3 Scintillators

The emitted optical light per MeV deposited in the scintillator material must be absolutely calibrated for the geometrical layout of the camera system and the individual scintillator crystals. A schematic of the proportion of light captured by a lens is shown in Figure A.4(a) and the quantum-efficiency (QE) of the CCD considered is shown in Figure A.4(b).

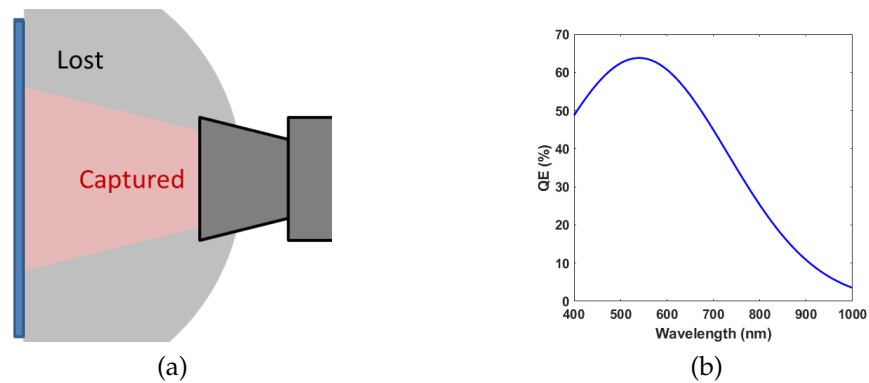


Figure A.4: (a) Schematic of a lens field of view from a scintillator. (b) QE curve for an AVT Manta Camera. Data taken from AVT Website: <https://www.alliedvision.com/en/products/cameras/detail/Manta/G-1236.html>

For LYSO, the scintillator considered in this model, the typical values are 30 photons emitted per keV deposited [295]. An AVT manta camera coupled with an f0.95 lens can be focused onto the front surface of the LYSO crystals and is relatively sensitive, with a $\sim 5\%$ capture efficiency from scintillator to CCD. The minimum detectable signal is set to 1 keV and the maximum to 43 MeV (1 and 65534 counts respectively) per 32.5 μm^2 of LYSO.

A.3 Kramer's law for electron to x-ray energy

Determining the specific electrons responsible can be generalised analytically by considering Kramers Law for the x-ray distribution from an incident electron [29]:

$$I(\lambda) \propto \left(\frac{\lambda}{\lambda_{min}} - 1 \right) \frac{1}{\lambda^2} \quad (\text{A.2})$$

where the incident electron energy determines the cut-off λ_{min} by the deBroglie equation ($E_e = \hbar\lambda$) [296], and the chance of radiative collision between an electron and a target material to be increasing with energy [14]. Figure A.5 shows the results of this for a gold target of unit thickness and density and electron energies ranging from 1 keV to 20 MeV. At higher electron energies the distribution of emitted x-rays will be broader and therefore less efficient at generating the *relatively* narrow band of emission that is suitable for industrial radiography.

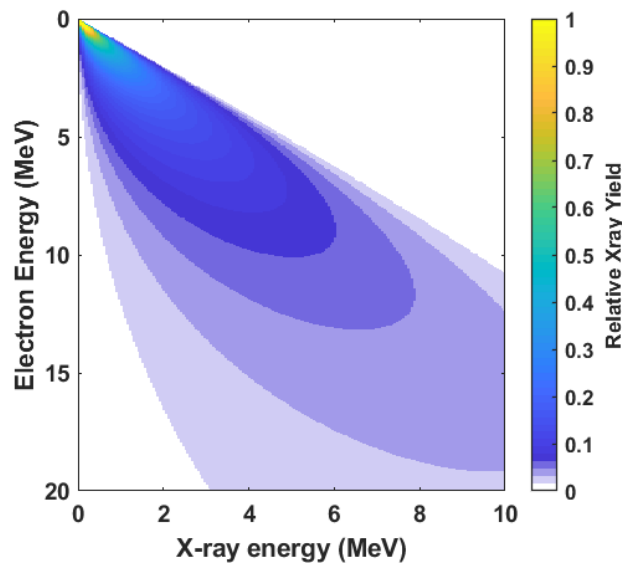


Figure A.5: The relative x-ray yield for electrons in a gold target, computed from Kramers Law Eq. A.2 [29].

Appendix B

B.1 Comparison of laser-wakefield acceleration to “conventional” techniques

“Conventional” acceleration techniques use alternating electric fields to drive charged particles forward and accelerate them to high energies. Typically, these fields are at radio-wave frequencies (400 MHz for the LHC [297]) hence the name RF Accelerators. The acceleration process is as follows:

- An external field is applied to the accelerator channel.
- This creates a negative potential that attracts the ion.
- The ion travels through the field potential, to a neutral region.
- The field is reversed, the ion travels out of the neutral region and is accelerated by the reverse field.

This process is repeated as many times as necessary to reach the desired energy ions, or electrons via the same principle, during acceleration the particles are confined by exterior fields. This takes one of two forms, either a linear series of accelerators (i.e. a linac), or a circular system contained by additional magnetic fields to allow the electrons/ions to propagate indefinitely (cyclotron/synchrotron). The electric fields used to accelerate the ions are limited in maximum field strength to $\sim 10^7$ V/m, beyond this the accelerator materials can begin to ionise and breakdown. The beam paths of conventional accelerators have to be on the order of hundreds of meters in size to accelerate charged particles to GeV energies. In comparison, field strengths can safely exceed the material breakdown limit in laser-plasma accelerators (LPA), reaching

Appendix B.

TV/m under typical conditions [53]. As a result, LPA have accelerated electron beams to energies in excess of GeV within a few centimetres [298, 299]. At the Central Laser Facility (CLF) a recent result on the Gemini laser system [300] demonstrated electron energies in excess of 2 GeV from a gas cell 10-20 mm in length [301]. By comparison, the Diamond synchrotron (based near the CLF) uses a 158 m circumference booster ring to accelerate electrons to 3 GeV [302]. A recent study has set a record in peak electron energies for laser-wakefield acceleration, researchers at the BELLA laser, in Berkeley, have used a capillary wave-guide to achieve ~ 8 GeV electrons from a 20 cm plasma channel [303].

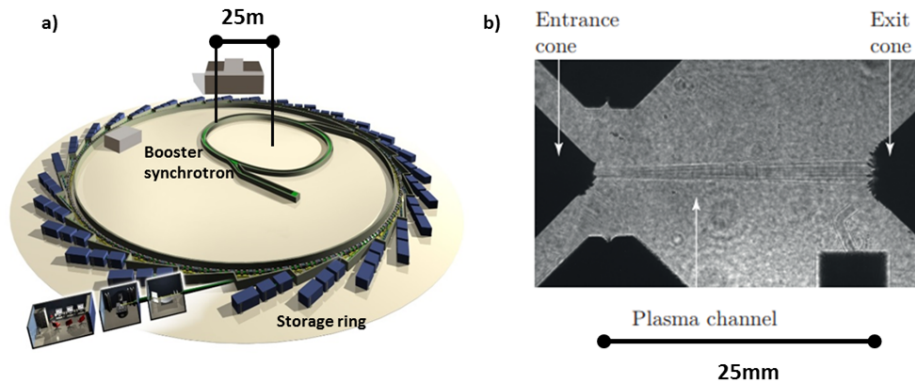


Figure B.1: Comparison of scale between conventional RF accelerators and laser-wakefield interactions. (a) A schematic of the Diamond Light Source at RAL (b) shadowgraph of a plasma channel in a laser-wakefield gas cell, edited from Cole [30].

B.2 Derivation of the dispersion relation

Starting from the curl of Faradays law:

$$\nabla \times (\nabla \times \mathbf{E}) = -\frac{d}{dt}(\nabla \times \mathbf{B}) \quad (\text{B.1})$$

and the vector identity, $\nabla \times (\nabla \times \mathbf{A}) = \nabla(\nabla \cdot \mathbf{A}) - \nabla^2 \mathbf{A}$. This links the electric

field and plasma current as such:

$$\nabla^2 \mathbf{E} = \frac{1}{c^2} \frac{d^2 \mathbf{E}}{dt^2} + \mu_0 \frac{d\mathbf{j}}{dt} \quad (\text{B.2})$$

By substituting in the general solution for the electric field (Eq. ??), and describing the current density as the number of electrons moving past a certain area ($\mathbf{j} = -en_e \frac{d\mathbf{r}}{dt}$) each derivative can be individually solved to show that:

$$\nabla^2 \mathbf{E} = -k^2 \mathbf{E} \quad (\text{B.3}) \quad \frac{d^2 \mathbf{E}}{dt^2} = -\frac{\omega_L^2}{c^2} \mathbf{E} \quad (\text{B.4}) \quad \frac{d\mathbf{j}}{dt} = -en_e \frac{d^2 \mathbf{r}}{dt^2} \quad (\text{B.5})$$

$$-k^2 = -\frac{\omega_L^2}{c^2} - \mu_0 \frac{d^2 \mathbf{r}}{dt^2} \quad (\text{B.6})$$

Using $c^2 = (\mu_0 \epsilon_0)^{-1}$ and $\frac{d^2 \mathbf{r}}{dt^2} = \frac{e\mathbf{E}}{m}$, the dispersion relationship for a EM field and plasma can be expressed as:

$$\omega_L^2 - \omega_p^2 = k^2 c^2 \quad (\text{B.7})$$

B.3 Vulcan laser system

Vulcan is a near IR, PW, laser with two target areas, Petawatt (TAP) and West (TAW), each with differing parameters. TAP is seeded by a commercial Ti:Sapphire laser delivering a chain of 200 fs pulses with nanojoules of energy from which a single pulse is selected and sent to an *optical-parametric-chirped-pulse-amplification* (OPCPA) pre-amplifier [198]. The OPCPA stretches and amplifies to a few nanoseconds in length and several millijoules of energy, combining the two techniques described before. There are then two main amplifier stages, the rod and the disc amplifiers. After the rod chain the pulse

Appendix B.

contains ~ 85 J, it is then sent through the final amplification stage. 6 flash-lamp driven disc amplifiers are used to bring the final energy up to ~ 700 J pre-compressor. During amplification the pulse is focused through pinholes many times the diffraction limit to remove the higher frequency components of the pulse, this ensures that the final delivered pulse has minimal spatial aberrations. It is then expanded to 600 mm before being delivered, under vacuum, into the laser area. Here, it is compressed in a single pass compressor and focused into the target chamber using an off-axis $f/3$ parabola, bringing the spot size down to $\sim 3.5 \mu\text{m}$ and a typical maximum intensity of (5×10^{20} W/cm²).

		Petawatt		West	
		<i>short</i>	<i>short</i>	<i>long</i>	<i>ns (x6)</i>
Energy	J	700	150	300	50-300
Pulse duration		0.5 ps	1.2 ps	14 ps	0.5-8 ns
Compressor throughput	%	65	85	65	-
Final optic	#	3.1	3	3-15	8-15
Nominal Intensity	W/cm ²	10^{20-21}	10^{19-20}	10^{18-19}	10^{14-16}

Table B.1: Summary of laser parameters for each target area in the Vulcan laser system. For both areas the primary wavelength is $1.054 \mu\text{m}$. The shot rate is one per 20-45 minutes, some amplifiers are shared between the areas requiring delay between TAP and West shots.

The second target area, West, is capable of delivering a range of laser parameters and utilising all 8 beam paths that are part of the Vulcan laser system. Beam 7 and 8 are short pulse beams for West, delivering 1 ps and 10 ps at 100 and 250 J respectively. These rely on an alternate final amplifier chain compared to TAP and a Nd:glass seed laser instead of the Ti:Sapphire. The 6 remaining beams are long nanosecond lasers capable of being amplified to ~ 300 J each using a series of rod amplifiers, these are seeded with higher energy initial pulses than the short pulse trains used in TAP and B7/B8. Table B.1 shows the primary differences between the target areas.

B.4 Numerical Modelling

In EPOCH the PIC sequence, shown in Figure 4.16 is broken down and half-steps are introduced in the temporal evolution of the simulation. On each full time step, $X^{n,n+1}$, the magnetic field and particle momenta is updated and each half step, $X^{n+1/2,n+3/2}$, the electric field and particle position is updated, in doing so this reduces inconsistencies caused by the finite temporal steps that the simulation can evolve through. This "leapfrog" technique is akin to another technique deployed by numerous other numerical codes, a schematic of the process is outlined in Figure B.2(a).

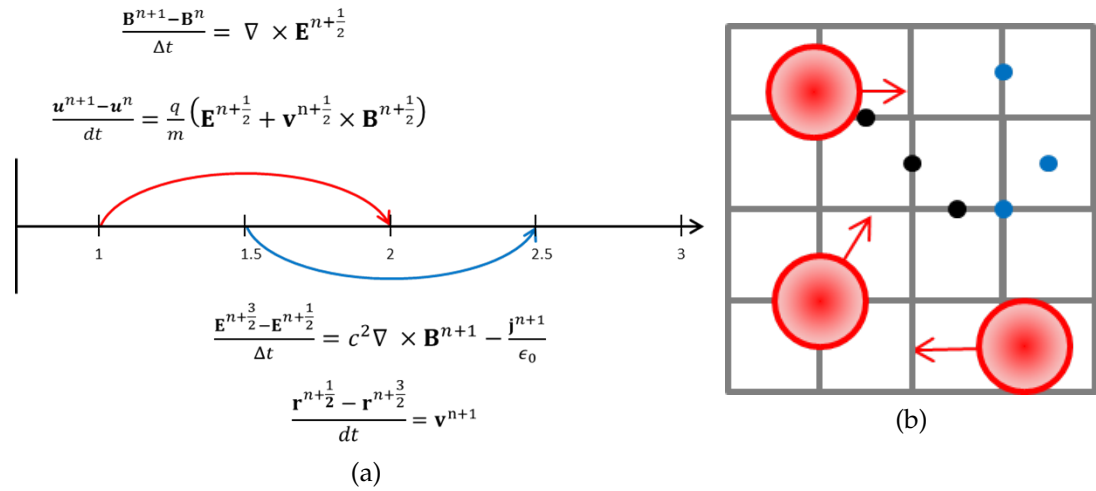


Figure B.2: (a) Leap-frog calculations of field and momenta in EPOCH - equations are taken from Arber *et al.* [31]. (b) Schematic of macro-particle operation within PIC simulations; the macro-particles are the large red circles with a gradient fill demonstrating the relative particle density at the limits of the macro-particle volume, the black and blue dots at fixed cell positions represent the current density and field calculation points respectively

Each distribution system has 6 dimensions that need to be determined at each point, 3 spatial, and 3 momenta, - i.e. where the particle is and where the particle is going. This is clearly an enormous task considering the 10^{15}

electrons readily accelerated by a laser-plasma interaction. Current modelling makes some assumptions to simplify this, often assuming that the systems are collision-less, and weighting particles to significantly reduce the number to be computed. These weighted macro-particles represent a large number of particles that are influenced by the surrounding conditions as one, and exist as a cloud of finite volume and density able to move throughout the simulation. The macro-particles do not exert force internally, however, they are effected by the field structure as a set of particles with a set energy and influence the surrounding fields as a spatial distribution of charges. A schematic of the grid and macro-particles within a simulation is displayed in Figure B.2(b), the macro-particles are the large red circles with a gradient fill demonstrating the relative particle density at the limits of the macro-particle volume, the black and blue dots at fixed cell positions represent the current density and field calculation points respectively.

Both the leapfrog technique and macro-particles are methods to mitigate the effects of solving continuous evolution in finite steps. However, an issue that presents itself across PIC simulations is self-heating. As the particle densities at each time-step inform the subsequent field evolution, any statistical error (or noise) in the particle density can cause a cascade which in turn heats the simulation in a way that is not physically valid. For example, if a target is defined in a PIC simulation to exist at the boundary and its initial electron thermal distribution gives it some finite chance of losing an electron to the boundary then the previously charge-neutral cell will no longer be charge neutral and on the subsequent step this will be reflected in the field, causing further electrons to be displaced.

Bibliography

- [1] P. Gibbon. *Short Pulse Laser Interactions with Matter*. Imperial College Press, 2004.
- [2] C. N. Danson, P. A. Brummitt, R. J. Clarke, J. L. Collier, B. Fell, A. J. Frackiewicz, S. Hancock, S. Hawkes, C. Hernandez-Gomez, P. Holligan, M. H. R. Hutchinson, A. Kidd, W. J. Lester, I. O. Musgrave, D. Neely, D. R. Neville, P. A. Norreys, D. A. Pepler, C. J. Reason, W. Shaikh, T. B. Winstone, R. W. W. Wyatt, and B. E. Wyborn. Vulcan petawatt - An ultra-high-intensity interaction facility. *Nuclear Fusion*, 44(12), 2004.
- [3] I. Musgrave, M. Galimberti, A. Boyle, C. Hernandez-Gomez, A. Kidd, B. Parry, D. Pepler, T. Winstone, and J. Collier. Review of laser diagnostics at the Vulcan laser facility. *High Power Laser Science and Engineering*, 3(February 2016):e26, 2015.
- [4] S.-W. Bahk, P. Rousseau, T. A. Planchon, V. Chvykov, G. Kalintchenko, A. Maksimchuk, G. A. Mourou, and V. Yanovsky. Generation and characterization of the highest laser intensities (10^{22} W/cm²). *Optics Letters*, 29(24):2837, 2004.
- [5] J. C. Gauthier, F. Amiranoff, C. Chenais-Popovics, G. Jamelot, M. Koenig, C. Labaune, E. Leboucher-Dalimier, C. Sauteret, and A. Migus. Activities in the field of high-power laser-matter interaction. *Laser and Particle Beams*, 17(2):195–208, 1999.
- [6] J. C. Kieffer, P. Audebert, M. Chaker, J. P. Matte, H. Pépin, T. W. Johnston, P. Maine, D. Meyerhofer, J. Delettrez, D. Strickland, P. Bado, and

- G. Mourou. Short-pulse laser absorption in very steep plasma density gradients. *Physical Review Letters*, 62(7):760–763, 1989.
- [7] L. J. Waxer, D. N. Maywar, J. H. Kelly, T. J. Kessler, B. E. Kruschwitz, S. J. Loucks, R. L. McCrory, D. D. Meyerhofer, S. F. B. Morse, C. Stoeckl, and J. D. Zuegel. High-Energy Petawatt Capability for the Omega Laser. *Opt. Photon. News*, 16(7):30–36, 2005.
- [8] J. Myatt, W. Theobald, J. A. Delettrez, C. Stoeckl, M. Storm, T. C. Sangster, A. V. Maximov, and R. W. Short. High-intensity laser interactions with mass-limited solid targets and implications for fast-ignition experiments on OMEGA EP. *Physics of Plasmas*, 14(5), 2007.
- [9] E.-N. P. working Groups. The White Book of ELI Nuclear Physics, 2013. URL <http://www.eli-np.ro/documents/ELI-NP-WhiteBook.pdf>.
- [10] C. M. M. Brenner, S. R. Mirfayzi, D. R. Rusby, C. Armstrong, A. Alejo, L. A. Wilson, R. Clarke, H. Ahmed, N. M. H. Butler, D. Haddock, A. Higginson, A. McClymont, C. Murphy, M. Notley, P. Oliver, R. Allott, C. Hernandez-Gomez, S. Kar, P. McKenna, and D. Neely. Laser-driven source development for industrial applications of plasma accelerators. *Plasma Physics and Controlled Fusion*, 58(1):14039, 2015.
- [11] A. V. Arefiev, V. N. Khudik, A. P. L. Robinson, G. Shvets, L. Willingale, and M. Schollmeier. Beyond the ponderomotive limit: Direct laser acceleration of relativistic electrons in sub-critical plasmas. *Physics of Plasmas*, 23(5), 2016.
- [12] J. E. Calvert, A. J. Palmer, I. V. Litvinyuk, and R. T. Sang. Metastable noble gas atoms in strong-field ionization experiments. *High Power Laser Science and Engineering*, 4:1–27, 2016.

- [13] P. Gibbon. Short Pulse Laser Interactions with Matter: An Introduction. *Short Pulse Laser Interactions with Matter: An Introduction*, page 328, 2005.
- [14] M. J. Berger, J. S. Coursey, M. A. Zucker, and J. Chang. Stopping-Power and Range Tables for Electrons, Protons, and Helium Ions — NIST, 1998. URL <https://www.nist.gov/pml/stopping-power-range-tables-electrons-protons-and-helium-ions>.
- [15] M. J. Berger, J. H. Hubbell, S. M. Seltzer, J. Chang, J. S. Coursey, R. Sukumar, and D. S. Zucker. XCOM: photon cross sections database. *NIST Standard Reference Database*, 8:87–3597, 1998.
- [16] R. Wilson. *On the role of focal spot size in ultra-intense laser-solid interaction physics*. PhD thesis, University of Strathclyde, 2018. URL <http://ethos.bl.uk/OrderDetails.do?uin=uk.bl.ethos.742074>.
- [17] D. Rusby, R. Gray, N. Butler, R. Dance, G. Scott, V. Bagnoud, B. Zielbauer, P. McKenna, and D. Neely. Escaping Electrons from Intense Laser-Solid Interactions as a Function of Laser Spot Size. *EPJ Web of Conferences*, 167: 2001, 2018.
- [18] F. N. Beg, A. R. Bell, A. E. Dangor, C. N. Danson, A. P. Fews, M. E. Glin-sky, B. A. Hammel, P. Lee, P. A. Norreys, and M. Tatarakis. A study of picosecond laser–solid interactions up to 10^{19} W/cm². *Physics of Plasmas*, 4(2):447–457, 1997.
- [19] J. R. Davies. Laser absorption by overdense plasmas in the relativistic regime. *Plasma Physics and Controlled Fusion*, 51(1), 2009.
- [20] J. S. Green, V. M. Ovchinnikov, R. G. Evans, K. U. Akli, H. Azechi, F. N. Beg, C. Bellei, R. R. Freeman, H. Habara, R. Heathcote, M. H. Key, J. A. King, K. L. Lancaster, N. C. Lopes, T. Ma, A. J. MacKinnon, K. Markey, A. McPhee, Z. Najmudin, P. Nilson, R. Onofrei, R. Stephens, K. Takeda,

- K. A. Tanaka, W. Theobald, T. Tanimoto, J. Waugh, L. Van Woerkom, N. C. Woolsey, M. Zepf, J. R. Davies, and P. A. Norreys. Effect of laser intensity on fast-electron-beam divergence in solid-density plasmas. *Physical Review Letters*, 100(1):1–4, 2008.
- [21] D. R. Rusby. *Study of Escaping Electron Dynamics and Applications from High-Power Laser-Plasma Interactions*. PhD thesis, University of Strathclyde, 2017.
- [22] C. Ziener, P. S. Foster, E. J. Divall, C. J. Hooker, M. H. Hutchinson, A. J. Langley, and D. Neely. Specular reflectivity of plasma mirrors as a function of intensity, pulse duration, and angle of incidence. *Journal of Applied Physics*, 93(1):768–770, 2003.
- [23] B. Dromey, S. Kar, M. Zepf, and P. Foster. The plasma mirror - A sub-picosecond optical switch for ultrahigh power lasers. *Review of Scientific Instruments*, 75(3):645–649, 2004.
- [24] M. J. Streeter, P. S. Foster, F. H. Cameron, M. Borghesi, C. Brenner, D. C. Carroll, E. Divall, N. P. Dover, B. Dromey, P. Gallegos, J. S. Green, S. Hawkes, C. J. Hooker, S. Kar, P. McKenna, S. R. Nage, Z. Najmudin, C. A. Palmer, R. Prasad, K. E. Quinn, P. P. Rajeev, A. P. Robinson, L. Romagnani, J. Schreiber, C. Spindloe, S. Ter-Avetisyan, O. Tresca, M. Zepf, and D. Neely. Relativistic plasma surfaces as an efficient second harmonic generator. *New Journal of Physics*, 13, 2011.
- [25] T. Kluge, S. A. Gaillard, K. A. Flippo, T. Burris-Mog, W. Enghardt, B. Gall, M. Geissel, A. Helm, S. D. Kraft, T. Lockard, J. Metzkes, D. T. Offermann, M. Schollmeier, U. Schramm, K. Zeil, M. Bussmann, and T. E. Cowan. High proton energies from cone targets: Electron acceleration mechanisms. *New Journal of Physics*, 14, 2012.

- [26] D. R. Rusby, C. D. Armstrong, C. M. Brenner, P. Mckenna, and D. Neely. Novel Scintillator based x-ray spectrometer for use on high repetition laser plasma interaction. *Review of Scientific Instruments*, 89(7), 2018.
- [27] J. D. Palmer and G. A. Fairhall. Properties of cement systems containing intermediate level wastes. *Cement and Concrete Research*, 22(2-3):325–330, 1992.
- [28] G. A. Fairhall and J. D. Palmer. The encapsulation of Magnox Swarf in cement in the United Kingdom. *Cement and Concrete Research*, 22(2-3): 293–298, 1992.
- [29] H. A. Kramers. XCIII. On the theory of X-ray absorption and of the continuous X-ray spectrum. *The London, Edinburgh, and Dublin Philosophical Magazine and Journal of Science*, 46(275):836–871, 1923.
- [30] J. M. Cole. *Diagnosis and Application of Laser Wakefield Accelerators*. PhD thesis, Imperial College London, 2016.
- [31] T. D. Arber, K. Bennett, C. S. Brady, A. Lawrence-Douglas, M. G. Ramsay, N. J. Sircombe, P. Gillies, R. G. Evans, H. Schmitz, A. R. Bell, and C. P. Ridgers. Contemporary particle-in-cell approach to laser-plasma modelling. *Plasma Physics and Controlled Fusion*, 57(11):113001, 2015.
- [32] D. M. O'Neill, C. L. S. Lewis, D. Neely, S. J. Davidson, S. J. Rose, and R. W. Lee. Characterization of a laser produced plasma using the technique of point projection absorption spectroscopy. *Physical Review A*, 44(4), 1991.
- [33] C. D. Chen, J. A. King, M. H. Key, K. U. Akli, F. N. Beg, H. Chen, R. R. Freeman, A. Link, A. J. MacKinnon, A. G. MacPhee, P. K. Patel, M. Porkolab, R. B. Stephens, and L. D. Van Woerkom. A Bremsstrahlung spectrometer using k-edge and differential filters with image plate dosimeters. *Review of Scientific Instruments*, 79(10):130–133, 2008.

- [34] A. L. Meadowcroft and R. D. Edwards. High-Energy Bremsstrahlung Diagnostics to Characterize Hot-Electron Production in. *Ieee Transactions on Plasma Science*, 40(8):1992–2001, 2012.
- [35] M. D. Perry, J. A. Sefcik, T. Cowan, S. Hatchett, A. Hunt, M. Moran, D. Pennington, R. Snavely, and S. C. Wilks. Hard x-ray production from high intensity laser solid interactions (invited). *Review of Scientific Instruments*, 70(1):265–269, 1999.
- [36] R. D. Edwards, M. A. Sinclair, T. J. Goldsack, K. Krushelnick, F. N. Beg, E. L. Clark, A. E. Dangor, Z. Najmudin, M. Tatarakis, B. Walton, M. Zepf, K. W. D. Ledingham, I. Spencer, P. A. Norreys, R. J. Clarke, R. Kodama, Y. Toyama, and M. Tambo. Characterization of a gamma-ray source based on a laser-plasma accelerator with applications to radiography. *Applied Physics Letters*, 80(12):2129–2131, 2002.
- [37] P. A. Norreys, M. Santala, E. Clark, M. Zepf, I. Watts, F. N. Beg, K. Krushelnick, M. Tatarakis, A. E. Dangor, X. Fang, P. Graham, T. McCanny, R. P. Singhal, K. W. D. Ledingham, A. Creswell, D. C. W. Sanderson, J. Magill, A. Machacek, J. S. Wark, R. Allott, B. Kennedy, and D. Neely. Observation of a highly directional γ -ray beam from ultrashort, ultraintense laser pulse interactions with solids. *Physics of Plasmas*, 6(5):2150–2156, 1999.
- [38] F. Fiorini, D. Neely, R. J. Clarke, and S. Green. Characterization of laser-driven electron and photon beams using the Monte Carlo code FLUKA. *Laser and Particle Beams*, 32(02):233–241, 2014.
- [39] K. Vaughan, A. S. Moore, V. Smalyuk, K. Wallace, D. Gate, S. G. Glendinning, S. McAlpin, H. S. Park, C. Sorce, and R. M. Stevenson. High-resolution 22-52keV backlighter sources and application to X-ray radiography. *High Energy Density Physics*, 9(3):635–641, 2013.

- [40] A. Einstein. Zur quantentheorie der strahlung. *Phys. Z.*, 18:121–128, 1917.
- [41] A. L. Schawlow and C. H. Townes. Infrared and optical masers. *Physical Review*, 112(6):1940–1949, 1958.
- [42] T. H. Maiman. Stimulated optical radiation in Ruby. *Nature*, 1960.
- [43] D. Strickland and G. Mourou. Compression of Amplified Chirped Optical Pulses. *Optics Communications*, 55(6):447–449, 1985.
- [44] NobelPrize.org. The Nobel Prize in Physics 2018, 2019. URL <https://www.nobelprize.org/prizes/physics/2018/summary/>.
- [45] I. Langmuir. Oscillations in ionized gases. *Proceedings of the National Academy of Sciences*, 14(8):627–637, 1928.
- [46] J. M. Dawson. On the production of plasma by giant pulse lasers. *The Physics of Fluids*, 7(7):981–987, 1964.
- [47] P. Kaw and J. Dawson. Relativistic nonlinear propagation of laser beams in cold overdense plasmas. *The Physics of Fluids*, 13(2):472–481, 1970.
- [48] D. Evans and J. Katzenstein. Laser light scattering in laboratory plasmas. *Reports on Progress in Physics*, 32(1):207, 1969.
- [49] W. I. Linlor. Ion energies produced by laser giant pulse. *Applied Physics Letters*, 3(11):210–211, 1963.
- [50] M. Bernstein and G. Comisar. X-ray production in laser-heated plasmas. *Journal of Applied Physics*, 41(2):729–733, 1970.
- [51] T. Tajima and J. M. Dawson. Laser electron accelerator. *Physical Review Letters*, 1979.

- [52] P. McKenna, D. C. Carroll, O. Lundh, F. Nrnberg, K. Markey, S. Bandyopadhyay, D. Batani, R. G. Evans, R. Jafer, S. Kar, D. Neely, D. Pepler, M. N. Quinn, R. Redaelli, M. Roth, C. G. Wahlström, X. H. Yuan, and M. Zepf. Effects of front surface plasma expansion on proton acceleration in ultraintense laser irradiation of foil targets. *Laser and Particle Beams*, 26(4):591–596, 2008.
- [53] S. Kar, K. Markey, P. T. Simpson, C. Bellei, J. S. Green, S. R. Nagel, S. Kneip, D. C. Carroll, B. Dromey, L. Willingale, E. L. Clark, P. McKenna, Z. Najmudin, K. Krushelnick, P. Norreys, R. J. Clarke, D. Neely, M. Borghesi, and M. Zepf. Dynamic control of laser-produced proton beams. *Physical Review Letters*, 100(10):1–4, 2008.
- [54] D. Neely, P. Foster, A. Robinson, F. Lindau, O. Lundh, A. Persson, C. G. Wahlström, and P. McKenna. Enhanced proton beams from ultrathin targets driven by high contrast laser pulses. *Applied Physics Letters*, 89(2):87–90, 2006.
- [55] A. J. MacKinnon, P. K. Patel, M. Borghesi, R. C. Clarke, R. R. Freeman, H. Habara, S. P. Hatchett, D. Hey, D. G. Hicks, S. Kar, M. H. Key, J. A. King, K. Lancaster, D. Neely, A. Nikkro, P. A. Norreys, M. M. Notley, T. W. Phillips, L. Romagnani, R. A. Snavely, R. B. Stephens, and R. P. Town. Proton radiography of a laser-driven implosion. *Physical Review Letters*, 97(4):13–16, 2006.
- [56] M. Hegelich, S. Karsch, G. Pretzler, D. Habs, K. Witte, W. Guenther, M. Allen, A. Blazevic, J. Fuchs, J. C. Gauthier, M. Geissel, P. Audebert, T. Cowan, and M. Roth. MeV ion jets from short-pulse-laser interaction with thin foils. *Physical Review Letters*, 89(8):085002/1—085002/4, 2002.
- [57] M. Roth, D. Jung, K. Falk, N. Guler, O. Deppert, M. Devlin, A. Favalli, J. Fernandez, D. Gautier, M. Geissel, et al. Bright laser-driven neutron

- source based on the relativistic transparency of solids. *Physical review letters*, 110(4):044802, 2013.
- [58] I. B. Földes, J. S. Bakos, G. Veres, Z. Bakonyi, T. Nagy, and S. Szatmári. Harmonic generation in a UV laser plasma. *IEEE Journal on Selected Topics in Quantum Electronics*, 2(3):776–780, 1996.
- [59] P. A. Norreys, M. Zepf, S. Moustazis, A. P. Fews, J. Zhang, P. Lee, M. Bakarezos, C. N. Danson, A. Dyson, P. Gibbon, P. Loukakos, D. Neely, F. N. Walsh, J. S. Wark, and A. E. Dangor. Efficient extreme UV harmonics generated from picosecond laser pulse interactions with solid targets. *Physical Review Letters*, 76(11):1832–1835, 1996.
- [60] B. Dromey, S. Rykovanov, M. Yeung, R. Hörlein, D. Jung, D. Gautier, T. Dzelzainis, D. Kiefer, S. Palaniyppan, R. Shah, et al. Coherent synchrotron emission from electron nanobunches formed in relativistic laser–plasma interactions. *Nature Physics*, 8(11):804, 2012.
- [61] Y. Nomura, R. Hörlein, P. Tzallas, B. Dromey, S. Rykovanov, Z. Major, J. Osterhoff, S. Karsch, L. Veisz, M. Zepf, et al. Attosecond phase locking of harmonics emitted from laser-produced plasmas. *Nature Physics*, 5(2):124, 2009.
- [62] Y. T. Li, C. Li, M. L. Zhou, W. M. Wang, F. Du, W. J. Ding, X. X. Lin, F. Liu, Z. M. Sheng, X. Y. Peng, L. M. Chen, J. L. Ma, X. Lu, Z. H. Wang, Z. Y. Wei, and J. Zhang. Strong terahertz radiation from relativistic laser interaction with solid density plasmas. *Applied Physics Letters*, 100(25):1–5, 2012.
- [63] G. Q. Liao, Y. T. Li, C. Li, H. Liu, Y. H. Zhang, W. M. Jiang, X. H. Yuan, J. Nilsen, T. Ozaki, W. M. Wang, Z. M. Sheng, D. Neely, P. McKenna, and J. Zhang. Intense terahertz radiation from relativistic laser-plasma interactions. *Plasma Physics and Controlled Fusion*, 59(1), 2017.

- [64] K. W. D. Ledingham and W. Galster. Laser-driven particle and photon beams and some applications. *New Journal of Physics*, 12(4):45005, 2010.
- [65] F. Albert, A. G. R. Thomas, S. P. D. Mangles, S. Banerjee, A. Flacco, M. Litos, D. Neely, J. Viera, R. Bingham, C. Joshi, T. Katsouleas, S. Corde, A. Flacco, M. Litos, D. Neely, J. Vieira, Z. Najmudin, R. Bingham, C. Joshi, and T. Katsouleas. Laser wakefield accelerator based light sources: potential applications and requirements. *Plasma Physics and Controlled Fusion*, 56(8):84015, 2014.
- [66] E. Esarey, C. B. Schroeder, and W. P. Leemans. Physics of laser-driven plasma-based electron accelerators. *Reviews of Modern Physics*, 81(3):1229–1285, 2009.
- [67] G. A. Cirrone, M. Carpinelli, G. Cuttone, S. Gammino, S. B. Jia, G. Korn, M. Maggiore, L. Manti, D. Margarone, J. Prokupek, et al. Elimed, future hadrontherapy applications of laser-accelerated beams. *Nuclear Instruments and Methods in Physics Research Section A: Accelerators, Spectrometers, Detectors and Associated Equipment*, 730:174–177, 2013.
- [68] M. Tabak, J. Hammer, M. E. Glinsky, W. L. Kruer, S. C. Wilks, J. Woodworth, E. M. Campbell, M. D. Perry, and R. J. Mason. Ignition and high gain with ultrapowerful lasers. *Physics of Plasmas*, 1(5):1626–1634, 1994.
- [69] M. Roth, T. Cowan, M. Key, S. Hatchett, C. Brown, W. Fountain, J. Johnson, D. Pennington, R. Snavely, S. Wilks, et al. Fast ignition by intense laser-accelerated proton beams. *Physical review letters*, 86(3):436, 2001.
- [70] G. G. Scott. *On the use of multiple high intensity laser pulses in ion acceleration experiments*. PhD thesis, University of Strathclyde, 2014.
- [71] R. J. Gray. *On Mechanisms of Laser-Coupling to Fast Electrons in Ultraintense Laser-Solid Interactions* by. PhD thesis, University of Strathclyde, 2013.

- [72] R. Kidder. Application of lasers to the production of high-temperature and high-pressure plasma. *Nuclear Fusion*, 8(1):3–12, 1968.
- [73] J. Nuckolls, L. Wood, A. Thiessen, and G. Zimmerman. Laser compression of matter to super-high densities: Thermonuclear (CTR) applications. *Nature*, 239(5368):139–142, 1972.
- [74] J. D. Lindl, P. Amendt, R. L. Berger, S. G. Glendinning, S. H. Glenzer, S. W. Haan, R. L. Kauffman, O. L. Landen, and L. J. Suter. The physics basis for ignition using indirect-drive targets on the National Ignition Facility. *Physics of Plasmas*, 11(2):339–491, 2004.
- [75] R. S. Craxton, K. S. Anderson, T. R. Boehly, V. N. Goncharov, D. R. Harding, J. P. Knauer, R. L. McCrory, P. W. McKenty, D. D. Meyerhofer, J. F. Myatt, A. J. Schmitt, J. D. Sethian, R. W. Short, S. Skupsky, W. Theobald, W. L. Kruer, K. Tanaka, R. Betti, T. J. Collins, J. A. Delettrez, S. X. Hu, J. A. Marozas, A. V. Maximov, D. T. Michel, P. B. Radha, S. P. Regan, T. C. Sangster, W. Seka, A. A. Solodov, J. M. Soures, C. Stoeckl, and J. D. Zuegel. Direct-drive inertial confinement fusion: A review. *Physics of Plasmas*, 22(11), 2015.
- [76] C. P. Jones, C. M. Brenner, C. A. Stitt, C. D. Armstrong, D. R. Rusby, S. R. Mirfayzi, L. A. Wilson, H. Ahmed, R. Allott, N. M. H. Butler, R. J. Clarke, D. Haddock, C. Hernandez-Gomez, A. Higginson, C. D. Murphy, C. Paraskevoulakos, P. McKenna, D. Neely, S. Kar, and T. B. Scott. Evaluating laser driven photon sources for the analytical scanning of nuclear waste. *Journal of Hazardous Materials*, 2015.
- [77] C. Courtois, A. Compant La Fontaine, O. Landoas, G. Lidove, V. Mot, P. Morel, R. Nuter, E. Lefebvre, A. Boscheron, J. Grenier, M. M. Alonard, M. Gerbaux, F. Gobet, F. Hannachi, G. Malka, J. N. Scheurer, and M. Tarisien. Effect of plasma density scale length on the properties of

- bremsstrahlung x-ray sources created by picosecond laser pulses. *Physics of Plasmas*, 16(1), 2009.
- [78] H. S. Park, B. R. Maddox, E. Giraldez, S. P. Hatchett, L. T. Hudson, N. Izumi, M. H. Key, S. Le Pape, A. J. MacKinnon, A. G. MacPhee, P. K. Patel, T. W. Phillips, B. A. Remington, J. F. Seely, R. Tommasini, R. Town, J. Workman, and E. Brambrink. High-resolution 17-75 keV backlighters for high energy density experiments. *Physics of Plasmas*, 15(7), 2008.
- [79] E. Brambrink, H. G. Wei, B. Barbrel, P. Audebert, A. Benuzzi-Mounaix, T. Boehly, T. Endo, C. Gregory, T. Kimura, R. Kodama, N. Ozaki, H. S. Park, M. R. Le Gloahec, and M. Koenig. X-ray source studies for radiography of dense matter. *Physics of Plasmas*, 16(3), 2009.
- [80] R. Tommasini, A. MacPhee, D. Hey, T. Ma, C. Chen, N. Izumi, W. Unites, A. MacKinnon, S. P. Hatchett, B. A. Remington, H. S. Park, P. Springer, J. A. Koch, O. L. Landen, J. Seely, G. Holland, and L. Hudson. Development of backlighting sources for a Compton radiography diagnostic of inertial confinement fusion targets. *Review of Scientific Instruments*, 79(10):1–5, 2008.
- [81] L. Willingale, G. Petrov, A. Maksimchuk, J. Davis, R. Freeman, A. Joglekar, T. Matsuoka, C. Murphy, V. Ovchinnikov, A. Thomas, et al. Comparison of bulk and pitcher-catcher targets for laser-driven neutron production. *Physics of Plasmas*, 18(8):083106, 2011.
- [82] S. Kar, A. Green, H. Ahmed, A. Alejo, A. Robinson, M. Cerchez, R. Clarke, D. Doria, S. Dorkings, J. Fernandez, et al. Beamed neutron emission driven by laser accelerated light ions. *New Journal of Physics*, 18(5):053002, 2016.
- [83] C. Zulick, F. Dollar, V. Chvykov, J. Davis, G. Kalinchenko, A. Maksimchuk, G. Petrov, A. Raymond, A. Thomas, L. Willingale, et al. Energetic

- neutron beams generated from femtosecond laser plasma interactions. *Applied Physics Letters*, 102(12):124101, 2013.
- [84] P. Mason, M. Divoký, K. Ertel, J. Pilař, T. Butcher, M. Hanuš, S. Banerjee, J. Phillips, J. Smith, M. De Vido, A. Lucianetti, C. Hernandez-Gomez, C. Edwards, T. Mocek, and J. Collier. Kilowatt average power 100 J-level diode pumped solid state laser. *Optica*, 4(4):438, 2017.
- [85] A. K. Gujba and M. Medraj. Laser Peening Process and Its Impact on Materials Properties in Comparison with Shot Peening and Ultrasonic Impact Peening. *Materials*, 7:7925–7974, 2014.
- [86] H. Yoshida, K. Tsubakimoto, Y. Fujimoto, K. Mikami, H. Fujita, N. Miyanaga, H. Nozawa, H. Yagi, T. Yanagitani, Y. Nagata, and H. Kinoshita. Optical properties and Faraday effect of ceramic terbium gallium garnet for a room temperature Faraday rotator. *Optics Express*, 19(16):15181, 2011.
- [87] J. C. Maxwell. A Dynamical Theory of the Electromagnetic Field. *Phil. Trans. of the Royal Soc. of London*, 155(January):459–512, 1865.
- [88] A. P. L. Robinson, A. V. Arefiev, and D. Neely. Generating “superponderomotive” electrons due to a non-wake-field interaction between a laser pulse and a longitudinal electric field. *Physical Review Letters*, 111(6):1–5, 2013.
- [89] A. Gold and H. B. Bebb. Theory of multiphoton ionization. *Physical Review Letters*, 14(3):60–63, 1965.
- [90] P. Agostini, G. Barjot, J. Bonnal, G. Mainfray, C. Manus, and J. Morelle. Multiphoton ionization of hydrogen and rare gases. *IEEE Journal of Quantum Electronics*, 4(10):667–669, 1968.

- [91] G. S. Voronov and N. B. Delone. Ionization of the xenon atom by the electric field of ruby laser emission, 1965. URL http://www.jetpletters.ac.ru/ps/1590/article_{-}24398.pdf.
- [92] C. Mainfray, G; Manus. Multiphoton Ionization of Atoms. *Rep. Prog. Phys*, 1333, 1991.
- [93] J. Morellec, D. Normand, and G. Petite. Nonresonant Multiphoton Ionization of Atoms. *Advances in Atomic and Molecular Physics*, 18(C):97–164, 1982.
- [94] Y. Gontier, M. Poirier, and M. Trahin. Multi-photon absorptions above the ionization threshold. *Journal of physics B-Atomic molecular optical physics*, 13(7):1381, 1980.
- [95] P. Agostini, F. Fabre, G. Mainfray, G. Petite, and N. K. Rahman. Free-free transitions following six-photon ionization of xenon atoms. *Physical Review Letters*, 42(17):1127–1130, 1979.
- [96] Y. Gontier and M. Trahin. Energetic electron generation by multiphoton absorption. *Journal of Physics B: Atomic and Molecular Physics*, 13(22):4383–4390, 1980.
- [97] N. B. Delone and V. P. Krainov. Tunneling and barrier-suppression ionization of atoms and ions in a laser radiation field. *Physics-Uspokhi*, 41(5):469–485, 1998.
- [98] W. Crookes. I. on a fourth state of matter, in a letter to the secretary. by w. crookes, fr s. *Proceedings of the Royal Society of London*, 30(200-205):469–472, 1880.
- [99] A. Piel. *Plasma physics: An introduction to laboratory, space, and fusion plasmas*. Springer, 2010.

- [100] R. J. Gray, D. C. Carroll, X. H. Yuan, C. M. Brenner, M. Burza, M. Coury, K. L. Lancaster, X. X. Lin, Y. T. Li, D. Neely, M. N. Quinn, O. Tresca, C. G. Wahlström, and P. McKenna. Laser pulse propagation and enhanced energy coupling to fast electrons in dense plasma gradients. *New Journal of Physics*, 16, 2014.
- [101] V. M. Ovchinnikov, D. W. Schumacher, M. McMahon, E. A. Chowdhury, C. D. Chen, A. Morace, and R. R. Freeman. Effects of preplasma scale length and laser intensity on the divergence of laser-generated hot electrons. *Physical Review Letters*, 110(6):1–4, 2013.
- [102] M. Santala, M. Zepf, I. Watts, F. Beg, E. Clark, M. Tatarakis, K. Krushelnick, A. Dangor, T. McCanny, I. Spencer, R. Singhal, K. Ledingham, S. Wilks, A. Machacek, J. Wark, R. Allott, R. Clarke, and P. Norreys. Effect of the plasma density scale length on the direction of fast electrons in relativistic laser-solid interactions. *Physical review letters*, 84(7):1459–1462, 2000.
- [103] O. Culfa, G. J. Tallents, A. K. Rossall, E. Wagenaars, C. P. Ridgers, C. D. Murphy, R. J. Dance, R. J. Gray, P. McKenna, C. D. R. Brown, S. F. James, D. J. Hoarty, N. Booth, A. P. L. Robinson, K. L. Lancaster, S. A. Pikuz, A. Y. Faenov, T. Kampfer, K. S. Schulze, I. Uschmann, and N. C. Woolsey. Plasma scale-length effects on electron energy spectra in high-irradiance laser plasmas. *Physical Review E*, 93(4):1–10, 2016.
- [104] J. S. Green, N. Booth, R. J. Dance, R. J. Gray, D. A. MacLellan, A. Marshall, P. McKenna, C. D. Murphy, C. P. Ridgers, A. P. L. Robinson, D. Rusby, R. H. H. Scott, and L. Wilson. Time-resolved measurements of fast electron recirculation for relativistically intense femtosecond scale laser-plasma interactions. *Scientific Reports*, 8(1):1–9, 2018.
- [105] Z. E. Davidson, B. Gonzalez-Izquierdo, A. Higginson, K. L. Lancaster,

- S. D. R. Williamson, M. King, D. Farley, D. Neely, P. McKenna, and R. J. Gray. An optically multiplexed single-shot time-resolved probe of laser–plasma dynamics. *Optics Express*, 27(4):4416, 2019.
- [106] D. C. Barnes, T. Kurki-Suonio, and T. Tajima. Laser self-trapping for the plasma fiber aeeelerator. *IEEE Transactions on Plasma Science*, 15(2):154–160, 1987.
- [107] H. S. Brandi, C. Manus, G. Mainfray, and T. Lehner. Relativistic self-focusing of ultraintense laser pulses in inhomogeneous underdense plasmas. *Physical Review E*, 47(5):3780–3783, 1993.
- [108] G.-Z. Sun, E. Ott, Y. C. Lee, and P. Guzdar. Self-focusing of short intense pulses in plasmas. *Physics of Fluids*, 30(2):526, 1987.
- [109] C. E. Max, J. Arons, and A. B. Langdon. Self-modulation and self-focusing of electromagnetic waves in plasmas. *Physical Review Letters*, 33(4):209–212, 1974.
- [110] J. F. Seely and E. G. Harris. Heating of a plasma by multiphoton inverse bremsstrahlung. *Physical Review A*, 7(3):1064, 1973.
- [111] W. Kruer. The physics of laser plasma interactions westview. *Boulder, CO*, page 6, 2003.
- [112] J. P. Freidberg, R. W. Mitchell, R. L. Morse, and L. I. Rudsinski. Resonant absorption of laser light by plasma targets. *Physical Review Letters*, 28(13):795–799, 1972.
- [113] D. D. Meyerhofer, H. Chen, J. A. Delettrez, B. Soom, S. Uchida, and B. Yaakobi. Resonance absorption in high-intensity contrast, picosecond laser-plasma interactions. *Physics of Fluids B*, 5(7):2584–2588, 1993.

- [114] D. W. Forslund, J. M. Kindel, and K. Lee. Theory of Hot-Electron Spectra at High Laser Intensity D. *Phys. Rev. Lett.*, 39(5), 1977.
- [115] N. G. Denisov. On a Singularity of the Field of an Electromagnetic Wave. *Soviet Physics JETP*, 4(4):544–553, 1957.
- [116] W. L. Kruer and K. Estabrook. J×B heating by very intense laser light. *Physics of Fluids*, 28(1):430–432, 1985.
- [117] B. Bezzerides and J. Gitomer. Role of Thermalization for Electron Distributions in Resonance Absorption. *Physical Review Letters*, 46(23):2674–2677, 1987.
- [118] F. Jüttner. Das Maxwellsche Gesetz der geschwindigkeitsverteilung in der relativtheorie. *Annalen der Physik*, 339(5):856–882, 1911.
- [119] P. Gibbon. Efficient Production of Fast Electrons from Femtosecond Laser Interaction with Solid Targets. *Physical Review Letters*, 73(5):664–667, 1994.
- [120] J. R. Davies, A. R. Bell, M. G. Haines, and S. M. Guérin. Short-pulse high-intensity laser-generated fast electron transport into thick solid targets. *Physical Review E - Statistical Physics, Plasmas, Fluids, and Related Interdisciplinary Topics*, 56(6):7193–7203, 1997.
- [121] S. C. Wilks, A. B. Langdon, T. E. Cowan, M. Roth, M. Singh, S. Hatchett, M. H. Key, D. Pennington, A. MacKinnon, and R. A. Snavely. Energetic proton generation in ultra-intense laser-solid interactions. *Physics of Plasmas*, 8(2):542–549, 2001.
- [122] M. G. Haines, M. S. Wei, F. N. Beg, and R. B. Stephens. Hot-electron temperature and laser-light absorption in fast ignition. *Physical Review Letters*, 102(4):1–4, 2009.

- [123] H. Chen, S. C. Wilks, W. L. Kruer, P. K. Patel, and R. Shepherd. Hot electron energy distributions from ultraintense laser solid interactions. *Physics of Plasmas*, 16(2), 2009.
- [124] A. J. Kemp, Y. Sentoku, and M. Tabak. Hot-electron energy coupling in ultraintense laser-matter interaction. *Physical Review E - Statistical, Nonlinear, and Soft Matter Physics*, 79(6):1–9, 2009.
- [125] M. Sherlock. Universal scaling of the electron distribution function in one-dimensional simulations of relativistic laser-plasma interactions. *Physics of Plasmas*, 16:103101, 2009.
- [126] T. Kluge, T. Cowan, A. Debus, U. Schramm, K. Zeil, and M. Bussmann. Electron temperature scaling in laser interaction with solids. *Physical Review Letters*, 107(20):1–5, 2011.
- [127] Y.-Q. Cui, W.-M. Wang, Z.-M. Sheng, Y.-T. Li, and J. Zhang. Laser absorption and hot electron temperature scalings in laser–plasma interactions. *Plasma Physics and Controlled Fusion*, 55(8):85008, 2013.
- [128] H. Alfven. On the motion of cosmic rays in interstellar space. *Physical Review*, 55(5), 1939.
- [129] J. Lawson. On the adiabatic self-constriction of an accelerated electron beam neutralized by positive ions. *INTERNATIONAL JOURNAL OF ELECTRONICS*, 3(6):587–594, 1957.
- [130] A. R. Bell†, J. R. Davies†, S. Guerint†, H. Ruhl‡, C. Fusion, A. R. Bell, J. R. Davies, S. Guerin, and H. Ruhl. Fast-electron transport in high-intensity short-pulse laser – solid experiments. *Plasma Phys. Control. Fusion*, 39: 653–659, 1997.
- [131] J. R. Davies. Alfvén limit in fast ignition. *Physical Review E - Statistical Physics, Plasmas, Fluids, and Related Interdisciplinary Topics*, 69(6):4, 2004.

- [132] J. R. Davies. The Alfvén limit revisited and its relevance to laser-plasma interactions. *Laser and Particle Beams*, 24(2):299–310, 2006.
- [133] D. A. Hammer and N. Rostoker. Propagation of high current relativistic electron beams. *Physics of Fluids*, 13(7):1831–1850, 1970.
- [134] A. Debayle, J. J. Honrubia, E. D’Humières, and V. T. Tikhonchuk. Divergence of laser-driven relativistic electron beams. *Physical Review E - Statistical, Nonlinear, and Soft Matter Physics*, 82(3), 2010.
- [135] M. Coury, D. C. Carroll, A. P. L. Robinson, X. H. Yuan, C. M. Brenner, M. Burza, R. J. Gray, K. L. Lancaster, Y. T. Li, X. X. Lin, D. A. MacLellan, H. Powell, M. N. Quinn, O. Tresca, C. G. Wahlström, D. Neely, and P. McKenna. Injection and transport properties of fast electrons in ultraintense laser-solid interactions. *Physics of Plasmas*, 20(4), 2013.
- [136] X. H. Yuan, A. P. L. Robinson, M. N. Quinn, D. C. Carroll, M. Borghesi, R. J. Clarke, R. G. Evans, J. Fuchs, P. Gallegos, L. Lancia, D. Neely, K. Quinn, L. Romagnani, G. Sarri, P. A. Wilson, and P. McKenna. Effect of self-generated magnetic fields on fast-electron beam divergence in solid targets. *New Journal of Physics*, 12, 2010.
- [137] D. Margarone, O. Klimo, I. J. Kim, J. Prokūpek, J. Limpouch, T. M. Jeong, T. Mocek, J. Pkal, H. T. Kim, J. Proka, K. H. Nam, L. Tolcová, I. W. Choi, S. K. Lee, J. H. Sung, T. J. Yu, and G. Korn. Laser-driven proton acceleration enhancement by nanostructured foils. *Physical Review Letters*, 109(23):1–5, 2012.
- [138] M. Roth and M. Schollmeier. Ion Acceleration - Target Normal Sheath Acceleration. In *Laser-Plasma Interactions and Applications*, pages 303–350. Springer, 2017. URL <http://arxiv.org/abs/1705.10569>{%}0Ahttp://dx.doi.org/10.5170/CERN-2016-001.231.

- [139] F. N. Beg, M. S. Wei, E. L. Clark, A. E. Dangor, R. G. Evans, P. Gibbon, A. Gopal, K. L. Lancaster, K. W. Ledingham, P. McKenna, P. A. Norreys, M. Tatarakis, M. Zepf, and K. Krushelnick. Return current and proton emission from short pulse laser interactions with wire targets. *Physics of Plasmas*, 11(5 PART 2):2806–2813, 2004.
- [140] J. J. Honrubia and J. Meyer-Ter-Vehn. Three-dimensional fast electron transport for ignition-scale inertial fusion capsules. *Nuclear Fusion*, 46(11), 2006.
- [141] J. J. Honrubia and J. Meyer-Ter-Vehn. Fast ignition of fusion targets by laser-driven electrons. *Plasma Physics and Controlled Fusion*, 51(1), 2009.
- [142] C. I. Moore, J. P. Knauer, and D. D. Meyerhofer. Observation of the transition from thomson to compton scattering in multiphoton interactions with low-energy electrons. *Physical Review Letters*, 74(13):2439–2442, 1995.
- [143] A. Debayle, L. Gremillet, J. J. Honrubia, and E. D’Humières. Reduction of the fast electron angular dispersion by means of varying-resistivity structured targets. *Physics of Plasmas*, 20(1), 2013.
- [144] D. D. Meyerhofer. High-Intensity-Laser-Electron Scattering. *IEEE journal of quantum electronics*, 33(11):1935–1941, 1997.
- [145] A. L. S.C. Wilks, W. L. Kruer, M. Tabak, S. Wilks, W. Kruer, M. Tabak, and A. Langdon. Absorption of ultra-intense laser pulses. *Physical review letters*, 69(9):1383–1386, 1992.
- [146] Z. Sheng, Y. Sentoku, K. Mima, J. Zhang, and W. Yu. Angular Distributions of Fast Electrons, Ions, and Bremsstrahlung x / g -Rays $y \theta \propto$ Laser beam $\theta \propto x$. *Physical Review Letters*, 85(25):5340–5343, 2000.

- [147] J. D. Lawson. Angular distribution of Synchrotron Target Radiation. *Proc. Phys. Soc. A*, 63(653), 1950.
- [148] L. O. Silva, R. A. Fonseca, J. W. Tonge, W. B. Mori, and J. M. Dawson. On the role of the purely transverse Weibel instability in fast ignitor scenarios. *Physics of Plasmas*, 9(6):2458, 2002.
- [149] J. R. Davies. Electric and magnetic field generation and target heating by laser-generated fast electrons. *Physical Review E - Statistical Physics, Plasmas, Fluids, and Related Interdisciplinary Topics*, 68(5):1–7, 2003.
- [150] R. B. Campbell, J. S. DeGroot, T. A. Mehlhorn, D. R. Welch, and B. V. Oliver. Collimation of PetaWatt laser-generated relativistic electron beams propagating through solid matter. *Physics of Plasmas*, 10(10):4169–4172, 2003.
- [151] A. P. L. Robinson and M. Sherlock. Magnetic collimation of fast electrons produced by ultraintense laser irradiation by structuring the target composition. *Physics of Plasmas*, 14(8), 2007.
- [152] D. A. Maclellan, D. C. Carroll, R. J. Gray, N. Booth, M. Burza, M. P. Desjarlais, F. Du, B. Gonzalez-Izquierdo, D. Neely, H. W. Powell, A. P. L. Robinson, D. R. Rusby, G. G. Scott, X. H. Yuan, C. G. Wahlström, and P. McKenna. Annular fast electron transport in silicon arising from low-temperature resistivity. *Physical Review Letters*, 111(9), 2013.
- [153] R. Kodama, Y. Sentoku, Z. L. Chen, G. R. Kumar, S. P. Hatchett, Y. Toyama, T. E. Cowan, R. R. Freeman, J. Fuchs, Y. Izawa, M. H. Key, Y. Kitagawa, K. Kondo, T. Matsuoka, H. Nakamura, M. Nakatsutsumi, P. A. Horreys, T. Norimatsu, R. A. Snavely, R. B. Stephens, M. Tampo, K. A. Tanaka, and T. Yabuuchi. Plasma devices to guide and collimate a high density of MeV electrons. *Nature*, 432(7020):1005–1008, 2004.

- [154] R. H. H. Scott, C. Beaucourt, H. P. Schlenvoigt, K. Markey, K. L. Lancaster, C. P. Ridgers, C. M. Brenner, J. Pasley, R. J. Gray, I. O. Musgrave, A. P. L. Robinson, K. Li, M. M. Notley, J. R. Davies, S. D. Baton, J. J. Santos, J. L. Feugeas, P. Nicolai, G. Malka, V. T. Tikhonchuk, P. McKenna, D. Neely, S. J. Rose, and P. A. Norreys. Controlling fast-electron-beam divergence using two laser pulses. *Physical Review Letters*, 109(1):1–5, 2012.
- [155] S. Kar, A. P. L. Robinson, D. C. Carroll, O. Lundh, K. Markey, P. McKenna, P. Norreys, and M. Zepf. Guiding of relativistic electron beams in solid targets by resistively controlled magnetic fields. *Physical Review Letters*, 102(5):1–4, 2009.
- [156] P. McKenna, D. C. Carroll, R. J. Clarke, R. G. Evans, K. W. D. Ledingham, F. Lindau, O. Lundh, T. McCanny, D. Neely, A. P. L. Robinson, L. Robson, P. T. Simpson, C. G. Wahlström, and M. Zepf. Lateral electron transport in high-intensity laser-irradiated foils diagnosed by ion emission. *Physical Review Letters*, 98(14):1–4, 2007.
- [157] D. A. Maclellan, D. C. Carroll, R. J. Gray, A. P. Robinson, M. P. Desjarlais, D. Neely, and P. McKenna. Influence of laser-drive parameters on annular fast electron transport in silicon. *Plasma Physics and Controlled Fusion*, 56(8), 2014.
- [158] V. T. Tikhonchuk. Interaction of a beam of fast electrons with solids. *Physics of Plasmas*, 9(4):1416, 2002.
- [159] B. Ramakrishna, S. Kar, A. P. Robinson, D. J. Adams, K. Markey, M. N. Quinn, X. H. Yuan, P. McKenna, K. L. Lancaster, J. S. Green, R. H. Scott, P. A. Norreys, J. Schreiber, and M. Zepf. Laser-driven fast electron collimation in targets with resistivity boundary. *Physical Review Letters*, 105(13):1–4, 2010.

- [160] Y. Sentoku, T. E. Cowan, A. Kemp, and H. Ruhl. High energy proton acceleration in interaction of short laser pulse with dense plasma target. *Physics of Plasmas*, 10(5 II):2009–2015, 2003.
- [161] P. Mora. Plasma Expansion into a Vacuum. *Physical Review Letters*, 90(18):4, 2003.
- [162] M. Passoni, L. Bertagna, and A. Zani. Target normal sheath acceleration: Theory, comparison with experiments and future perspectives. *New Journal of Physics*, 12, 2010.
- [163] P. McKenna, D. Neely, R. Bingham, and D. Jaroszynski. *Laser-plasma interactions and applications*. Springer, 2013.
- [164] J. L. Dubois, F. Lubrano-Lavaderci, D. Raffestin, J. Ribolzi, J. Gazave, A. C. L. Fontaine, E. D’Humieres, S. Hulin, P. Nicolai, A. Poye, and V. T. Tikhonchuk. Target charging in short-pulse-laser-plasma experiments. *Physical Review E - Statistical, Nonlinear, and Soft Matter Physics*, 89(1):1–15, 2014.
- [165] S. P. Hatchett, C. G. Brown, T. E. Cowan, E. a. Henry, J. S. Johnson, M. H. Key, J. a. Koch, a. B. Langdon, B. F. Lasinski, R. W. Lee, A. J. Mackinnon, D. M. Pennington, M. D. Perry, T. W. Phillips, M. Roth, T. C. Sangster, M. S. Singh, R. a. Snavely, M. a. Stoyer, S. C. Wilks, and K. Yasuike. Electron , photon , and ion beams from the relativistic interaction of Petawatt laser pulses with solid targets Electron , photon , and ion beams from the relativistic interaction of Petawatt laser pulses with solid targets *. *Physics of Plasmas*, 2076(5):2076–2082, 2000.
- [166] A. Link, R. R. Freeman, D. W. Schumacher, and L. D. Van Woerkom. Effects of target charging and ion emission on the energy spectrum of emitted electrons. *Physics of Plasmas*, 18(5), 2011.

- [167] T. Grismayer, P. Mora, J. C. Adam, and A. Héron. Electron kinetic effects in plasma expansion and ion acceleration. *Physical Review E - Statistical, Nonlinear, and Soft Matter Physics*, 77(6):1–11, 2008.
- [168] D. R. Rusby, C. D. Armstrong, G. G. Scott, M. King, P. McKenna, and D. Neely. Effect of Rear Surface Fields on Hot, Refluxing, and Escaping Electron Populations via PIC Simulations. *High Power Laser Science and Engineering*, forthcoming.
- [169] A. Higginson, R. J. Gray, M. King, R. J. Dance, S. D. Williamson, N. M. Butler, R. Wilson, R. Capdessus, C. Armstrong, J. S. Green, S. J. Hawkes, P. Martin, W. Q. Wei, S. R. Mirfayzi, X. H. Yuan, S. Kar, M. Borghesi, R. J. Clarke, D. Neely, and P. McKenna. Near-100 MeV protons via a laser-driven transparency-enhanced hybrid acceleration scheme. *Nature Communications*, 9(1), 2018.
- [170] C. M. Brenner, P. McKenna, and D. Neely. Modelling the effect of laser focal spot size on sheath-accelerated protons in intense laser-foil interactions. *Plasma Physics and Controlled Fusion*, 56(8), 2014.
- [171] C. M. Brenner, J. S. Green, A. P. Robinson, D. C. Carroll, B. Dromey, P. S. Foster, S. Kar, Y. T. Li, K. Markey, C. Spindloe, M. J. Streeter, M. Tolley, C. G. Wahlström, M. H. Xu, M. Zepf, P. McKenna, and D. Neely. Dependence of laser accelerated protons on laser energy following the interaction of defocused, intense laser pulses with ultra-thin targets. *Laser and Particle Beams*, 29(3):345–351, 2011.
- [172] E. L. Clark, K. Krushelnick, J. R. Davies, M. Zepf, M. Tatarakis, F. N. Beg, A. Machacek, P. A. Norreys, M. I. K. Santala, I. Watts, and A. E. Dangor. Measurements of energetic proton transport through magnetized plasma from intense laser interactions with solids. *Physical Review Letters*, 84(4):670–673, 2000.

- [173] J. Fuchs, P. Antici, E. D’Humières, E. Lefebvre, M. Borghesi, E. Brambrink, C. A. Cecchetti, M. Kaluza, V. Malka, M. Manclossi, S. Meyroneinc, P. Mora, J. Schreiber, T. Toncian, H. Pépin, and P. Audebert. Laser-driven proton scaling laws and new paths towards energy increase. *Nature Physics*, 2(1):48–54, 2006.
- [174] C. Li, Y.-Q. Cui, M.-L. Zhou, F. Du, Y.-T. Li, W.-M. Wang, L.-M. Chen, Z.-M. Sheng, J.-L. Ma, X. Lu, and J. Zhang. Role of resonance absorption in terahertz radiation generation from solid targets. *Optics Express*, 22(10):11797, 2014.
- [175] D. von der Linde, T. Engers, G. Jenke, P. Agostini, G. Grillon, E. Nibbering, A. Mysyrowicz, and A. Antonetti. Generation of high-order harmonics from solid surfaces by intense femtosecond laser pulses. *Physical Review A*, 52(1), 1995.
- [176] Spielmann, C., Burnett, N., Sartania, S., Koppitsch, R., Schnurer, M., Kan, Lenzner, Wobrauschek, P., Krausz, and F. Generation of Coherent X-ray Pulses in the Water Window Using 5 fs Laser Pulses. *Science*, 278 (October):661–664, 1997.
- [177] J. Larmor. On the theory of the magnetic influence on spectra; and on the radiation from moving ions. *The London, Edinburgh, and Dublin Philosophical Magazine and Journal of Science*, 44(271):503–512, 1897.
- [178] E. M. Purcell and D. J. Morin. *Electricity and magnetism*, volume 2nd. Cambridge University Press, 2013.
- [179] D. Giulietti and L. A. Gizzi. X-ray emission from laser-produced plasmas. *La Rivista del Nuovo Cimento*, 21(10):1–93, 1998.
- [180] M. Chatzikos, G. J. Ferland, R. J. R. Williams, R. Porter, and P. A. M. Van

- Hoof. Effects of external radiation fields on line emission - Application to star-forming regions. *Astrophysical Journal*, 779(2), 2013.
- [181] S. X. Hu and C. H. Keitel. Hollowing out single ions with high-power lasers. *Europhysics Letters*, 47(3):318–323, 1999.
- [182] F. B. Rosmej and R. W. Lee. Hollow ion emission driven by pulsed intense X-ray fields. *Epl*, 77(2), 2007.
- [183] J. Colgan, A. Y. Faenov, S. A. Pikuz, E. Tubman, N. M. Butler, J. Abdallah, R. J. Dance, T. A. Pikuz, I. Y. Skobelev, M. A. Alkhimova, N. Booth, J. Green, C. Gregory, A. Andreev, R. Löttsch, I. Uschmann, A. Zhidkov, R. Kodama, P. McKenna, and N. Woolsey. Evidence of high-n hollow-ion emission from Si ions pumped by ultraintense x-rays from relativistic laser plasma. *Epl*, 114(3), 2016.
- [184] K. L. Lancaster, J. S. Green, D. S. Hey, K. U. Akli, J. R. Davies, R. J. Clarke, R. R. Freeman, H. Habara, M. H. Key, R. Kodama, K. Krushelnick, C. D. Murphy, M. Nakatsutsumi, P. Simpson, R. Stephens, C. Stoeckl, T. Yabuuchi, M. Zepf, and P. A. Norreys. Measurements of energy transport patterns in solid density laser plasma interactions at intensities of $5 \times 10^{20} \text{Wcm}^{-2}$. *Physical Review Letters*, 98(12):1–4, 2007.
- [185] M. N. Quinn, X. H. Yuan, X. X. Lin, D. C. Carroll, O. Tresca, R. J. Gray, M. Coury, C. Li, Y. T. Li, C. M. Brenner, A. P. L. Robinson, D. Neely, B. Zielbauer, B. Aurand, J. Fils, T. Kuehl, and P. McKenna. Refluxing of fast electrons in solid targets irradiated by intense, picosecond laser pulses. *Plasma Physics and Controlled Fusion*, 53(2):1–12, 2011.
- [186] L. C. Jarrott, A. J. Kemp, L. Divol, D. Mariscal, B. Westover, C. McGuffey, F. N. Beg, M. Suggit, C. Chen, D. Hey, B. Maddox, J. Hawreliak, H. S. Park, B. Remington, M. S. Wei, and A. Macphee. $K\alpha$ and bremsstrahlung

- x-ray radiation backlighter sources from short pulse laser driven silver targets as a function of laser pre-pulse energy. *Physics of Plasmas*, 21(3), 2014.
- [187] H. S. Park, N. Izumi, M. H. Key, J. A. Koch, O. L. Landen, P. K. Patel, T. W. Phillips, and B. B. Zhang. Characteristics of high energy $K\alpha$ and Bremsstrahlung sources generated by short pulse petawatt lasers. *Review of Scientific Instruments*, 75(10 II):4048–4050, 2004.
- [188] H. S. Park, D. M. Chambers, H. K. Chung, R. J. Clarke, R. Eagleton, E. Giraldez, T. Goldsack, R. Heathcote, N. Izumi, M. H. Key, J. A. King, J. A. Koch, O. L. Landen, A. Nikroo, P. K. Patel, D. F. Price, B. A. Remington, H. F. Robey, R. A. Snavely, D. A. Steinman, R. B. Stephens, C. Stoeckl, M. Storm, M. Tabak, W. Theobald, R. P. J. Town, J. E. Wickersham, and B. B. Zhang. High-energy $K\alpha$ radiography using high-intensity, short-pulse lasers. *Physics of Plasmas*, 13(5), 2006.
- [189] P. Neumayer, B. Aurand, M. Basko, B. Ecker, P. Gibbon, D. C. Hochhaus, A. Karmakar, E. Kazakov, T. Köhl, C. Labaune, O. Rosmej, A. Tauschwitz, B. Zielbauer, and D. Zimmer. The role of hot electron refluxing in laser-generated K -alpha sources. *Physics of Plasmas*, 17(10), 2010.
- [190] P. Kirkpatrick. On the Theory and Use of Ross Filters. *Review of Scientific Instruments*, 10(186), 1939.
- [191] B. R. Maddox, H. S. Park, B. A. Remington, N. Izumi, S. Chen, C. Chen, G. Kimminau, Z. Ali, M. J. Haugh, and Q. Ma. High-energy x-ray backlighter spectrum measurements using calibrated image plates. *Review of Scientific Instruments*, 82(2), 2011.
- [192] A. Compant La Fontaine. X-ray emission reduction and photon dose lowering by energy loss of fast electrons induced by return current dur-

- ing the interaction of a short-pulse high-intensity laser on a metal solid target. *Physics of Plasmas*, 25(4), 2018.
- [193] H. Hall. The Theory of Photoelectric Absorption for X-Rays and γ -Rays. *Reviews of Modern Physics*, 8, 1936.
- [194] A. H. Compton. A Quantum Theory of the Scattering of X-rays by Light Elements. *Physical Review*, 21(5):483–502, 1923.
- [195] O. Klein and Y. Nishina. Über die Streuung von Strahlung durch freie Elektronen nach der neuen relativistischen Quantendynamik von Dirac. *Zeitschrift für Physik*, 52(11-12):853–868, 1929.
- [196] H. Hirayama. Lecture note on photon interactions and cross sections. *International Conference on the Monte Carlo 2000*, January, 2000.
- [197] J. H. \tilde{A} . Hubbell. Electron – positron pair production by photons : A historical overview. *Radiation Physics and Chemistry*, 75:614–623, 2006.
- [198] I. N. Ross, P. Matousek, M. Towrie, A. J. Langley, and J. L. Collier. The prospects for ultrashort pulse duration and ultrahigh intensity using optical parametric chirped pulse amplifiers. *Optics Communications*, 144(1-3):125–133, 1997.
- [199] J. L. Miquel, C. Lion, and P. Vivini. The Laser Mega-Joule : LMJ & PETAL status and Program Overview. *Journal of Physics: Conference Series*, 688(1):0–6, 2016.
- [200] A. Lévy, T. Ceccotti, P. D’Oliveira, F. Réau, M. Perdrix, F. Quéré, P. Monot, M. Bougeard, H. Lagadec, P. Martin, J.-P. Geindre, and P. Audebert. Double plasma mirror for ultrahigh temporal contrast ultraintense laser pulses. *Optics Letters*, 32(3):310, 2007.

- [201] C. Thaury, F. Quéré, J. P. Geindre, A. Levy, T. Ceccotti, P. Monot, M. Bougeard, F. Réau, P. D'Oliveira, P. Audebert, R. Marjoribanks, and P. Martin. Plasma mirrors for ultrahigh-intensity optics. *Nature Physics*, 3(6):424–429, 2007.
- [202] G. G. Scott, V. Bagnoud, C. Brabetz, R. J. Clarke, J. S. Green, R. I. Heathcote, H. W. Powell, B. Zielbauer, T. D. Arber, P. McKenna, and D. Neely. Optimization of plasma mirror reflectivity and optical quality using double laser pulses. *New Journal of Physics*, 17, 2015.
- [203] R. Wilson, M. King, R. J. Gray, D. C. Carroll, R. J. Dance, C. Armstrong, S. J. Hawkes, R. J. Clarke, D. Neely, P. McKenna, R. Wilson, M. King, R. J. Gray, D. C. Carroll, R. J. Dance, and C. Armstrong. Ellipsoidal plasma mirror focusing of high power laser pulses to ultra-high intensities Ellipsoidal plasma mirror focusing of high power laser pulses to ultra-high intensities. *Physics of Plasmas*, 23:33106, 2016.
- [204] R. J. Clarke, D. Neely, R. D. Edwards, P. N. Wright, K. W. Ledingham, R. Heathcote, P. McKenna, C. N. Danson, P. A. Brummitt, J. L. Collier, P. E. Hatton, S. J. Hawkes, C. Hernandez-Gomez, P. Holligan, M. H. Hutchinson, A. K. Kidd, W. J. Lester, D. R. Neville, P. A. Norreys, D. A. Pepler, T. B. Winstone, R. W. Wyatt, and B. E. Wyborn. Radiological characterisation of photon radiation from ultra-high-intensity laser-plasma and nuclear interactions. *Journal of Radiological Protection*, 26(3):277–286, 2006.
- [205] I. Sedgwick, D. Das, N. Guerrini, B. Marsh, and R. Turchetta. Wafer-Scale CMOS Sensor using a novel grid- addressing architecture. *Proceedings of the 2013 International Image Sensor Workshop*, pages 3–6, 2013.
- [206] A. L. Meadowcroft, C. D. Bentley, and E. N. Stott. Evaluation of the

- sensitivity and fading characteristics of an image plate system for x-ray diagnostics. *Review of Scientific Instruments*, 79(11):2–6, 2008.
- [207] T. Bonnet, M. Comet, D. Denis-Petit, F. Gobet, F. Hannachi, M. Tarisien, M. Versteegen, and M. M. Aléonard. Response functions of imaging plates to photons, electrons and 4He particles. *Review of Scientific Instruments*, 84(10), 2013.
- [208] C. Zulick, B. Hou, F. Dollar, A. Maksimchuk, J. Nees, A. G. R. Thomas, Z. Zhao, and K. Krushelnick. High resolution bremsstrahlung and fast electron characterization in ultrafast intense laser-solid interactions. *New Journal of Physics*, 15, 2013.
- [209] D. R. Rusby, L. A. Wilson, R. J. Gray, R. J. Dance, N. M. Butler, D. A. MacLellan, G. G. Scott, V. Bagnoud, B. Zielbauer, P. McKenna, and D. Neely. Measurement of the angle, temperature and flux of fast electrons emitted from intense laser-solid interactions. *Journal of Plasma Physics*, 81(5):1–9, 2015.
- [210] L. Wcislak, J. Schneider, T. Tschentscher, H. Klein, and H. Bunge. Hard X-ray texture measurements with an on-line image plate detector. *Nuclear Instruments and Methods in Physics Research Section A: Accelerators, Spectrometers, Detectors and Associated Equipment*, 467-468:1257–1260, 2001.
- [211] R. H. H. Scott, E. L. Clark, F. Pérez, M. J. V. Streeter, J. R. Davies, H. P. Schlenvoigt, J. J. Santos, S. Hulin, K. L. Lancaster, S. D. Baton, S. J. Rose, and P. A. Norreys. Measuring fast electron spectra and laser absorption in relativistic laser-solid interactions using differential bremsstrahlung photon detectors. *Review of Scientific Instruments*, 84(8), 2013.
- [212] S. G. Gales and C. D. Bentley. Image plates as x-ray detectors in plasma physics experiments. *Review of Scientific Instruments*, 75(10 II):4001–4003, 2004.

- [213] G. Fiksel, F. J. Marshall, C. Mileham, and C. Stoeckl. Note: Spatial resolution of Fuji BAS-TR and BAS-SR imaging plates. *Review of Scientific Instruments*, 83(8):88–91, 2012.
- [214] J. Seely, R. Doron, A. Bar-Shalom, L. T. Hudson, and C. Stoeckl. Hard X-ray emission from laser-produced plasmas of U and Pb recorded by a transmission crystal spectrometer. *Journal of Quantitative Spectroscopy & Radiative Transfer*, 81(1-4):421–429, 2003.
- [215] A. Pak, G. Gregori, J. Knight, K. Campbell, D. Price, B. Hammel, O. L. Landen, and S. H. Glenzer. X-ray line measurements with high efficiency Bragg crystals. *Review of Scientific Instruments*, 75(10 II):3747–3749, 2004.
- [216] D. C. Eder, G. Pretzler, E. Fill, K. Eidmann, and A. Saemann. Spatial characteristics of K-alpha radiation from weakly relativistic laser plasmas. *Applied Physics B*, 217:211–217, 2000.
- [217] W. Q. Wei, X. H. Yuan, Y. Fang, G. Q. Liao, H. H. An, Y. Q. Deng, J. Gao, X. L. Ge, N. Hua, P. Hu, W. M. Jiang, Y. F. Li, M. T. Li, S. Yang, T. Yang, X. P. Zhang, L. M. Chen, Y. T. Li, G. Y. Hu, C. B. Fu, F. Liu, M. Chen, B. Q. Zhu, J. Q. Zhu, Z. M. Sheng, and J. Zhang. Proton acceleration from vacuum-gapped double-foil target with low-contrast picosecond intense laser. *Physics of Plasmas*, 25(7):73108, 2018.
- [218] B. Bachmann, T. Hilsabeck, J. Field, N. Masters, C. Reed, T. Pardini, J. R. Rygg, N. Alexander, L. R. Benedetti, T. Döppner, A. Forsman, N. Izumi, S. Lepape, T. Ma, A. G. Macphee, S. Nagel, P. Patel, B. Spears, and O. L. Landen. Resolving hot spot microstructure using x-ray penumbral imaging (invited). *Review of Scientific Instruments*, 87(11), 2016.
- [219] K. A. Nugent and B. Luther-Davies. Penumbral imaging of high energy X-rays from laser-produced plasmas. *Optics Communications*, 49(6):393–396, 1984.

- [220] A. Ben-Ismaïl, O. Lundh, C. Rechatin, J. K. Lim, J. Faure, S. Corde, and V. Malka. Compact and high-quality gamma-ray source applied to 10 μm -range resolution radiography. *Applied Physics Letters*, 98(26):98–101, 2011.
- [221] A. Compant La Fontaine, C. Courtois, E. Lefebvre, J. L. Bourgade, O. Landoas, K. Thorp, and C. Stoeckl. Effects of electron recirculation on a hard x-ray source observed during the interaction of a high intensity laser pulse with thin Au targets. *Physics of Plasmas*, 20(12), 2013.
- [222] A. Döpp, E. Guillaume, C. Thauray, A. Lifschitz, F. Sylla, J. P. Goddet, A. Tafzi, G. Iaquanello, T. Lefrou, P. Rousseau, E. Conejero, C. Ruiz, K. Ta Phuoc, and V. Malka. A bremsstrahlung gamma-ray source based on stable ionization injection of electrons into a laser wakefield accelerator. *Nuclear Instruments and Methods in Physics Research, Section A: Accelerators, Spectrometers, Detectors and Associated Equipment*, 830:515–519, 2016.
- [223] B. Dolgoshein, V. Balagura, P. Buzhan, M. Danilov, L. Filatov, E. Garutti, and M. Groll. Status report on silicon photomultiplier development and its applications \$. *Nuclear Inst. and Methods in Physics Research, A*, 563: 368–376, 2006.
- [224] M. D. Wilson, L. Dummott, D. D. Duarte, F. H. Green, S. Pani, A. Schneider, J. W. Scuffham, P. Seller, and M. C. Veale. A 10 cm \times 10 cm CdTe Spectroscopic Imaging Detector based on the HEXITEC ASIC. *Journal of Instrumentation*, 10(10), 2015.
- [225] J. S. Green, M. Borghesi, C. M. Brenner, D. C. Carroll, N. P. Dover, P. S. Foster, P. Gallegos, S. Green, D. Kirby, K. J. Kirkby, P. McKenna, M. J. Merchant, Z. Najmudin, C. A. J. Palmer, D. Parker, R. Prasad, K. E. Quinn, P. P. Rajeev, M. P. Read, L. Romagnani, J. Schreiber, M. J. V.

Streeter, O. Tresca, C.-G. Wahlström, M. Zepf, and D. Neely. Scintillator-based ion beam profiler for diagnosing laser-accelerated ion beams. *Proc. SPIE 8079*, 807919(May 2011):807919, 2011.

[226] C. D. Chen. *Spectrum and Conversion Efficiency Measurements of Suprathermal Electrons from Relativistic Laser Plasma Interactions*. PhD thesis, Diss. Massachusetts Institute of Technology, 2009.

[227] S. Agostinelli, J. Allison, K. Amako, J. Apostolakis, H. Araujo, P. Arce, M. Asai, D. Axen, S. Banerjee, G. Barrand, F. Behner, L. Bellagamba, J. Boudreau, L. Broglia, A. Brunengo, H. Burkhardt, S. Chauvie, J. Chuma, R. Chytracsek, G. Cooperman, G. Cosmo, P. Degtyarenko, A. Dell'Acqua, G. Depaola, D. Dietrich, R. Enami, A. Feliciello, C. Ferguson, H. Fesefeldt, G. Folger, F. Foppiano, A. Forti, S. Garelli, S. Giani, R. Giannitrapani, D. Gibin, J. J. Gomez Cadenas, I. Gonzalez, G. Gracia Abril, G. Greeniaus, W. Greiner, V. Grichine, A. Grossheim, S. Guatelli, P. Gumplinger, R. Hamatsu, K. Hashimoto, H. Hasui, A. Heikkinen, A. Howard, V. Ivanchenko, A. Johnson, F. W. Jones, J. Kallenbach, N. Kanaya, M. Kawabata, Y. Kawabata, M. Kawaguti, S. Kelner, P. Kent, A. Kimura, T. Kodama, R. Kokoulin, M. Kossov, H. Kurashige, E. Lamanna, T. Lampen, V. Lara, V. Lefebure, F. Lei, M. Liendl, W. Lockman, F. Longo, S. Magni, M. Maire, E. Medernach, K. Minamimoto, P. Mora de Freitas, Y. Morita, K. Murakami, M. Nagamatu, R. Nartallo, P. Nieminen, T. Nishimura, K. Ohtsubo, M. Okamura, S. O'Neale, Y. Oohata, K. Paech, J. Perl, A. Pfeiffer, M. G. Pia, F. Ranjard, A. Rybin, S. Sadilov, E. di Salvo, G. Santin, T. Sasaki, N. Savvas, Y. Sawada, S. Scherer, S. Sei, V. Sirotenko, D. Smith, N. Starkov, H. Stoecker, J. Sulkimo, M. Takahata, S. Tanaka, E. Tcherniaev, E. Safai Tehrani, M. Tropeano, P. Truscott, H. Uno, L. Urban, P. Urban, M. Verderi, A. Walkden, W. Wander, H. Weber, J. P. Wellisch, T. We-

- naus, D. C. Williams, D. Wright, T. Yamada, H. Yoshida, and D. Zscheische. GEANT4 - A simulation toolkit. *Nuclear Instruments and Methods in Physics Research, Section A: Accelerators, Spectrometers, Detectors and Associated Equipment*, 506(3):250–303, 2003.
- [228] J. Allison, K. Amako, J. Apostolakis, H. Araujo, P. A. Dubois, M. Asai, G. Barrand, R. Capra, S. Chauvie, R. Chytracsek, G. A. P. Cirrone, G. Cooperman, G. Cosmo, G. Cuttone, G. G. Daquino, M. Donszelmann, M. Dressel, G. Folger, F. Foppiano, J. Generowicz, V. Grichine, S. Guatelli, P. Gumplinger, A. Heikkinen, I. Hrivnacova, A. Howard, S. Incerti, V. Ivanchenko, T. Johnson, F. Jones, T. Koi, R. Kokoulin, M. Kossov, H. Kurashige, V. Lara, S. Larsson, F. Lei, F. Longo, M. Maire, A. Mantero, B. Mascialino, I. McLaren, P. M. Lorenzo, K. Minamimoto, K. Murakami, P. Nieminen, L. Pandola, S. Parlati, L. Peralta, J. Perl, A. Pfeiffer, M. G. Pia, A. Ribon, P. Rodrigues, G. Russo, S. Sadilov, G. Santin, T. Sasaki, D. Smith, N. Starkov, S. Tanaka, E. Tcherniaev, B. Tomé, A. Trindade, P. Truscott, L. Urban, M. Verderi, A. Walkden, J. P. Wellisch, D. C. Williams, D. Wright, H. Yoshida, and M. Peirgentili. Geant4 developments and applications. *IEEE Transactions on Nuclear Science*, 53(1):270–278, 2006.
- [229] J. Allison, L. Garnier, A. Kimura, and J. Perl. The Geant4 visualization system—a multi-driver graphics system. *International Journal of Modeling, Simulation, and Scientific Computing*, 4(supp01):1340001, 2013.
- [230] C. Reich, P. Gibbon, I. Uschmann, and E. Forster. Yield optimization and time structure of femtosecond laser plasma kalpha sources. *Physical review letters*, 84(21):4846–4849, 2000.
- [231] M. S. Wei, A. A. Solodov, J. Pasley, R. B. Stephens, D. R. Welch, and F. N. Beg. Study of relativistic electron beam production and transport

in high-intensity laser interaction with a wire target by integrated LSP modeling. *Physics of Plasmas*, 15(8):0–7, 2008.

- [232] A. Poyé, S. Hulin, M. Bailly-Grandvaux, J. L. Dubois, J. Ribolzi, D. Raffestin, M. Bardon, F. Lubrano-Lavaderci, E. D’Humières, J. J. Santos, P. Nicolai, and V. Tikhonchuk. Physics of giant electromagnetic pulse generation in short-pulse laser experiments. *Physical Review E - Statistical, Nonlinear, and Soft Matter Physics*, 91(4):1–7, 2015.
- [233] H. Chen and S. C. Wilks. Evidence of enhanced effective hot electron temperatures in ultraintense laser-solid interactions due to reflexing. *Laser and Particle Beams*, 23(4):411–416, 2005.
- [234] A. J. Mackinnon, Y. Sentoku, P. K. Patel, D. W. Price, S. Hatchett, M. H. Key, C. Andersen, R. Snavely, and R. R. Freeman. Enhancement of proton acceleration by hot-electron recirculation in thin foils irradiated by ultraintense laser pulses. *Physical Review Letters*, 88(21):2150061–2150064, 2002.
- [235] C. A. Cecchetti, M. Borghesi, J. Fuchs, G. Schurtz, S. Kar, A. MacChi, L. Romagnani, P. A. Wilson, P. Antici, R. Jung, J. Osterholtz, C. A. Pipahl, O. Willi, A. Schiavi, M. Notley, and D. Neely. Magnetic field measurements in laser-produced plasmas via proton deflectometry. *Physics of Plasmas*, 16(4), 2009.
- [236] L. Romagnani, M. Borghesi, C. A. Cecchetti, S. Kar, P. Antici, P. Audebert, S. Bandhoupadjay, F. Ceccherini, T. Cowan, J. Fuchs, M. Galimberti, L. A. Gizzi, T. Grismayer, R. Heathcote, R. Jung, T. V. Liseykina, A. MacChi, P. Mora, D. Neely, M. Notley, J. Osterholtz, C. A. Pipahl, G. Pretzler, A. Schiavi, G. Schurtz, T. Toncian, P. A. Wilson, and O. Willi. Proton probing measurement of electric and magnetic fields generated by ns

- and ps laser-matter interactions. *Laser and Particle Beams*, 26(2):241–248, 2008.
- [237] K. Quinn, P. A. Wilson, B. Ramakrishna, L. Romagnani, G. Sarri, C. A. Cecchetti, L. Lancia, J. Fuchs, A. Pipahl, T. Toncian, O. Willi, R. J. Clarke, D. Neely, M. Notley, P. Gallegos, D. C. Carroll, M. N. Quinn, X. H. Yuan, P. McKenna, and M. Borghesi. Modified proton radiography arrangement for the detection of ultrafast field fronts. *Review of Scientific Instruments*, 80(11), 2009.
- [238] L. Romagnani, J. Fuchs, M. Borghesi, P. Antici, P. Audebert, F. Ceccherini, T. Cowan, T. Grismayer, S. Kar, A. MacChi, P. Mora, G. Pretzler, A. Schiavi, T. Toncian, and O. Willi. Dynamics of electric fields driving the laser acceleration of multi-MeV protons. *Physical Review Letters*, 95(19):4–7, 2005.
- [239] P. Bradford, N. C. Woolsey, G. G. Scott, G. Liao, H. Liu, Y. Zhang, B. Zhu, C. Armstrong, S. Astbury, C. Brenner, P. Brummitt, F. Consoli, I. East, R. Gray, D. Haddock, P. Huggard, P. J. R. Jones, E. Montgomery, I. Musgrave, P. Oliveira, D. R. Rusby, C. Spindloe, B. Summers, E. Zemaityte, Z. Zhang, Y. Li, P. McKenna, and D. Neely. EMP control and characterization on high-power laser systems. *High Power Laser Science and Engineering*, 6(e21):8, 2018.
- [240] H. Liu, G. Liao, Y. Zhang, B. Zhu, Z. Zhang, Y. Li, G. G. Scott, D. R. Rusby, C. Armstrong, D. C. Carroll, S. Astbury, P. Bradford, N. C. Woolsey, P. Mckenna, D. Neely, H. Liu, G. Liao, Y. Zhang, B. Zhu, Z. Zhang, Y. Li, G. G. Scott, N. C. Woolsey, P. Mckenna, and D. Neely. Cherenkov radiation-based optical fibre diagnostics of fast electrons generated in intense laser-plasma interactions Cherenkov radiation-based optical fibre

diagnostics of fast electrons generated in intense laser-plasma interactions. *Review of Scientific Instruments*, 083302, 2018.

- [241] C. Reich, I. Uschmann, F. Ewald, S. Düsterer, A. Lübcke, H. Schwoerer, R. Sauerbrey, E. Förster, and P. Gibbon. Spatial characteristics of K-alpha x-ray emission from relativistic femtosecond laser plasmas. *Physical Review E*, 68(5):56408, 2003.
- [242] D. Riley, J. J. Angulo-Gareta, F. Y. Khattak, M. J. Lamb, P. S. Foster, E. J. Divall, C. J. Hooker, A. J. Langley, R. J. Clarke, and D. Neely. $K\alpha$ yields from Ti foils irradiated with ultrashort laser pulses. *Physical Review E - Statistical, Nonlinear, and Soft Matter Physics*, 71(1):1–7, 2005.
- [243] P. M. Nilson, A. A. Solodov, J. F. Myatt, W. Theobald, P. A. Jaanimagi, L. Gao, C. Stoeckl, R. S. Craxton, J. A. Delettrez, B. Yaakobi, J. D. Zuegel, B. E. Kruschwitz, C. Dorrer, J. H. Kelly, K. U. Akli, P. K. Patel, A. J. Mackinnon, R. Betti, T. C. Sangster, and D. D. Meyerhofer. Scaling hot-electron generation to long-pulse, high-intensity laser-solid interactions. *Physics of Plasmas*, 18(5):1–4, 2011.
- [244] Y. Ping, R. Shepherd, B. F. Lasinski, M. Tabak, H. Chen, H. K. Chung, K. B. Fournier, S. B. Hansen, A. Kemp, D. A. Liedahl, K. Widmann, S. C. Wilks, W. Rozmus, and M. Sherlock. Absorption of short laser pulses on solid targets in the ultrarelativistic regime. *Physical Review Letters*, 100(8):6–9, 2008.
- [245] R. J. Gray, R. Wilson, M. King, S. D. R. Williamson, R. J. Dance, C. Armstrong, C. Brabetz, F. Wagner, B. Zielbauer, V. Bagnoud, D. Neely, and P. McKenna. Enhanced laser-energy coupling to dense plasmas driven by recirculating electron currents. *NJP*, 2018.
- [246] J. Peebles, M. S. Wei, A. V. Arefiev, C. McGuffey, R. B. Stephens, W. Theobald, D. Haberberger, L. C. Jarrott, A. Link, H. Chen, H. S.

- McLean, A. Sorokovikova, S. Krasheninnikov, and F. N. Beg. Investigation of laser pulse length and pre-plasma scale length impact on hot electron generation on OMEGA-EP. *New Journal of Physics*, 19(2), 2017.
- [247] Y. Oishi, T. Nayuki, T. Fujii, Y. Takizawa, X. Wang, T. Yamazaki, K. Nemoto, T. Kayoiji, T. Sekiya, K. Horioka, Y. Okano, Y. Hironaka, K. G. Nakamura, K. Kondo, and A. A. Andreev. Dependence on laser intensity and pulse duration in proton acceleration by irradiation of ultrashort laser pulses on a Cu foil target. *Physics of Plasmas*, 12(7):1–5, 2005.
- [248] C. D. Armstrong, C. M. Brenner, E. Zemaityte, G. G. Scott, and D. R. Rusby. Bremsstrahlung emission profile from intense laser-solid interactions as a function of laser focal spot size. *Plasma Physics and Controlled Fusion*, 61:034001, 2019.
- [249] R. Kodama, P. A. Norreys, K. Mima, A. E. Dangor, R. G. Evans, H. Fujita, Y. Kitagawa, K. Krushelnick, T. Miyakoshi, N. Miyanaga, T. Norimatsu, S. J. Rose, T. Shozaki, K. Shigemori, A. Sunahara, M. Tambo, K. A. Tanaka, Y. Toyama, T. Yamanaka, and M. Zepf. Fast heating of ultrahigh-density plasma as a step towards laser fusion ignition. *Nature*, 2001.
- [250] A. G. MacPhee, L. Divol, A. J. Kemp, K. U. Akli, F. N. Beg, C. D. Chen, H. Chen, D. S. Hey, R. J. Fedosejevs, R. R. Freeman, M. Henesian, M. H. Key, S. Le Pape, A. Link, T. Ma, A. J. MacKinnon, V. M. Ovchinnikov, P. K. Patel, T. W. Phillips, R. B. Stephens, M. Tabak, R. Town, Y. Y. Tsui, L. D. Van Woerkom, M. S. Wei, and S. C. Wilks. Limitation on prepulse level for cone-guided fast-ignition inertial confinement Fusion. *Physical Review Letters*, 104(5):1–4, 2010.
- [251] J. S. Green, K. L. Lancaster, K. U. Akli, C. D. Gregory, F. N. Beg, S. N. Chen, D. Clark, R. R. Freeman, S. Hawkes, C. Hernandez-Gomez,

- H. Habara, R. Heathcote, D. S. Hey, K. Highbarger, M. H. Key, R. Kodama, K. Krushelnick, I. Musgrave, H. Nakamura, M. Nakatsutsumi, N. Patel, R. Stephens, M. Storm, M. Tambo, W. Theobald, L. Van Wierkom, R. L. Weber, M. S. Wei, N. C. Woolsey, and P. A. Norreys. Surface heating of wire plasmas using laser-irradiated cone geometries. *Nature Physics*, 3(12):853–856, 2007.
- [252] K. U. Akli, R. B. Stephens, M. H. Key, T. Bartal, F. N. Beg, S. Chawla, and C. D. Chen. Hot Electron Generation and Transport Using K (alpha) Emission. *Journal of Physics*, 2009.
- [253] D. P. Higginson, A. Link, H. Sawada, S. C. Wilks, T. Bartal, S. Chawla, C. D. Chen, K. A. Flippo, L. C. Jarrott, M. H. Key, H. S. McLean, P. K. Patel, F. Pérez, M. S. Wei, and F. N. Beg. High-contrast laser acceleration of relativistic electrons in solid cone-wire targets. *Physical Review E - Statistical, Nonlinear, and Soft Matter Physics*, 92(6):1–6, 2015.
- [254] A. P. L. Robinson, R. M. G. M. Trines, J. Polz, and M. Kaluza. Absorption of circularly polarized laser pulses in near-critical plasmas. *Plasma Physics and Controlled Fusion*, 53(6), 2011.
- [255] M. Dunne, M. Borghesi, A. Iwase, M. W. Jones, R. Taylor, O. Willi, R. Gibson, S. R. Goldman, J. Mack, and R. G. Watt. Evaluation of a foam buffer target design for spatially uniform ablation of laser-irradiated plasmas. *Physical Review Letters*, 75(21):3858–3861, 1995.
- [256] J. Limpouch, N. N. Demchenko, S. Y. Gus'kov, M. Kálal, A. Kasperczuk, V. N. Kondrashov, E. Krouský, K. Mašek, P. Pisarczyk, T. Pisarczyk, and V. B. Rozanov. Laser interactions with plastic foam - Metallic foil layered targets. *Plasma Physics and Controlled Fusion*, 46(12 A):1831–1841, 2004.
- [257] H. B. Cai, S. P. Zhu, X. T. He, S. Z. Wu, M. Chen, C. Zhou, W. Yu, and H. Nagatomo. Magnetic collimation of fast electrons in specially engi-

- neered targets irradiated by ultraintense laser pulses. *Physics of Plasmas*, 18(2), 2011.
- [258] A. P. L. Robinson, H. Schmitz, J. S. Green, C. P. Ridgers, N. Booth, and J. Pasley. Control of wire heating with resistively guided fast electrons through an inverse conical taper. *Physics of Plasmas*, 22(4), 2015.
- [259] L. Willingale, S. R. Nagel, A. G. R. Thomas, C. Bellei, R. J. Clarke, A. E. Dangor, R. Heathcote, M. C. Kaluza, C. Kamperidis, S. Kneip, K. Krushelnick, N. Lopes, S. P. D. Mangles, W. Nazarov, P. M. Nilson, and Z. Najmudin. Characterization of high-intensity laser propagation in the relativistic transparent regime through measurements of energetic proton beams. *Physical Review Letters*, 102(12):1–4, 2009.
- [260] D. Riley. Generation and characterisation of warm dense matter in the laboratory. *Plasma Physics and Controlled Fusion*, page 44, 2018.
- [261] S. Jiang, A. G. Krygier, D. W. Schumacher, K. U. Akli, and R. R. Freeman. Enhancing Bremsstrahlung production from ultraintense laser-solid interactions with front surface structures. *European Physical Journal D*, 68(10):55–57, 2014.
- [262] J. Jarrett, M. King, R. J. Gray, N. Neumann, L. Döhl, C. D. Baird, T. Ebert, M. Hesse, A. Tebartz, D. R. Rusby, N. C. Woolsey, D. Neely, M. Roth, and P. McKenna. Reflection of intense laser light from microstructured targets as a potential diagnostic of laser focus and plasma temperature. *High Power Laser Science and Engineering*, 7:1–7, 2018.
- [263] D. R. Rusby, C. D. Armstrong, C. M. Brenner, P. McKenna, and D. Neely. Novel Scintillator based x-ray spectrometer for use on high repetition laser plasma interaction. *Review of Scientific Instruments*, 073502, 2018.

- [264] M. Zepf, M. Castro-colin, D. Chambers, S. G. Preston, J. S. Wark, J. Zhang, C. N. Danson, D. Neely, P. A. Norreys, A. E. Dangor, A. Dyson, P. Lee, A. P. Fews, P. Gibbon, S. Moustazis, and M. H. Key. Measurements of the hole boring velocity from Doppler shifted harmonic emission from solid targets. *Physics of Plasmas*, 1996.
- [265] E. C. Welch, P. Zhang, F. Dollar, Z. H. He, K. Krushelnick, and A. G. Thomas. Time dependent Doppler shifts in high-order harmonic generation in intense laser interactions with solid density plasma and frequency chirped pulses. *Physics of Plasmas*, 22(5), 2015.
- [266] H. Vincenti, S. Monchocé, S. Kahaly, G. Bonnaud, P. Martin, and F. Quéré. Optical properties of relativistic plasma mirrors. *Nature Communications*, 5:1–9, 2014.
- [267] J. C. Kieffer, A. Krol, Z. Jiang, C. C. Chamberlain, E. Scalzetti, and Z. Ichalalene. Future of laser-based X-ray sources for medical imaging. *Applied Physics B: Lasers and Optics*, 74(SUPPL.):75–81, 2002.
- [268] M. P. Kalashnikov, P. V. Nickles, T. Schlegel, M. Schnuerer, F. Billhardt, I. Will, W. Sandner, and N. N. Demchenko. Dynamics of laser-plasma interaction at 1018 W/cm². *Physical Review Letters*, 73(2):260–263, 1994.
- [269] T. Nakamura, S. Kato, H. Nagatomo, and K. Mima. Surface-magnetic-field and fast-electron current-layer formation by ultraintense laser irradiation. *Physical Review Letters*, 93(26 I):1–4, 2004.
- [270] Y. Y. Ma, Z. M. Sheng, Y. T. Li, W. W. Chang, X. H. Yuan, M. Chen, H. C. Wu, J. Zheng, and J. Zhang. Dense quasi-monoenergetic attosecond electron bunches from laser interaction with wire and slice targets. *Physics of Plasmas*, 13(11), 2006.

- [271] M. Chen, Z.-m. Sheng, J. Zheng, Y.-y. Ma, M. Bari, Y.-t. Li, and J. Zhang. Surface electron acceleration in relativistic laser-solid interactions. *Optics Express*, 14(7):3093, 2006.
- [272] J. Y. Mao, L. M. Chen, X. L. Ge, L. Zhang, W. C. Yan, D. Z. Li, G. Q. Liao, J. L. Ma, K. Huang, Y. T. Li, X. Lu, Q. L. Dong, Z. Y. Wei, Z. M. Sheng, and J. Zhang. Spectrally peaked electron beams produced via surface guiding and acceleration in femtosecond laser-solid interactions. *Physical Review E - Statistical, Nonlinear, and Soft Matter Physics*, 85(2):1–4, 2012.
- [273] N. E. Andreev, L. P. Pugachev, M. E. Povarnitsyn, and P. R. Levashov. Electron acceleration at grazing incidence of a subpicosecond intense laser pulse onto a plane solid target. *Laser and Particle Beams*, 34(1):115–122, 2016.
- [274] A. Pukhov. Strong field interaction of laser radiation. *Reports on Progress in Physics*, 66(1):47, 2003.
- [275] R. J. Gray, X. H. Yuan, D. C. Carroll, C. M. Brenner, M. Coury, M. N. Quinn, O. Tresca, B. Zielbauer, B. Aurand, V. Bagnoud, J. Fils, T. Kühl, X. X. Lin, C. Li, Y. T. Li, M. Roth, D. Neely, and P. McKenna. Surface transport of energetic electrons in intense picosecond laser-foil interactions. *Applied Physics Letters*, 99(17):8–11, 2011.
- [276] Y. T. Li, X. H. Yuan, M. H. Xu, Z. Y. Zheng, Z. M. Sheng, M. Chen, Y. Y. Ma, W. X. Liang, Q. Z. Yu, Y. Zhang, F. Liu, Z. H. Wang, Z. Y. Wei, W. Zhao, Z. Jin, and J. Zhang. Observation of a fast electron beam emitted along the surface of a target irradiated by intense femtosecond laser pulses. *Physical Review Letters*, 96(16):2–5, 2006.
- [277] A. Sorokovikova, A. V. Arefiev, C. McGuffey, B. Qiao, A. P. Robinson, M. S. Wei, H. S. McLean, and F. N. Beg. Generation of superponderomo-

- tive electrons in multipicosecond interactions of kilojoule laser beams with solid-density plasmas. *Physical Review Letters*, 116(15):1–5, 2016.
- [278] A. Pukhov, Z. M. Sheng, and J. Meyer-ter Vehn. Particle acceleration in relativistic laser channels. *Physics of Plasmas*, 6(7):2847–2854, 1999.
- [279] Z. Gong, A. P. L. Robinson, X. Q. Yan, and A. V. Arefiev. Highly collimated electron acceleration by longitudinal laser fields in a hollow-core target. *Plasma Physics and Controlled Fusion*, pages 1–15, 2018.
- [280] P. Goby. New Application of the X-rays: Micro-radiography. *Journal of the Royal Microscopical Society*, 33(4):373–375, 1913.
- [281] B. H. Hasegawa. *The physics of medical x-ray imaging*. Medical Physics Pub Co, 1990.
- [282] R. A. Lewis. Medical phase contrast x-ray imaging: Current status and future prospects. *Physics in Medicine and Biology*, 49(16):3573–3583, 2004.
- [283] P. Cloetens, R. Barrett, J. Baruchel, J. P. Guigay, and M. Schlenker. Phase objects in synchrotron radiation hard x-ray imaging. *Journal of Physics D: Applied Physics*, 29(1):133–146, 1996.
- [284] C. A. Stitt, N. J. Harker, K. R. Hallam, C. Paraskevoulakos, A. Banos, S. Rennie, J. Jowsey, and T. B. Scott. An investigation on the persistence of uranium hydride during storage of simulant nuclear waste packages. *PLoS ONE*, 10(7):1–13, 2015.
- [285] L. Auditore, R. C. Barna, D. De Pasquale, A. Italiano, A. Trifiro, and M. Trimarchi. Study of a 5 MeV electron linac based neutron source. *Nuclear Instruments and Methods in Physics Research, Section B: Beam Interactions with Materials and Atoms*, 229(1):137–143, 2005.

- [286] F. Pfeiffer, T. Weitkamp, O. Bunk, and C. David. Phase retrieval and differential phase-contrast imaging with low-brilliance X-ray sources. *Nature Physics*, 2(4):258–261, 2006.
- [287] R. J. Gray, R. Wilson, M. King, S. D. R. Williamson, R. J. Dance, C. Armstrong, C. Brabetz, F. Wagner, B. Zielbauer, V. Bagnoud, D. Neely, and P. McKenna. Enhanced laser-energy coupling to dense plasmas driven by recirculating electron currents. *New Journal of Physics*, 20(3), 2018.
- [288] G. H. McCall. Calculation of X-ray bremsstrahlung and characteristic line emission produced by a Maxwellian electron distribution. *Journal of Physics D: Applied Physics*, 15(5):823–831, 1982.
- [289] J. Galy, M. Maučec, D. J. Hamilton, R. Edwards, and J. Magill. Bremsstrahlung production with high-intensity laser matter interactions and applications. *New Journal of Physics*, 9(23), 2007.
- [290] C. Courtois, R. Edwards, A. Compant La Fontaine, C. Aedy, S. Bazzoli, J. L. Bourgade, J. Gazave, J. M. Lagrange, O. Landoas, L. L. Dain, D. Mastro Simone, N. Pichoff, G. Pien, and C. Stoeckl. Characterisation of a MeV Bremsstrahlung x-ray source produced from a high intensity laser for high areal density object radiography. *Physics of Plasmas*, 20(8):083114, 2013.
- [291] E. Acosta, X. Llovet, and F. Salvat. Monte Carlo simulation of bremsstrahlung emission by electrons. *Applied Physics Letters*, 80(17):3228–3230, 2002.
- [292] C. P. Jones, C. M. Brenner, C. D. Armstrong, D. R. Rusby, Z. Davidson, J. Wragg, Y. Zhang, S. Richards, M. Notley, S. R. Mirfayzi, A. Adamska, J. Jowsey, S. Kar, D. Neely, and T. B. Scott. Assessing High-energy, Laser-driven, X-ray Sources as a Technique to Analyse ILW Containers. *WM2018 Conference*, 18242, 2018.

- [293] M. Endrizzi. X-ray phase-contrast imaging. *Nuclear Instruments and Methods in Physics Research, Section A: Accelerators, Spectrometers, Detectors and Associated Equipment*, 878:88–98, 2018.
- [294] J. Cole, J. Wood, N. Lopes, K. Poder, R. Abel, S. Alatabi, J. Bryant, A. Jin, S. Kneip, K. Mecseki, et al. Laser-wakefield accelerators as hard x-ray sources for 3d medical imaging of human bone. *Scientific reports*, 5:13244, 2015.
- [295] S. Gobain. Saint Gobain Scintillator Properties, 2018. URL <https://www.crystals.saint-gobain.com/products/crystal-scintillation-materials>.
- [296] L. De Broglie. The wave nature of the electron. *Nobel lectures, Physics 1922-1941*, pages 244–256, 1929.
- [297] G. Aad, J. Butterworth, J. Thion, U. Bratzler, P. Ratoff, R. Nickerson, J. Seixas, I. Grabowska-Bold, F. Meisel, S. Lokwitz, et al. The atlas experiment at the cern large hadron collider. *Jinst*, 3:S08003, 2008.
- [298] S. P. Mangles, C. Murphy, Z. Najmudin, A. G. R. Thomas, J. Collier, A. E. Dangor, E. Divall, P. Foster, J. Gallacher, C. Hooker, et al. Monoenergetic beams of relativistic electrons from intense laser–plasma interactions. *Nature*, 431(7008):535, 2004.
- [299] J. Faure, Y. Glinec, A. Pukhov, S. Kiselev, S. Gordienko, E. Lefebvre, J.-P. Rousseau, F. Burgy, and V. Malka. A laser–plasma accelerator producing monoenergetic electron beams. *Nature*, 431(7008):541, 2004.
- [300] C. Hooker, J. Collier, O. Chekhlov, R. Clarke, E. Divall, K. Ertel, B. Fell, P. Foster, S. Hancock, A. Langley, et al. The astra gemini project—a dual-beam petawatt ti: Sapphire laser system. In *Journal de Physique IV (Proceedings)*, volume 133, pages 673–677. EDP sciences, 2006.

- [301] K. Poder, M. Tamburini, G. Sarri, A. Di Piazza, S. Kuschel, C. Baird, K. Behm, S. Bohlen, J. Cole, D. Corvan, et al. Experimental signatures of the quantum nature of radiation reaction in the field of an ultraintense laser. *Physical Review X*, 8(3):031004, 2018.
- [302] J. F. W. Mosselmans, P. D. Quinn, A. J. Dent, S. A. Cavill, S. D. Moreno, A. Peach, P. J. Leicester, S. J. Keylock, S. R. Gregory, D. Atkinson, and J. Roque. research papers I18 – the microfocus spectroscopy beamline at the Diamond Light Source research papers. *Journal of Synchrotron Radiation*, pages 818–824, 2009.
- [303] A. J. Gonsalves, K. Nakamura, J. Daniels, C. Benedetti, C. Pieronek, T. C. De Raadt, S. Steinke, J. H. Bin, S. S. Bulanov, J. Van Tilborg, C. G. Geddes, C. B. Schroeder, C. Tóth, E. Esarey, K. Swanson, L. Fan-Chiang, G. Bagdasarov, N. Bobrova, V. Gasilov, G. Korn, P. Sasorov, and W. P. Leemans. Petawatt Laser Guiding and Electron Beam Acceleration to 8 GeV in a Laser-Heated Capillary Discharge Waveguide. *Physical Review Letters*, 122(8):84801, 2019.